

J/ψ Production in High Energy Heavy Ion
Collisions at RHIC

Taku Gunji

Submitted to the Department of Physics,
Graduate School of Science
in partial fulfillment of the requirements
for the the degree of Doctor of Science
at University of Tokyo

February, 2007

Abstract

High-energy heavy-ion collision is a powerful tool in the laboratory to realize the phase transition from ordinary nuclear matter to a deconfined quarks and gluons, called Quark-Gluon-Plasma (QGP), which is predicted to be formed above a temperature of order $T_c \sim 170$ MeV in lattice Quantum Chromodynamics (QCD). Suppression of J/ψ production has been considered as one of the most promising signatures for the deconfinement of matter since J/ψ production is expected to be suppressed due to the color Debye screening in QGP.

J/ψ production has been measured by the PHENIX experiment, which is one of the major experiments at the Relativistic Heavy Ion Collider (RHIC) at Brookhaven National Laboratory (BNL), in $p+p$, $d+Au$, $Au+Au$ and $Cu+Cu$ collisions at the center of mass energy per nucleon ($\sqrt{s_{NN}}$) of 200 GeV.

The measurement of J/ψ production in $Au+Au$ collisions at $\sqrt{s_{NN}} = 200$ GeV has been performed at mid-rapidity region ($|\eta| \leq 0.5$) using the PHENIX detector in order to understand the J/ψ production in hot and dense medium created at RHIC energy.

It is observed that the yield of J/ψ is strongly suppressed by a factor of ~ 4 in central $Au+Au$ collisions with respect to that in $p+p$ collisions scaled by the average number of nucleon-nucleon collisions. This is the first high statistic result which clearly shows that J/ψ production is suppressed in $Au+Au$ collisions at RHIC energy. J/ψ suppression in $Au+Au$ collisions is stronger than the expectation from cold nuclear matter effects such as nuclear absorption of J/ψ in nuclear environment and gluon shadowing, which were extrapolated from $d+Au$ collisions performed at RHIC. Survival probability of J/ψ in hot and dense medium created in $Au+Au$ collisions was calculated by dividing J/ψ yield in $Au+Au$ collisions by the expectation of J/ψ yield with only the cold nuclear matter effects. The survival probability of J/ψ at RHIC energy is quite similar to that observed at SPS energies from peripheral to mid-central $Au+Au$ collisions and stronger in central $Au+Au$ collisions.

The author constructed the model to study J/ψ suppression at RHIC energy, which incorporated the recent lattice QCD results for J/ψ melting and feed down effect from χ_c and ψ' decay to J/ψ , into the hydrodynamical space-time evolution of the colliding system. With this model, J/ψ suppression at RHIC can be reproduced well as a result of sequential melting of J/ψ , first from χ_c and ψ' decay in mid-central $Au+Au$ collisions and second from “directly” produced J/ψ in central $Au+Au$ collisions. The melting temperature of “directly” produced J/ψ is estimated to be $(2.12^{+0.09}_{-0.03})T_c$ with this model. This result is in good agreement with the predictions from lattice QCD calculations and potential model analyses.

Contents

1	Introduction	1
1.1	Objectives of This Thesis	1
1.2	Quark-Gluon-Plasma (QGP)	2
1.3	Relativistic Heavy Ion Collisions	4
1.3.1	Collision geometry of heavy-ion collisions	5
1.3.2	Evolution of the matter in heavy-ion collisions	5
1.3.3	Initial energy density	7
1.4	Organization of This Thesis	9
1.5	Major Contributions	9
2	Physics Background	11
2.1	Charmonium Family	11
2.2	J/ψ Production Mechanism	12
2.2.1	Color singlet model (CSM)	12
2.2.2	Color evaporation model (CEM)	14
2.2.3	Color octet model (COM)	14
2.3	Feed-down Effects	15
2.4	J/ψ Production in Heavy Ion Collisions	17
2.4.1	Final state effects on J/ψ production	17
2.4.2	Cold nuclear matter effects on J/ψ Production	25
2.5	J/ψ Production at SPS	27
3	Experimental Setup	31
3.1	RHIC Accelerator Complex	31
3.2	The PHENIX Experiment	34
3.2.1	Overview of detector complex	34
3.2.2	Global coordinate	36
3.3	PHENIX Global Detectors	37
3.3.1	Beam-Beam-Counters	37
3.3.2	Zero-Degree-Calorimeters	39
3.4	PHENIX Central Arms	41
3.4.1	Drift Chamber	41
3.4.2	Pad Chamber	45
3.4.3	Ring Imaging Cherenkov Counter	46

3.4.4	Electromagnetic Calorimeter	49
3.5	PHENIX Central Magnet System	52
3.6	Data Acquisition System in PHENIX	55
4	Run Condition of 2004 Au+Au Collisions	57
4.1	Beam Conditions	57
4.1.1	z_{vtx} distribution	58
4.1.2	Beam position motion	58
4.2	Trigger Conditions	60
4.2.1	Minimum bias trigger (MB) and trigger efficiency	60
5	Data Analysis 1 - Electron Identification	61
5.1	Tracking and Momentum Reconstruction	61
5.1.1	DC-PC1 tracking	61
5.1.2	Momentum determination	62
5.1.3	Momentum resolution	63
5.1.4	RICH calibration	66
5.2	Electron Identification	67
5.2.1	List of variables used in electron identification	69
5.2.2	Electron identification with the RICH	69
5.2.3	Electron identification with the EMCal	71
5.2.4	Conversion electrons	78
6	Data Analysis 2 - Yield extraction	81
6.1	Invariant Yield and Nuclear Modification Factor	81
6.2	Event Classification	84
6.2.1	Glauber model	84
6.2.2	Centrality determination	85
6.2.3	Glauber simulation	85
6.3	Run Selection for the J/ψ Analysis	87
6.3.1	Fluctuation of the electron yield	87
6.4	Signal Extraction of J/ψ	89
6.4.1	Cut parameters used in signal extraction	89
6.4.2	Additional pair cut	90
6.4.3	Invariant mass spectrum	91
6.4.4	Background evaluation	92
6.5	Correction Factors	100
6.5.1	Single J/ψ detection efficiency ϵ_{det}	100
6.5.2	Embedding efficiency ϵ_{embed}	102
6.5.3	Internal bremsstrahlung and efficiency for the mass cut ϵ_{mass}	103
6.5.4	Smearing effect $\epsilon_{smearing}$	105
6.5.5	Run-by-Run efficiency $\epsilon_{run-by-run}$	108
6.5.6	Bin width correction $\epsilon_{bin-width}$	110
6.5.7	Overall J/ψ detection efficiency ϵ_{tot}	111

6.5.8	Mean overall efficiency	112
6.6	Systematic Error Evaluation	113
6.6.1	Signal extraction of J/ψ	113
6.6.2	Corrections	113
6.6.3	Summary of the systematic errors	117
7	Experimental Results	119
7.1	Transverse Momentum Distributions	119
7.2	Extraction of $\langle p_T^2 \rangle$ and Centrality Dependence of $\langle p_T^2 \rangle$	119
7.3	R_{AA} as a function of p_T	122
7.4	Integrated Invariant Yield	125
7.5	Centrality Dependence of R_{AA}	125
8	Discussion	129
8.1	Comparison of R_{AA} to SPS Energy Results	129
8.2	Comparison of R_{AA} to the Theoretical Models	129
8.2.1	Cold nuclear matter effects	131
8.2.2	Dissociation by comovers	133
8.2.3	Dissociation by thermal gluons in QGP	134
8.2.4	Dissociation \oplus recombination of J/ψ	136
8.2.5	Sequential melting	141
8.2.6	Threshold model	143
8.2.7	χ^2 test for the theoretical models	146
8.3	Model Calculation for J/ψ Suppression	147
8.3.1	Picture of the evolution of the medium	148
8.3.2	Definition of the survival probability	148
8.3.3	Result of model calculations	152
8.4	Toward the Future Experiments	169
9	Conclusion	171
A	Kinematic Variables	175
A.1	Transverse momentum	175
A.2	Rapidity and pseudo-rapidity	175
A.3	Relation to the space-time coordinate	176
B	Performance of the Drift Chamber	177
B.1	Single wire resolution	177
B.2	Single wire efficiency and tracking efficiency	178
C	Background Normalization for Mixed Event	181
C.1	Ratio of like-sign and mixed like-sign spectra in real data	181
C.2	Toy model simulation	185
C.2.1	Electron multiplicity distribution	187

C.3	Results of toy model simulations	189
C.3.1	Case of zero centrality resolution	189
C.3.2	Case of finite centrality resolution	189
D	Invariant Mass Distributions	195
E	Comparison of Simulation with Real Data	199
E.1	Comparison of momentum resolution	199
E.2	Comparison of the eID parameters	200
E.3	Comparison of the detector acceptance	201
E.4	Comparison of the eID efficiency	205
E.5	Centrality dependence of eID parameters	206
F	Internal Bremsstrahlung of J/ψ	207
G	Data Table of the Experimental Results	209
G.1	Invariant p_T yield of J/ψ	209
G.2	$\langle p_T^2 \rangle$ of J/ψ	209
G.3	R_{AA} as a function of centrality	212
H	J/ψ Production in $p + p$ Collisions at RHIC	215

List of Figures

1.1	Left : ϵ/T^4 of quark system as a function of T calculated with Lattice QCD, where ϵ and T are the energy density and temperature, respectively [11]. At the critical temperature T_c , ϵ/T^4 is increasing rapidly. Right: $(\epsilon - 3P)/T^4$ as a function of T , where P is the pressure of the system. [11]	3
1.2	Free energy of the color singlet quark and anti-quark pair as a function of distance between them at different temperatures (T/T_c) [12]. Here σ is the string tension and order of $\sigma \sim (0.4)^2$ (GeV) ²	3
1.3	The phase diagram in temperature and baryon density	4
1.4	The view of the colliding nuclei before (left) and after (right) collisions. They approach each other with nearly speed of light and the impact parameter b before collisions. After the collisions, the system consists of two components: spectator and participants.	6
1.5	Space time evolution of the medium created at relativistic heavy ion collisions [13]. Mixed phase would exist only if the transition is first order.	8
2.1	The spectrum and transitions of the charmonium family [19].	12
2.2	Examples of heavy-quark production diagrams. (a),(b) Leading order Gluon fusion, (c) Leading order pair annihilation, (d) Pair creation with gluon emissions, (d) flavor excitation, (e) gluon splitting [20].	13
2.3	An example of the lowest order diagram for direct J/ψ production from gluon fusion with the color singlet model. The $c\bar{c}$ pair is in the color singlet state. . . .	13
2.4	An example of the lowest order diagram for direct J/ψ production from gluon fusion with the color evaporation model. Multiple soft-gluon emissions destroy the information on quantum numbers of $c\bar{c}$ pair.	14
2.5	An example of the lowest order diagram for direct J/ψ production from gluon fusion with the color octet model. The $c\bar{c}$ pair is in the color octet state.	15
2.6	the ratio of χ_c production cross section which decayed to J/ψ to the production cross section of (inclusive) J/ψ (R_{χ_c}) as a function of \sqrt{s} . Solid and dashed lines are the predictions from NRQCD (COM) and CSM, respectively [35].	16
2.7	The $B\sigma(\psi')/B\sigma(J/\psi)$ ratio as a function of the center of mass energy [37]. . . .	16
2.8	Spectral functions for J/ψ (Left) and for η_c at the temperature T/T_c of (a) 0.78, 1.38, 1.62 and (b) 1.87, 2.33 [42]	19
2.9	The spectral functions for (a) pseudo-scalar and (b) vector channels at the temperature T/T_c of 1.5, 2.25 and 3 [43].	20

2.10	Temperature dependence of binding energy for J/ψ (a) and for χ_c and ψ' (b).	20
2.11	J/ψ dissociation cross section by gluons (green) and hadrons (blue) [39, 49].	22
2.12	Left : Ratio of the structure function F in He, C and Ca nuclei to that in deuteron from New Muon Collaboration [66]. Right : Expected ratio of gluon distribution function in Au+Au nuclei at 200 GeV collisions with the $Q = 2m_c = 2.4$ GeV [67].	26
2.13	Left : Ratio of J/ψ cross section to Drell-Yan cross section as a function of path length for several collision systems. Normal nuclear absorption pattern is also shown as solid line. Right : Ratio of J/ψ cross section to Drell-Yan cross section divided by the nuclear absorption pattern as a function of path length for various collision systems. The measured data have been re-scaled to 158 GeV/nucleon.	28
2.14	$\langle p_T^2 \rangle$ as a function of path length. The measurements performed at 200 GeV/nucleon are also included. The lines are linear fits to the data points, one for each beam energy.	29
3.1	RHIC Accelerator Complex	32
3.2	RHIC Acceleration scenario for Au beams	33
3.3	PHENIX Detector Complex. Upper is from beam stream and bottom is from the perpendicular to the beam stream.	35
3.4	PHENIX Global coordinate	37
3.5	(a)One BBC element consisting of 1-inch mesh-dynode photomultiplier tube with 3 cm quartz radiator. (b) BBC array consisting 64 identical elements. (c)The BBC is mounted in the PHENIX [98].	38
3.6	(a) Distribution of timing deviation for a certain BBC element from the average time. (b) Distribution of timing resolution over all BBC elements [98].	39
3.7	Schematic View around the interaction region and the location of ZDC. A) Top view B) from Beam view (cross section). Outgoing beams are bent by DX dipole magnet and only neutrons can reach to ZDC.	40
3.8	Cross section of the ZDC module [101]. Neutron passes through 27 Tungsten absorbers and fibers collect lights.	41
3.9	Construction of DC frame [99]	43
3.10	Left : The layout of wire position in one sector from the beam view [99]. Right : The schematic diagram of the stereo wire orientation [99].	43
3.11	Wire configurations in the DC [104].	44
3.12	The drift lines for six sense wires ion X1 net. Different types of wires are marked by arrows [104].	44
3.13	The Pad Chamber layers of the PHENIX central tracking system. Several sectors of PC3 and PC3 in west are removed in this Figure [105].	45
3.14	The pad and pixel geometry (left). A cell defined by three pixels is at the center of the right picture [99].	46
3.15	The cut-away view of RICH detector [106]	47
3.16	Schematic view of RICH along with the beam axis [106]	48
3.17	One of the RICH PMT arrays in the PHENIX [106]	49

3.18	Cut-away view of a PbSc module showing a stack of scintillator and lead plates, wavelength shifting fiber.	51
3.19	A PbGl super-module	51
3.20	Invariant mass of 2γ and π^0 peak [109].	52
3.21	Invariant mass of 2γ in real data (black) and in Monte Carlo simulation (blue), where the background is subtracted in real data [109].	52
3.22	Line drawings of the PHENIX magnets, shown in perspective and cut away to show the interior structure [111].	53
3.23	Vertical cutaway drawing of the central and north muon magnets showing the coil positions for both magnets [111].	53
3.24	Upper a) CM and MM field lines shown on a cutaway drawing of the PHENIX magnets. The beams travel along the $R = 0$ -axis in this figure and collide at $R = z = 0$. Arrows indicate the field direction [111]. Lower b) z component of the magnetic field, B_z as a function of the radial distance from beam line for various z locations [104].	54
3.25	The total strength $B(R)$ as a function of R for + (Outer), ++ (Outer + Inner), and +- (Outer-Inner) field configurations. [111].	55
3.26	Schematic diagram of the data acquisition flow.	56
4.1	History of delivered luminosity in Au+Au collisions	58
4.2	Left : Accumulated z vertex distribution reconstructed with BBCs in Year-4 Au+Au collisions. Right : Mean of z vertex distribution as a function of the run number.	59
4.3	Beam position motion in transverse plane as a function of run number. Red is x_0 and blue is y_0	59
5.1	Left: A schematic view of the track in the DC $x - y$ ($r - \phi$) plane. The X1 and X2 hits in the DC are shown as small circles. ϕ and α are the feature space variables in the CHT transformation. Right: A schematic view of the track in the DC $r - z$ plane. β is the polar angle of the track.	62
5.2	Left : Hits in a portion of the DC X1 and X2 wires. Right : Corresponding hough amplitude as a function of feature space for X1 and X2 wires	63
5.3	$\sigma(E/p)/(E/p)$ as a function of electron momentum for PbGl (Left) and PbSc (Right). Black open circles are the data points. Red lines are the contribution from EMCAL energy resolution extracted by using the points below 2 GeV/c and blue lines are the contribution from DC momentum resolution extracted by fitting the points for PbGl and PbSc simultaneously. Black lines are the results of the $\sigma(E/p)/(E/p)$ from EMCAL energy resolution and DC momentum resolution.	65
5.4	Raw ADC spectrum for one RICH PMT channel. Raw ADC distribution is fitted with Gaussian and Poisson distributions to extract pedestal position, one photo-electron and 2nd photo-electron position.	66
5.5	The number of photo-electron distribution after the gain calibration.	67
5.6	Example of the track association to RICH PMT plane	68

5.7	Left : Accumulated ring imaging before the alignment calibration. Right : After the alignment calibration.	68
5.8	Ring radius obtained after the alignment calibration	69
5.9	The schematic description of the definition of variable which characterize the RICH ring. The track projection vector and five hit PMT are shown as an example. The distance between the center of hit PMT 1, 3 and the track projection vector are represented as r_{cor}^1 and r_{cor}^3 , respectively.	70
5.10	a), b), c), d), e) and f) show $n0$, $n1$, $npe0$, $npe1$, $disp$ and $chi2/npe1$ in MB collisions, respectively. The raw distribution, $z - flipped$ distribution and net signal (subtracted) distribution are expressed as solid, dashed lines and shaded histograms, respectively.	72
5.11	Left: E/p distribution for all charged particles (dashed-dotted line), for the particles passed with RICH cut ($n1 \geq 4$) (solid line) and for the particles passed with z-flipped RICH cut ($sn1 \geq 4$) (dashed line), which corresponds to the particles associated to the RICH randomly. Right: E/p distributions for the particles passed with RICH cuts (solid), for the particles with z-flipped RICH cuts (dashed line) and for the net particles of the subtraction of the random association to the RICH (shaded histogram). They are from MB collisions and the momentum range of charged particles are $0.7 \leq p_T \leq 5.0$	73
5.12	D_ϕ as a function of the z position at the DC (zed). Upper (bottom) left and upper (bottom) right are D_ϕ for electrons (positrons) with $0.5 \leq p \leq 0.6$ GeV/ c and $1.4 \leq p \leq 1.6$ GeV/ c , respectively.	74
5.13	Momentum dependence of p_0 , p_1 and p_2 , which were extracted by fitting zed dependence of mean D_ϕ with $p_0(p) + p_1zed + p_2zed^2$. Solid lines were fitting results using $c_0exp(-c_1 \times p) + c_2$ function.	75
5.14	EMCal ϕ dependence of D_ϕ , where the zed dependence of D_ϕ was corrected. . .	76
5.15	D_z as a function of the polar angle θ for electrons. Upper (bottom) left and upper (bottom) right are D_z for electrons (positrons) with $0.5 \leq p \leq 0.6$ GeV/ c and $1.4 \leq p \leq 1.6$ GeV/ c , respectively.	76
5.16	Momentum dependence of σ_ϕ at various zed for electrons (left) and positrons (right). Solid lines are the fitting results of momentum dependence of σ_ϕ with $\sqrt{c_0 + c_1/p^{c_2}}$	77
5.17	Momentum dependence of σ_z for various θ is shown. Solid lines are the fitting results of momentum dependence of σ_z with $\sqrt{c_0 + c_1/p^{c_2}}$	77
5.18	a) : dep distribution. Solid and dashed lines are the distribution for the particles with RICH cut and with z-flipped RICH cut (random association), respectively. Shaded histogram is the subtracted distribution. b) : $emcsdphi_e$ distribution. c) $emcsdz_e$ distribution.	78
5.19	(a) The production of conversion electrons.	78
5.20	Left : invariant mass spectrum in Au+Au collision for lower mass region. without $phiv$ cut. Black is real, red is combinatorial background and blue is the net signal of e^+e^- pairs. Right: invariant mass spectrum after $phiv < 0.015$ cut is applied. Clear peak from conversion pairs is seen.	79

5.21	eID parameters from conversion pairs (black) and simulation (red). a) n_0 , b) n_1 , c) npe_0 , d) npe_1 , e) $disp$, f) $chi2/npe_1$, g) dep , h) $emcsdphi_e$ and i) $emcsdz_e$.	80
6.1	The correlation between the fraction of BBC charge Q_{BBC}/Q_{BBC}^{max} and the fraction of ZDC energy E_{ZDC}/E_{ZDC}^{max} . The boundaries for the classification of the event into the centrality class of 0-5/5-10/10-15/15-20/20-30/30-40/40-60/60-93% were shown.	87
6.2	The correlation between the fraction of BBC charge Q_{BBC}/Q_{BBC}^{max} and the fraction of ZDC energy E_{ZDC}/E_{ZDC}^{max} in Glauber simulation.	87
6.3	$N_e \times N_p$ as a function of run number. Closed symbols are the good runs and open are bad runs. The lines corresponds to $\langle N_e \times N_p \rangle$ and the threshold to select the good runs.	88
6.4	Left : Difference in DC ϕ position between any two same-charge tracks. Right : Difference in DC β position between any two same-charge tracks. Black was extracted from each event, while red was extracted from event mixing method as described later and no correlation between any two pairs in event mixing method.	90
6.5	Left : The distribution of $\cos(PFOA)$ for the same-charge tracks in each event (black) and mixed event (red). Right : Zoom up distribution of $\cos(PFOA)$.	91
6.6	Left : Invariant mass spectra of unlike-sign pairs in MB data and all p_T region. Right : Invariant mass spectrum spectrum of unlike-sign pairs between $2.7 \leq M_{ee} \leq 3.5 \text{ GeV}/c^2$.	92
6.7	Left : Invariant mass spectra of unlike-sign pairs (black) and mixed unlike-sign pairs(red) in MB data and all p_T region. Right : Invariant mass spectrum after the subtraction by mixed unlike-sign pairs. Shaded area corresponds to the mass range for signal counting region, which gives best significance of J/ψ peak.	94
6.8	Invariant mass spectra of unlike-sign pairs (black) and mixed unlike-sign pairs (red) for 0-1/1-2/2-3/3-4/4-5/0-10 GeV/c p_T bin in MB data sample	94
6.9	Invariant mass spectra of unlike-sign pairs (black) and mixed unlike-sign pairs (red) for 0-1/1-2/2-3/3-4/4-5/0-10 GeV/c p_T bin in 0-20% data sample	95
6.10	Invariant mass spectra of unlike-sign pairs (black) and mixed unlike-sign pairs (red) for 0-1/1-2/2-3/3-4/4-5/0-10 GeV/c p_T bin in 20-40% data sample	95
6.11	Invariant mass spectra of unlike-sign pairs (black) and mixed unlike-sign pairs (red) for 0-1/1-2/2-3/3-4/4-5/0-10 GeV/c p_T bin in 40-93% data sample	96
6.12	Invariant mass spectra in MB (Upper Left), 0-20% (Upper Right), 20-40% (Lower left) and 40-93% (Lower right). Black open symbols are from the real data and blue closed symbols are the mass spectrum from PYTHIA ($c\bar{c}$ and $b\bar{b}$ events). Green is the fitting result with the all the functions, red and blue are the Gaussian shape which correspond to the J/ψ signals, respectively. Black solid line is the continuum shape.	97
6.13	The invariant cross section of electrons from heavy quarks as a function of p_T in run5 p+p (red) and PYTHIA events (blue from $c\bar{c}$ events, green from $b\bar{b}$ events and black is summed up between them). The $\sigma_{b\bar{b}}$ is 8.32 μb and $\sigma_{c\bar{c}}$ is 567 μb [56].	99

6.14	single electron spectrum in PYTHIA events for each centrality class. Open blue and open green are the single electron spectrum in $c\bar{c}$ and $b\bar{b}$ events, respectively. Black is the summation between them. Red points are the non-photon single electron spectrum in Run4 Au+Au. Magenta is the run5 p+p best fit result [58].	99
6.15	acceptance \times efficiency as a function of input J/ψ p_T . Left is for the standard cuts and right is for loose cuts. Open and closed symbols are the results with and without E0 sector, respectively.	101
6.16	Embedding efficiency ϵ_{embed} as a function of J/ψ p_T for the centrality of 0-5/20-25/40-45/60-65%.	102
6.17	Embedding efficiency as a function of centrality. Left is for the standard eID cuts. Right is for the loose eID cuts. Open in both panels are the efficiency without E0 sector and Closed are the efficiency with E0 sector	103
6.18	Left : Invariant mass spectrum in $p + p$ collisions (black). Right : Invariant mass spectrum in Au+Au collisions (black). Red, green and blue in both panels are the invariant mass spectrum in the simulation study with the internal and external bremsstrahlung effect and with the mass resolution of 1.0%, 1.25% and 1.5%, respectively.	104
6.19	p_T dependence of the J/ψ mass resolution	104
6.20	Left:Correlation between input and reconstructed J/ψ p_T . Right: Resolution of reconstructed J/ψ p_T as a function of input J/ψ p_T .	105
6.21	$P(A, B)$ as a function of J/ψ p_T . Black, red, green, blue, yellow, magenta, light blue, dark green and purple corresponds to the $P(A, B)$ of $A = B$ (diagonal), $A = B + 1$, $A = B - 1$, $A = B + 2$, $A = B - 2$, $A = B + 3$, $A = B - 3$, $A = B + 4$ and $A = B - 4$, respectively.	106
6.22	Left : Input J/ψ p_T distribution (black) and reconstructed p_T distribution calculated by using $P(A, B)$ and input p_T distribution based on Eq.(6.34).	107
6.23	$N_e \times N_p$ as a function of run number from G2 to G3 runs. The Green line in each run group is the average of $N_e \times N_p$ per MB event and blue line is its RMS.	108
6.24	$N_e \times N_p$ as a function of run number from G4 to G10 runs. The Green line in each run group is the average of $N_e \times N_p$ and blue line is its RMS.	109
6.25	Left: ϵ_{tot} as a function of p_T for MB/0-20/20-40/40-93. Right : ϵ_{tot} as a function of p_T for 0-10/10-20/20-30/30-40/40-60/60-93.	111
6.26	Left : z vertex distribution in Au+Au collisions (MB). Right : ϵ_{det} as a function of J/ψ p_T with flat z vertex distribution (closed) and the z vertex distribution in real data (open).	114
6.27	Left 2 \times 2 : 4 types of the J/ψ rapidity distribution extracted by PYTHIA with GRV94LO (red), GRV94HO (green), MRSTHO (blue) and CTEQ5M (yellow) PDF. Right 2 \times 2: ϵ_{det} as a function of J/ψ p_T for these 4 rapidity distribution of J/ψ with GRV94LO (red), GRV94HO (green), MRSTHO (blue) and CTEQ5M (yellow) PDF. The difference from different PDFs is very small.	115

7.1	Invariant p_T distribution for MB, 0-20%, 20-40% and 40-93%. Bars are the stat. error and the brackets are the total sys. errors calculated by the quadratic summation of uncorrelated and correlated sys. errors.	120
7.2	Invariant p_T distribution for 0-10%, 10-20%, 20-30%, 30-40%, 40-60% and 60-93%. Bars are the stat. error and the brackets are the total sys. error.	120
7.3	Left : Invariant p_T distributions in MB/0-20/20-40/40-93% centrality and in $p+p$ collisions. Right : Invariant p_T distributions in 0-10/10-20/20-30/30-40/40-60/60-93% centrality and in $p+p$ collisions. Error shown in this figure is only statistic error.	121
7.4	$\langle p_T^2 \rangle$ as a function of N_{col} in $p+p$ (black) $d+Au$ MB (green) and $Au+Au$ (MB/0-20/20-40/40-93% in left and 0-10/10-20/20-30/30-40/40-60/60-93% in right) collisions.	122
7.5	R_{AA} as a function of p_T for MB, 0-20%, 20-40% and 40-93% centrality. Bars are the stat. error and the brackets are the total sys. error. Shaded area on each point corresponds to the $p+p$ stat. and sys. error and band corresponds to the systematic error from T_{AB}	123
7.6	R_{AA} as a function of p_T for 0-10, 10-20%, 20-30% 30-40, 40-60 and 60-93% centrality bins. Bars are the stat. error and the brackets are the total sys. error. Shaded area on each point corresponds to the $p+p$ stat. and sys. error. Band corresponds to the systematic error from T_{AB}	124
7.7	R_{AA} as a function of the number of participants. The centrality binning is 0-5/5-10/10-15/15-20/20-30/30-40/40-60/60-93. The band corresponds to the quadratic sum of statistic error and systematic error from Year-5 $p+p$ J/ψ results. The shaded area in each point is the systematic error of T_{AB}	126
8.1	R_{AA} as a function of the number of participants from PHENIX data (red) and NA50 data (black). Bar in PHENIX data corresponds to the quadratic summation of stat. error and uncorrelated sys. error. Bracket in PHENIX data corresponds to the correlated sys. error, where T_{AB} error is included.	130
8.2	R_{dAu} as a function of rapidity. 12% overall normalization uncertainty is not shown here. The theoretical curves are described in text.	132
8.3	R_{AA} as a function of the number of participants. Bar corresponds to the quadratic summation of stat. error and uncorrelated sys. error. Bracket corresponds to the correlated sys. error, where T_{AB} error is included. Solid, dashed and dotted lines are the prediction of R_{AA} from cold nuclear matter effects with EKS shadowing and the nuclear absorption cross section of 0, 1 and 2 mb, respectively.	132
8.4	R_{AA} as a function of the number of participants. Bar corresponds to the quadratic summation of stat. error and uncorrelated sys. error. Bracket corresponds to the correlated sys. error, where T_{AB} error is included. Solid line is the prediction of R_{AA} from comover dissociation model, where the cold matter effects were taken into account (shadowing and the absorption cross section of 0 mb).	133

8.5	R_{AA} as a function of the number of participants. Bar corresponds to the quadratic summation of stat. error and uncorrelated sys. error. Bracket corresponds to the correlated sys. error, where T_{AB} error is included. The solid and dashed lines are explained in text.	135
8.6	R_{AA} as a function of the number of participants. Bar corresponds to the quadratic summation of stat. error and uncorrelated sys. error. Bracket corresponds to the correlated sys. error, where T_{AB} error is included. Solid lines in “a)” and “b)” are the calculation from kinetic formation model described in text. Solid and dashed lines in “c)” are from transport model, where charm quark distribution was taken from pQCD or thermal one, respectively. Solid lines in “d)” and “e)” are from statistical hadronization model and HSD model, respectively.	140
8.7	Upper : $S_{J/\psi}$ as a function of energy density in NA50 Pb+Pb collisions (Black), NA60 In+In collisions (Brawn) and calculated probability $0.6+0.4S_{\psi'}$ by using ψ' measurement in NA50 Pb+Pb collisions [156]. Systematic error approximately 16% shown in Fig. 8.1are not shown here. Bottom : $S_{J/\psi}$ as a function of energy density in NA50 Pb+Pb (black), NA60 In+In (brawn) and PHENIX Au+Au collisions (red). Additional systematic error due to the uncertainty in cold nuclear matter effects are shown as box on PHENIX data points.	142
8.8	Transverse participants density in Cu+Cu (left) and Au+Au (right) collisions for various values of the impact parameter, $b=0, 2, 4, \dots$ (from top to bottom). The origin is at a distance, $d = b/(1 + R_A/R_B)$ from the center of the nucleus A [161].	144
8.9	R_{AA} as a function of the number of participants. Bar corresponds to the quadratic summation of stat. error and uncorrelated sys. error. Bracket corresponds to the correlated sys. error, where T_{AB} error is included. Red, green and blue lines are the calculations of this model with the threshold density of $n_c = 4.0, 3.8, 3.6 \text{ fm}^{-2}$, respectively. Black line is the calculation, where only the nuclear absorption is taken into account.	145
8.10	Left : Temperature at each space-time points with $b = 3.1 \text{ fm}/c$. Right : Parton density at each space-time points with $b = 3.1 \text{ fm}/c$, where the temperature is above 170 MeV.	149
8.11	Left : Temperature at each space-time points with $b = 10.8 \text{ fm}/c$. Right : Parton density at each space-time points with $b = 10.8 \text{ fm}/c$, where the temperature is above 170 MeV.	150
8.12	Temperature (left) and the parton density (right) as a function of t along the trajectory of J/ψ for various impact parameters (centrality), where J/ψ p_T is $0.5 \text{ GeV}/c$ and the production of J/ψ is set to $\mathbf{x}_0 = (0, 0)$	151
8.13	Survival probability of J/ψ as a function of the number of participants. Red points are the real data as shown in Fig. 8.7. Blue and green lines are the survival probability for direct J/ψ and χ , respectively, and black line is the survival probability of J/ψ , which was extracted based on Eq. (8.38) with $(T_{diss}(J/\psi), T_{diss}(\chi), f_{FD}) = (2.12T_c, 1.34T_c, 0.25)$	153

8.14	Survival probability of J/ψ as a function of the number of participants, where red points are from real data and solid lines are the results from model calculations with $T_{diss}(J/\psi)/T_c = 1.9$ (a), 2.0 (b), 2.05 (c), 2.12 (d), 2.15 (e), 2.2 (f) and 2.15 (g) and with feed down contribution of 10%. Different colors correspond to different $T_{diss}(\chi_c)$ explained in text.	155
8.15	Survival probability of J/ψ as a function of the number of participants, where red points are from real data and solid lines are the results from toy model calculations with $T_{diss}(J/\psi)/T_c = 1.9$ (a), 2.0 (b), 2.05 (c), 2.12 (d), 2.15 (e), 2.2 (f) and 2.15 (g) and with feed down contribution of 25%. Different colors correspond to different $T_{diss}(\chi_c)$ explained in text.	156
8.16	Survival probability of J/ψ as a function of the number of participants, where red points are from real data and solid lines are the results from toy model calculations with $T_{diss}(J/\psi)/T_c = 1.9$ (a), 2.0 (b), 2.05 (c), 2.12 (d), 2.15 (e), 2.2 (f) and 2.15 (g) and with feed down contribution of 40%. Different colors correspond to different $T_{diss}(\chi_c)$ explained in text.	157
8.17	Survival probability of J/ψ as a function of the number of participants, where red points are from real data and solid lines are the results from toy model calculations with $T_{diss}(J/\psi)/T_c = 1.9$ (a), 2.0 (b), 2.05 (c), 2.12 (d), 2.15 (e), 2.2 (f) and 2.15 (g) and with feed down contribution of 60%. Different colors correspond to different $T_{diss}(\chi_c)$ explained in text.	158
8.18	Same figure as shown in Fig. 8.14. Difference is that the real data points are moved up according to point-to-point correlated systematic errors. Feed down contribution is assumed to be 10%.	159
8.19	Same figure as shown in Fig. 8.16. Difference is that the real data points are moved down according to point-to-point correlated systematic errors. Feed down contribution is assumed to be 40%.	160
8.20	χ^2 as a function of $(T_{diss}(J/\psi), T_{diss}(\chi_c))$ for various feed down contribution f . χ^2 contours for 1σ and 2σ are shown as solid and dashed lines, respectively. Feed down contribution is written in each title box.	162
8.21	Contour plots on $(T_{diss}(J/\psi), T_{diss}(\chi_c))$ plane for various feed down contribution f . Solid and dotted lines are 1σ and 2σ contour levels, respectively. data points are moved up according to correlated errors.	163
8.22	Contour plots on $(T_{diss}(J/\psi), T_{diss}(\chi_c))$ plane for various feed down contribution f , where the 1σ χ^2 region exist on the plane. Solid and dotted lines are 1σ and 2σ contour levels, respectively. data points are moved down according to correlated errors.	164
8.23	The survival probability as a function of the number of participants. Red points are real data, blue solid lines are best fit results and shaded area corresponds to the 1σ deviation of survival probability. Real data in middle and bottom are moved up and down according to correlated systematic errors.	166
8.24	Survival probability $S_{J/\psi}$ as a function of J/ψ p_T for 0-10% (upper left), 10-20% (upper right), 20-30% (lower left) and 30-40% (lower right). Data points are explained in text.	168

B.1	Illustration of three point method. T_i corresponds to the drift time for the anode wire i	177
B.2	Residual distribution of the tracks for the each arm (left) and west arm (right). .	178
B.3	The single wire efficiency calculated by three point method.	179
B.4	Tracking efficiency of the DC as a function of input momentum.	179
C.1	Left : Invariant mass spectrum of like-sign pairs (black) and mixed like-sign pairs (red). Right : The ratio of the invariant mass spectrum between like-sign pairs and mixed like-sign pairs. The centrality shown in this figure is 0-5/5-10/10-15/15-20% centrality.	182
C.2	Left : Invariant mass spectrum of like-sign pairs (black) and mixed like-sign pairs (red). Right : The ratio of the invariant mass spectrum between like-sign pairs and mixed like-sign pairs. The centrality shown in this figure is 20-25/25-30/30-35/35-40% centrality.	183
C.3	Left : Invariant mass spectrum of like-sign pairs (black) and mixed like-sign pairs (red). Right : The ratio of the invariant mass spectrum between like-sign pairs and mixed like-sign pairs. The centrality shown in this figure is 40-45/45-50/50-60/60-93% centrality.	184
C.4	The resolution of the average number of participants ($\delta\langle N_{part}\rangle/\langle N_{part}\rangle$) as a function of the number of participants (black closed points). Black line is the fitting result and the function was written in this plot.	186
C.5	Multiplicity distribution of electrons (open circle) and positrons (closed circle) in each centrality class (0-5/5-10/10-15/15-20/20-25/25-30/30-35/35-40/40-45/45-50/50-60/60-93% centrality classes). Dashed-lines and Solid lines are the Poisson distributions for electrons and positrons, respectively.	187
C.6	μ of the Poisson distribution as a function of the number of participants for positrons (Left) and electrons (Right). Solid lines are the fitting results as described in Eq. (C.2) and Eq. (C.3).	188
C.7	Left : Ratio of the like-sign spectrum over the mixed like-sign spectrum. Right : Ratio of the unlike-sign spectrum over the mixed unlike-sign spectrum. Centrality range is 0-5/5-10/10-15/15-20% from upper to lower. No smearing of the number of participants was taken into account.	189
C.8	Left : Ratio of the like-sign spectrum over the mixed like-sign spectrum. Right : Ratio of the unlike-sign spectrum over the mixed unlike-sign spectrum. Centrality range is 0-5/5-10/10-15/15-20% from upper to lower.	190
C.9	Left : Ratio of the like-sign spectrum over the mixed like-sign spectrum. Right : Ratio of the unlike-sign spectrum over the mixed unlike-sign spectrum. Centrality range is 20-25/25-30/30-35/35-40% from upper to lower.	191
C.10	Left : Ratio of the like-sign spectrum over the mixed like-sign spectrum. Right : Ratio of the unlike-sign spectrum over the mixed unlike-sign spectrum. Centrality range is 40-45/45-50/50-60/60-93% from upper to lower.	192
D.1	Invariant mass spectra of unlike-sign pairs (black) and mixed unlike-sign pairs (red) for 0-1/1-2/2-3/3-4/4-5/0-10 GeV/ c p_T bin in 0-10% data sample	195

D.2	Invariant mass spectra of unlike-sign pairs (black) and mixed unlike-sign pairs (red) for 0-1/1-2/2-3/3-4/4-5/0-10 GeV/ c p_T bin in 10-20% data sample	196
D.3	Invariant mass spectra of unlike-sign pairs (black) and mixed unlike-sign pairs (red) for 0-1/1-2/2-3/3-4/4-5/0-10 GeV/ c p_T bin in 20-30% data sample	196
D.4	Invariant mass spectra of unlike-sign pairs (black) and mixed unlike-sign pairs (red) for 0-1/1-2/2-3/3-4/4-5/0-10 GeV/ c p_T bin in 30-40% data sample	197
D.5	Invariant mass spectra of unlike-sign pairs (black) and mixed unlike-sign pairs (red) for 0-1/1-2/2-3/3-4/4-5/0-10 GeV/ c p_T bin in 40-60% data sample	197
D.6	Invariant mass spectra of unlike-sign pairs (black) and mixed unlike-sign pairs (red) for 0-1/1-2/2-3/3-4/4-5/0-10 GeV/ c p_T bin in 60-93% data sample	198
E.1	Momentum difference between input GEANT momentum and reconstructed momentum (symbols) and momentum difference extracted from real data (solid line).	199
E.2	Comparison of eID parameters in real (black) and simulation (red). a) n_0 , b) n_1 , c) npe_0 , d) npe_1 , e) $disp$, f) chi^2/npe_1 , g) dep , h) $emcsdphi_e$ and i) $emcsdz_e$.	200
E.3	Left : DC dead maps for each sector (East South, East North, West South and West North). Right : DC dead maps in simulation. X1 and X2 wires corresponds to the plane of 0-11 and 20-31, respectively. UV1 and UV2 wires corresponds to the plane number of 12-19 and 32-39, respectively.	202
E.4	Left from up to bottom: PC1 East, PC1 West, PC2 West, PC3 East, PC3 West dead maps. Right : Pad Chamber dead maps in simulation.	203
E.5	Left from up to bottom: EMCAL E0, E1, E2, E3, W0, W1, W2 and W3 dead maps. Right : EMCAL dead maps in simulation.	203
E.6	Upper left, upper right, lower left and lower right are the ϕ distribution at the DC south, ϕ distribution at the DC north, zed distribution at the East DC and zed distribution at the West DC, respectively. Black is for real data and red for simulation.	204
E.7	eID efficiency as a function electron p_T from real (Red) and Simulation (Blue) for ES (Upper-Left), EN (Upper-Right), WS (Lower-Left) and WN (Lower-Right).	205
E.8	eID parameters of dep (left column), $emcsdphi_e$ (middle column) and $emcsdz_e$ (right column) for 0-20% (upper), 20-40% (middle) and 40-93% (bottom) centrality classes. Black is from conversion pairs and red is from embedding simulation.	206
F.1	Parameter C_{hard} as a function of minimal energy E_{min} of photon in the J/ψ rest frame for radiative decay $J/\psi \rightarrow \mu^+\mu^-\gamma$ (solid line) and $e^+e^-\gamma$ (dashed-line). The point with errors was evaluated from the E760 result.	208
H.1	Left : J/ψ invariant cross section as a function of p_T at mid-rapidity in 200 GeV $p + p$ collisions. Dashed line is the fitting result of Kaplan function. Right : PHENIX $\langle p_T^2 \rangle$ measurement compared to measurements at other energies as a function of \sqrt{s} [86]. Dashed line represents $-2.4 + 1.2 \ln \sqrt{s}$	216
H.2	Total cross section of J/ψ as a function of \sqrt{s} . Solid and dashed lines are the prediction of color octet model with GRV98NLO and MRST2001NLO PDF function, respectively.	216

List of Tables

1.1	Past, current and future accelerator for heavy ion collisions.	5
2.1	Properties of charmonium bound states. In Quantum numbers, n , S , L and J show the radial quantum number, total intrinsic spin, orbital angular momentum, and total angular momentum, respectively.	11
2.2	Summary of the radius of each charmonium states $\langle r^2 \rangle^{1/2}$ and binding energy of them ΔE [39, 40].	18
2.3	Dissociation temperature T_d/T_c for quarkonia inferred from lattice QCD calculations and potential model analyses [39].	21
3.1	The parameters of RHIC accelerator [19, 96].	34
3.2	Summary of the PHENIX subsystem detectors.	36
3.3	Potential for different types of wires used in the DC [104]	45
3.4	Performance of Pad Chambers in Year-2 and cosmic ray test [105]	46
3.5	Specifications of RICH [106]	50
4.1	Summary of beam conditions in RHIC Year-4 Au+Au collisions	57
5.1	The materials in front of DC	64
5.2	Summary of the variables in electron identification	69
6.1	Results of the Glauber calculation in Au+Au collisions at $\sqrt{s_{NN}} = 200$ GeV showing the average b , N_{part} , N_{col} and T_{AB} for each centrality class. Error is the systematic error [116].	86
6.2	run group, run range, number of runs, number of MB events	88
6.3	The number of events used in this analysis after the good run selection.	89
6.4	R_{cont} for MB/0-20/20-40/40-93% centrality classes. The last error is the deviation of R_{cont} when the fitted parameter p_0 was moved according to $\pm 1 \sigma$ error of p_0	98
6.5	Summary of initial conditions for generated J/ψ	100
6.6	efficiency of the mass cut for each 1.0 GeV/ c p_T bin	105
6.7	Correction factors due to smearing effect for 1 GeV/ c bin	107
6.8	Run-by-run efficiency from G2 to G3 groups	108
6.9	Run-by-run efficiency from G4 to G10 groups	109
6.10	Bin shift correction factors	110
6.11	ϵ_{tot} as a function of p_T and for each centrality class (MB/0-20/20-40/40-93%)	111

6.12	ϵ_{tot} as a function of p_T and for each centrality class (0-10/10-20/20-30/30-40/40-60/60-93%)	112
6.13	$\langle\epsilon_{tot}\rangle$ for 0-5/5-10/10-15/15-20% centrality calculated from the J/ψ p_T distribution for 0-20% centrality	112
6.14	Correction factors due to smearing effect for 1 GeV/ c bin with the input $\langle p_T^2 \rangle = 3.0$ and 5.0 [(GeV/ c) ²]	116
6.15	$\langle\epsilon_{tot}\rangle$ with different p_T distribution	117
6.16	summary of the systematic error	117
7.1	$BdN/dy/N_{col}$ of J/ψ for MB, 0-20/20-40/40-93%, 0-10/10-20/20-30/30-40/40-60/60-93% and 0-5/5-10/10-15/15-20% centrality classes. The first error in the last column is stat. error and second is total sys. errors.	125
7.2	R_{AA} as a function of the number of participants	127
8.1	$S_{J/\psi}$ in Au+Au collisions as a function of centrality.	143
8.2	Summary of D and χ^2 between data points and various theoretical models.	146
C.1	Ratio of like-sign to the mixed like-sign for each centrality class in real data. In real data, statistical error is negligible up to 60% and is $\sim 2\%$ in 60-93% bin.	185
C.2	Ratio of like-sign to the mixed like-sign and the ratio of the unlike-sign and mixed unlike-sign spectrum for each centrality class with the smearing effect for the number of participants.	193
E.1	R_{acc} for DC south and north.	201
E.2	eID efficiency for real and simulation for each sector	205
G.1	Invariant Yield of J/ψ in MB Au+Au collisions	209
G.2	Invariant Yield for 0-20/20-40/40-93% centrality classes	210
G.3	Invariant Yield for 0-10, 10-20, 20-30, 30-40, 40-60, 60-93%	211
G.4	$\langle p_T^2 \rangle$ for each centrality class and $p+p$ obtained by data points and fitting results truncated up to 5 GeV/ c	212
G.5	R_{AA} for MB, 0-20, 20-40 and 40-93 centrality classes.	213
G.6	R_{AA} for 0-10/10-20/20-30/30-40/40-60/60-93% centrality bins	214
H.1	Invariant cross section as a function of p_T (0.25 and 1 GeV/ c bin) in $p+p$ collisions at $\sqrt{s} = 200$ GeV at RHIC-PHENIX.	217
H.2	Invariant cross section as a function of p_T (1 GeV/ c bin) in $p+p$ collisions at $\sqrt{s} = 200$ GeV at RHIC-PHENIX.	217

Chapter 1

Introduction

1.1 Objectives of This Thesis

Quark-Gluon-Plasma (QGP) is a new state of matter composed of deconfined quarks and gluons, which is predicted by lattice Quantum Chromodynamics (QCD) calculations to be formed above a temperature of order $T_c \sim 170$ MeV [1].

High-energy heavy-ion collision is a powerful tool in the laboratory to realize such high temperature and the transition from normal nuclear matter to QGP [2].

Heavy quarkonia (J/ψ , ψ' , χ_c and Υ) have long been considered as one of the most promising probes to study the formation and properties of QGP. In the deconfined state, the attraction between heavy quarks and anti-quarks is believed to be reduced due to color screening effects, leading to the suppression of heavy quarkonia yield. The strength of the suppression depends on the binding energies of the quarkonia and the temperature of the surrounding system [3].

“Anomalous” J/ψ suppression in high-energy heavy-ion collisions was first observed at Super Proton Synchrotron (SPS) in European Center for Nuclear Research (CERN) by NA50 experiment at a center of mass energy per nucleon ($\sqrt{s_{NN}}$) of 17.3 GeV in Pb+Pb collisions [4].

Relativistic Heavy Ion Collider (RHIC) at Brookhaven National Laboratory (BNL) is a dedicated facility to accelerate heavy-ion beams with the energy of 100 GeV per nucleon to search for the QGP and to study its properties. RHIC started its operation in 2000 and high luminosity Au+Au collisions with $\sqrt{s_{NN}} = 200$ GeV was performed in 2004.

The PHENIX experiment, which is one of two largest experiments at RHIC, has the capability to measure J/ψ via e^+e^- decay channel at mid-rapidity and $\mu^+\mu^-$ decay channel at forward and backward rapidities. J/ψ measurement has been performed in Au+Au collisions with $\sqrt{s_{NN}} = 200$ GeV using the data taken in 2004. Since the collision energy is ~ 10 times larger at RHIC than at SPS, the stronger suppression of J/ψ is expected at RHIC. Therefore it is very important to measure the J/ψ production as functions of collision geometry (temperature) and J/ψ p_T to discuss the formation of QGP and understand the properties.

The author has participated in the PHENIX experiment since 2002, worked on the Ring Imaging Cherenkov Counter in PHENIX and concentrated on the J/ψ analysis in Au+Au collisions. The objectives in this work are to understand the J/ψ production in Au+Au collisions and to understand the properties of the created hot and dense medium in Au+Au collisions at

RHIC energy.

1.2 Quark-Gluon-Plasma (QGP)

Quarks (and anti-quarks) are the elementary particles with three additional internal degrees of freedom called “color” in the strong interaction. Gluon is the massless gauge boson and has eight degrees of freedom in color. Strong interaction between them is described by Quantum Chromodynamics (QCD).

The strong interaction is characterized by the running coupling constant α_s . The running coupling constant α_s can be expressed in terms of the four momentum transfer Q^2 , the number of quark flavors n_f and the typical QCD scale $\Lambda_{QCD} \simeq 0.2$ GeV as follows:

$$\alpha_s(Q^2) = \frac{12\pi}{(33 - 2n_f) \ln(\frac{Q^2}{\Lambda_{QCD}^2})}. \quad (1.1)$$

For the Q^2 value of order of Λ_{QCD} (long distance), α_s is order of 1 and quarks and gluons interact strongly in non-perturbative way and form color neutral particles called hadrons. However, as Q^2 becomes larger compared to Λ_{QCD} (short distance), $\alpha_s(Q^2)$ decreases and the interaction can be described perturbatively. This feature is called as “asymptotic freedom” [5, 6].

One of the characteristics of QCD is that quarks and gluons are confined in hadrons in the normal conditions. Quark-Gluon-Plasma (QGP) is a new state of matter which is composed of deconfined quarks and gluons. Lattice QCD is one of the theories to describe the interaction of quarks and gluons in the non-perturbative regime of QCD [7, 8]. Lattice QCD calculations show that there is a phase transition from hadronic matter, where quarks and gluons are confined in hadrons, to a QGP at extreme high temperature $T_c \simeq 170$ MeV and the high energy density $\epsilon_c \simeq 1$ GeV/fm³ [9, 10, 11].

Left in Fig. 1.1 shows ϵ/T^4 as a function of T , where ϵ and T are energy density and temperature in the system, respectively, for different flavor compositions. Right in Fig. 1.1 shows $(\epsilon - 3P)/T^4$ as a function of T , where P is the pressure of the system. From Fig. 1.1, it is seen that the energy density is increasing rapidly at the critical temperature T_c , which is interpreted as breaking of the confinement states and releasing of the additional degree of freedom of colors. It is seen that $(\epsilon - 3P)/T^4$ increases, reaches the maximum around T_c and decreases as T becomes higher than T_c . In case that a QGP is ideal gas composed of massless quarks and gluons, $\epsilon = 3P$. However, finite value of $(\epsilon - 3P)/T^4$ suggests that interactions of quarks and gluons are rather strong near T_c [10].

Figure 1.2 shows the free energy $F(R, T)$ between a heavy quark and an anti-heavy quark as a function of distance R between them at various temperatures of the system (T/T_c) [12]. Solid line is the potential in case of $T=0$, where the potential is composed of the Coulomb potential and confining potential. It is evident that the asymptotic value of $F(\infty, T)$, which corresponds to the energy needed to separate quark and anti-quark pair, decreases with increasing temperature.

In QGP environment, the color charge of a quark is screened due to the existence of light quarks, anti-quarks and gluons, and, as a result, the confining potential disappears as shown in

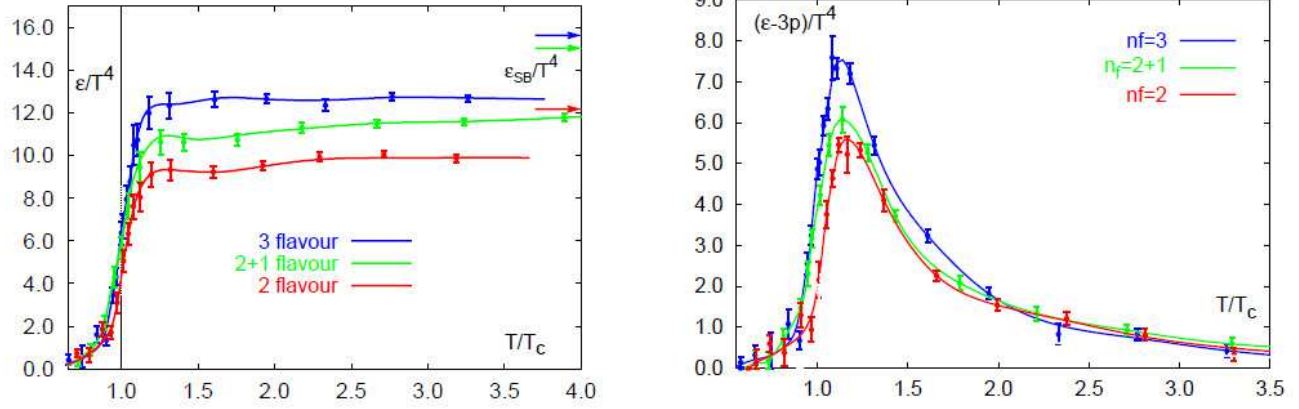


Figure 1.1: Left : ϵ/T^4 of quark system as a function of T calculated with Lattice QCD, where ϵ and T are the energy density and temperature, respectively [11]. At the critical temperature T_c , ϵ/T^4 is increasing rapidly. Right: $(\epsilon - 3P)/T^4$ as a function of T , where P is the pressure of the system. [11]

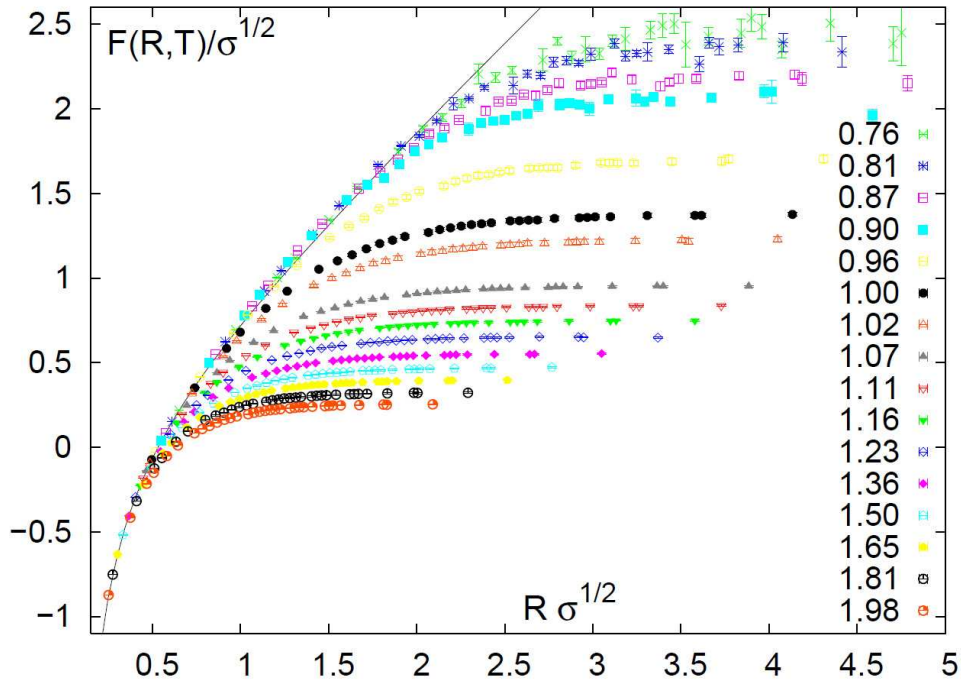


Figure 1.2: Free energy of the color singlet quark and anti-quark pair as a function of distance between them at different temperatures (T/T_c) [12]. Here σ is the string tension and order of $\sigma \sim (0.4)^2$ (GeV)².

Fig. 1.2. This phenomenon is called as “color screening”, in analogy to the Debye screening of an electric charge in Quantum ElectroDynamics (QED). This leads to the suppression of the charmonia and bottomonia production in QGP.

Suppression of quarkonia yield in QGP was first predicted by T. Matsui and H. Satz [3], which is outlined in Sec. 2.4.1. Suppression of charmonia and bottomonia production has been considered as one of the unambiguous signatures of the formation of QGP.

Figure 1.3 shows the phase diagram between temperature and net baryon density in the system. QGP is believed to exist at early universe, of the order of 10^{-6} seconds after the Big Bang.

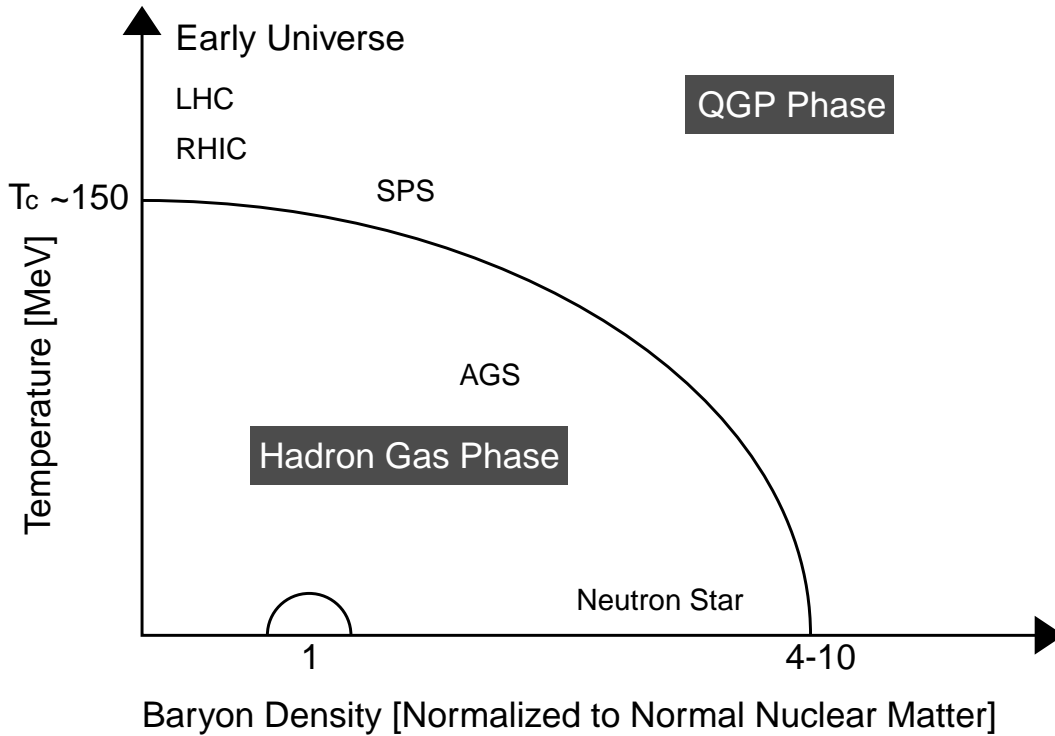


Figure 1.3: The phase diagram in temperature and baryon density

1.3 Relativistic Heavy Ion Collisions

Relativistic heavy ion collision is the tool in the laboratory to realize such a high temperature and to provide the characteristic of QGP [2]. There are many nucleons in the heavy nucleus and many nucleon-nucleon collisions are involved in heavy ion collisions. Longitudinal kinetic energies carried by the colliding nuclei are dissipated by the collisions and release huge energy into the tiny colliding region, which leads to energy density of matter very high enough to form hot and dense QCD matter.

Historically, experiments with high-energy heavy-ion collisions were performed at Bevalac in Lawrence Berkeley Laboratory from middle of 1970’s to the end of 1980’s. In the middle of 1980’s, various experiments have been carried out at Alternating Gradient Synchrotron (AGS)

at Brookhaven National Laboratory (BNL) and Super Proton Synchrotron (SPS) at European Center for Nuclear Research (CERN)

The Relativistic Heavy Ion Collider (RHIC) at BNL started its operation in 2000. In near future, Large Hadron Collider (LHC) at CERN will be ready for the heavy ion collisions with ~ 30 times larger collision energy compared at RHIC. Table 1.1 is the summary of the accelerator, collision energy in center-of-mass frame and collision species for heavy ion collisions.

Accelerator	collisions energy in center-of-mass frame	collisions species
AGS (BNL, 1986-)	~ 5 A GeV	$p+A$, $O+A$, $Si+A$, $Au+Au$
SPS (CERN, 1986-)	17.3 A GeV, 19.4 A GeV	$p+A$, $S+U$, $Pb+Pb$, $In+In$
RHIC (BNL, 2000-)	200 A GeV, 62.4 A GeV	$p+p$, $d+Au$, $Au+Au$, $Cu+Cu$
LHC (CERN, 2008-)	5.5 A TeV (Pb+Pb)	$p+p$, $p+Pb$, $Pb+Pb$

Table 1.1: Past, current and future accelerator for heavy ion collisions.

1.3.1 Collision geometry of heavy-ion collisions

Relativistic high-energy heavy-ion collisions can be described by “participants-spectator picture”, which is based on a geometrical picture of two colliding nuclei at a certain impact parameter b .

As shown in Fig. 1.4, the colliding nuclei are highly Lorentz contracted and look like thin pancakes at the relativistic collisions. Nucleons in the overlap region in transverse plane participate in the collisions. The nucleons in this region are called as “*participants*”. The nucleons in other region of nuclei, which are called as “*spectator*”, do not participate in the collisions and pass through the region with the same velocity before the collision. Participants deposit large energy in the tiny area in the collisions, and the released energy is closely related to the total number of participants in the collisions. If $b \sim 0$, almost all the nucleons participate in the collisions and collisions with small impact parameter is called “*central collisions*”, while the smaller nucleons participate in the collisions in case of larger impact parameter and such collisions is called “*peripheral collisions*”.

The impact parameter b controls the size of the overlap region, the number of participants (N_{part}) and the number of nucleon-nucleon collisions occurred in the participant region (N_{col}). The number of participants (N_{part}) and the number of inelastic nucleon-nucleon collisions (N_{col}) in a collision with an impact parameter b are calculated using the Glauber model, which is explained in Sec. 6.2.

1.3.2 Evolution of the matter in heavy-ion collisions

The evolution of the matter created in high-energy heavy-ion collisions may be viewed through the following stages as shown by the space-time diagram with the space coordinate in beam

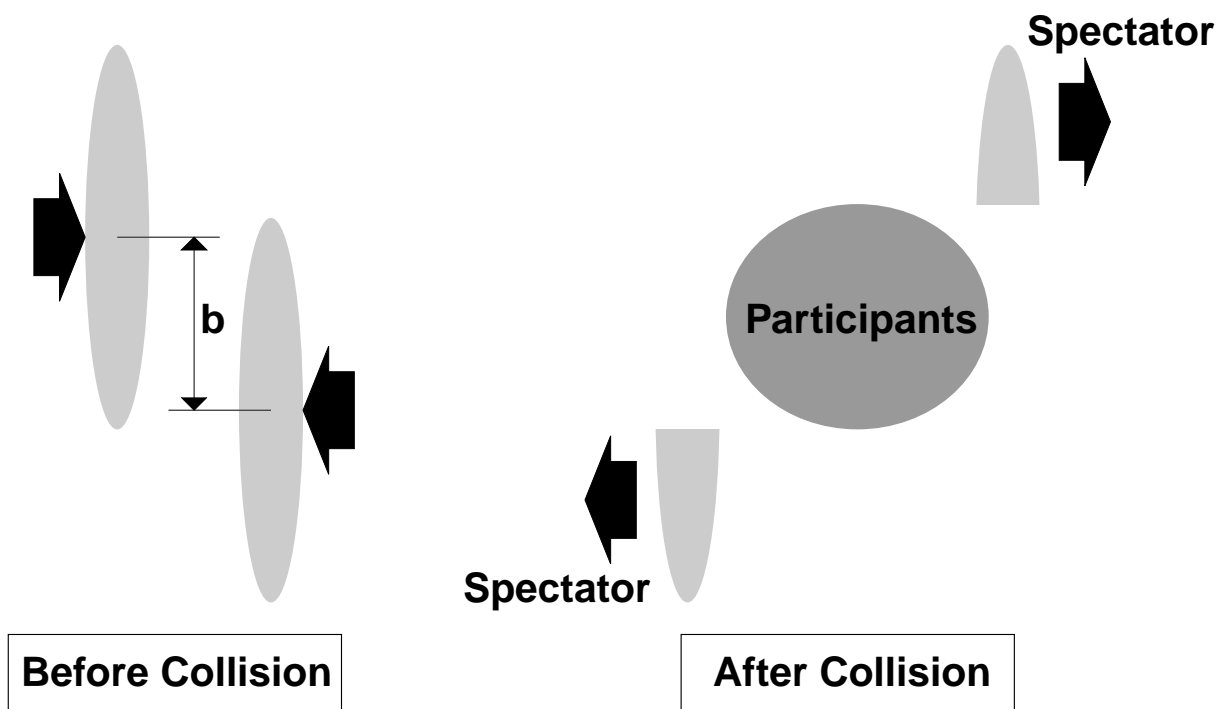


Figure 1.4: The view of the colliding nuclei before (left) and after (right) collisions. They approach each other with nearly speed of light and the impact parameter b before collisions. After the collisions, the system consists of two components: spectator and participants.

going direction z and the time coordinate t . This is shown in Fig 1.5, which was established by Bjorken [13].

1. pre-equilibrium

Scattering between partons occurs. A huge energy is released into a tiny volume. The energy density is expected to be so high to form the deconfined matter of quarks and gluons. The matter initially may not be in thermal equilibrium.

2. deconfined state of partons in thermal (and/or chemical) equilibrium

Subsequent multiple scattering of partons leads the matter to the thermal equilibrated system (QGP) at the proper time of τ_0 . The QGP then evolves according to hydrodynamics.

3. mixed phase between QGP and hadrons

As the QGP evolves, the temperature drops. As the temperature reaches T_c , the QGP begins to hadronize and the system is composed of the deconfined quarks and gluons and hadrons. This state would exist only if the transition is first order.

4. a gas of hot interacting hadrons and a freeze out state

While the system hadronizes, hadrons keep interacting until the temperature drops below the freeze-out temperature. At the freeze-out temperature, the interaction between hadrons ceases and the hadrons stream out.

This picture assumes that the space-time evolution of the system looks essentially the same as a function of rapidity [13]. Therefore the formation of equilibrium states of partons, mixed states between hadrons and partons and a gas state of hadrons occur at the certain proper time $\tau = \sqrt{t^2 - z^2}$. The relationship between space-time coordinate and the rapidity is described in Appendix A.

1.3.3 Initial energy density

Bjorken has provided the estimation of the initial energy density in a collision system based on the physics observables: multiplicity of particles and transverse energy [13]. Given that the A_\perp and Δz are the overlap area in transverse plane between two colliding nuclei and the longitudinal thickness of overlap region, respectively, the colliding volume can be expressed as $A_\perp \Delta z$. Taking ΔN as a number of particles in this volume, the particle density can be extracted as follows:

$$\frac{\Delta N}{A_\perp \Delta z} = \frac{1}{A_\perp} \frac{dN}{dy} \frac{dy}{dz} = \frac{1}{A_\perp} \frac{dN}{dy} \frac{1}{\tau_0 \cosh y}, \quad (1.2)$$

where the proper time τ_0 corresponds to the formation time of QGP. Energy density at the proper time τ_0 , ϵ_0 , can be written:

$$\begin{aligned} \epsilon_0 &= E_T \frac{\Delta N}{A_\perp \Delta z} = m_T \cosh y \frac{\Delta N}{A_\perp \Delta z}, \\ &= \frac{m_T}{A_\perp \tau_0} \frac{dN}{dy} = \frac{1}{A_\perp \tau_0} \frac{dE_T}{dy}, \end{aligned} \quad (1.3)$$

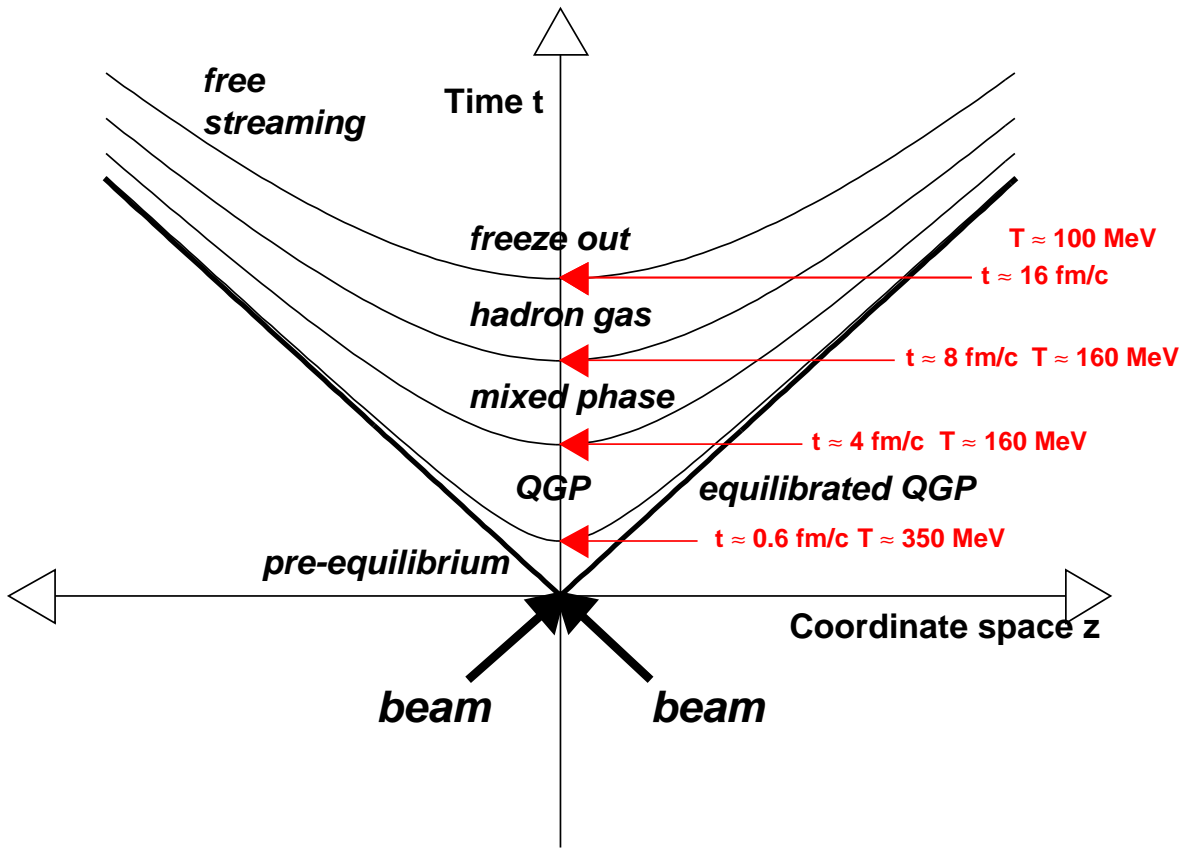


Figure 1.5: Space time evolution of the medium created at relativistic heavy ion collisions [13]. Mixed phase would exist only if the transition is first order.

where $m_T \equiv \sqrt{p_T^2 + m^2}$ and E_T are the transverse mass and transverse energy, respectively.

When τ_0 is taken to be 1 fm/c, Bjorken energy density reaches ~ 2.9 GeV/fm³ at SPS ($\sqrt{s_{NN}} = 17.3$ GeV) [14] and ~ 5 GeV/fm³ at RHIC ($\sqrt{s_{NN}} = 200$ GeV) [15]. These energy densities exceed the critical density of $\epsilon_c \sim 1$ GeV/fm³ for the phase transition.

1.4 Organization of This Thesis

The J/ψ production in high-energy Au+Au collisions at RHIC will be discussed in this thesis. Di-electron decay channel of J/ψ was used in this study.

The organization of this thesis is as follows. Chapter 2 introduces theoretical and experimental backgrounds for the J/ψ production in high-energy heavy-ion collisions. In Chapter 3, the accelerator complex at BNL and the detectors in the PHENIX are described. In Chapter 4, the beam condition, luminosity conditions and the trigger condition in 2004 (Year-4) Au+Au runs are explained. Particle tracking, momentum determination and electron identification using PHENIX detectors are explained in Chapter 5.

The observable quantities to discuss the J/ψ production in A+A collisions are introduced in Chapter 6. Determination of collision geometry, identification of J/ψ and the corrections such as acceptance and detection efficiency of $J/\psi \rightarrow e^+e^-$ are also discussed in Chapter 6. In Chapter 7, the results of the J/ψ production in Au+Au collisions at $\sqrt{s_{NN}} = 200$ GeV at mid-rapidity are described and the interpretations of them are discussed in Chapter 8. Chapter 9 concludes this work.

1.5 Major Contributions

The major contributions of the author as a PHENIX collaborator are listed as follows:

- Operation of Ring Imaging CHerenkov detector (RICH)
- Development of online and offline system for RICH
- Calibration of RICH mirror alignment in Au+Au collisions
- Calibration of electron identification parameters in Au+Au collisions
- Organization of the small physics working group, which concentrates on the electron related analysis
- Publication of the paper “ *J/ψ Production vs Centrality, Transverse Momentum, and Rapidity in Au+Au collisions at $\sqrt{s_{NN}} = 200$ GeV*” [16] on behalf of the PHENIX Collaboration

Chapter 2

Physics Background

This chapter describes the important features of charmonium states and medium effects on J/ψ production in heavy-ion collisions. Experimental results of J/ψ production in heavy-ion collisions at SPS energies are also shown.

2.1 Charmonium Family

J/ψ is a bound state of $c\bar{c}$ pair, which was discovered at AGS in BNL [17] and at Stanford Linear Accelerator Center electron-positron storage ring (SPEAR) in Stanford Linear Accelerator Center (SLAC) [18]. Table 2.1 shows the properties of charmonium states such as J/ψ as well as other charmonium states (η_c , χ_{c0} , χ_{c1} , χ_{c2} and ψ') [19]. Figure 2.1 shows the spectrum and

Resonance	$n^{2S+1}L_J$	J^{PC}	Mass [GeV]	Width [MeV]	Decay Mode	Branching Ratio [%]
η_c	1^1S_0	0^{-+}	2.980	16.0	[19]	[19]
J/ψ	1^3S_1	1^{--}	3.097	0.093	hadrons e^+e^- $\mu^+\mu^-$	87.7 ± 0.5 5.94 ± 0.10 5.93 ± 0.10
χ_{c0}	1^3P_0	0^{++}	3.415	10.5	$J/\psi + \gamma$	1.30 ± 0.11
χ_{c1}	1^3P_1	1^{++}	3.511	0.89	$J/\psi + \gamma$	35.6 ± 1.9
χ_{c2}	1^3P_2	2^{++}	3.556	1.95	$J/\psi + \gamma$	20.2 ± 1.0
ψ'	2^3S_1	1^{--}	3.686	0.277	hadrons $J/\psi + X$ e^+e^- $\mu^+\mu^-$	97.9 ± 0.3 56.1 ± 0.9 0.74 ± 0.18 0.73 ± 0.8

Table 2.1: Properties of charmonium bound states. In Quantum numbers, n , S , L and J show the radial quantum number, total intrinsic spin, orbital angular momentum, and total angular momentum, respectively.

transitions of the charmonium family [19].

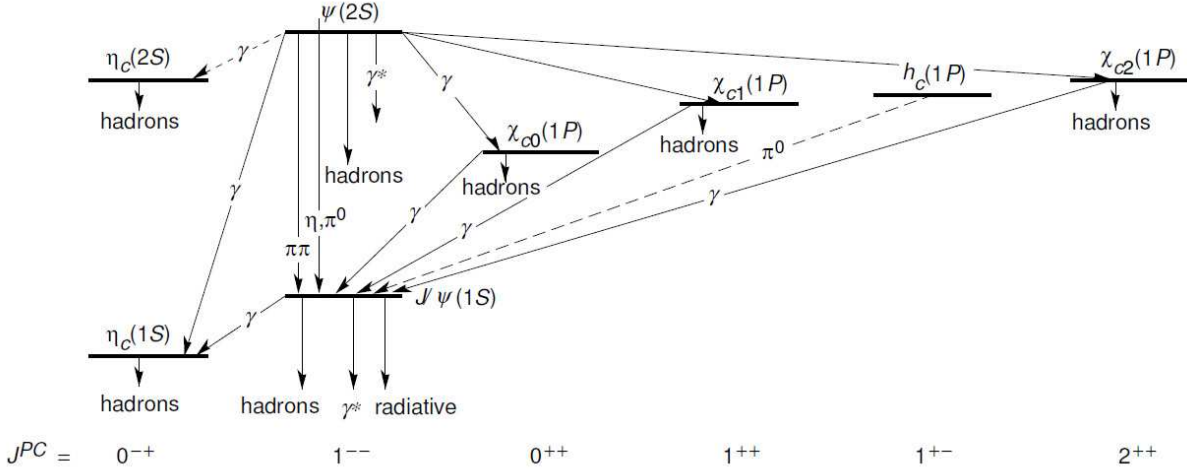


Figure 2.1: The spectrum and transitions of the charmonium family [19].

2.2 J/ψ Production Mechanism

In this section, production mechanism of J/ψ is briefly described.

The production of heavy quark pairs is expected to be a perturbative process since the mass of charm quarks are heavy compared to the typical QCD scale $\Lambda_{QCD} \simeq 0.2$ GeV, which corresponds to $\alpha_s(m_c) \ll 1$. Figure 2.2 shows the examples of heavy quark production diagrams [20], where (a)-(c) are the leading order (LO) processes [21] and (d)-(f) are higher order processes [22]. The dominant process for $c\bar{c}$ production is gluon fusion process as shown in (a) and (b) of Fig. 2.2 and this process takes place in a very short time $\tau_{pert} \simeq 1/2m_c$ [23].

There are some models such as Color Singlet Model (CSM), Color Evaporation Model (CEM) and Color Octet Model (COM) to describe the mechanism of J/ψ formation, which derives from different assumptions on the non-perturbative transition from $c\bar{c}$ pair to J/ψ and are explained briefly in the following sections.

2.2.1 Color singlet model (CSM)

The color singlet model (CSM) was first proposed shortly after the discovery of J/ψ [24, 25, 26]. The CSM requires that $c\bar{c}$ pair is created to have the same quantum numbers as the J/ψ to be formed. Figure 2.3 shows an example of the lowest order diagram of J/ψ production in CSM, where the $c\bar{c}$ pair should have $^{2S+1}L_J = ^3S_1$ and should be in color singlet state as J/ψ . In this model, hard-gluon emission is necessary to conserve the C -parity. This model can describe the J/ψ production cross section in photo-production ($\gamma + N$) [25] but failed to explain differential cross section of Tevatron data in $p + \bar{p}$ collisions at $\sqrt{s} = 1.8$ TeV by a factor of ~ 60 [27].

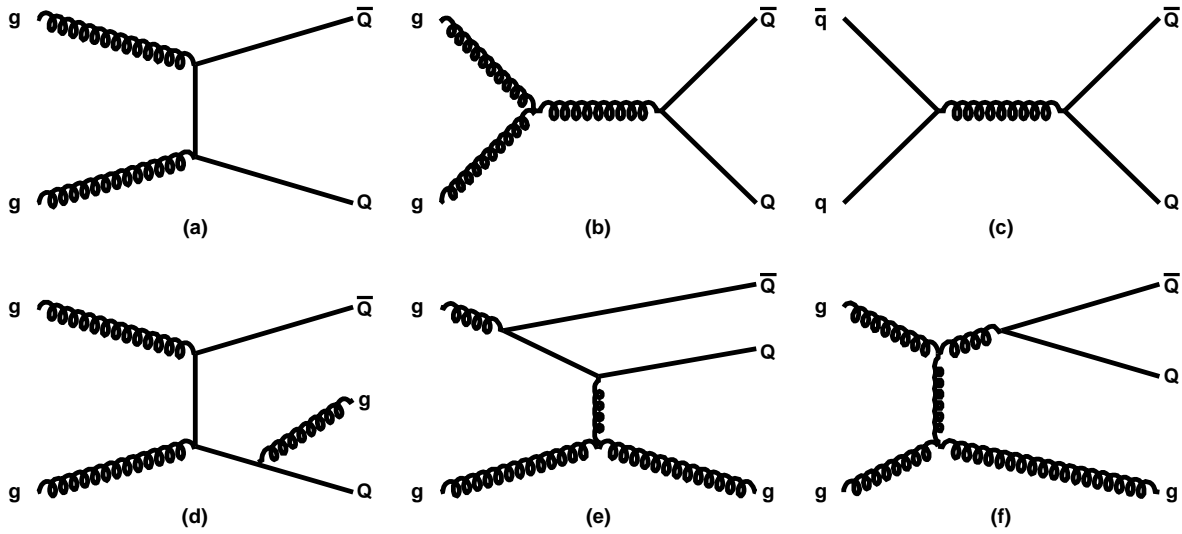


Figure 2.2: Examples of heavy-quark production diagrams. (a),(b) Leading order Gluon fusion, (c) Leading order pair annihilation, (d) Pair creation with gluon emissions, (d) flavor excitation, (e) gluon splitting [20].

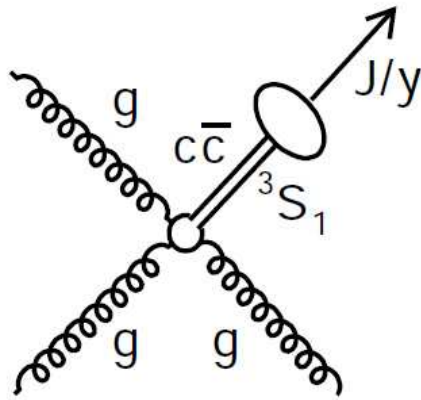


Figure 2.3: An example of the lowest order diagram for direct J/ψ production from gluon fusion with the color singlet model. The $c\bar{c}$ pair is in the color singlet state.

2.2.2 Color evaporation model (CEM)

The color evaporation model was first proposed in 1977 [28, 29]. In the CEM, production cross section of quarkonia state ψ is some of the fraction f_ψ of the cross section for the production of $c\bar{c}$ pairs with the invariant mass below the $D\bar{D}$ threshold. CEM model has the restriction on the $c\bar{c}$ mass of below $D\bar{D}$ mass but doesn't have the constraints on the color or other quantum numbers for $c\bar{c}$ pairs. The $c\bar{c}$ pair is assumed to neutralize its color by interaction with the collision-induced color field, that is, by "color evaporation". In the CEM, charmonium state is formed through multiple soft-gluon emissions as shown in Fig. 2.4. The CEM describes

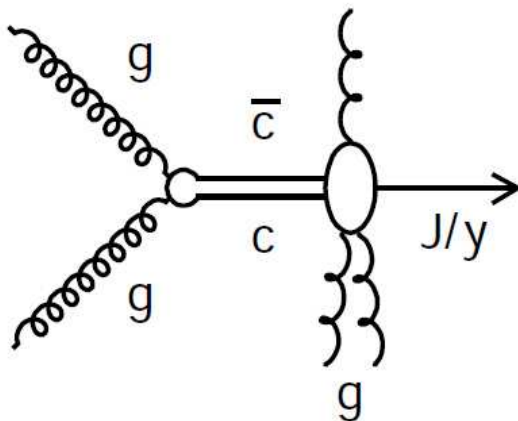


Figure 2.4: An example of the lowest order diagram for direct J/ψ production from gluon fusion with the color evaporation model. Multiple soft-gluon emissions destroy the information on quantum numbers of $c\bar{c}$ pair.

J/ψ total cross sections in both hadro-production and photo-production at lower energies [30]. Also the CEM predicts zero polarization of J/ψ , which is consistent with the lower p_T but seems not to be consistent at inter-mediate and high p_T region [31].

2.2.3 Color octet model (COM)

The color octet model (COM) has been developed in the 1990's based on the non-relativistic QCD (NRQCD) framework [32]. The COM allows the formation of a charmonium from a color-octet $c\bar{c}$ pair with one or some soft gluon emissions as illustrated in Fig. 2.5. Using appropriate color-octet matrix elements, which are additional free parameters needed to be extracted from experimental data, the COM has successfully reproduced p_T distributions at CDF [27] and total cross section at lower-energy experiments [33, 34]. However, the COM predicts large transverse polarization of J/ψ , which is not seen in experimental data [31].

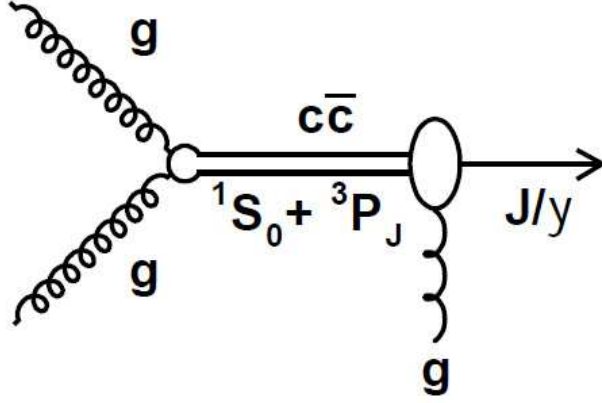


Figure 2.5: An example of the lowest order diagram for direct J/ψ production from gluon fusion with the color octet model. The $c\bar{c}$ pair is in the color octet state.

2.3 Feed-down Effects

There is an important feature to be noted for J/ψ production in hadron-hadron collisions. The J/ψ 's actually measured in hadron-hadron collisions have three distinct origins: $\sim 60\%$ are directly produced J/ψ , while $30\sim 40\%$ come from the decay of χ_c states and $5\sim 10\%$ are from ψ' [35, 36, 37, 38]. Feed down fraction from χ_c (R_χ) and ψ' (R_ψ) to J/ψ can be expressed as follows:

$$R_\chi = Br(\chi \rightarrow J/\psi + X) \frac{\sigma(\chi)}{\sigma(J/\psi)} \quad (2.1)$$

$$R_\psi = Br(\psi \rightarrow J/\psi + X) \frac{\sigma(\psi)}{\sigma(J/\psi)}, \quad (2.2)$$

where $Br(\chi \rightarrow J/\psi + X)$ and $Br(\psi \rightarrow J/\psi + X)$ are the branching ratio of χ and ψ decaying to J/ψ , respectively. σ_χ , $\sigma_{J/\psi}$ and σ_ψ are the production cross section of χ , J/ψ and ψ , respectively.

Figure 2.6 shows the ratio of χ_c production cross section which decayed to J/ψ to the production cross section of inclusive J/ψ (R_{χ_c}) as a function of the collision energy (\sqrt{s}). Solid and dashed lines are the predictions from NRQCD (COM) and CSM, respectively [35]. The world average of R_χ is $\sim 35\%$. Ratio of the production cross section for ψ' to that for J/ψ was measured at various experiments [36, 37, 38]. Figure 2.7 shows the ratio $B(\psi' \rightarrow \mu^+\mu^-)\sigma(\psi')/B(J/\psi \rightarrow \mu^+\mu^-)\sigma(J/\psi)$ as a function of the center of mass energy [37]. Average gives $B(\psi' \rightarrow \mu^+\mu^-)\sigma(\psi')/B(J/\psi \rightarrow \mu^+\mu^-)\sigma(J/\psi) \sim 1.6\%$, which leads to $R_\psi \sim 7.5\%$.

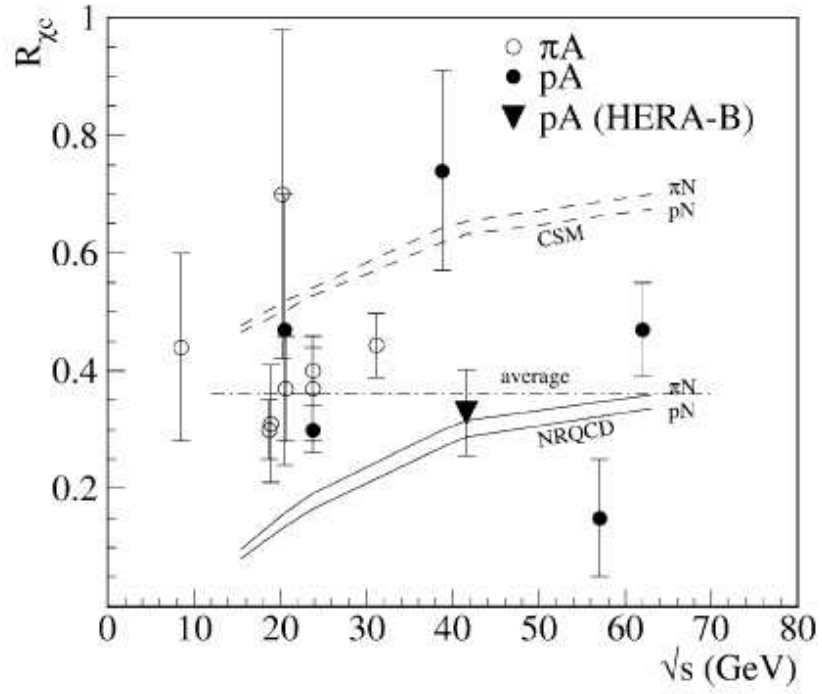


Figure 2.6: the ratio of χ_c production cross section which decayed to J/ψ to the production cross section of (inclusive) J/ψ (R_{χ_c}) as a function of \sqrt{s} . Solid and dashed lines are the predictions from NRQCD (COM) and CSM, respectively [35].

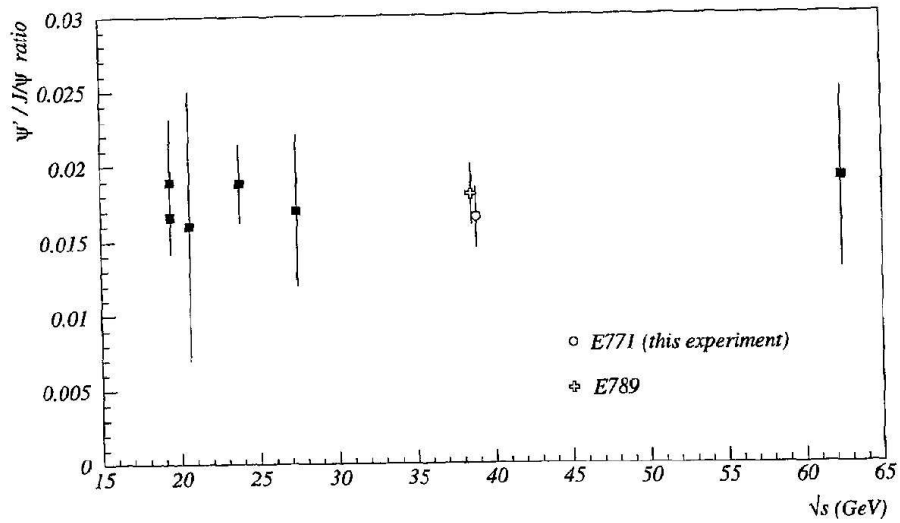


Figure 2.7: The $B\sigma(\psi')/B\sigma(J/\psi)$ ratio as a function of the center of mass energy [37].

2.4 J/ψ Production in Heavy Ion Collisions

Since the mass of charm quarks is heavy, the creation of charm quark pairs takes place only at the beginning of the collisions. Pre-resonance $c\bar{c}$ state exists before J/ψ is formed. The time scale of the color neutralization to form J/ψ from pre-resonance $c\bar{c}$ is estimated to be $\tau_8 \simeq 1/\sqrt{2m_c\Lambda_{\text{QCD}}} \simeq 0.25 \text{ fm}/c$, where m_c and Λ_{QCD} are the charm mass ($\simeq 1.5 \text{ GeV}$) and typical QCD scale ($\simeq 0.2 \text{ GeV}$), respectively [23]. Since heavy quarks are created at the short time scale of the collisions and J/ψ may be formed before the formation of QGP, pre-resonance $c\bar{c}$ state and J/ψ are involved in the evolution of the matter as well as the initial conditions inside the nuclei.

Medium effects on the J/ψ production in heavy-ion collisions can be categorized into two groups. One is the effects on the J/ψ production after the formation of QGP, called as “final state effects”. The other is the effects before the formation of QGP, called as “initial state effects” or “cold nuclear matter effects (CNM)”.

As the final state effects, following mechanisms are the possible contributions to the modification of J/ψ production in heavy-ion collisions [39].

- Color screening and/or dissociation of $c\bar{c}$ and/or J/ψ by the thermal partons in QGP
- Recombination of J/ψ from uncorrelated $c\bar{c}$ pairs in QGP and/or at the phase boundary
- Interaction of J/ψ with secondary comoving particles

As the cold nuclear matter effects, the following are the possible contributions to the modification of J/ψ production.

- Depletion of gluon distribution function in heavy nuclei at small x (Gluon shadowing, Color Glass Condensate)
- Interaction of pre-resonance $c\bar{c}$ state or J/ψ with the target/projectile nucleons (Nuclear absorption)
- Multiple interactions of partons inside the nuclei (Cronin effect)

Each effect is explained in the following sections.

2.4.1 Final state effects on J/ψ production

In this section, final state effects on the J/ψ production such as color screening, dissociation of J/ψ by thermal gluons, recombination of J/ψ from uncorrelated $c\bar{c}$ pairs and comover interactions are explained.

Color screening in QGP

The potential energy of a $q\bar{q}$ system in vacuum can be described in terms of Coulomb potential and confining linear potential as follows [40]:

$$V(r) = (-q)\frac{q}{4\pi r} + \kappa r, \quad (2.3)$$

where q is the color charge, r is the separation between $q\bar{q}$ and κ is the string tension coefficient. The Hamiltonian for the $q\bar{q}$ system is:

$$H = \frac{\mathbf{p}^2}{2\mu} - \frac{\alpha_{eff}}{r} + \kappa r, \quad (2.4)$$

where $\mu = m_c/2$ is the reduced mass of the $c\bar{c}$ system and $\alpha_{eff} = q^2/4\pi$. The observed spectroscopy of charmonium states is described well by the Hamiltonian with the set of parameters: $\alpha_{eff} = 0.52$, $\kappa = 0.926$ GeV/fm and $m_c = 1.84$ GeV [40]. Table 2.2 is the summary of the calculated radius of each charmonium states $\langle r^2 \rangle^{1/2}$ and binding energy of them ΔE [39, 40].

Resonance	State	Mass	$\langle r^2 \rangle^{1/2}$ [fm]	ΔE [GeV]
J/ψ	1S	3.098	0.47	0.64
χ_c	1P	~ 3.522	0.74	0.20
ψ'	2S	3.686	0.96	0.05
Υ	1S	9.46	0.20	1.10

Table 2.2: Summary of the radius of each charmonium states $\langle r^2 \rangle^{1/2}$ and binding energy of them ΔE [39, 40].

As shown in Fig. 1.2, the potential energy between heavy $q\bar{q}$ pair is modified in QGP. T. Matsui and H. Satz proposed that the potential between $q\bar{q}$ pair is modified from the long-range Coulomb potential as described in Eq. (2.3) to the short-range Yukawa potential as follows [3]:

$$V(r) = \frac{q}{4\pi} \frac{e^{-r/\lambda_D}}{r}, \quad (2.5)$$

where λ_D is the Debye screening length and r is the separation between $q\bar{q}$ pair.

Using Eq. (2.5), the Hamiltonian of $q\bar{q}$ system in QGP can be written:

$$H = \frac{\mathbf{p}^2}{2\mu} - \frac{\alpha_{eff} e^{-r/\lambda_D}}{r}. \quad (2.6)$$

From the uncertainty relation $\langle \mathbf{p}^2 \rangle \sim 1/r^2$, the energy of the $q\bar{q}$ system can be expressed:

$$E(r) = \frac{1}{2\mu r^2} - \frac{\alpha_{eff} e^{-r/\lambda_D}}{r}. \quad (2.7)$$

A bound state is possible if $E(r)$ has a minimum with respect to r . This requirement leads to the following conclusion [3].

$$q\bar{q} \text{ will not be bound if } \frac{1}{0.84} R_{\text{Bohr}} \geq \lambda_D, \quad (2.8)$$

where $R_{\text{Bohr}} = 1/(\alpha_{eff}\mu)$ is the Bohr radius of $q\bar{q}$ pair.

Debye screening length is evaluated by the one-loop calculations in perturbative QCD framework as follows [41]:

$$\lambda_D(\text{pQCD}) = \frac{1}{\sqrt{(\frac{N_c}{3} + \frac{N_f}{6})g^2 T}}, \quad (2.9)$$

where N_c is the degree of freedom of color, N_f is the number of quark flavors, T is the temperature of the medium and $g^2 = 4\pi\alpha_{eff}$. It is seen that the Debye screening length depends on temperature and that Debye screening length becomes smaller as temperature goes higher, which means that J/ψ is easily melt at higher temperature.

For the QGP with $N_c = 3$, $N_f = 3$ and $T = 200$ MeV in Eq. (2.9), the screening length with $\alpha_{eff} = 0.52$ becomes

$$\lambda_D(\text{pQCD}) = 0.36 \text{ fm}. \quad (2.10)$$

For a $c\bar{c}$ system with $\alpha_{eff} = 0.52$ and reduced mass of $\mu = 1840 \text{ MeV}/2$, R_{Bohr} becomes 0.41 fm. In this case, R_{Bohr} is larger than λ_D , which indicates that a $c\bar{c}$ cannot be bound in QGP at $T = 200$ MeV ($\sim 1.1T_c$).

Recent quenched lattice QCD calculations and the analyses based on $q\bar{q}$ potential (internal or free energy) can extract the dissociation temperature of each charmonium and bottomonium state [42, 43, 44, 45, 46, 47].

Figure 2.8 and Figure 2.9 show the spectral functions based on the quenched lattice QCD calculations for J/ψ (vector channel) and η_c (pseudo-scalar channel), respectively [42, 43]. Both results shows that the J/ψ and η_c are stable even up to $1.6 T_c \sim 2.25T_c$.

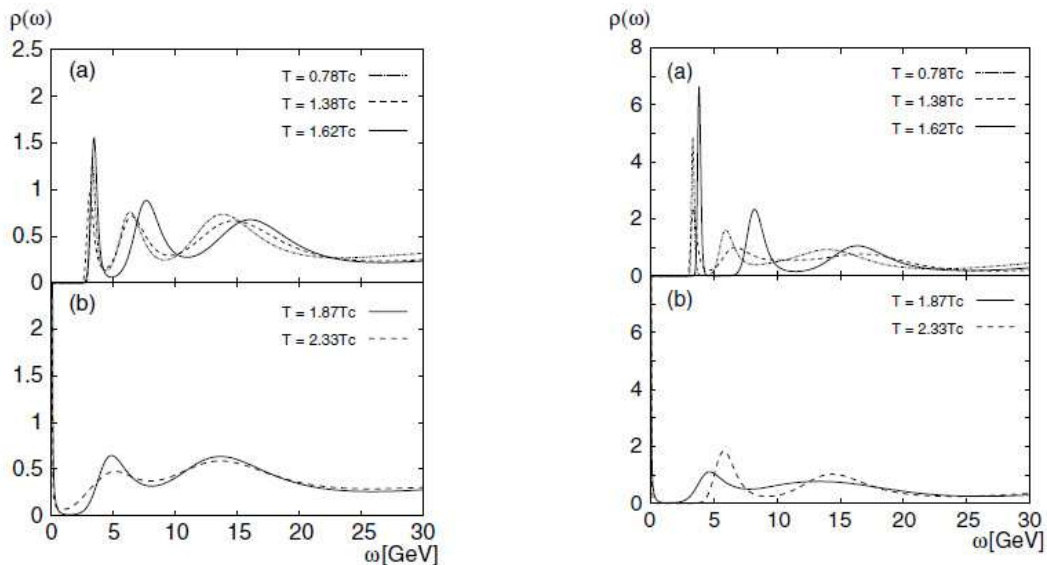


Figure 2.8: Spectral functions for J/ψ (Left) and for η_c at the temperature T/T_c of (a) 0.78, 1.38, 1.62 and (b) 1.87, 2.33 [42]

Figure 2.10 shows the temperature dependence of the binding energy for J/ψ (a) and for χ_c and ψ' (b) based on the potential model analysis [39], from which the dissociation temperature of J/ψ , χ_c and ψ' are $\sim 2 T_c$, $1.16 T_c$ and $1.12 T_c$, respectively.

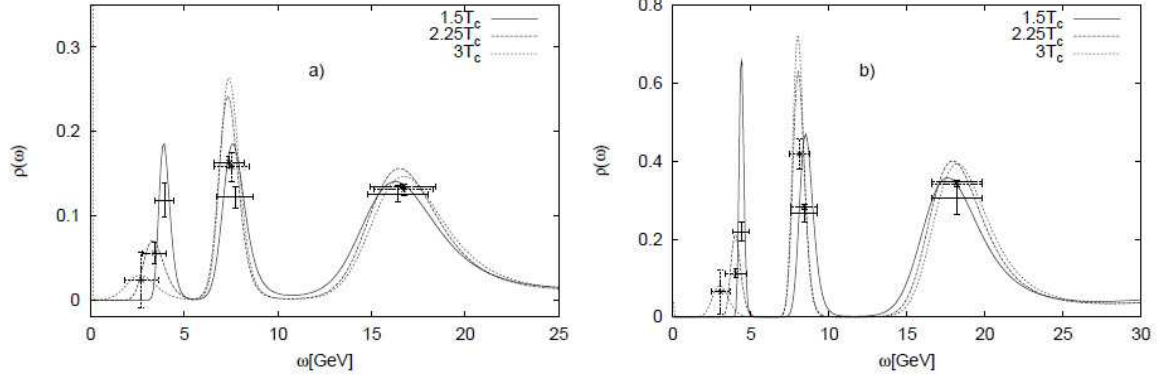


Figure 2.9: The spectral functions for (a) pseudo-scalar and (b) vector channels at the temperature T/T_c of 1.5, 2.25 and 3 [43].

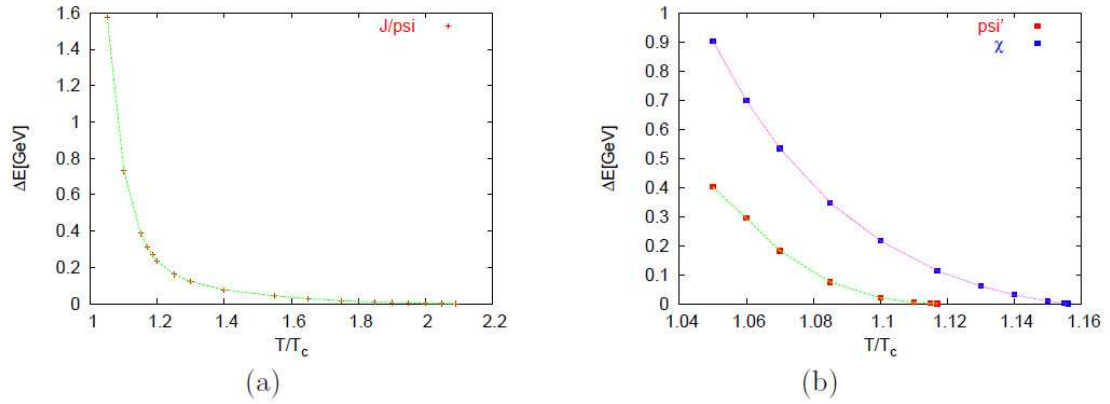


Figure 2.10: Temperature dependence of binding energy for J/ψ (a) and for χ_c and ψ' (b).

Table 2.3 is the summary of the dissociation temperature T_d/T_c for quarkonia inferred from potential model analyses [39].

Resonance	J/ψ (1S)	χ_c (1P)	ψ' (2S)	Υ (1S)	χ_b (1P)	Υ (2S)	χ_b (2P)	Υ (3S)
T_d/T_c	2.10	1.16	1.12	≥ 4.0	1.76	1.60	1.19	1.17

Table 2.3: Dissociation temperature T_d/T_c for quarkonia inferred from lattice QCD calculations and potential model analyses [39].

These dissociation temperatures indicates that J/ψ may survive at SPS and begin to be melt at RHIC central Au+Au collisions, while χ_c and ψ' are dissolved at both SPS and RHIC energies.

Color screening can be interpreted as the dissociation of $c\bar{c}$ or J/ψ by thermal partons in QGP [39].

Since J/ψ is small system and tightly bound system, only a sufficiently high-energy projectile can break the binding. Therefore it is expected that J/ψ can only be dissociated by the interaction with a hard gluons of the hadron, not with the hadron as a whole. The gluon momentum distribution $g(x)$ with the gluon momentum k_h , hadron momentum p_h and $x = k_h/p_h$ in mesons can be parameterized for large x as follows:

$$g(x) \sim (1 - x)^3. \quad (2.11)$$

This gives the average momentum of gluons inside hadrons as

$$\langle k_h \rangle = \frac{1}{5} \langle p_h \rangle. \quad (2.12)$$

For the massless thermal hadrons in confined matter, average momentum of hadrons is given by:

$$\langle p_h \rangle = \frac{\int p \times p^2 \exp(-p/T) dp}{\int p^2 \exp(-p/T) dp} = 3T \quad (2.13)$$

When the temperature of hadronic matter is $T \leq 175$ MeV, the average of momentum of gluons becomes:

$$\langle k_h \rangle = \frac{3}{5} T \sim 0.1 \text{ GeV}. \quad (2.14)$$

On the other hand, in the deconfined matter, the average momentum of thermal gluon can be:

$$\langle k_g \rangle = 3T \sim 0.6 \text{ GeV} \quad (2.15)$$

Figure 2.11 shows the dissociation cross section of J/ψ by thermal gluons and hadrons [39, 48, 49]. The cross section between J/ψ by gluons was calculated from leading order diagram [48]. From Eq. (2.14) and Eq. (2.15), the dissociation cross section of J/ψ by thermal gluons is significant larger compared to that by hadrons, which indicates that the J/ψ can be dissolved in QGP and survive in confined medium.

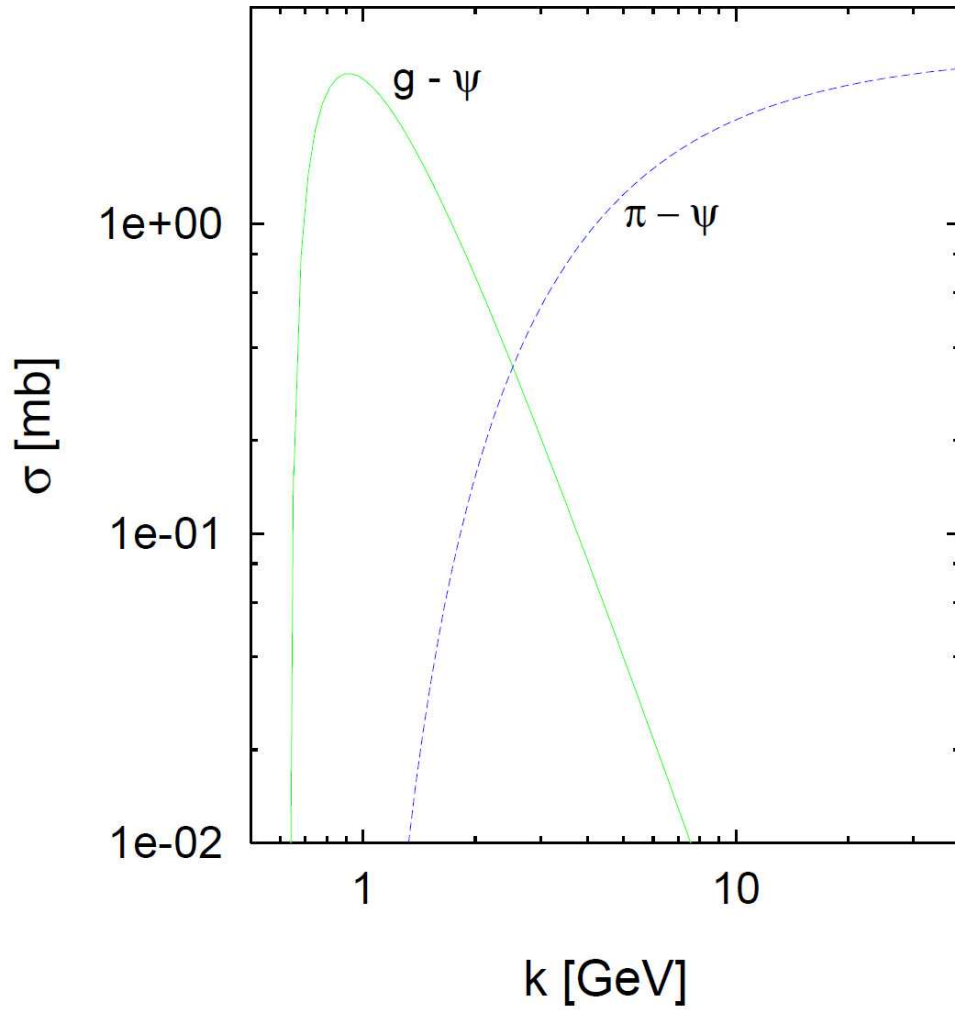


Figure 2.11: J/ψ dissociation cross section by gluons (green) and hadrons (blue) [39, 49].

Recombination of J/ψ

Recent theoretical models predict that the J/ψ yield would be enhanced due to the recombination of uncorrelated $c\bar{c}$ pairs at RHIC energy, where $c\bar{c}$ pairs are created by different nucleon-nucleon collisions abundantly [50, 51, 52, 53, 54, 55]. This scenario is derived from the assumption that the number of J/ψ from recombination are approximately proportional to N_c^2/N_h , where N_c and N_h are the number of created charm quarks and the number of produced hadrons. This effect cannot be negligible at RHIC energy since the charm production cross section increases faster with \sqrt{s} and scales with the number of inelastic nucleon-nucleon collisions, while the multiplicity of hadrons (N_h) is scaled with the number of the participant nucleons. Since the number of nucleon-nucleon collisions is sufficiently larger in more central collisions than the number of participant nucleons at RHIC energy *, N_c^2/N_h leads to the higher value at higher collision energy and in more central collisions.

There are various models (kinetic formation, transport model, statistical coalescence and hadron-string dynamics) which take into account the recombination of J/ψ from $c\bar{c}$ pairs and/or $D\bar{D}$ pairs. Each of them is explained briefly.

- **Kinetic formation**

The kinetic formation model takes into account the recombination of J/ψ as well as the initial J/ψ productions. The population of J/ψ is related to the dissociation process of J/ψ by thermal gluons and the inverse reaction in which charm quarks and gluons interact to form J/ψ . This can be expressed in the following balance equation [51].

$$\frac{dN_\psi}{dt} = -\Gamma_\psi(N_\psi - N_\psi^{eq}), \quad (2.16)$$

where Γ_ψ is the dissociation rate, N_ψ^{eq} is the number of J/ψ in thermal equilibrium.

- **Transport model**

The motion of J/ψ in QGP is taken account into in this model. The evolution of J/ψ number is described by kinetic theory within a Boltzmann equation. The dissociation and recombination of J/ψ is controlled by the loss and gain term in Boltzmann equation. The J/ψ distribution function $f_{J/\psi}$ can be expressed as follows [52]:

$$\frac{\partial f_{J/\psi}}{\partial \tau} + \mathbf{v}_{J/\psi} \cdot \nabla f_{J/\psi} = -\alpha_{J/\psi} f_{J/\psi} + \beta_{J/\psi}, \quad (2.17)$$

where $\mathbf{v}_{J/\psi}$ is the transverse velocity of J/ψ , the first and second term in r.h.s correspond to the loss and gain term due to dissociation and recombination of J/ψ , respectively.

- **Statistical coalescence model**

*Detail of the number of nucleon-nucleon collisions and the number of participant nucleons in the collisions is described in Sec. 6.2.

The idea of statistical coalescence model was derived from the fact that the J/ψ yield relative to hadron yield at SPS energies does not have the collisions geometry (impact parameter) dependence [50] and that the hadron production at SPS energies can be described by the statistical model [53]. In this model, primordial J/ψ is completely suppressed in QGP and J/ψ is created at the hadronization stage from uncorrelated $c\bar{c}$ pairs and the number of created J/ψ follows the statistical law as:

$$N_{c\bar{c}}^{dir} = \frac{1}{2}\gamma_c N_{oc}^{th} \frac{I_1(\gamma N_{oc}^{th})}{I_0(\gamma N_{oc}^{th})} + \gamma_c^2 N_{c\bar{c}}^{th}, \quad (2.18)$$

where $N_{c\bar{c}}^{dir}$ stands for the number of produced $c\bar{c}$ pairs, I_n is modified Bessel function, γ_c is fugacity parameter. N_{oc}^{th} and $N_{c\bar{c}}^{th}$ are the total number of open and hidden charm hadrons calculated from their grand-canonical densities, respectively [54]. $N_{c\bar{c}}^{dir}$ is given by pQCD calculations or the experimental results of charm production cross section [54]. Fugacity parameter γ_c corresponds to the normalization factor to match r.h.s to the $N_{c\bar{c}}^{dir}$.

- **Hadron-string dynamics**

Hadron-string dynamics is the model to describe the J/ψ suppression by the break-up interactions with comover hadrons and reproduction of J/ψ from the backward reactions by $D\bar{D}$ channels employing the detailed balance [55]. This model predicts that the re-creation of charmonium is comparable to the dissociation by comovers at RHIC energies.

It should be noted that the charm production such as cross section as functions of charm p_T and rapidity and its modification in hot and dense medium need to be understood to study the recombination of J/ψ . At RHIC energy, charm production cross section in $p + p$ collisions is higher by a factor of ~ 2 compared to FNOLL calculation [56] and rapidity shape seems to be flatter than the theoretical expectation [57]. In Au+Au collisions at RHIC, it has been observed that charm quarks lose sufficient energy in hot and dense medium as light quarks lose their energy by gluon bremsstrahlung effect in the medium [58]. Also it has been observed that the charm quarks participate in the partonic flow with light quarks, which suggests the short relaxation time for charm quarks (comparable to the duration of the QGP phase, $\tau_{QGP} = 5 \text{ fm}/c$) and indicates that charm quarks move in hot and dense medium diffusively rather than freely [58].

Currently none of the recombination models take into account these observed properties on charm production in Au+Au collisions.

Comover Interactions of J/ψ

The comover scattering of J/ψ is an additional absorption of J/ψ by hadronic secondaries called comovers, which is occurred in hadronic phase [59]. The survival probability of J/ψ can be expressed as follows:

$$S_{co} = \exp\left(-\int d\tau n \sigma_{co} v_{ref}\right), \quad (2.19)$$

where n is the comover density at the time τ , σ_{co} is the J/ψ absorption cross section by comovers and v_{ref} is J/ψ velocity relative to comovers. The interaction cross section of J/ψ with light

hadrons are evaluated by various methods, which are summarized in Ref. [60]. At present, some of the predictions differ by orders of magnitude. For example, the color-dipole model based on perturbative QCD calculation predicts that the dissociation cross section by comovers is less than 1 mb [49], meson exchange calculations based on hadronic effective Lagrangians show that the cross section is 1-10 mb [61] and the quark interchange models based on the description of non-relativistic quark wave functions for the external hadrons predict the cross section is 0-6 mb [62].

Although the dissociation cross section of J/ψ with comovers is difficult to be determined theoretically, dual parton model, which takes into account the dissociation process by comovers, can reproduce the J/ψ suppression at SPS energies with the dissociation cross section σ_{co} of 0.65 mb [63, 64].

2.4.2 Cold nuclear matter effects on J/ψ Production

In this section, gluon shadowing, nuclear absorption and Cronin effect are described. They are referred as “cold nuclear matter effects (CNM)” since they contribute to J/ψ production even without the formation of the QGP.

Gluon shadowing

The quark and anti-quark distributions as a function of momentum fraction x have been probed through the deep inelastic scattering (DIS) of leptons and neutrinos from nuclei. European Muon Collaboration (EMC) experiment shows that the parton distribution in nucleus is modified compared to that in proton or deuteron (light nucleus) [65, 66]. This modification, referred as “shadowing”, depends on the parton momentum fraction x and the square of the momentum transfer Q^2 . Since the production of $c\bar{c}$ pairs and J/ψ depends on the parton distribution function, the J/ψ yield is expected to be modified in nucleus-nucleus collisions due to the shadowing effect.

Left in Fig. 2.12 shows the ratio of structure function F_2 of He, C and Ca nuclei to that of deuteron measured in $\mu+A$ scattering [66]. Right in Fig. 2.12 shows the expectation of the structure function of gluons in Au nuclei relative to that in proton, where the square of momentum transfer is taken to be $2m_c$ [67]. Solid and dashed lines are the expectation of gluon shadowing based on Eskola-Klein-Salgado (EKS) parameterization of PDF [68] and Frankfurt-Guzey-Strikman (FGS) parameterization of PDF [69]. The momentum fraction carried by partons of incident and target nucleon x_1 and x_2 is related to the rapidity y as follows:

$$x_1 = \frac{m_T}{\sqrt{s}} e^y \quad (2.20)$$

$$x_2 = \frac{m_T}{\sqrt{s}} e^{-y}, \quad (2.21)$$

where $m_T (= \sqrt{p_T^2 + m^2})$ is the transverse mass of J/ψ . Rapidity dependence of J/ψ production clarifies the shadowing effect.

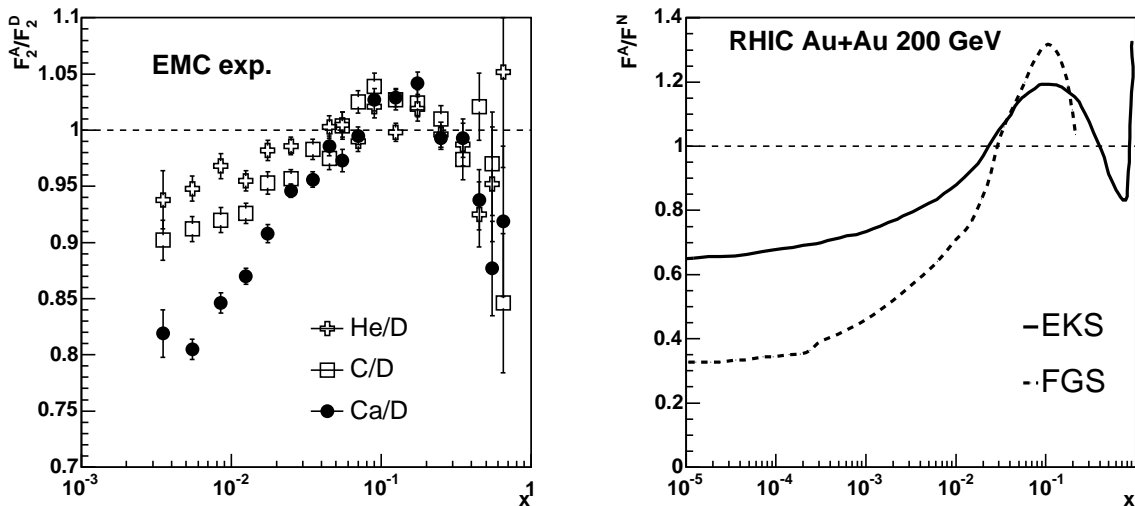


Figure 2.12: Left : Ratio of the structure function F in He, C and Ca nuclei to that in deuteron from New Muon Collaboration [66]. Right : Expected ratio of gluon distribution function in Au+Au nuclei at 200 GeV collisions with the $Q = 2m_c = 2.4$ GeV [67].

Nuclear absorption

After the creation of $c\bar{c}$ pair, pre-resonance $c\bar{c}$ state or J/ψ can interact with target/projectile nucleons and be broken up into $D\bar{D}$. If pre-resonance $c\bar{c}$ state or J/ψ interact incoherently with the nucleons along their trajectory, the survive probability of pre-resonance $c\bar{c}$ state or J/ψ (S_{AB}^{abs}) and the production cross section of J/ψ in A+B collisions ($\sigma_{J/\psi}^{AB}$) relative to that in nucleon-nucleon collisions ($\sigma_{J/\psi}^{NN}$) can be represented as follows [23, 70]:

$$S_{AB}^{abs} = \exp[-\rho_0 \sigma_{abs} L(A, B)], \quad (2.22)$$

$$\frac{\sigma_{J/\psi}^{AB}}{\sigma_{J/\psi}^{NN}} = AB \times S_{AB}^{abs}, \quad (2.23)$$

where ρ_0 is the nuclear matter density, σ_{abs} is the effective absorption cross section and $L(A, B)$ denotes effective pass length through the nuclear matter, which can be written as follows:

$$L(A, B) = L(A) + L(B), \quad (2.24)$$

$$L(A) = \frac{2\pi}{3} R_A^3 \int d\mathbf{b} (T_A(b_A))^2 \frac{A-1}{A}, \quad (2.25)$$

$$L(B) = \frac{2\pi}{3} R_B^3 \int d\mathbf{b} (T_B(b_B))^2 \frac{B-1}{B}, \quad (2.26)$$

where $R_A = r_0 A^{1/3}$ and $R_B = r_0 B^{1/3}$ are the radius of each nucleus, $T_A(b_A)$ and $T_B(b_B)$ are the thickness function defined as $T_A(b_A) = \int dz \rho(z, \mathbf{b}_A)$ and $T_B(b_B) = \int dz \rho(z, \mathbf{b}_B)$, respectively. Here ρ is the nucleon density inside the nucleus. Quantitative estimation of σ_{abs} for pre-resonance $c\bar{c}$ state and J/ψ was done by D. Kharzeev and H. Satz [23, 49] and the estimation

are as follows:

$$\sigma_{J/\psi}^{abs} = 2.5 - 3 \text{ mb}, \quad (2.27)$$

$$\sigma_{c\bar{c}g}^{abs} = 6 - 7 \text{ mb}. \quad (2.28)$$

Cronin effect

Partons suffer the multiple scattering while they traverse in the nuclei before producing J/ψ . Gluons from the projectile collides with various target nucleons exchanging transverse momentum at each collision vertex, which leads to the p_T distribution of J/ψ wider compared to that in $p + p$ collisions [71]. This is known as Cronin effect [72].

The mean squared transverse momentum $\langle p_T^2 \rangle(\mathbf{x})$ of the observed J/ψ is a function of the history of the projectile gluon and therefore depends on the point $\mathbf{x} = (\mathbf{b}, z)$ of the production point

$$\langle p_T^2 \rangle(\mathbf{b}, x) = \langle p_T^2 \rangle_{pp} + \langle p_T^2 \rangle_{gN} \sigma_{gN} \int_{-\infty}^z dz' \rho_A(\mathbf{b}, z'), \quad (2.29)$$

where $\langle p_T^2 \rangle_{pp}$ is the mean squared transverse momentum in $p + p$ collisions, σ_{gN} is gluon-nucleon cross section, $\langle p_T^2 \rangle_{gN}$ is the mean squared transverse momentum acquired in one gluon-nucleon collisions and ρ_A is the nucleon number density normalized to the total nucleon number A . Equivalently, Eq. (2.29) can be written simply in terms of the pass length L as follows:

$$\langle p_T^2 \rangle = \langle p_T^2 \rangle_{pp} + a_{gN} L, \quad (2.30)$$

where a_{gN} is composed of cross section of gluon-nucleon interaction and mean squared transverse momentum exchanged in one gluon-nucleon interaction.

2.5 J/ψ Production at SPS

The experimental study of charmonia production in relativistic light and heavy-ion collisions was carried out at the CERN SPS. NA38 experiment [73, 74, 75, 76] performed $p+A$, O+U and S+U collisions at $\sqrt{s_{NN}} = 19.4$ GeV, NA50 [77, 78, 79, 80] carried out Pb+Pb and $p+A$ ($A=\text{Be, Al, Cu, Ag, W, Pb}$) collisions at $\sqrt{s_{NN}} = 17.3$ GeV and 27.4 GeV and NA51 experiment [81] performed $p + p$ and $p + d$ collisions at $\sqrt{s_{NN}} = 27.4$ GeV.

J/ψ production was studied from the measurement of $\mu^+\mu^-$ pairs and the production cross section was extracted relative to the production cross section of Drell-Yan pairs (DY), where DY production is scaled with the number of inelastic nucleon-nucleon collisions [77]. Left in Fig. 2.13 shows the relative cross section of J/ψ and DY as a function of effective path length of J/ψ (L) in NA51 $p + p$ and $p + d$ collisions, NA38 S+U collisions and NA50 $p+A$ and Pb+Pb collisions [82]. All the data points have been re-scaled to $\sqrt{s_{NN}} = 17.3$ GeV collisions [82]. Except the central Pb+Pb collisions, results of the relative cross section can be described by the exponential function, which suggests that the nuclear absorption played an important role and modified the J/ψ yield. From this tendency, nuclear absorption cross section was extracted to be $\sigma_{abs} = 4.18 \pm 0.35$ mb. Right in Fig. 2.13 shows the relative cross section of J/ψ to the DY cross section divided by the nuclear absorption pattern, which is shown in the solid line in

left of Fig. 2.13. This gives the information on the modification of J/ψ production by the final state effects. From Fig. 2.13, “anomalous” J/ψ suppression was observed in central Pb+Pb collisions, which cannot be explained by the traditional cold nuclear matter effects.

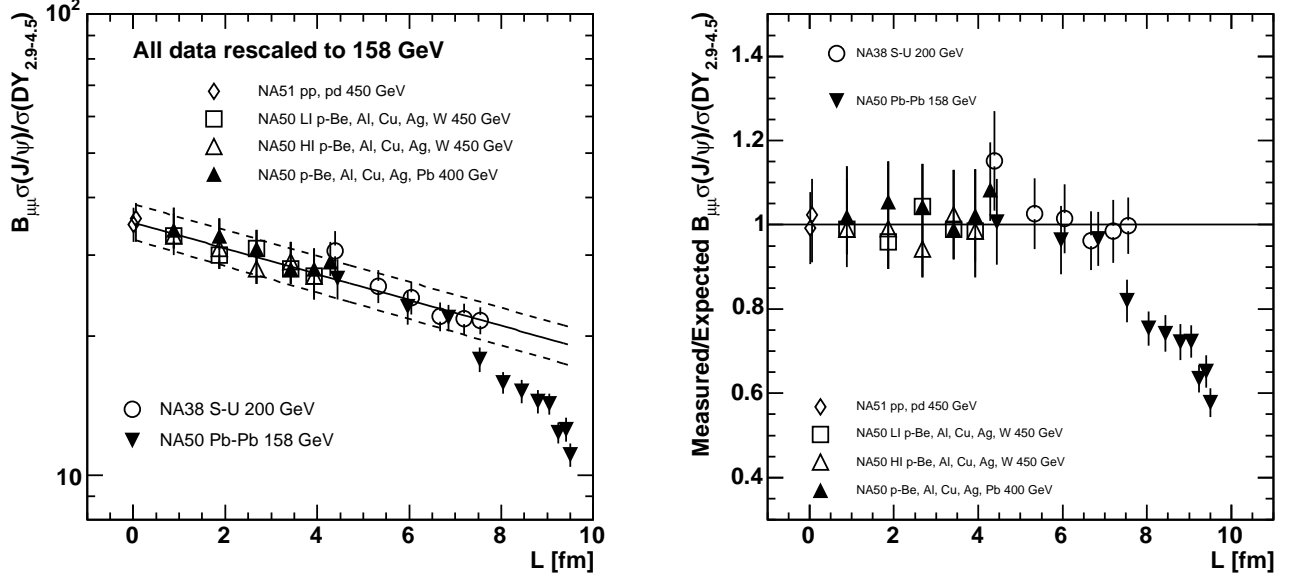


Figure 2.13: Left : Ratio of J/ψ cross section to Drell-Yan cross section as a function of path length for several collision systems. Normal nuclear absorption pattern is also shown as solid line. Right : Ratio of J/ψ cross section to Drell-Yan cross section divided by the nuclear absorption pattern as a function of path length for various collision systems. The measured data have been re-scaled to 158 GeV/nucleon.

Figure 2.14 shows $\langle p_T^2 \rangle$ as a function of path length in NA50 Pb+Pb collisions [79] and different measurements performed at 200 GeV/nucleon [84, 74, 85]. The results are fitted according to the formalism of Cronin effect as described in Eq. (2.29). The slope a_{gN} is 0.078 ± 0.006 $((\text{GeV}/c)^2 \text{fm}^{-1})$ and 0.081 ± 0.004 $((\text{GeV}/c)^2 \text{fm}^{-1})$ for 200 GeV/nucleon and 158 GeV/nucleon, respectively. This result shows that the observed $\langle p_T^2 \rangle$ is consistent with that estimated from Cronin effect.

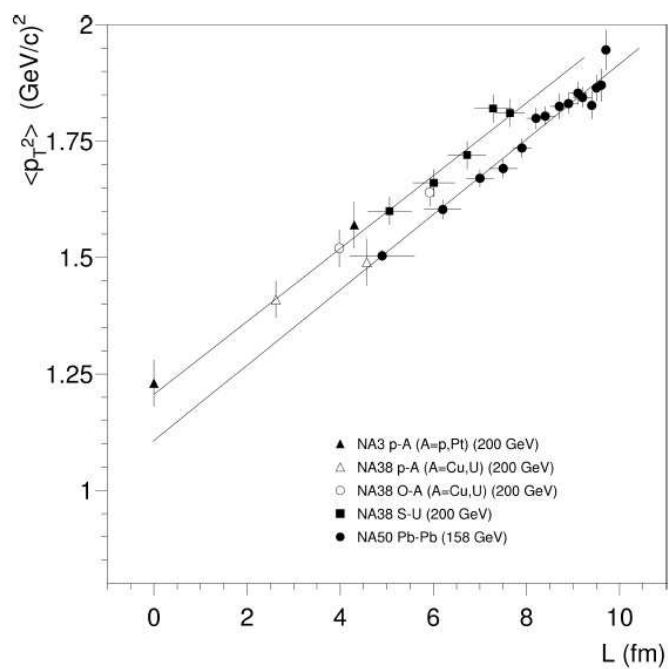


Figure 2.14: $\langle p_T^2 \rangle$ as a function of path length. The measurements performed at 200 GeV/nucleon are also included. The lines are linear fits to the data points, one for each beam energy.

Chapter 3

Experimental Setup

In this chapter, the RHIC Accelerator Complex and the PHENIX detector system are described.

3.1 RHIC Accelerator Complex

The Relativistic Heavy Ion Collider (RHIC) at Brookhaven National Laboratory has the capability to accelerate a wide variety of nuclei and ions from protons to Au ions. The top energy for heavy ion beams (e.g., for Au ions) is 100 GeV per nucleon and that for protons is 250 GeV.

Figure 3.1 shows the RHIC Accelerator Complex at Brookhaven National Laboratory [95, 96]. It consists of Tandem Van de Graaff, Booster Accelerator, Linear Accelerator Complex (Linac), Alternating Gradient Synchrotron (AGS) and the main rings of the Relativistic Heavy Ion Collider (RHIC). The collider consists of two quasi-circular concentric accelerator/storage rings on a common horizontal plane, one (“Blue Ring”) for clockwise and the other (“Yellow Ring”) for counter-clockwise beams. Rings are oriented to intersect with one another at six locations along their 3.8 km circumference.

Figure 3.2 shows the RHIC acceleration scenario for Au ions [96]. Negatively charged Au ions with the peak intensity of $\sim 100 \mu\text{A}$ and with the pulsed duration time of $\sim 700 \mu\text{s}$ from the pulsed sputter ion source at the Tandem Van de Graaff are partially stripped of their electrons with a foil at the Tandem’s high voltage terminal, and then accelerated to the energy of 1 MeV per nucleon by the second stage of the Tandem. After the further stripping at the exit of the Tandem and a charge selection by bending magnets, beams of Au ions with the charge state of +32 are delivered to the Booster Synchrotron and accelerated to 95 MeV per nucleon. Then ions are stripped again at the exit from the Booster to reach the charge state of +77, a helium-like ion, and injected to the AGS for the acceleration to RHIC injection energy of 10.8 GeV per nucleon. Au ions, injected into the AGS in 24 bunches, are de-bunched and then re-bunched to four bunches at the injection front porch prior to the acceleration. These four bunches are ejected at the top energy, one bunch as a time, and transferred to RHIC through the AGS-to-RHIC Beam Transfer Line. Au ions at the exit from the AGS are fully stripped to the charge state of +79.

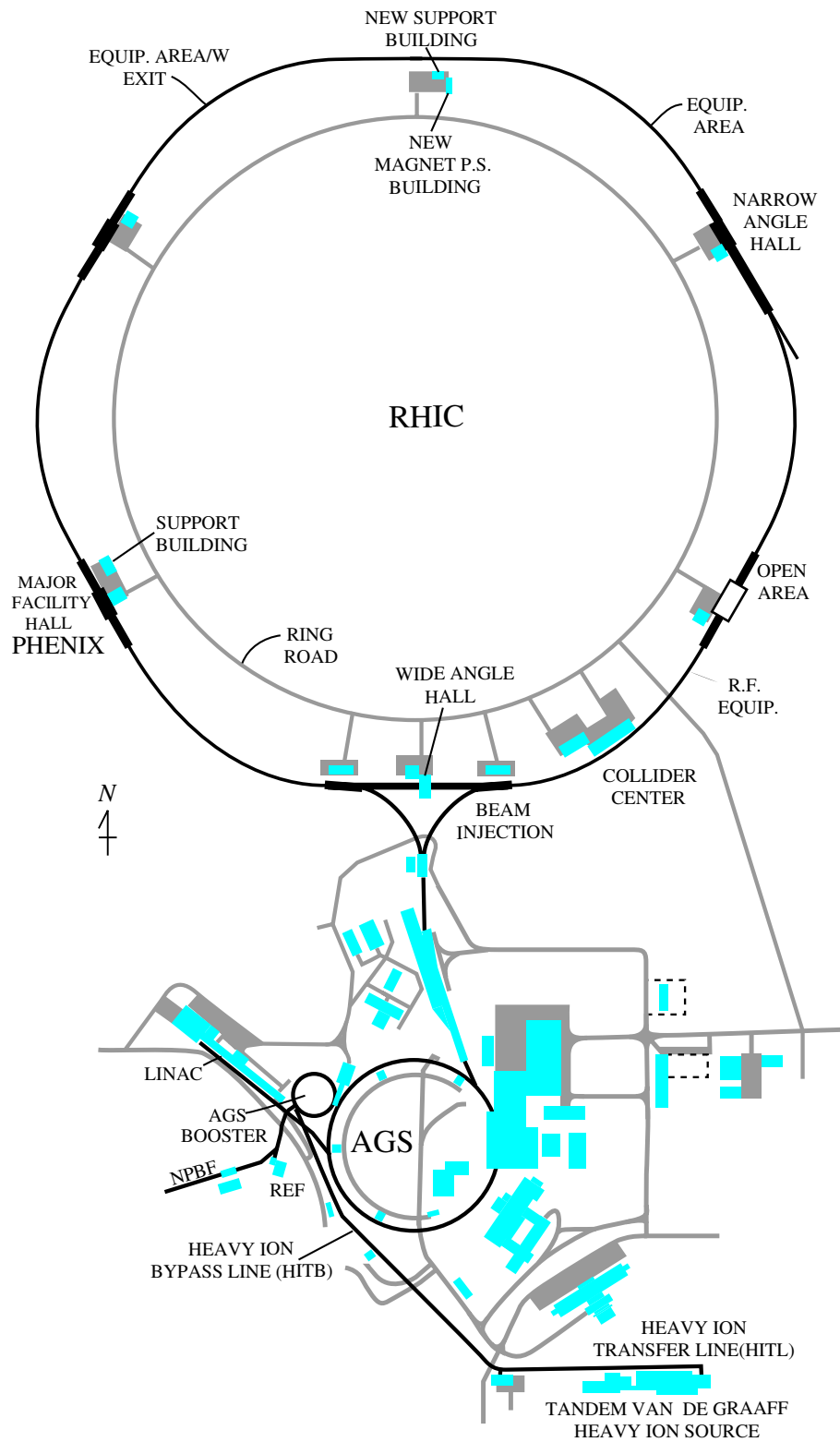


Figure 3.1: RHIC Accelerator Complex

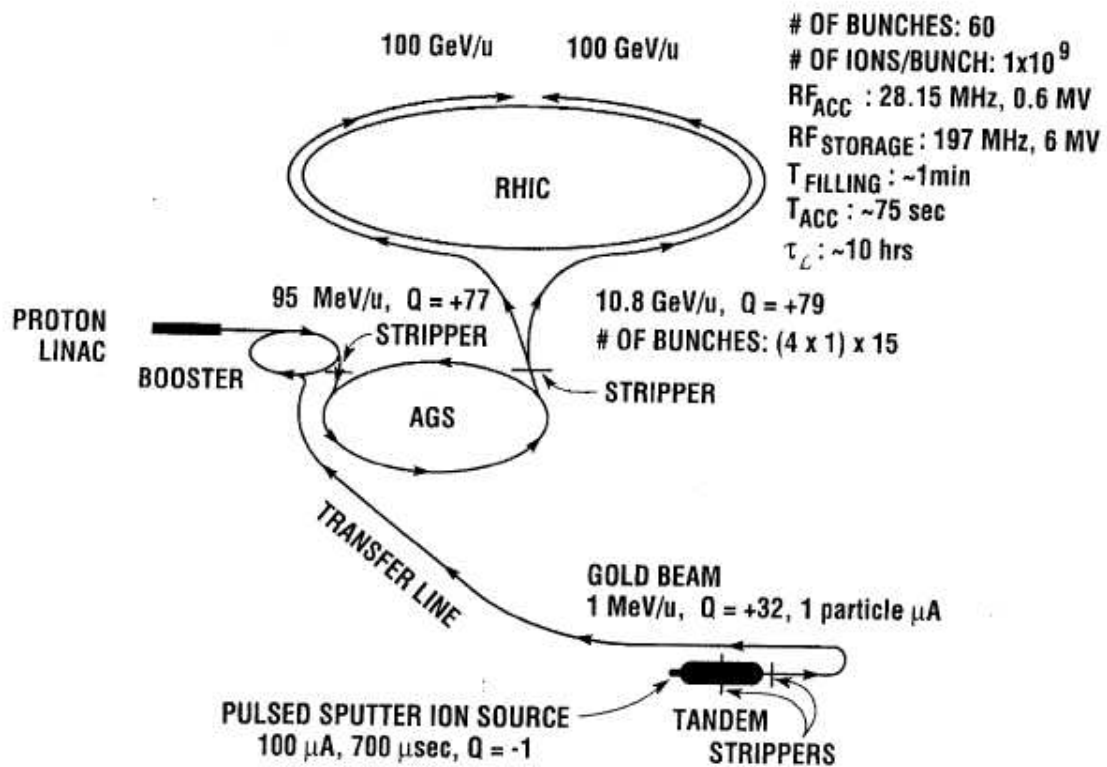


Figure 3.2: RHIC Acceleration scenario for Au beams

The beam luminosity (L) is given by,

$$L = \frac{f_{rev}}{4\pi} \frac{BN_Y N_B}{\sigma_H \sigma_V} \quad (3.1)$$

where $f_{rev} \sim 28$ MHz/360 is the revolution frequency, $B = 56$ is the number of bunches in each ring, N_Y and N_B are the number of particles (1.0×10^9 for Au or 1.0×10^{11} for p) per one bunch in yellow and blue ring, and σ_H and σ_V are the horizontal and vertical profile of the beam (~ 0.2 mm at the betatron amplitude at the interaction point (β^*) of 1 m) [96]. The design luminosity is 2×10^{26} cm⁻²sec⁻¹ for Au beams and 1.4×10^{31} cm⁻²sec⁻¹ for proton beams.

The RHIC collides two beams head-on at six interaction regions with the bunch crossing rate of 9.4 MHz. Four experiments (PHENIX, STAR, PHOBOS and BRAHMS) have being held at the four interaction regions.

Table 3.1 is the summary of the major design parameters of RHIC accelerator [19, 96].

	$p + p$	Au+Au
maximum beam energy	250 GeV	100 GeV/A
Luminosity [cm ⁻² sec ⁻¹]	1.4×10^{31}	2×10^{26}
Number of bunches	56	56
Number of particles/bunch	10^{11}	10^9
Crossing angle [μ rad]	0	0
Bunch length [cm]	40	15
Beam radius [mm]	0.2 ($\beta^*=1$)	0.2 ($\beta^*=1$)
Luminosity life time [hour]	10	3

Table 3.1: The parameters of RHIC accelerator [19, 96].

3.2 The PHENIX Experiment

The PHENIX experiment is the large experiment being held at RHIC [97]. The PHENIX experiment is designed to have the capability to measure hadrons, leptons and photons with good momentum resolution and energy resolution in $p + p$, $p+A$ and $A+A$ collisions.

3.2.1 Overview of detector complex

Figure 3.3 shows the schematic views of PHENIX detector complex. Top and bottom of Fig. 3.3 show the schematic view from beam stream and the perpendicular to beam stream, respectively. The PHENIX complex is categorized into the global detectors, two central spectrometer arms and two muon arms.

The global detectors consist of Beam-Beam-Counters (BBC), and Zero-Degree-Calorimeters (ZDC). They provide the trigger for the data acquisition, vertex position, start timing for Time-Of-Flight measurement and collision geometry which corresponds to the impact parameter of two

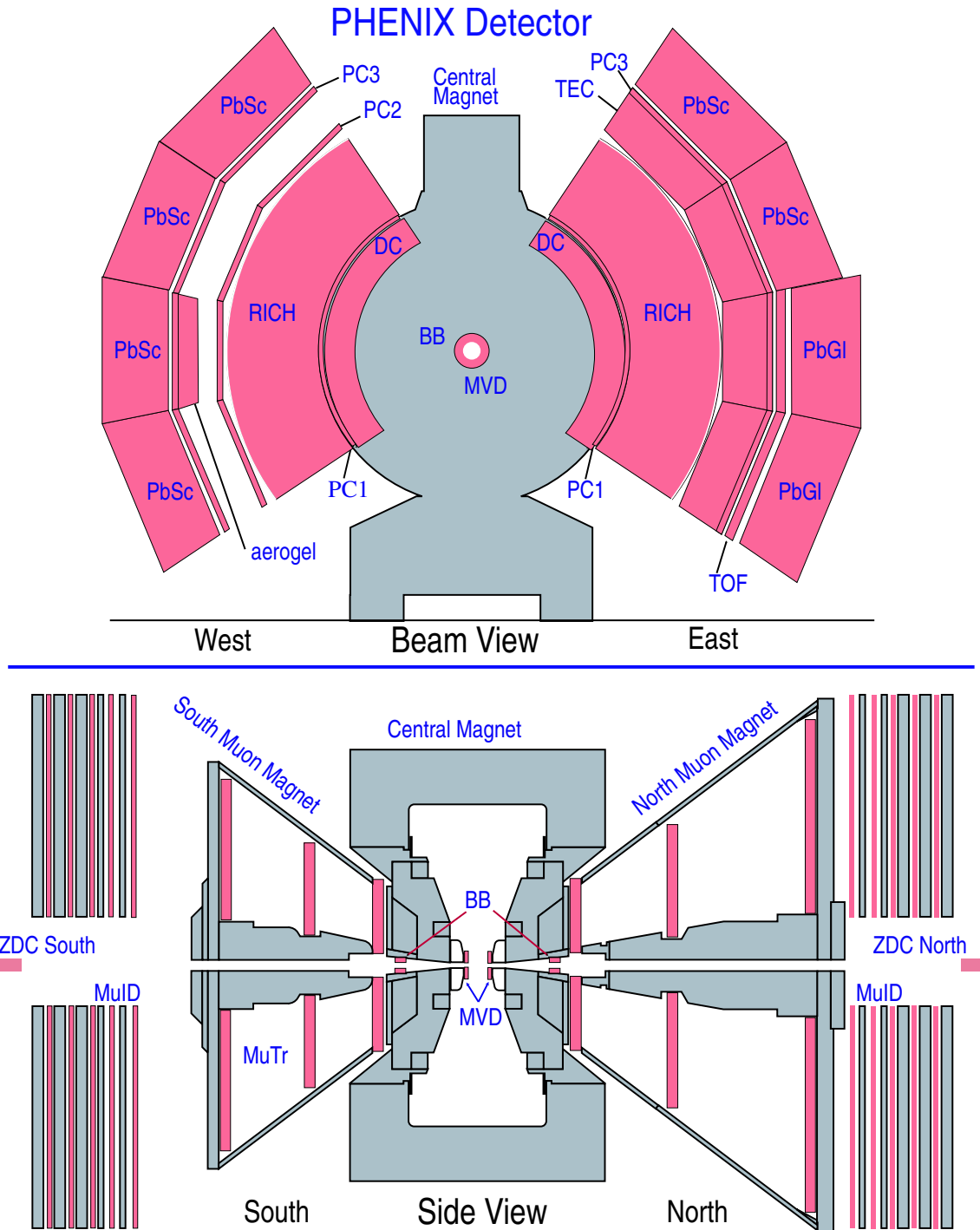


Figure 3.3: PHENIX Detector Complex. Upper is from beam stream and bottom is from the perpendicular to the beam stream.

colliding beams [98]. As seen in bottom of Fig. 3.3, they are installed in both north and south side of the PHENIX.

Central spectrometer arms [99] cover mid rapidity $|\eta| \leq 0.35$ and have the capability to measure the hadrons, electrons and photons. As seen in upper of Fig. 3.3, they consist of West and East arms, each of which has the coverage of $\pi/2$ in azimuthal angle. The configuration of detector subsystems is different between west and east. The east arm has a Drift Chamber (DC), two layers of Pad Chambers (PC1 and PC3), Ring Imaging Cherenkov counters (RICH), Time Expansion Chamber (TEC), Time of Flight detector (TOF) and Electromagnetic Calorimeter (EMCal), while the west arm has DC, three layers of Pad Chambers (PC1, PC2 and PC3), RICH, Aerogel Cherenkov Counters (ACC) and EMCal.

Muon arms [100] covers the forward rapidity region ($1.2 \leq |\eta| \leq 2.4$) and measure the muons. They consist of North and South muon arms, each of which has full azimuthal coverage.

The geometrical coverage and function of each subsystem detector are summarized in Table. 3.2.

Subsystem	Coverage in η	Coverage in ϕ	Functions
BBC	$\pm 3.1-3.9$	2π	trigger, start timing, vertex measurement collision geometry determination
ZDC	± 2 mrad	2π	trigger, start timing, vertex measurement collision geometry determination
DC	± 0.35	$\pi / 2 \times 2$	Particle tracking Momentum determination
PC	± 0.35	$\pi / 2 \times 2$	Particle tracking
RICH	± 0.35	$\pi / 2 \times 2$	Electron identification
TEC	± 0.35	$\pi / 2$	dE/dx measurement
Aerogel	± 0.35	$\pi / 8$	High momentum $p/K/\pi$ identification
TOF	± 0.35	$\pi / 4$	Hadron identification
EMCal	± 0.35	$\pi / 2 \times 2$	energy measurement photon and electron identification
Muon ID	$\pm 1.15 - 2.44$	2π	muon/hadron separation
Muon Tracker	$\pm 1.15 - 2.44$	2π	tracking for muons

Table 3.2: Summary of the PHENIX subsystem detectors.

3.2.2 Global coordinate

The global coordinate system of the PHENIX which is commonly used in this thesis is described. Figure 3.4 shows the PHENIX coordinate system.

The PHENIX coordinates are defined as follows. The origin is defined to be the middle of two Beam-Beam-Counters. In Cartesian coordinate, z axis is defined to be along the beam

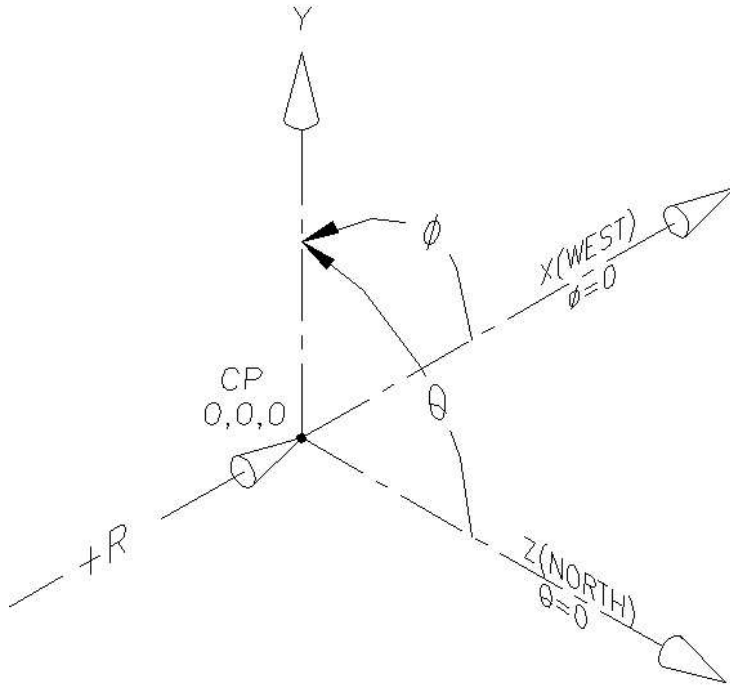


Figure 3.4: PHENIX Global coordinate

direction pointing to the “north” muon arm or “north” ZDC. The x axis is pointing to the west arm (see. upper of Fig. 3.3). The y axis is pointing to upwards.

3.3 PHENIX Global Detectors

The PHENIX global detectors consist of BBC and ZDC, which give the global trigger, start timing, vertex position and collision geometry of two colliding beams. Details on the BBC and the ZDC are described.

3.3.1 Beam-Beam-Counters

The BBC consists of two identical sets of detectors and they are installed on both north (BBCN) and south side (BBCS) of the PHENIX along the beam axis [98]. BBCN and BBCS, which surround He beam pipe, are located at 144 cm away from the interaction point, and covers the pseudo-rapidity ($|\eta|$) from 3.0 to 3.9 and full azimuthal angle.

Each counter is composed of 64 1-inch diameter mesh-dynode photomultiplier tubes (Hamamatsu R6178) equipped with 3-cm thick quartz on the head of the PMT as a Cherenkov radiator. Figure 3.5 (a) and (b) shows one BBC element and the BBC array mounted on the mechanical frame, respectively. The inner diameter is 10 cm and the outer diameter is 30 cm.

The start timing T_0 and the vertex position along the beam axis z_{vtx} are calculated as

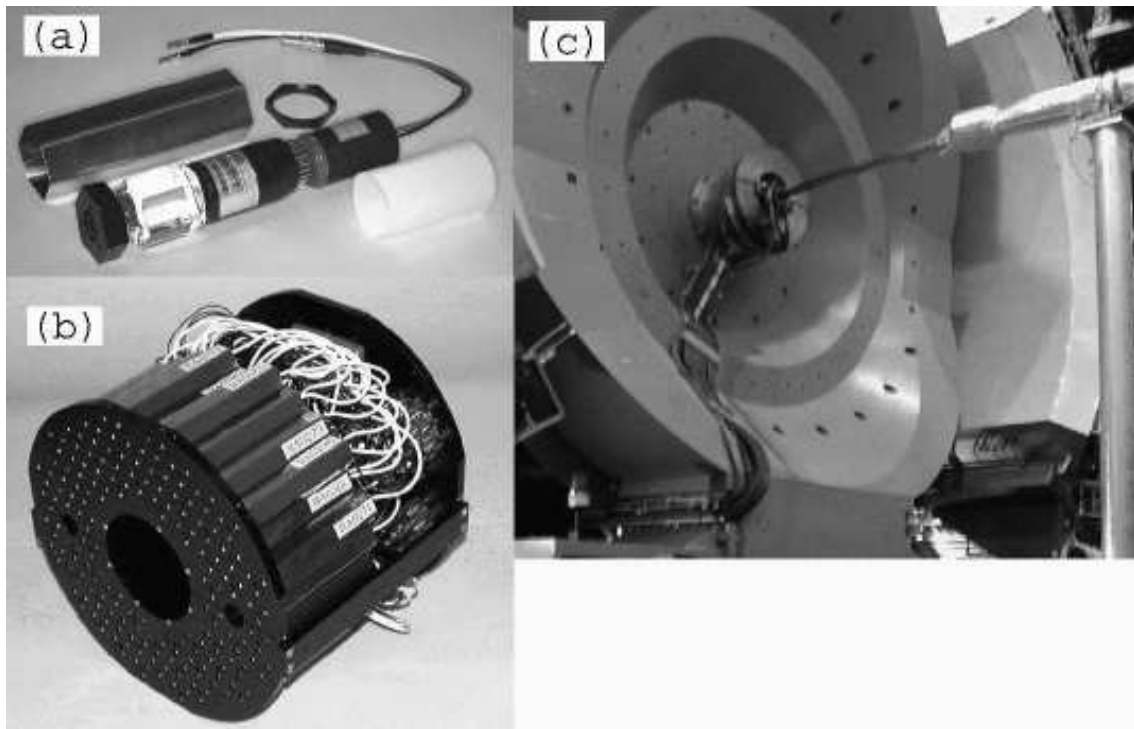


Figure 3.5: (a)One BBC element consisting of 1-inch mesh-dynode photomultiplier tube with 3 cm quartz radiator. (b) BBC array consisting of 64 identical elements. (c)The BBC is mounted in the PHENIX [98].

follows.

$$T_0 = (T_1 + T_2)/2 - z_{bbc}/c, \quad (3.2)$$

$$z_{vtx} = (T_1 - T_2)/2 \times c, \quad (3.3)$$

where T_1 and T_2 are the average measured time for the particles arriving at BBCN and BBCS, respectively.

Figure 3.6 (a) shows a distribution of timing deviations for a certain BBC element from the average time. Figure 3.6 (b) shows the distribution of timing resolution for all BBC elements. The timing resolution of a single BBC element is 52 ± 4 ps (rms) under the real experimental conditions [98].

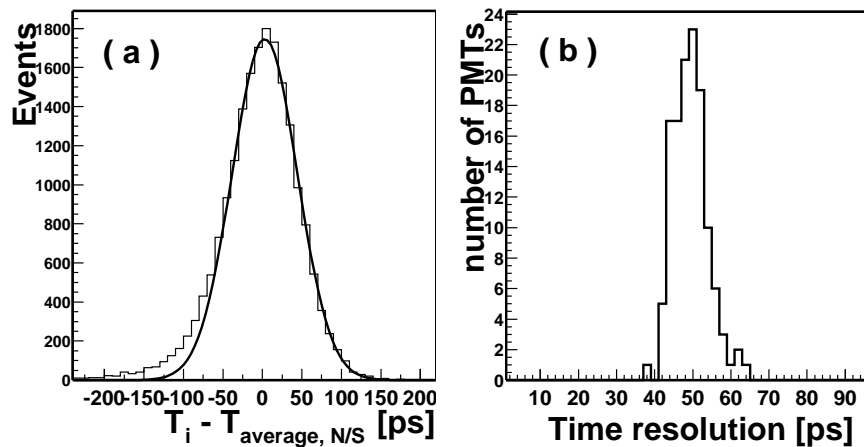


Figure 3.6: (a) Distribution of timing deviation for a certain BBC element from the average time. (b) Distribution of timing resolution over all BBC elements [98].

3.3.2 Zero-Degree-Calorimeters

The main purposes of zero-degree calorimeters (ZDC) are to provide the event characterization such as collision geometry and monitor the beam luminosity [98]. The ZDC measures the total energy of the forward neutron unbound by coulomb excitation or evaporated from an unstable spectator produced after the hadronic interaction between two colliding nuclei [101, 102, 103].

The PHENIX as well as the other three experiments use a pair of commonly designed ZDCs. They are sampling type hadron calorimeters which are located at 18 m from the interaction point and just behind the DX dipole magnet as shown in Fig. 3.7. The DX dipole magnets serve to bend the incoming beams to the interaction region and to bend the outgoing beams to the collider beam line. Due to the DX dipole magnets, only the neutrons can reach to the ZDC.

Each ZDC consists of three modules. Figure 3.8 shows the cross section of one ZDC module. Each ZDC module consists of 27 layers of Tungsten alloy plates, optical fibers and a

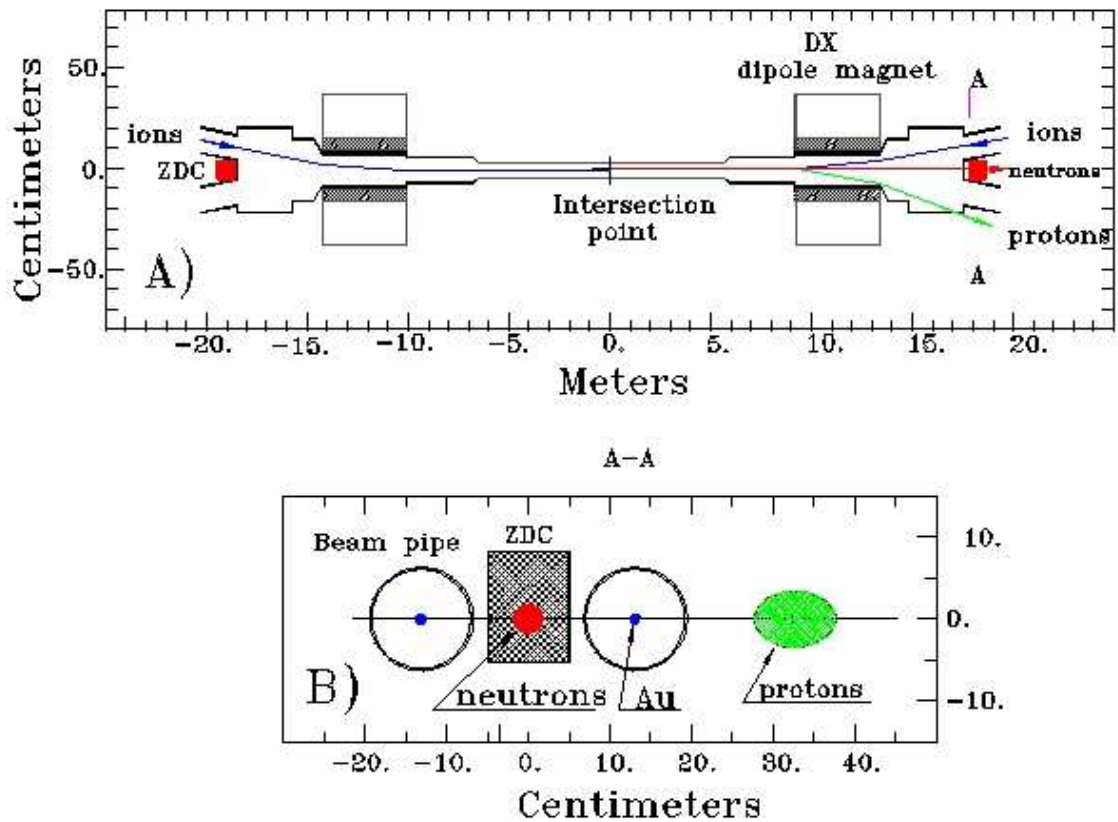


Figure 3.7: Schematic View around the interaction region and the location of ZDC. A) Top view B) from Beam view (cross section). Outgoing beams are bent by DX dipole magnet and only neutrons can reach to ZDC.

photo-multiplier tube (PMT: Hamamatsu R329-2). The thickness corresponds to 2 hadronic interaction length. Each ZDC covers 2 mrad of forward angular cone which corresponds to the pseudo-rapidity region $|\eta| \geq 6$. The energy resolution of ZDC was obtained to be $\delta E/E \simeq 218/\sqrt{E(\text{GeV})}\%$ from beam test experiment [101].

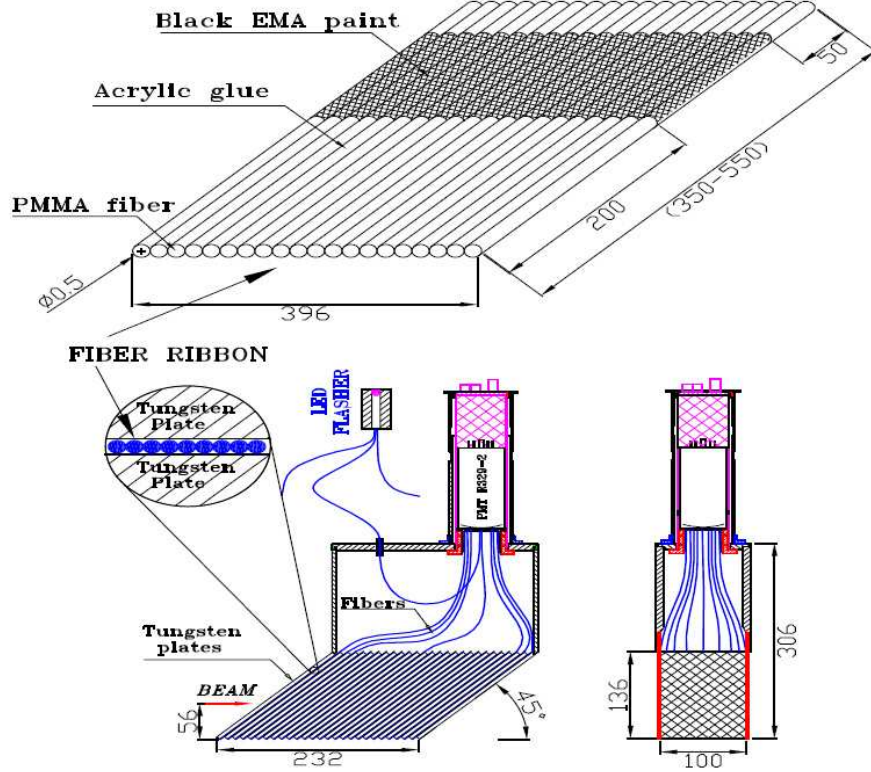


Figure 3.8: Cross section of the ZDC module [101]. Neutron passes through 27 Tungsten absorbers and fibers collect lights.

3.4 PHENIX Central Arms

The PHENIX Central arm detectors consist of tracking system for charged particles (DC and PC), particle identification detectors (RICH and TOF) and EMCAL. The DC and the PC provide the charged particle trajectory and determine the momentum. The RICH and the TOF serve to provide the particle identification of electrons and identified charged hadrons (pions, kaons and protons), respectively. The EMCAL provides the energy measurements for both photons and electrons. The following sections describe the parts of the detectors (DC, PC, RICH and EMCAL) that are used in this analysis.

3.4.1 Drift Chamber

The function of the DC is as follows [99]:

- Measurement of charged particle trajectories in $r - \phi$ plane and determine the transverse momentum (p_T) of charged particles, where r and ϕ defined as $r = \sqrt{x^2 + y^2}$ and $\phi = \arctan(y, x)$ in PHENIX coordinate system, respectively.
- Together with the hits measured by the first layer of the PC (PC1) and collision z -vertex measured by the BBC, determine the track polar angle and determine the total momentum p .
- Extrapolation of the charged particle trajectories to outer detectors and link together tracks and hits in outer detectors.

The requirements for the DC are [99]:

- single wire resolution better than $150 \mu\text{m}$ in $r - \phi$
- single wire two track separation better than 1.5 mm
- single wire efficiency better than 96% and tracking efficiency better than 99%
- spatial resolution in the z direction better than 2 mm

The DC system consists of two independent gas volumes located in the west and east arms, respectively. They are located between 2.02 and 2.46 m in the radial distance from the interaction region. They occupy the 180 cm in z direction and 90 degree per arm in azimuthal angle. The DC is operated with the gas mixture of Argon (50%) and Ethane (50%) and the drift velocity in the nominal working condition is $\sim 4.8 \text{ cm}/\mu\text{s}$ [104].

Each DC volume is defined by a cylindrical titanium frame as shown in Fig. 3.9 Each frame is filled with drift chamber modules and is divided in 20 identical drift chamber sectors covering the 4.5 degrees in ϕ . This is shown in left of Fig. 3.10. As shown in left of Fig. 3.10, there are 6 types of wire modules stacked radially in each sector: X1, U1, V1, X2, U2, and V2. The X1 and X2 wires run in parallel to the beam axis to measure the particle trajectory in $r - \phi$ precisely. These wires are followed by two sets of stereo wires (U and V wires). U1, V1, U2 and V2 wires have the stereo angle of 6 degrees relative to the X wires as shown in the right of Fig. 3.10. These stereo wires start in a sector on one side and end in a neighboring sector on the other side of DC. U and V wires give the measurement of particle trajectory in z direction.

The wire configuration of the DC is shown in Fig. 3.11 and the drift lines for six wires in X1 net is shown in Fig. 3.12. The drift cell in the DC is approximately 4 cm wide in azimuthal direction and 6 mm high in radial direction. The sense (anode) wires are separated by potential wires and surrounded by gate wires and back wires. Potential wires forms a strong electric field and separate sensitive region of individual sense wires. Gate wires limit track sample length to roughly 3 mm and minimize the time spread of drifting electrons from a single track. Back wires has a lower potential than gate wires and terminates most of drift lines from cathode wire at one side of the drift cell. This reduces the left-right ambiguity in the hit reconstruction. The operation voltage for each wires is summarized in Table 3.3.

Based on the analysis for Year2 (2002) Au+Au collisions, single wire resolution of $150 \mu\text{m}$ was achieved for both East and West DCs, single wire efficiency was better than 90% and tracking efficiency of better than 99% was achieved [104]. These results are described in Appendix B.

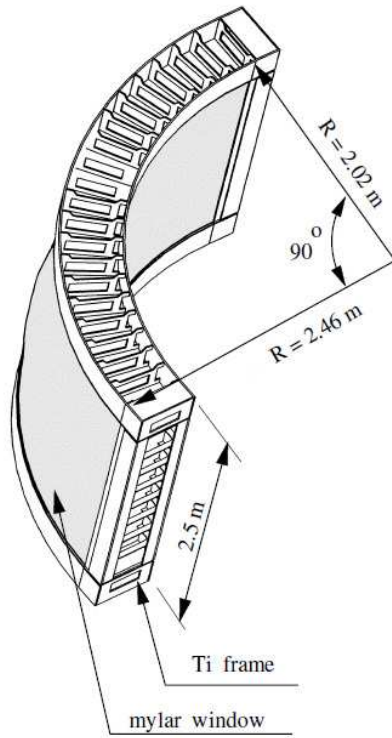


Figure 3.9: Construction of DC frame [99]

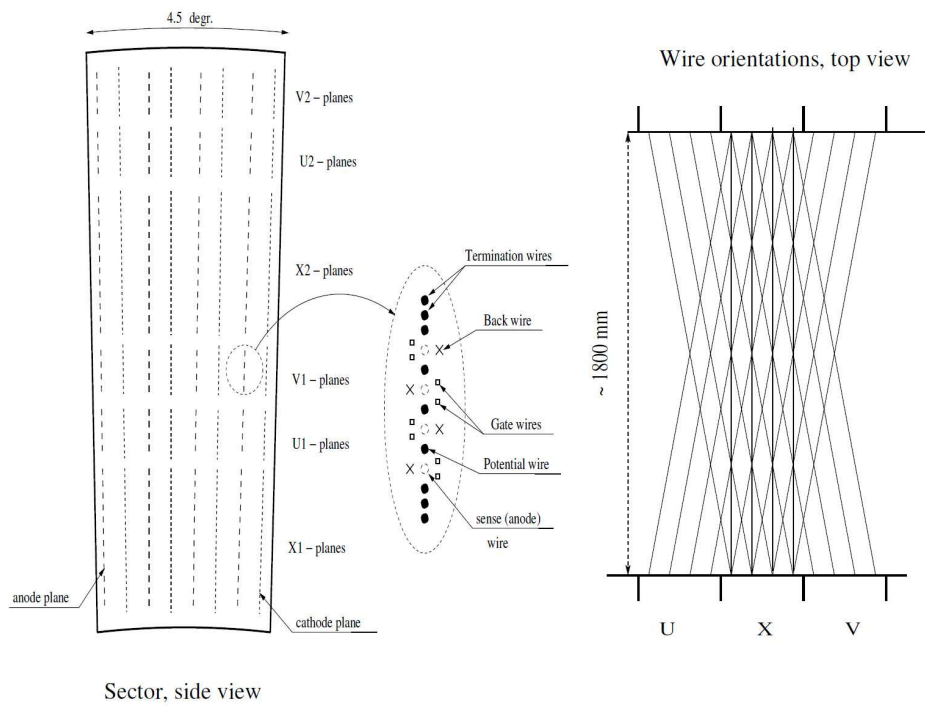


Figure 3.10: Left : The layout of wire position in one sector from the beam view [99]. Right : The schematic diagram of the stereo wire orientation [99].

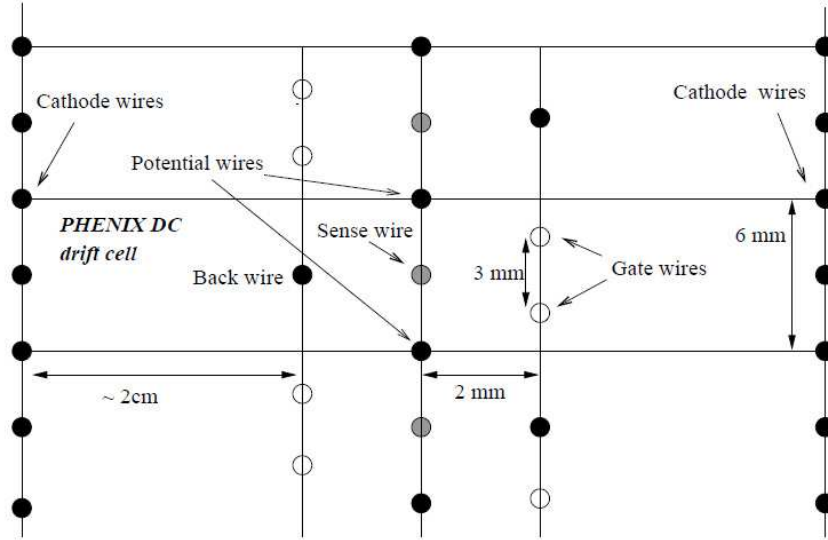


Figure 3.11: Wire configurations in the DC [104].

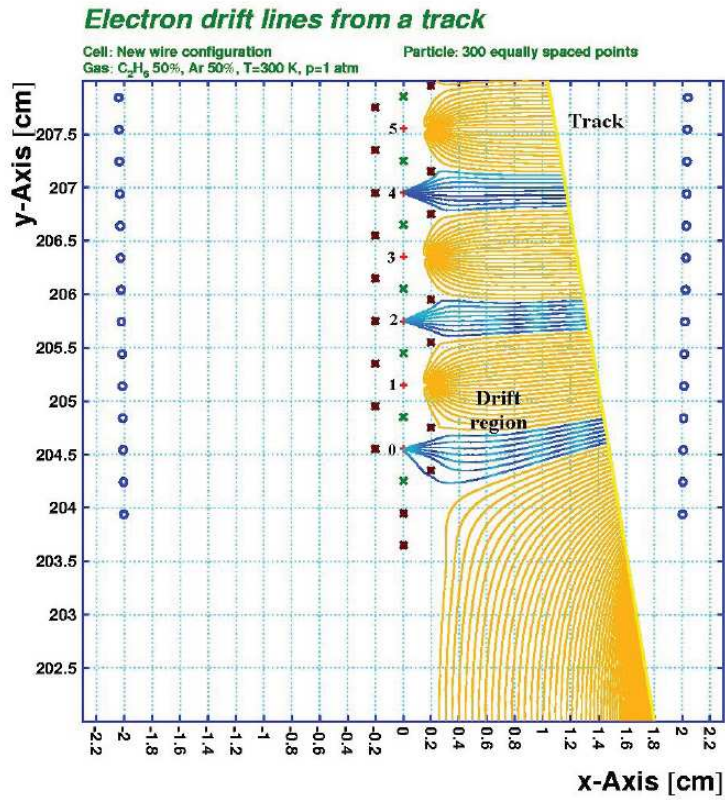


Figure 3.12: The drift lines for six sense wires ion X1 net. Different types of wires are marked by arrows [104].

wire type	sense	cathode	gate	potential	back
voltage(kV)	0	-4 to -4.7	-1.5 to -1.6	-2.3 to -2.65	-0.8 to -0.9

Table 3.3: Potential for different types of wires used in the DC [104]

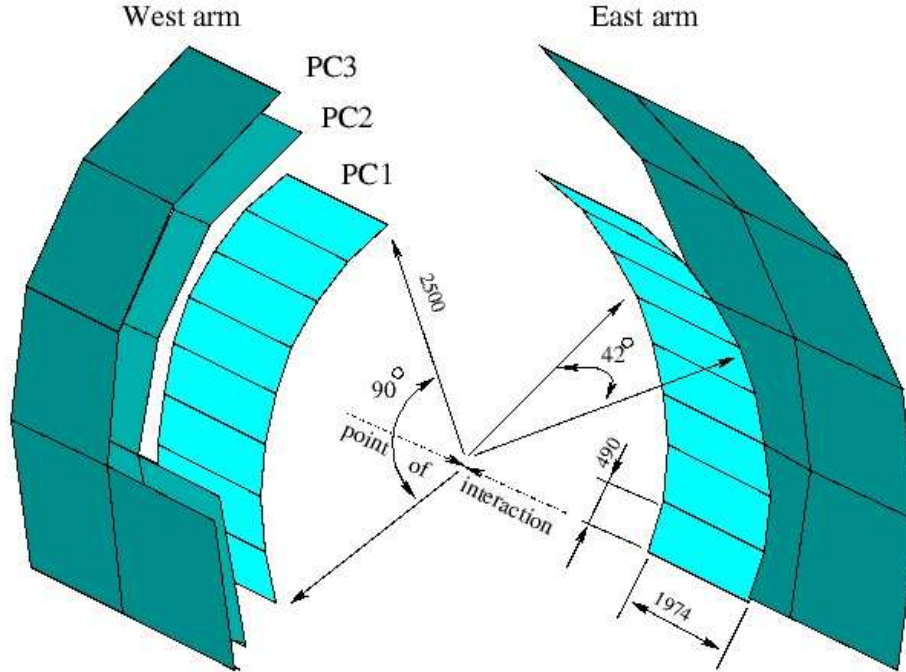


Figure 3.13: The Pad Chamber layers of the PHENIX central tracking system. Several sectors of PC3 and PC3 in west are removed in this Figure [105].

3.4.2 Pad Chamber

The primary functions of the PC are as follows [99]:

- Measurement of three dimensional spatial points, which are used for momentum determination in z direction (p_z)
- Measurement of the accurate pointing of charged tracks to the RICH and EMCal

The PC is a multi-wire proportional chamber with signal read out from cathode planes that form three separate layers of the PHENIX central tracking system (PC1, PC2 and PC3) [99]. The 3D view of the PC is shown in Fig. 3.13. The PC1 layer is the innermost chamber of the three layers, which is located at the 2.47 m to 2.52 m in radial distance from the interaction region and is located between DC and RICH on both East and West arms. The PC2 layer is placed behind the RICH and is present only in the West arm. The radial distance between PC2 and interaction region is 4.15 m to 4.21 m. The PC3 layer is mounted just in front of the EMCal and is present on both West and East arms.

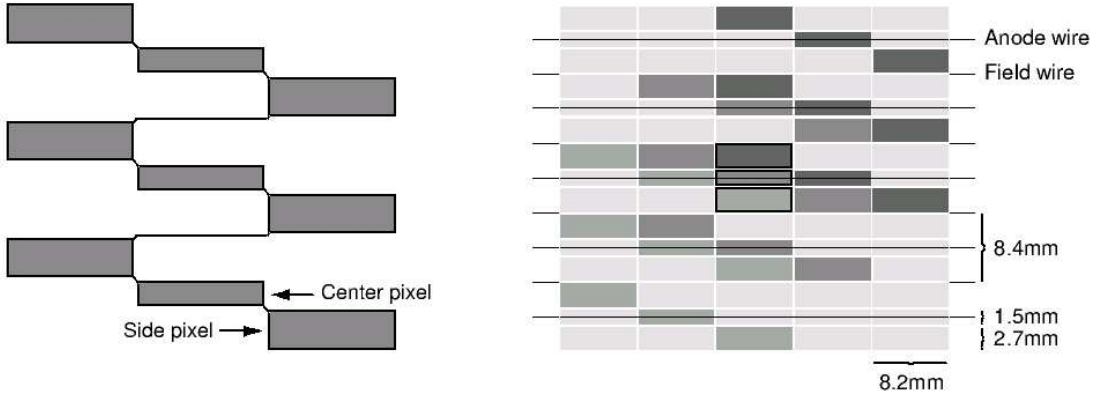


Figure 3.14: The pad and pixel geometry (left). A cell defined by three pixels is at the center of the right picture [99].

The PC1 is essential for determination of the three-dimensional momentum vector by providing the z coordinate at the exit of the DC. The PC information is also essential for electron identification by the RICH. The DC and PC1 information gives the direction vectors through the RICH, while PC2 and PC3 are needed to resolve the ambiguities of the tracks in the outer detectors.

Each detector consists of a cathode panel and a signal plane of anode and field wires. One cathode is finely segmented into an array of pixels as shown in Figs. 3.14. The gas was chosen to be the mixture of 50% Argon and 50% of Ethan at atmospheric pressure. The specifications of PCs achieved in Year2 (2002) Au+Au collisions and cosmic ray tests are listed in Table 3.4 [105].

Parameters	PC1	PC2	PC3
Pad size($r - \phi \times z$)	0.84×0.84	1.36×1.43	1.6×1.67
single hit resolution in z [mm]	1.7	3.1	3.6
efficiency	$\geq 99\%$	$\geq 99\%$	$\geq 99\%$

Table 3.4: Performance of Pad Chambers in Year-2 and cosmic ray test [105]

3.4.3 Ring Imaging Cherenkov Counter

The Ring Imaging Cherenkov counter (RICH) is the primary device for electron identification in the PHENIX [106].

The RICH detector has been constructed and developed by the RICH collaboration group, which consists of Center for Nuclear Study (CNS), University of Tokyo, Waseda University, Nagasaki Institute of Applied Science (NIAS), Institute of Nuclear Studies High Energy Accelerator Research Organization (KEK), State University of New York at Stony Brook (SUNY)

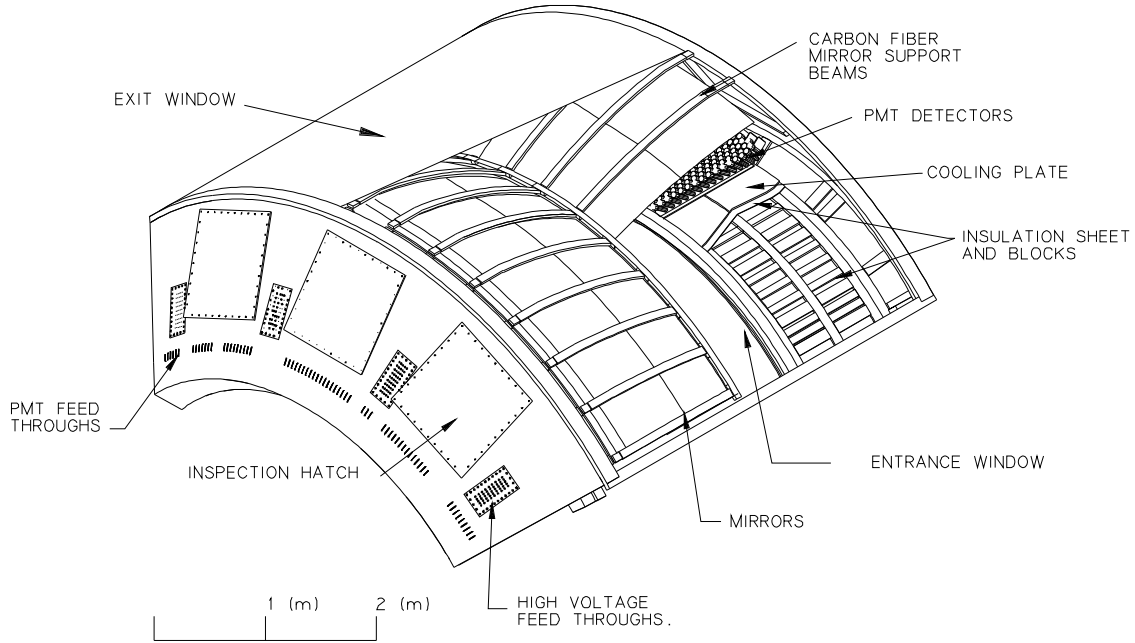


Figure 3.15: The cut-away view of RICH detector [106]

and Florida State University (FSU).

Figure 3.15 and 3.16 show a cutaway view of the RICH detector and cut view along with the beam axis, respectively. The RICH detector is mounted in both West and East arms behind the innermost Pad Chambers (PC1) and located in the radial position between 2.5 m and 4.1 m from the interaction region. The RICH detector covers from 70 to 110 degree in polar angle and 90 degree per arm in azimuthal angle. The RICH detector has a gas volume of 40 m³ per arm. The entrance windows and exit windows are made of aluminized Kapton with 125 μm thickness and have 8.9 m² and 21.6 m² area, respectively.

The RICH detector in PHENIX is a threshold type gas Cherenkov detector, where CO₂ gas is used as a radiator and operated in atmospheric pressure, and gives the e/π separation up to 4.84 GeV/ c .

The RICH in each arm contains 48 composite mirror panels, which is composed of two arrays of 24 aluminum-evaporated spherical mirrors and forms two intersecting spherical surfaces, where the sphere radius is 4.0 m and the center of the sphere is located at $|z| = 2$. The reflectivity was measured and found 83% at 200 nm and 90% at 250 nm [106]. The total reflecting area is 20 m². The spherical mirrors focus Cherenkov light onto two arrays of 1280 Hamamatsu H3171S UV photomultiplier tubes [107]. These tubes are located on either side of the RICH entrance window to avoid the direct hit of the particles on them as shown in Fig. 3.16. The PMT has a bi-alkaline photocathode and a linear-focused 10 stage of dynodes. The quantum efficiency is about 20% (5%) at the wavelength of 300 nm (200 nm). The typical operation voltage of PMT is ~ 1.5 kV and the typical gain is $\sim 10^7$. The PMT is equipped with 2 inch ϕ Winston cones and magnetic shields that allow the operation under the magnetic field of 100 G. In total, RICH detector has 5120 PMTs (2(arm) \times 2(side) \times 16(θ) \times 80 (ϕ)).

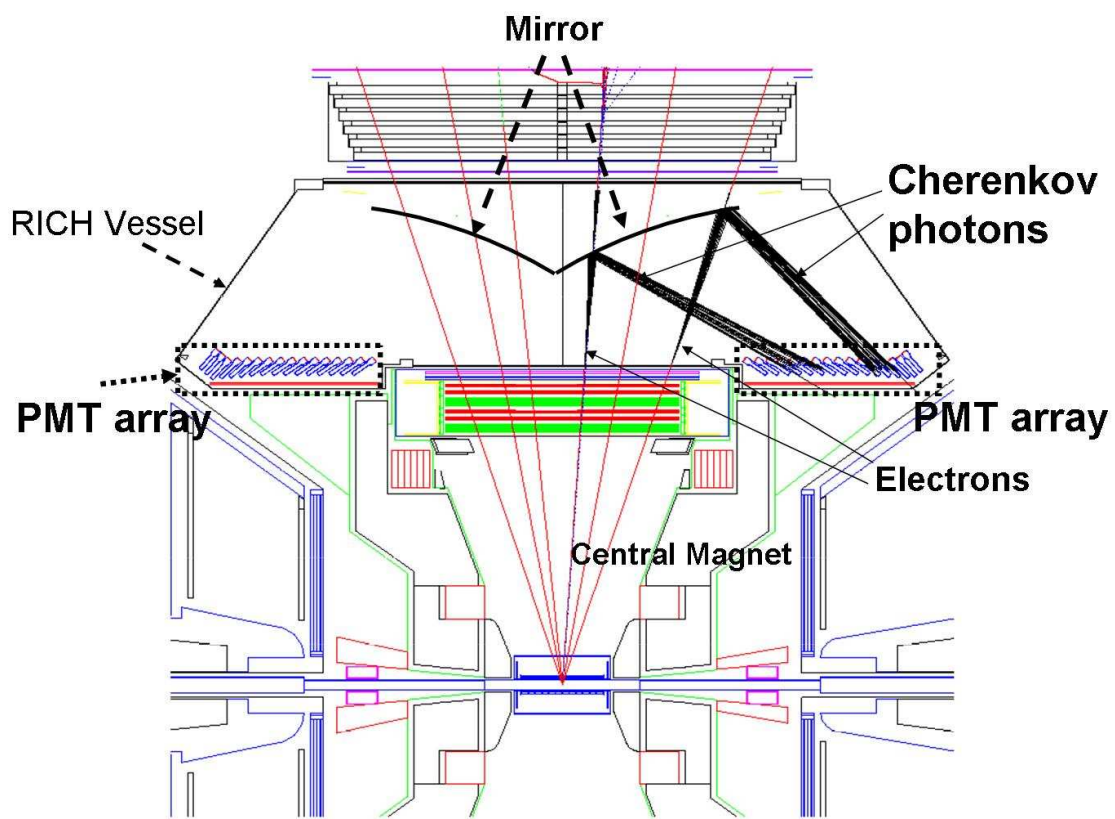


Figure 3.16: Schematic view of RICH along with the beam axis [106]

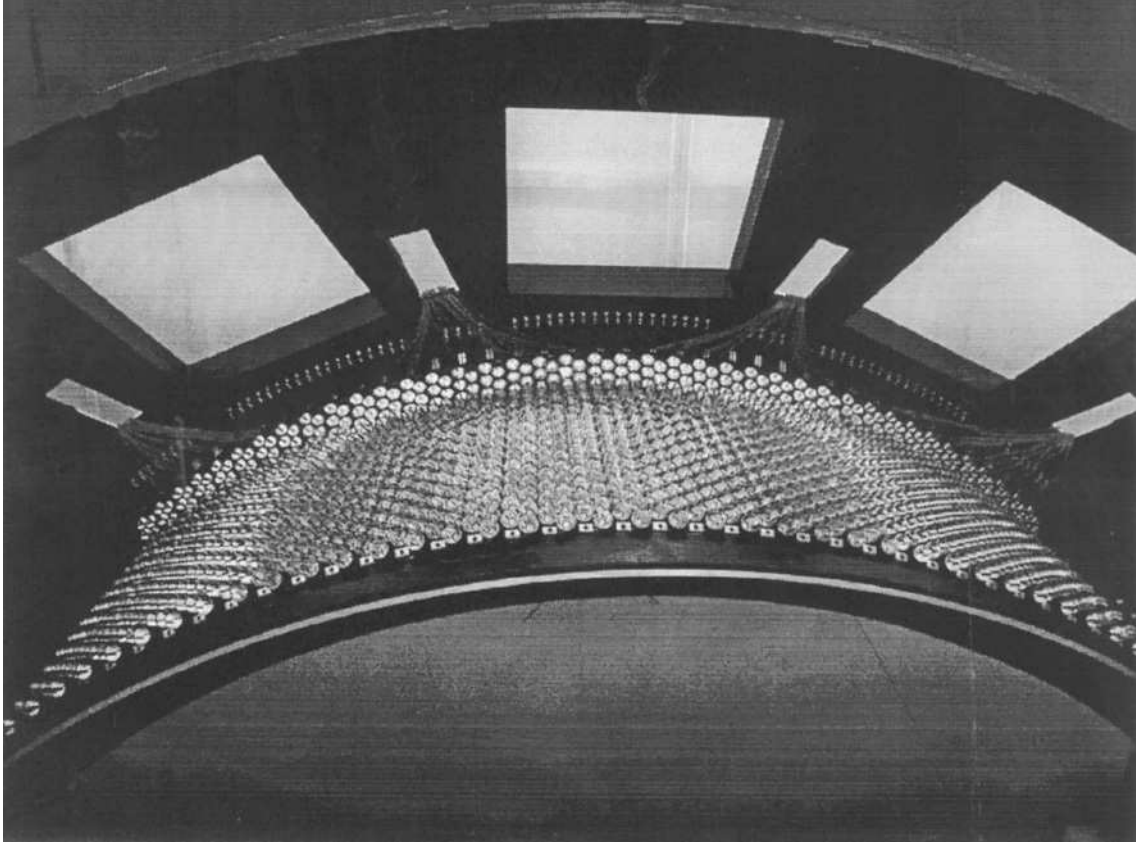


Figure 3.17: One of the RICH PMT arrays in the PHENIX [106]

The angular segmentation is approximately $1^\circ \times 1^\circ$ in θ and ϕ . One of the RICH PMT arrays is shown in Fig. 3.17. Table 3.5 is the summary of the specifications of the RICH detectors [106].

Charge calibration and Mirror alignment calibration

Acquired data contains the PMT ID, the charge information (ADC) and the timing information (TDC) of the RICH hit. Charge calibration was performed for each PMT by searching for the pedestal peak and single photo-electron peak in the ADC spectrum. ADC values for pedestal peak and single photo-electron peak were used to convert ADC value to the charge information.

RICH mirror alignment was performed by associating the hit PMTs with the reconstructed charged tracks. Adjustment of the mirror position was done so that ring centers calculated from the positions of hit PMTs match to the projected points of charged tracks on the PMT planes. Both charge calibration and mirror alignment calibration are described in Section 5.1.4.

3.4.4 Electromagnetic Calorimeter

The primary role of the Electromagnetic Calorimeter (EMCal) in the PHENIX is to measure the energy and spatial positions of photons and electrons [108].

RICH	Radial position	2.5 m to 4.1 m
	Gas volume	40 m ³
	Gas	CO ₂
	$\beta\gamma_{th}$	~ 35
	e/π separation	0.02 to 4.9 GeV/c
	Pion rejection factor	10 ⁴ for single tracks
	Radiation length	2.14%
PMT	Number of PMTs	5120
	Type	Hamamatsu H3171S UV photomultiplier tubes
	Tube diameter	29 mm
	Gain	10 ⁷
	quantum efficiency	20% (300 nm) 5% (200 nm)
Mirror	Number of mirrors	96
	type	Al-evaporated spherical mirrors
	focus point	$ z = 2$
	reflectivity	83% (200 nm) 90% (250 nm)

Table 3.5: Specifications of RICH [106]

The EMCal system consists of Pb-Scintillator calorimeter (PbSc) and Pb-Glass calorimeter (PbGl). Each arm covering 90 degrees in azimuth is divided into four sectors in azimuth. The two PbGl sectors occupy the lower two sectors of East arm and PbSc sectors occupy the other six sectors. The EMCal surface is 510 cm for PbSc and 550 cm for PbGl in radial distance from the interaction region.

Figure 3.18 shows a PbSc calorimeter module which is assembled from four towers. The PbSc is a sampling calorimeter made of alternating tiles of lead and scintillator. It consists of 15552 individual towers (5.2 cm \times 5.2 cm \times 37.5 cm). Total radiation length of PbSc is 18.2 X_0 and Moliere radius is ~ 6 cm. Each tower contains 66 sampling cells: 1.5 mm of lead and 4 mm of injection molded scintillator, ganged together by penetrating optical fibers doped with wave length shifter for light collection. Lights are read out by 30 mm ϕ PMT's (FEU115, MELS, Russia) which are implemented at the back of the towers.

Figure 3.19 shows a PbGl super-module which consists of 24 lead-glass towers in an array of 6 (wide) by 4 (high). The PbGl is a Cherenkov calorimeter with 1.648 of index of refraction. It consists of 9216 individual towers (4 cm \times 4 cm \times 40 cm), which were previously used in WA98 experiment at CERN. Total radiation length of PbGl is 14.4 X_0 and Moliere radius is ~ 4 cm. Each PbGl sector comprises 192 super-modules (SM) in an array of 16 (wide) by 12 (high). At the back of the towers, PMT's (FEU84) are implemented for readout.

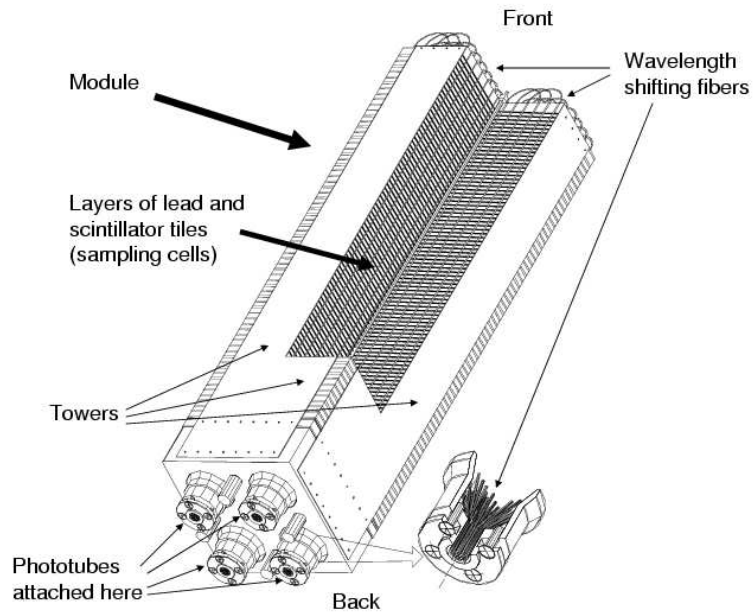


Figure 3.18: Cut-away view of a PbSc module showing a stack of scintillator and lead plates, wavelength shifting fiber.

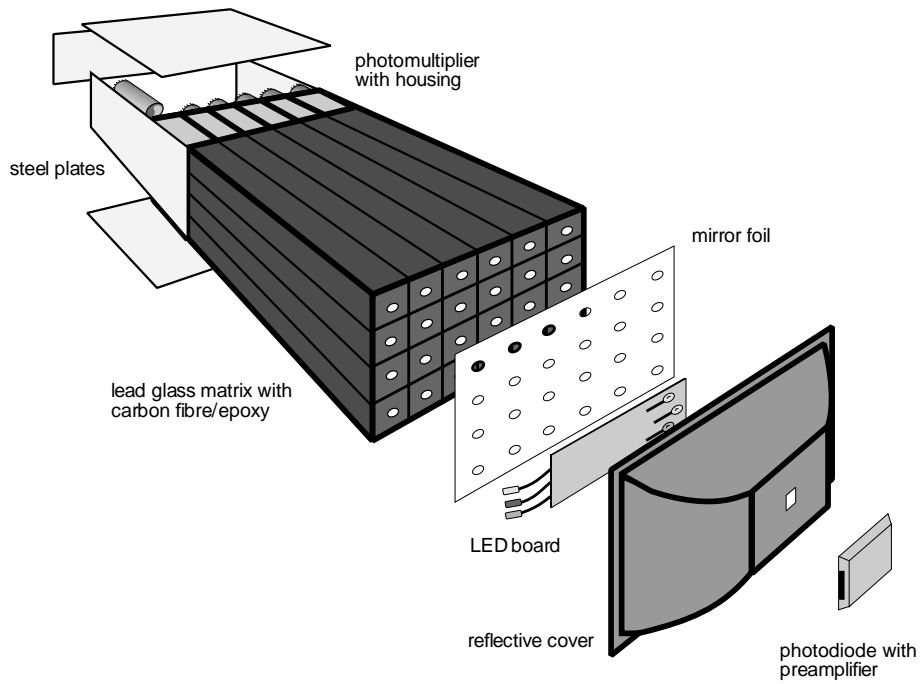


Figure 3.19: A PbG1 super-module

Energy calibration

During the experimental run period, the energy calibration is done mainly by [109, 110]:

- The measurements of the Minimum Ionization Peak (MIP)
- Reconstructing invariant mass of 2γ and adjust the position of π^0 mass peak

Both methods give the cross check of the energy calibration of EMCal [109] and detail iteration procedure can be found in Ref. [110]. Top of Fig. 3.20 shows the 2γ invariant mass spectra in Au+Au collisions after the energy calibration, where black is invariant mass of 2γ in real event and blue is the background invariant mass distribution obtained by event mixing method. Middle of Fig. 3.20 shows the subtracted invariant mass spectrum. Bottom of Fig. 3.20 shows the fitting results of π^0 peak. Figure 3.21 shows the π^0 peak obtained from real data (black)

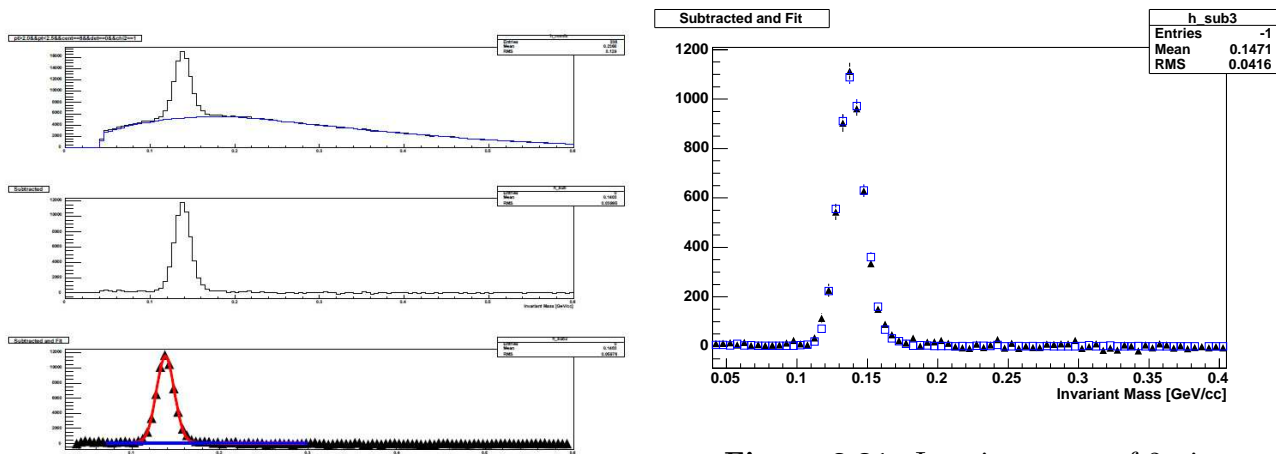


Figure 3.20: Invariant mass of 2γ and π^0 peak [109].

Figure 3.21: Invariant mass of 2γ in real data (black) and in Monte Carlo simulation (blue), where the background is subtracted in real data [109].

and from Monte Carlo simulation (blue). π^0 peak after energy calibration matches to the π^0 peak from Monte Carlo simulation.

Energy resolution of EMCal was evaluated using electrons and that is discussed in Sec. 5.1.3.

3.5 PHENIX Central Magnet System

The PHENIX magnet system is composed of three magnets with warm iron yokes and water-cooled copper coils as shown in Fig. 3.22 [111].

The Central Magnet (CM) is energized by two pairs of concentric coils and provides a field around the interaction vertex that is parallel to the beam. Charged particles bend in a plane perpendicular to the beam axis. This allows momentum measurement of charged particles in the pseudo-rapidity range of $-0.35 \leq \eta \leq 0.35$. The north and south Muon Magnets (MMN and MMS) use solenoid coils and produce the radial magnetic field for muon measurement. T

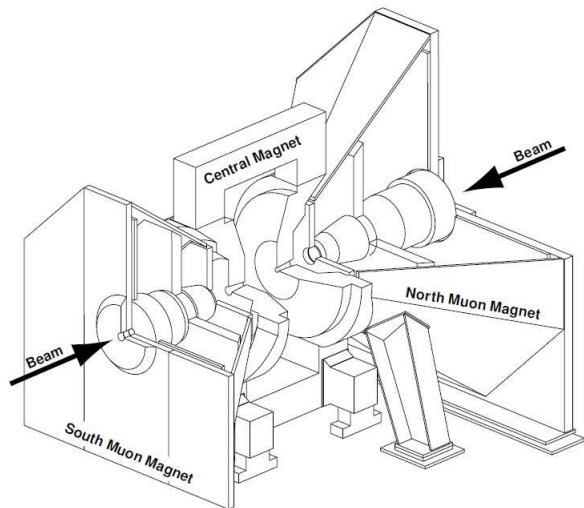


Figure 3.22: Line drawings of the PHENIX magnets, shown in perspective and cut away to show the interior structure [111].

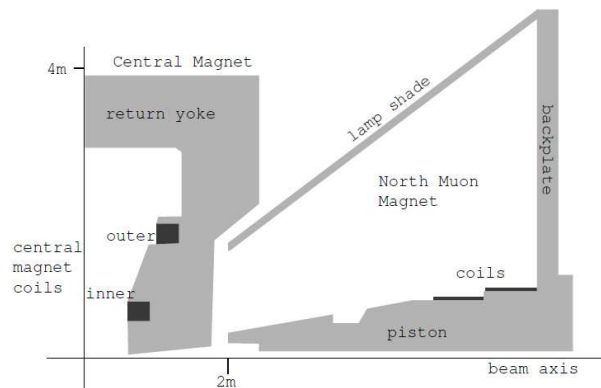


Figure 3.23: Vertical cutaway drawing of the central and north muon magnets showing the coil positions for both magnets [111].

The Central Magnet was designed to have two sets of circular coils as shown in Fig. 3.23. These “inner” and “outer” coils can be run with the fields adding (the “++” configuration) or bucking (“+-” configuration). Until 2002, only the outer coils were in place (“+” configuration) and since 2003, both inner and outer coils have been used.

Upper of Fig. 3.24 shows the cutaway view of the PHENIX magnets showing CM and MN field lines. The magnet field for the central arm spectrometer is axially symmetric with respect to the beam axis. At the center close to the beam axis, the field line uniformly points along the beam direction. However, the residual field at the DC distance (~ 2 m) is highly non-uniform and has a significant r component at large z . The z dependence of the field is shown in lower of Fig. 3.24, where the z component of the magnetic field (B_z) as a function of the radial distance from beam line is shown for various z location. The field is almost uniform for different z at $R < 2$ m. However, in the DC region, the residual field strength strongly varies with z .

Figure 3.25 shows the total field strength of the CM as a function of R at the $z = 0$ for “++”, “+” and “+-” field configurations. The field integral at $z \sim 0$ is 1.04, 0.78 and 0.43 [Tm] in “++”, “+” and “+-” configurations, respectively.

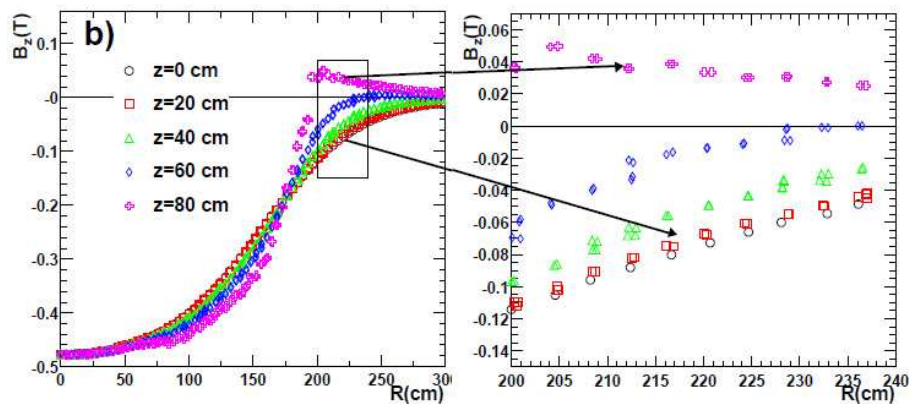
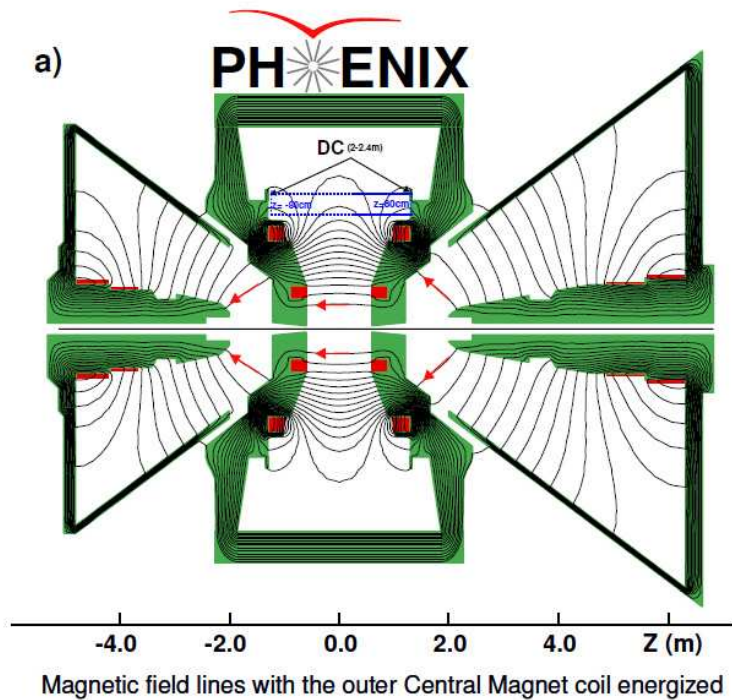


Figure 3.24: Upper a) CM and MM field lines shown on a cutaway drawing of the PHENIX magnets. The beams travel along the $R = 0$ -axis in this figure and collide at $R = z = 0$. Arrows indicate the field direction [111]. Lower b) z component of the magnetic field, B_z as a function of the radial distance from beam line for various z locations [104].

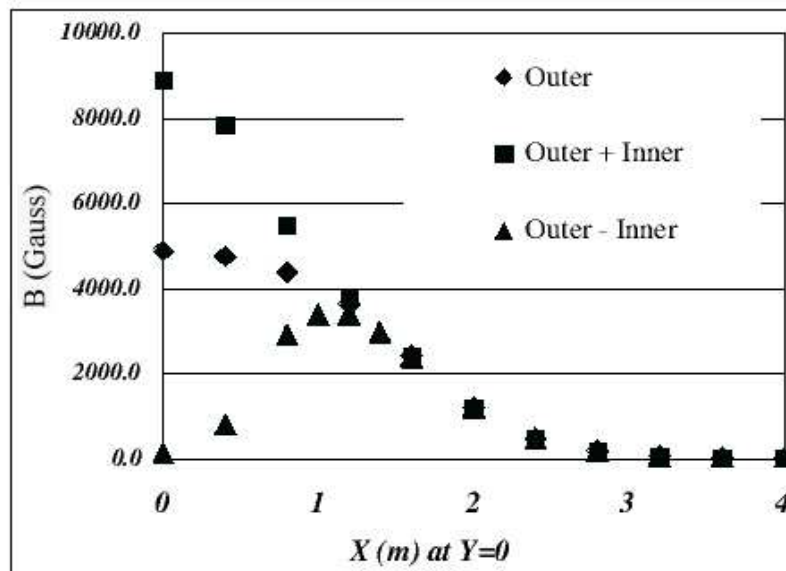


Figure 3.25: The total strength $B(R)$ as a function of R for + (Outer), ++ (Outer + Inner), and +- (Outer-Inner) field configurations. [111].

3.6 Data Acquisition System in PHENIX

The PHENIX data acquisition system processes the signals from each detector, produces the trigger decision, and stores the triggered data. The typical data logging rate of PHENIX was ~ 800 Hz for Au+Au collisions and ~ 5 kHz for p+p collisions. Average live rate for data acquisition was 80% for Au+Au collisions. The zero-suppressed event sizes are 160 kbytes for Au+Au and 60 kbytes for p+p, respectively. The block diagram of the data acquisition flow is shown in Fig. 3.26.

The data acquisition system employs the concept of granule and partition. A granule is the smallest unit, which consists of individual timing control and data collection for each detector. The partition is the combination of granules, that share busy signals and accept signals. This configuration makes it possible to run the data acquisition in desired combination of detectors.

Overall control of the data acquisition is provided by the Master Timing Module (MTM), the Granule Timing Module (GTM), and the Global Level-1 Trigger System (GL1). The MTM receives 9.4 MHz RHIC clock and deliver it to GTM and GL1. The MTM also receives LVL1 accept signal. The GTM deliver the clock, the control commands (Mode Bits), event accept signal to each detector's FEM. The GTM is capable of a fine delay tuning of the clock in ~ 50 ps step, in order to compensate the timing difference among FEM's. The GL1 produces the first Level-1 (LVL1) trigger decision, combining LVL1 signal from detector components.

The FEM of each detector is designed to convert the analog response of the detectors into the digitized signal. The LVL1 trigger signals are simultaneously generated. The generation of global decision, whether event should be taken or not, takes ~ 30 B.C. While the GL1 system is making decision, the event data is stored in AMU. After receiving the accept signal, each

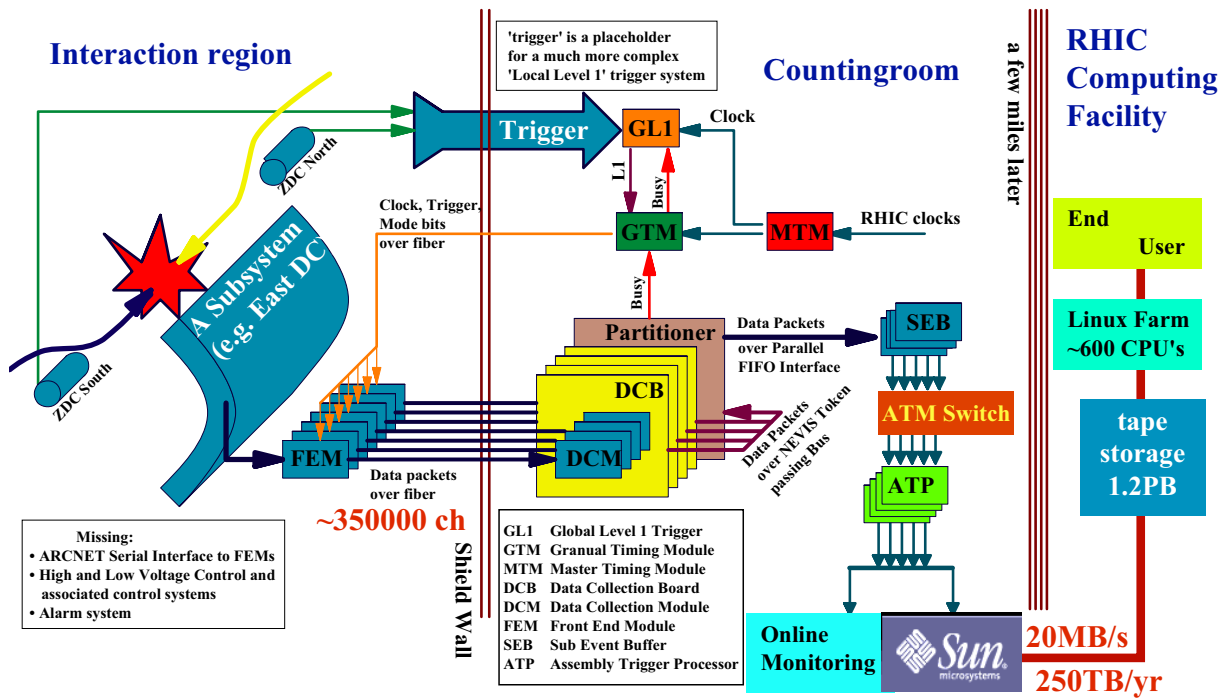


Figure 3.26: Schematic diagram of the data acquisition flow.

FEM starts to digitize the data.

The data collection from each FEM is performed by Data Collection Modules (DCM) via G-LINK. The DCM's have the capability to receive 100 Gbytes of uncompressed event data per second at the highest trigger rate. The DCM's provide data buffering, zero suppression, error checking, and data formatting. The DCM send the compressed data to PHENIX Event Builder (EvB).

The EvB is the system which consists of 32 Sub Event Buffers (SEB), Asynchronous Transfer Mode (ATM) switch, and 28 Assembly Trigger Processors (ATP). The SEB's are the front end of EvB and communicate with each granule. The SEB's transfer the data from granules to ATP via ATM, where event assemble is performed. The combined data is once stored to the disk and used for online monitoring and for generation of trigger decision by the second level (LVL2) software trigger.

The data storage is finally provided by HPSS-based tape storage robot system with maximum transfer rate of 20 Mbytes/s. Combining the buffering to local disk, the maximum data logging rate become ~ 60 Mbytes/s.

Chapter 4

Run Condition of 2004 Au+Au Collisions

Collection of data for Au+Au collisions at the center of mass energy per nucleon ($\sqrt{s_{NN}}$) of 200 GeV, which is the focus on this thesis, was done during the first three months in 2004 (“Year-4” run). The run conditions such as beam conditions, luminosity conditions and trigger conditions are described in this chapter.

4.1 Beam Conditions

The beam conditions in RHIC Year-4 Au+Au collisions are summarized in Table. 4.1. RHIC delivered the integrated luminosity of $1370 \mu\text{b}^{-1}$ to the PHENIX during the run period with the center of mass energy per nucleon ($\sqrt{s_{NN}}$) of 200 GeV. Figure 4.1 shows the delivered luminosity of Au+Au by RHIC as a function of weeks into the run. During the Au+Au run period, PHENIX recorded integrated luminosity of $\sim 240 \mu\text{b}^{-1}$.

Beam	Au+Au
$\sqrt{s_{NN}}$	200
bunch intensities	10^9 Au
number of bunches	56, 45
Initial luminosity [$\text{cm}^{-2}\text{s}^{-1}$]	10^{26}
Delivered luminosity [μb^{-1}]	1370

Table 4.1: Summary of beam conditions in RHIC Year-4 Au+Au collisions

Delivered luminosity to PHENIX is monitored using both south and north ZDCs. The integrated number of events counted by the coincidence between both south and north ZDCs are corrected according to the inelastic cross section of Au+Au collisions of 6.85 ± 0.54 b [116], which gives the integrated luminosity delivered to PHENIX.

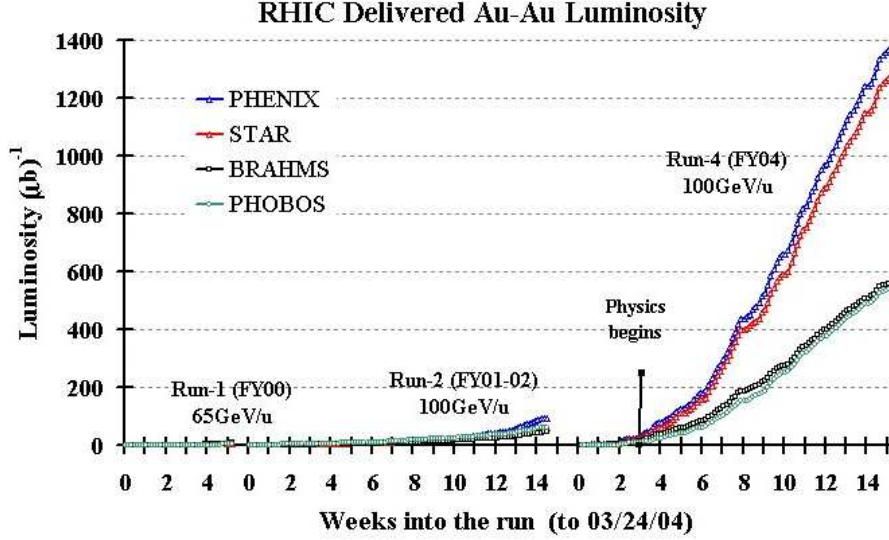


Figure 4.1: History of delivered luminosity in Au+Au collisions

The recorded luminosity by the PHENIX was calculated by dividing the total number of recorded events in Year4 Au+Au collisions by the inelastic cross section of Au+Au collisions (6.85 b) multiplied by the minimum bias trigger efficiency. The minimum bias trigger and its efficiency are described later.

4.1.1 z_{vtx} distribution

Left of Fig. 4.2 shows the z vertex distribution reconstructed with BBCs based on Eq. (3.3) accumulated for whole Year-4 Au+Au collisions. Right of Fig. 4.2 shows mean of z vertex as a function of the run numbers taken in Year-4 Au+Au collisions. The run dependence of the z vertex is 0.5 cm as *RMS* and stable in Year-4 Au+Au collisions.

4.1.2 Beam position motion

There is no guarantee that the collisions always take place at the origin. Beam position in the transverse plane can be monitored using measured charge with the BBCs. Beam position (x_0 , y_0) was evaluated as follows:

$$x_0 = \frac{\sum_{ipmt} Q_{ipmt} X_{ipmt}}{\sum_{ipmt} Q_{ipmt}} \quad (4.1)$$

$$y_0 = \frac{\sum_{ipmt} Q_{ipmt} Y_{ipmt}}{\sum_{ipmt} Q_{ipmt}}, \quad (4.2)$$

where Q_{ipmt} , X_{ipmt} and Y_{ipmt} are the measured charge with BBC element $ipmt$, position of BBC element $ipmt$ in x and y , respectively. Figure 4.3 shows the beam position in x and y as a function of the run numbers.

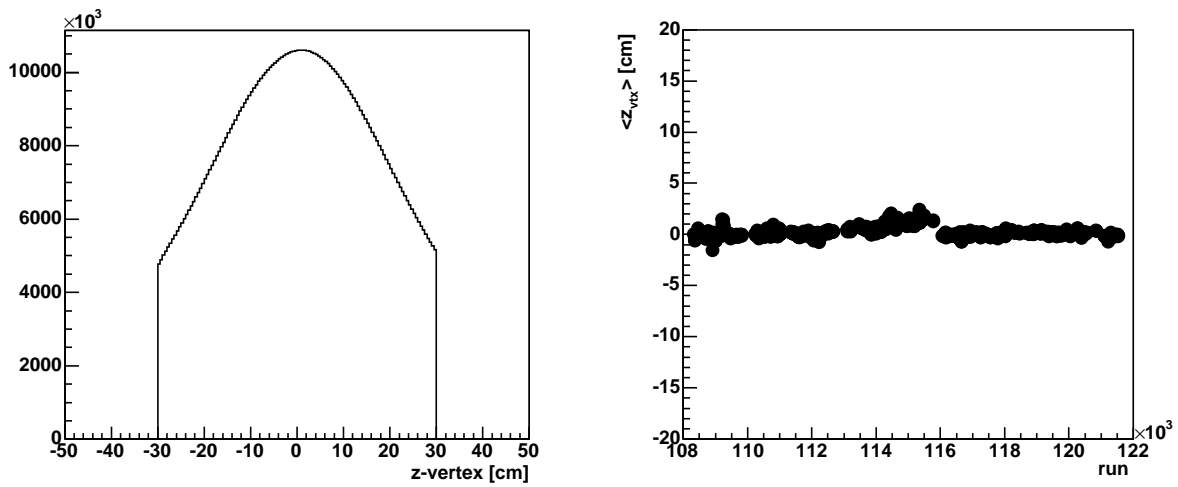


Figure 4.2: Left : Accumulated z vertex distribution reconstructed with BBCs in Year-4 Au+Au collisions. Right : Mean of z vertex distribution as a function of the run number.

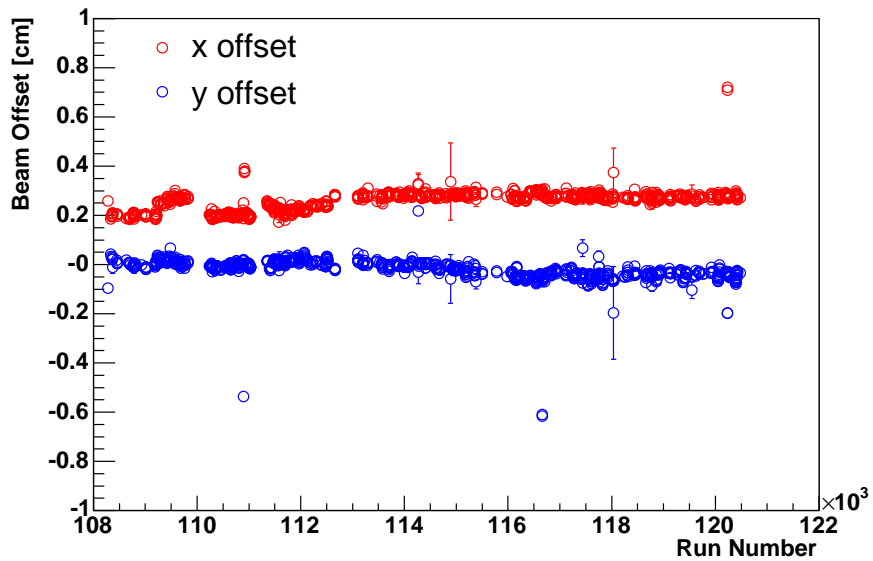


Figure 4.3: Beam position motion in transverse plane as a function of run number. Red is x_0 and blue is y_0 .

4.2 Trigger Conditions

4.2.1 Minimum bias trigger (MB) and trigger efficiency

During the Year-4 Au+Au collisions, PHENIX sampled the integrated luminosity of $\sim 240 \mu b^{-1}$ with $\sqrt{s_{NN}}$ of 200 GeV. Data was taken with the “minimum bias” trigger, which is generated with the BBC and ZDC.

The requirement for the generation of minimum bias trigger on BBC and ZDC are as follows.

- A coincidence between the north and south BBC with at least two PMTs fired in each BBC is required. The collisions vertex is also required to satisfy $|z_{vtx}| \leq 36$ cm, which is calculated online. This is called as “BBLL1 \geq 2” trigger.
- At least one forward neutron has to be detected in each of ZDCs. This is called as “ZDCNS” trigger.
- An offline collision vertex cut of $|z_{vtx}| \leq 30$ cm is required.

Minimum bias trigger is defined as follows:

$$\text{Minimum Bias (MB) Trigger} \equiv \text{BBLL1} \geq 2 \cap \text{ZDCNS} (|z_{vtx}| \leq 30 \text{ cm}). \quad (4.3)$$

The trigger efficiency for minimum bias Au nuclear interactions related to Eq. (4.3) is studied by a detail simulation of the BBC and the ZDC and using the HIJING event generator [117]. The minimum bias trigger efficiency was estimated to be $92.2^{+2.5}_{-3.0}\%$ [118, 119, 120] from this study. This means that the inelastic Au+Au cross section taken with minimum bias trigger is $92.2^{+2.5}_{-3.0}\%$ of the total inelastic Au+Au cross section.

Chapter 5

Data Analysis 1 - Electron Identification

In this chapter, track reconstruction, momentum determination and the calibration of RICH for electron identification are described. The way to identify electrons with PHENIX detectors is also described.

5.1 Tracking and Momentum Reconstruction

In this section, the reconstruction method of the charged particle tracks and the extraction method of the charged particle momentum are described.

5.1.1 DC-PC1 tracking

Figure 5.1 show the typical track in the DC bend plane ($r - \phi$ plane) (left) and the typical track in the $r - z$ plane, perpendicular to the bend plane (right). The variables which are measured with the DC and the PC1 and are used to reconstruct the tracks are summarized as follows:

- ϕ : The azimuthal angle at the intersection of the track with the “reference radius” at the mid-radius of the drift chamber. The reference radius is 220 cm.
- α : the inclination angle of the track at the intersection point with reference radius of the DC
- zed : The z coordinate of the tracks at the intersection point with the reference radius of the DC
- β : The inclination angle of the tracks with respect to the z -axis at the intersection point

To identify the track, hits produced in the detector by the same charged particle have to be found and combined. The tracking is done in the $r - \phi$ plane and $r - z$ plane, separately. The track reconstruction in $r - \phi$ plane is done by using the combinatorial hough transformation technique (CHT) [112]. Any pairs of hits can be mapped to a point in the space defined by

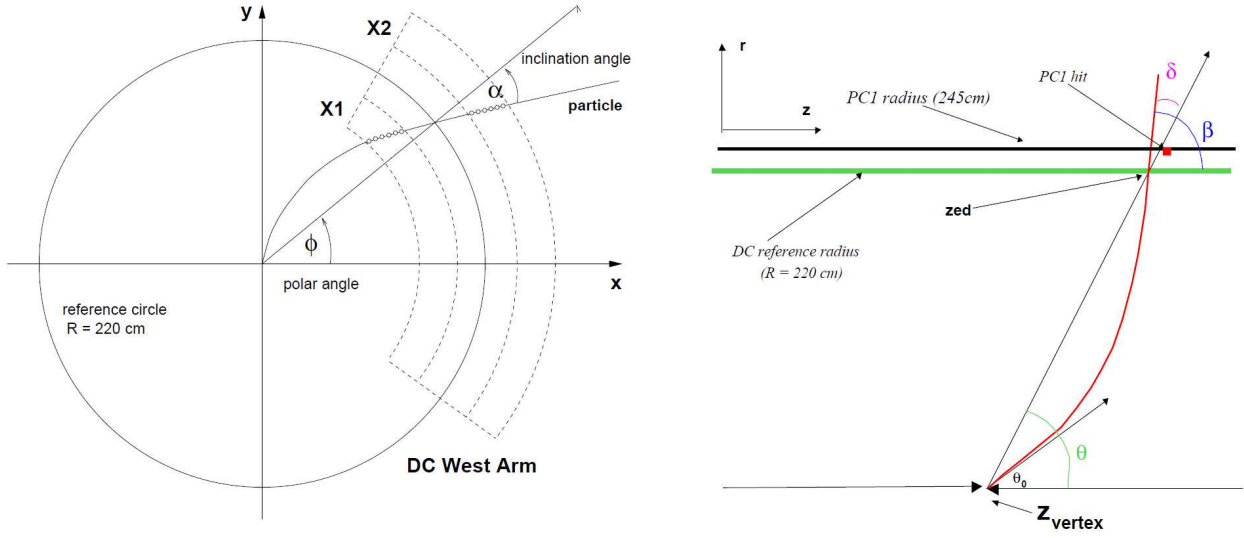


Figure 5.1: Left: A schematic view of the track in the DC $x - y$ ($r - \phi$) plane. The X1 and X2 hits in the DC are shown as small circles. ϕ and α are the feature space variables in the CHT transformation. Right: A schematic view of the track in the DC $r - z$ plane. β is the polar angle of the track.

azimuthal angle ϕ and track bending angle α . The basic assumption is that tracks are straight lines within the DC. In this case, all hit pairs for a given track will have same ϕ and α , thus resulting in a local maximum in the feature space. Figure 5.2 shows an example of a portion of the DC hits (left) and the resulting feature space (right) for a central Au+Au collisions. DC has total 12 hits in X1 and X2 wires and this gives 66 hit pairs, which is seen as maximum height in left of Fig. 5.2. After the reconstruction of the track in $r - \phi$ plane, the direction of a track is specified by ϕ and α . Tracks are then reconstructed in the non-bend plane by combining the information from the PC1 hits and the collision z vertex measured by the BBCs. First, the straight line of the track in $r - \phi$ plane is extended to PC1 detectors. If there is an unambiguous PC1 association (within 2 cm distance between the track projection points and PC1 hit position in $r - \phi$ plane), the track vector in the non-bend plane is fixed by the PC1 hit z position and the z vertex measured by the BBCs. Then the intersection points at the DC UV wires are calculated. UV1 hits are associated to the track if they are within ± 5 cm from the track in $r - z$ plane [113].

5.1.2 Momentum determination

The α in the DC is closely related to the field integral along the trajectory of the charged particle K and transverse momentum of charged particle p_T as follows:

$$\alpha \simeq \frac{K}{p_T}, \quad (5.1)$$

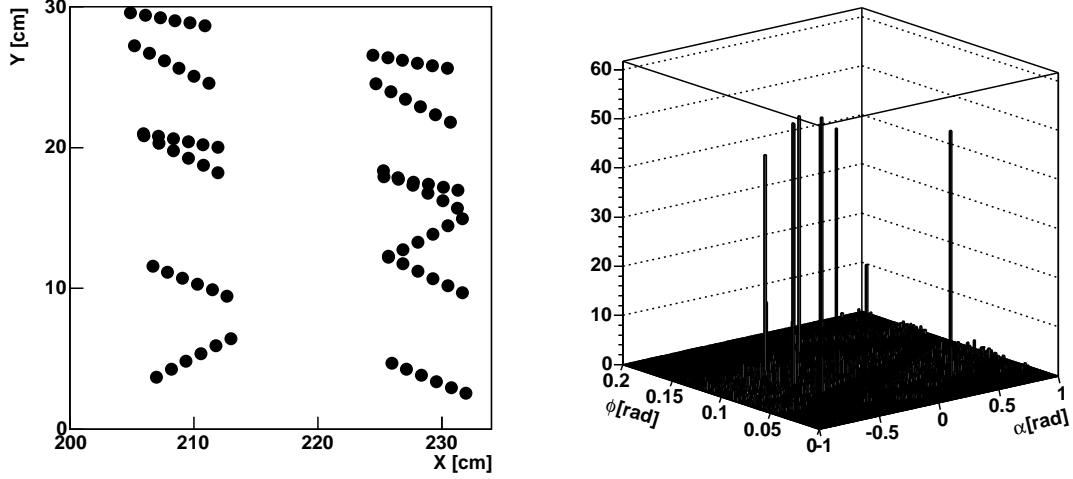


Figure 5.2: Left : Hits in a portion of the DC X1 and X2 wires. Right : Corresponding hough amplitude as a function of feature space for X1 and X2 wires

where $K = 104 \text{ mrad GeV}/c$ is the effective field integral and expressed as :

$$K = \frac{e}{R} \int B dl, \quad (5.2)$$

where e is the elementary charge in the hybrid unit ($e=0.2998 \text{ GeV}/c \text{ T}^{-1}\text{m}^{-1}$) and R is the DC reference radius ($R = 220 \text{ cm}$).

However, due to the small non-uniformity of the magnetic field along the particle trajectory, the momentum of the particle cannot be calculated analytically. The momentum of a track is determined by using the four-dimensional field grid. The variables in the grid are z_{vtx} , the polar angle of the particle at the vertex θ_0 , the total momentum p , and radius r at which the field integral $f(p, r, \theta_0, z_{vtx})$ is calculated. The field integral grid is generated by explicitly swimming particles through the magnetic field map from survey measurement and numerically integrating to obtain $f(p, r, \theta_0, z_{vtx})$ for each grid point. By using Eq. (5.1) as an initial guess, an iterative procedure is used to determine the momentum of the reconstructed tracks. The details of the iteration procedure can be found in [113, 114].

5.1.3 Momentum resolution

From Eq. (5.1), momentum resolution can be estimated as follows:

$$\left(\frac{\delta p}{p}\right)^2 = \left(\frac{\delta \alpha}{\alpha}\right)^2 \quad (5.3)$$

$$= \left(\frac{\sigma_{ms}}{K\beta}\right)^2 + \left(\frac{\sigma_{\alpha}^{int}}{K}p\right)^2, \quad (5.4)$$

where $\delta \alpha$ is the measured spread of the α angle and can be decomposed into the contribution from multiple scattering (σ_{ms}) and the contribution from the intrinsic angular resolution (σ_{α}^{int}).

The contribution of the multiple scattering to the momentum resolution can be directly estimated with the material thickness in front of DC which is summarized in Table 5.1. The width of the angular distribution (σ_{ms}) is expressed as follows [19]:

$$\sigma_{ms} = \frac{13.6\text{MeV}}{\beta cp} z \sqrt{\frac{X}{X_0}} \left(1 + 0.038 \ln \frac{X}{X_0}\right), \quad (5.5)$$

where p , βc and z are the momentum, velocity and the charge number of the incident particle and X/X_0 is the thickness of the medium in units of the radiation length. This leads to the

Medium	Material	Thickness X [mm]	Rad. Length X_0 [mm]	X/X_0 [%]
Beam pipe	Be	1.016	353.0	0.280
Air	Air	350	304200	0.115
He Bag	He gas	1630	5299000	0.031
DC window	Mylar	0.2	287	0.070
Total (before DC)				0.496

Table 5.1: The materials in front of DC

$$\sigma_{ms} = 0.76 \text{ [mrad GeV}/c^2 \text{] and } \sigma_{ms}/K = 0.75\%.$$

As described later, E/p is one of the variables to be used in the electron identification, where E and p is the energy measured with the EMCal and momentum measured with the DC, respectively. Since the mass of electron can be negligible compared to the momentum of electrons, E/p distributes around 1 for electrons. The width of E/p distribution can be parameterized as follows:

$$\frac{\sigma(E/p)}{E/p} = \sqrt{\left(\frac{\delta E}{E}\right)^2 + \left(\frac{\delta p}{p}\right)^2} \quad (5.6)$$

$$= \sqrt{c_1^2 + c_2^2/E + c_3^2 + c_4^2 \times p^2}, \quad (5.7)$$

where $c_1 \oplus c_2/\sqrt{E}$ corresponds to the energy resolution of the EMCal and $c_3 \oplus c_4 \times p$ corresponds to the momentum resolution of the DC. By assuming that E/p equals to be 1 for electrons, Eq. (5.7) can be expressed in terms of the electron momentum p as follows:

$$\frac{\sigma(E/p)}{E/p} = \sqrt{c_1^2 + c_2^2/p + c_3^2 + c_4^2 \times p^2}. \quad (5.8)$$

Figure 5.3 shows the $\sigma(E/p)/(E/p)$ as a function of electron momentum for PbGl (Left) and PbSc (Right). Since the contribution of the EMCal energy resolution to the $\sigma(E/p)/(E/p)$ is 7 times larger than that of the DC momentum resolution below the electron momentum of 2 GeV/ c , the energy resolution of the PbGl and PbSc was determined by fitting $\sigma(E/p)/(E/p)$ below the electron momentum of 2 GeV/ c with $c_3 = c_4 = 0$. The results of the energy resolution of the PbGl and PbSc are as follows:

$$\delta E/E = (4.25\% \pm 0.31\%) \oplus (7.69\% \pm 0.21\%)/\sqrt{E} \quad (\text{PbGl}) \quad (5.9)$$

$$\delta E/E = (4.53\% \pm 0.57\%) \oplus (8.28\% \pm 0.30\%)/\sqrt{E} \quad (\text{PbSc}), \quad (5.10)$$

where the errors are the statistical errors. The momentum resolution was extracted by fitting the $\sigma(E/p)/(E/p)$ for the PbGl and PbSc simultaneously with the function of Eq. (5.8), where the term of the energy resolution were fixed to be Eq. (5.9) and Eq. (5.10) and the multiple scattering term c_3 was also fixed to be 0.75 [%]. The result of the momentum resolution with this method is:

$$\frac{\delta p}{p} = (0.73 \pm 0.02) [\%] \times p \oplus 0.75 [\%]. \quad (5.11)$$

This leads to the mass width for the stationary J/ψ of ~ 30 [MeV], which corresponds to the mass resolution of $\sim 0.97\%$.

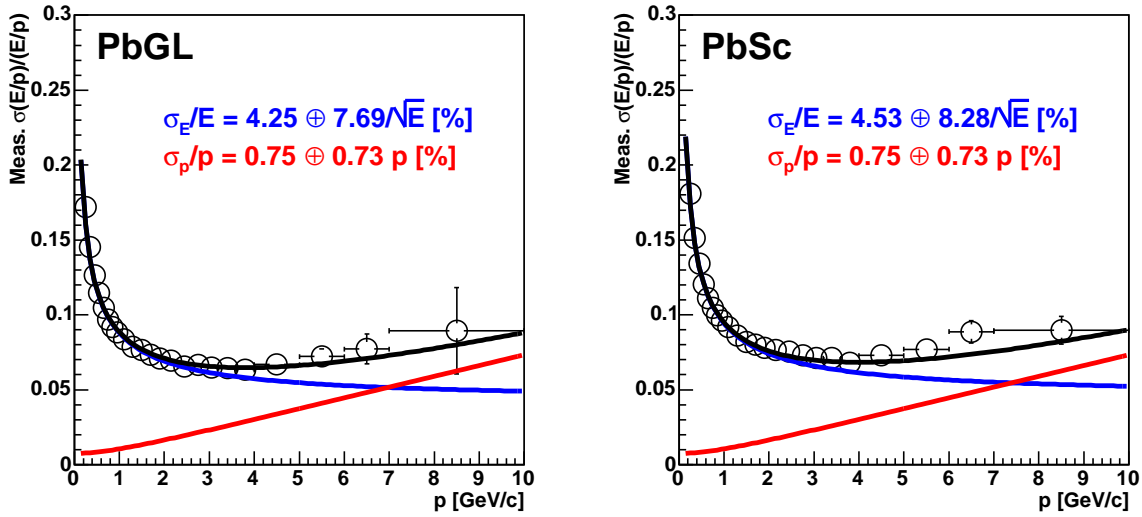


Figure 5.3: $\sigma(E/p)/(E/p)$ as a function of electron momentum for PbGl (Left) and PbSc (Right). Black open circles are the data points. Red lines are the contribution from EMCAL energy resolution extracted by using the points below 2 GeV/c and blue lines are the contribution from DC momentum resolution extracted by fitting the points for PbGl and PbSc simultaneously. Black lines are the results of the $\sigma(E/p)/(E/p)$ from EMCAL energy resolution and DC momentum resolution.

5.1.4 RICH calibration

The RICH is the main device for the electron identification. Gain calibration of RICH PMTs and alignment calibration of RICH mirrors are crucial for the electron related analysis. These two calibrations (charge calibration and mirror alignment calibration) are described here.

Charge calibration

Calibration for the number of photo-electrons was performed for each 5120 PMT channel by fitting raw ADC distribution with Gaussian and Poisson distributions, where former and the latter are for pedestal and one photo-electron peak, respectively. Example of the fitting is shown in Fig. 5.4. After the extraction of pedestal peak position and one photo-electron peak

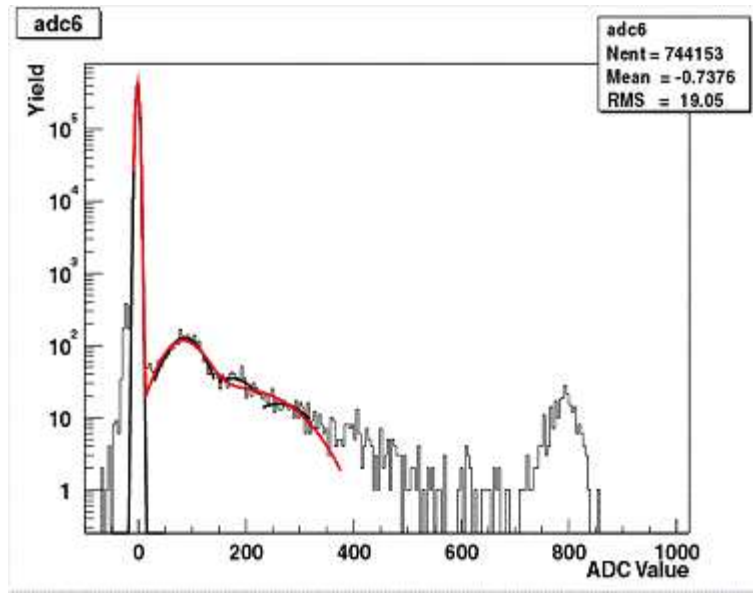


Figure 5.4: Raw ADC spectrum for one RICH PMT channel. Raw ADC distribution is fitted with Gaussian and Poisson distributions to extract pedestal position, one photo-electron and 2nd photo-electron position.

position, the number of photo-electron ($N_{p.e}$) is calculated as follows:

$$N_{p.e} = \frac{(ADC - ADC_{pedestal})}{ADC_{1.p.e}}, \quad (5.12)$$

where $ADC_{pedestal}$ and $ADC_{1.p.e}$ are the ADC channel for pedestal and one photo-electron peak, respectively.

Figure 5.5 shows the number of photo-electron distribution after the gain calibration. The hit PMT in RICH was defined to have greater than 0.3 photo-electrons.

Mirror alignment calibration

As shown in Fig. 3.16, spherical mirrors are used to reflect the Cherenkov radiation and lead to PMT planes. There are 24 mirrors per each arm and side and total $24 \times 2 \times 2 = 96$ mirrors are

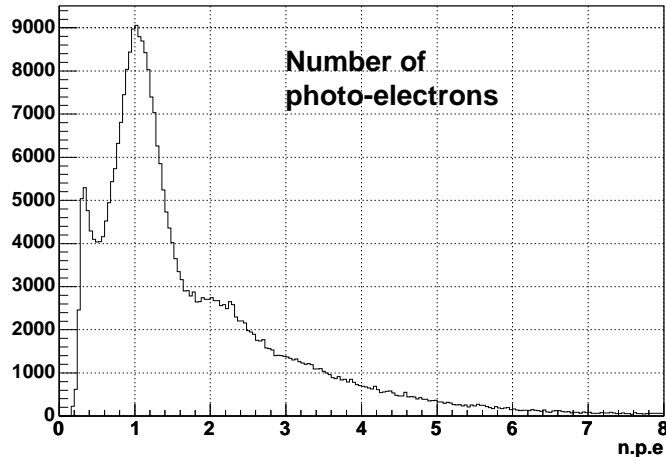


Figure 5.5: The number of photo-electron distribution after the gain calibration.

used in the RICH. Alignment calibration for 96 mirrors was performed in offline by adjusting the position of each mirror in z and ϕ direction. Electron candidates are selected by requiring $0.8 \leq E/p \leq 1.2$, where E is the energy measured with EMCal and p is the momentum. Also high p_T tracks ($p_T \geq 1 \text{ GeV}/c$) are selected to reject hadron backgrounds.

To do the alignment calibration, it is necessary to associate the charged particle tracks to the RICH PMT planes since the projection point at the RICH PMT planes corresponds to the ideal ring center. In this calibration, straight line between the hit position of the charged particle at PC1 and that at PC2 (PC3) are used as the track for West (East) arm. Then particle trajectories are reflected with respect to the RICH mirror plane and reflected tracks are associated to RICH PMT plane. Example of the track association to RICH PMT plane is shown in Fig. 5.6. After the association of the track to PMT plane, hit PMTs are searched around the track projection point. Mirror alignment calibration was done by adjusting the position of the mirror in z and ϕ such that the Cherenkov ring could be seen and the track projection point matched to the ring center obtained from the positions of hit PMTs. Changing the mirror alignment in z and ϕ corresponds to the change of reflection for electron tracks and the projection point to RICH PMT planes.

Figure 5.7 shows the hit PMT positions on the plane perpendicular to the reflected tracks before alignment calibration (left) and after alignment calibration (right).

Figure 5.8 shows the ring radius obtained after the alignment calibration. Blue dotted line is the result of the Gaussian fitting and mean ring radius is the $\langle r_{cor} \rangle = 5.9 \text{ cm}$.

5.2 Electron Identification

In this section, the strategy to identify electrons by the RICH and the EMCal is described.

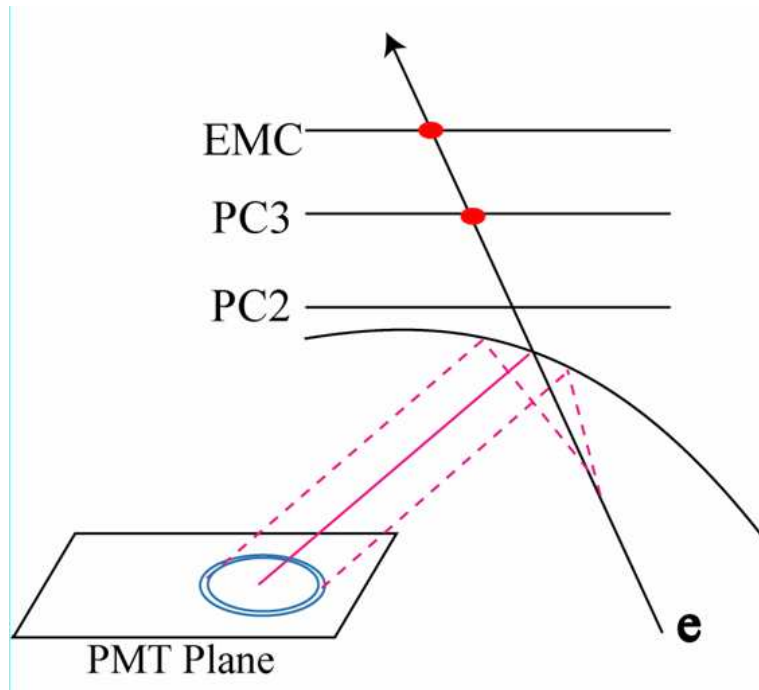


Figure 5.6: Example of the track association to RICH PMT plane

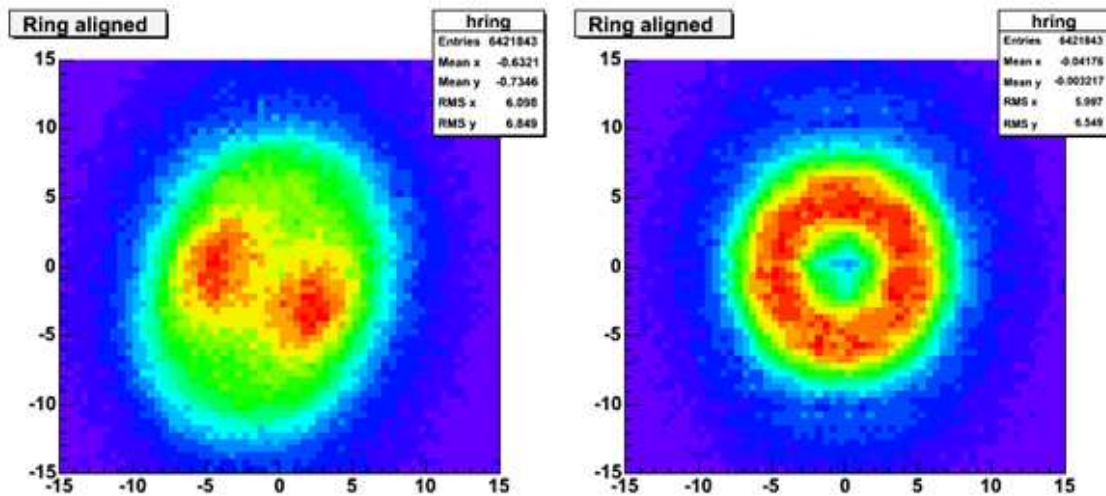


Figure 5.7: Left : Accumulated ring imaging before the alignment calibration. Right : After the alignment calibration.

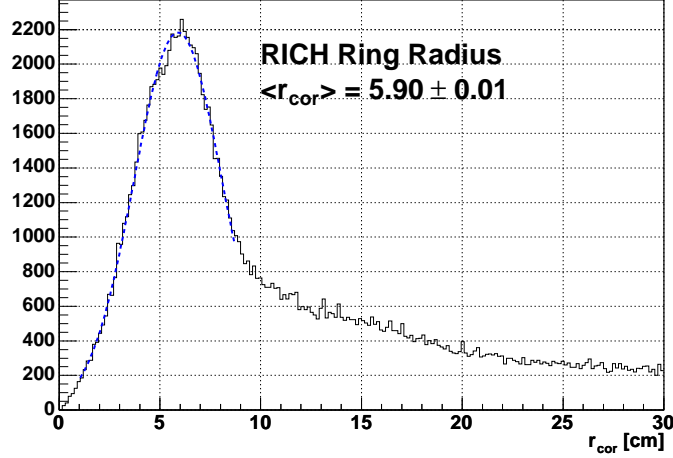


Figure 5.8: Ring radius obtained after the alignment calibration

5.2.1 List of variables used in electron identification

Table 5.2 is the summary of the variables used in the electron identification. Meaning of them are also explained in Table 5.2

Variables	Description
$n0$	the number of fired PMT's in standard ring radius ($3.8 \text{ [cm]} \leq r \leq 8.0 \text{ [cm]} $)
$n1$	the number of fired PMTs in larger ring radius ($r \leq 11.0 \text{ [cm]} $)
$npe0$	the number of photo electrons detected in standard ring radius
$npe1$	the number of photo electrons detected in larger ring radius
$chi2$	ring shape
$disp$	displacement between the projection point on the RICH PMT plane and the point reconstructed from the fired PMTs
E	energy detected at EMCAL (summed up for 3×3 towers)
$emcsdphi_e$	track matching in ϕ at EMCAL surface normalized by the width
$emcsdz_e$	track matching in z at EMCAL surface normalized by the width
dep	$(E/p-1)/\sigma(E/p)$

Table 5.2: Summary of the variables in electron identification

5.2.2 Electron identification with the RICH

After the tracks are extracted by the DC and the PC1, they are associated to the PC2, the PC3 and the EMCAL. Track association to the RICH is performed using the hit information of the PC1 and the PC2 (PC1-PC2 track) in West and the PC1 and the PC3 (PC1-PC3 track)

in East. If the hit cannot be found on the PC2 and the PC3, the hit position on the outer detectors (the PC3 for West and EMCAL for East) or projection points of the extracted tracks at the PC2 radial position are used for the association. Then they are reflected with respect to the RICH mirror and the reflected tracks are associated to RICH PMT planes. Then the hit PMTs are searched for around the projection points on the RICH PMT planes.

Figure 5.9 shows the schematic view of the definition of the variables which are used in the calculation of the variables listed in Table 5.2.

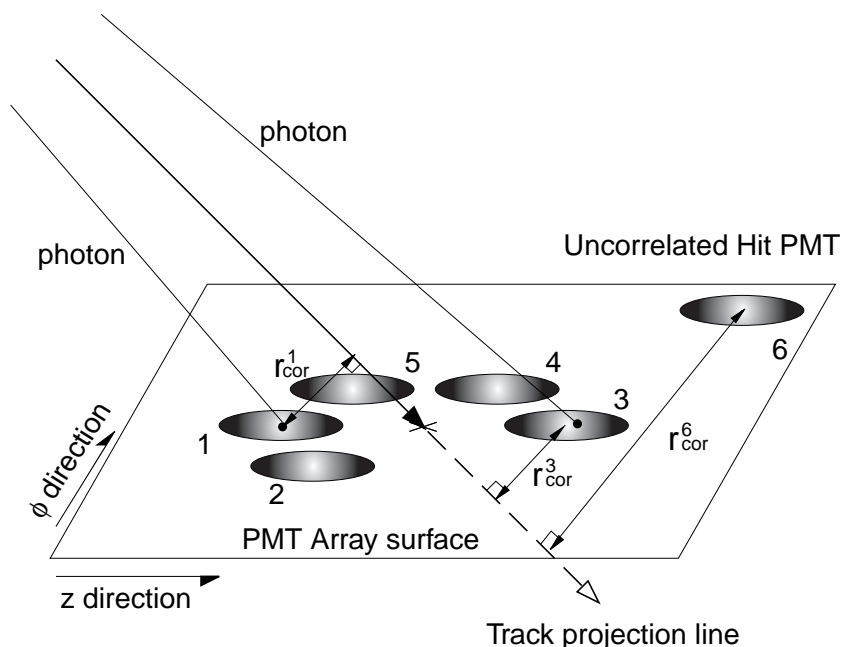


Figure 5.9: The schematic description of the definition of variable which characterize the RICH ring. The track projection vector and five hit PMT are shown as an example. The distance between the center of hit PMT 1, 3 and the track projection vector are represented as r_{cor}^1 and r_{cor}^3 , respectively.

Parameters of r_{cor}^i (r_{cor}^1 and r_{cor}^3 are shown in Fig.5.9) is the distance between the center of PMT i and the track projection vector.

The values of n_0 and n_1 are defined as follows:

$$n_0 \equiv \text{the number of Hit PMTs in } 3.4 \text{ cm} \leq r_{cor}^i \leq 8.4 \text{ cm}, \quad (5.13)$$

$$n_1 \equiv \text{the number of Hit PMTs in } r_{cor}^i \leq 11.0 \text{ cm}, \quad (5.14)$$

where hit PMT is defined to have greater than 0.3 photo-electrons. The variables of n_{pe0} and n_{pe1} are the summation of number of photo-electrons of hit PMTs in $3.4 \text{ cm} \leq r_{cor}^i \leq 8.4 \text{ cm}$ and $r_{cor}^i \leq 11.0 \text{ cm}$, respectively.

$$n_{pe0} \equiv \sum_{3.4 \text{ cm} \leq r_{cor}^i \leq 8.4 \text{ cm}} n.p.e(i), \quad (5.15)$$

$$npe1 \equiv \sum_{r_{cor}^i \leq 11.0 \text{ cm}} n.p.e(i). \quad (5.16)$$

The position of the ring center \mathbf{R}_{center} is calculated from the positions of hit PMTs \mathbf{R}_i by weighting them according to $n.p.e(i)$ as follows:

$$\mathbf{R}_{center} \equiv \frac{\sum_{3.4 \text{ cm} \leq r_{cor}^i \leq 8.4 \text{ cm}} n.p.e(i) \times \mathbf{R}_i}{npe0}, \quad (5.17)$$

where the origin of \mathbf{R}_i is the track projection point.

The distance between \mathbf{R}_{center} and the track projection line is defined as $disp$.

The variable $chi2$ gives the observed ring shape. It was the weighted average of the deviation of the hit PMT position from the ideal ring radius, $r_0 = 5.9 \text{ cm}$. The weight is the number of photo-electrons in each PMT. The definition of $chi2$ is:

$$chi2 \equiv \frac{\sum_{r_i < 11.0 \text{ cm}} (r_i - r_0)^2 \times n.p.e(i)}{npe1}, \quad (5.18)$$

where r_i represents the distance between PMT hit position and track projection point in the plane perpendicular to the track projection line, r_0 represents the mean ring radius $\langle r_{cor} \rangle$ as shown in Fig. 5.8.

Random association to the RICH

In order to estimate the background due to the accidental association of hadron tracks to the hit PMTs, the track projection point $\mathbf{R}_0 = (x, y, z)$ is flipped to $\mathbf{R}_0^{z-flipped} = (x, y, -z)$. Then hit PMTs are searched for around the $z - flipped$ projection point. This method gives the statistical evaluation of the random association of tracks and hit PMTs. The variables of $sn0$, $sn1$, $snpe0$, $snpe1$, $schi2$ and $sdisp$ correspond to the $n0$, $n1$, $npe0$, $npe1$, $chi2$ and $disp$ with the projection point of $\mathbf{R}_0^{z-flipped}$ instead of \mathbf{R}_0 , respectively.

Figure 5.10 shows the distributions of the RICH parameters in Au+Au collisions, where a), b), c), d), e) and f) show $n0$, $n1$, $npe0$, $npe1$, $disp$ and $chi2/npe1$, respectively. The raw distribution, $z - flipped$ distribution and net signal (subtracted) distribution are expressed as solid, dashed lines and shaded histograms, respectively.

5.2.3 Electron identification with the EMCal

The EMCal provides the measurement of the energy and hit position for the photons and electrons.

Energy calibration for each tower was performed by tagging π^0 and sector dependence of energy variation was corrected using the measured energy for MIP particles [109, 110].

Energy-Momentum matching

Since the mass of electrons is negligible compared to its momentum and the electrons deposit all of its energy in EMCal, the ratio of the energy E measured by the EMCal and momentum

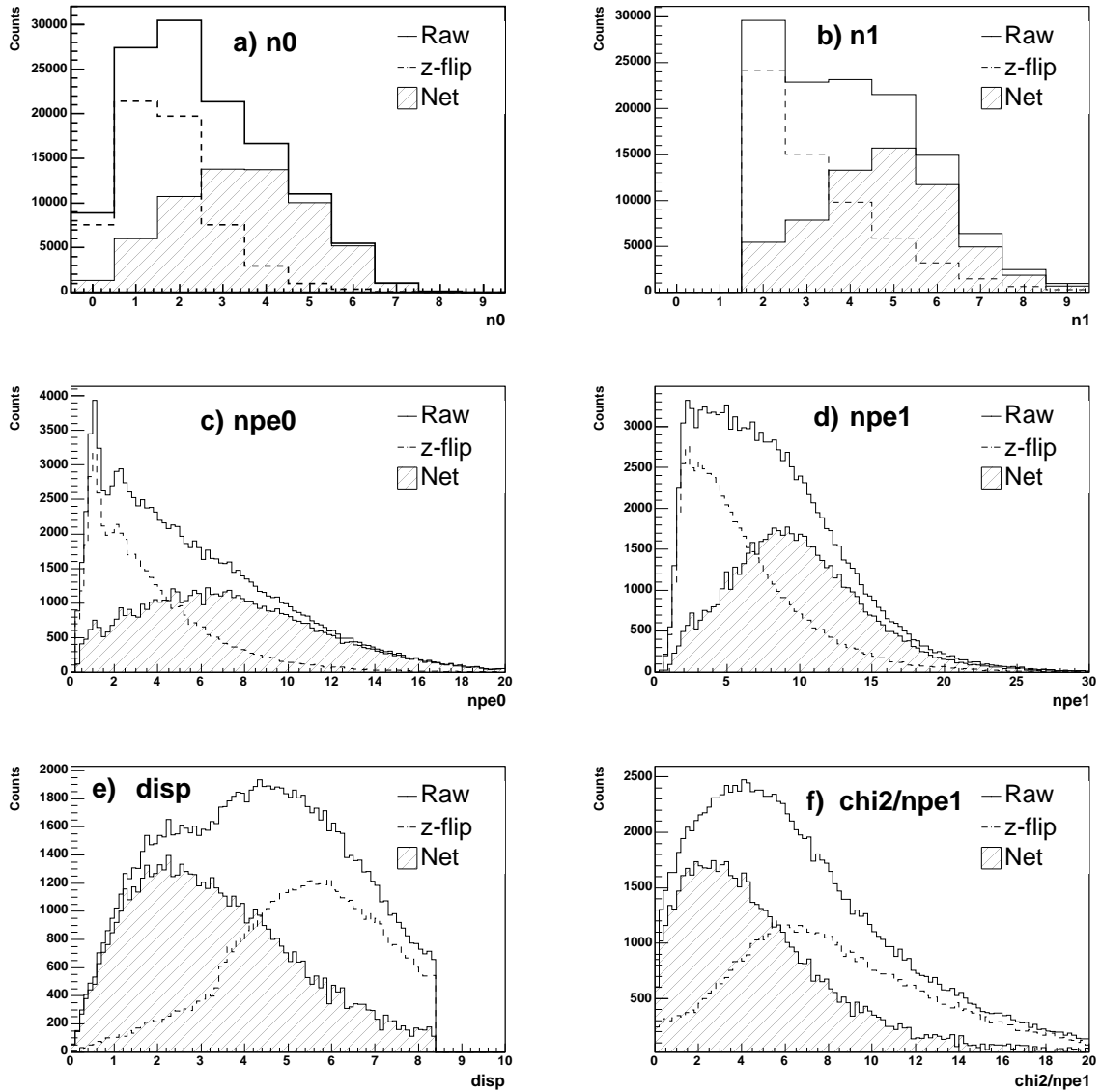


Figure 5.10: a), b), c), d), e) and f) show n_0 , n_1 , npe_0 , npe_1 , $disp$ and chi^2/npe_1 in MB collisions, respectively. The raw distribution, z -flipped distribution and net signal (subtracted) distribution are expressed as solid, dashed lines and shaded histograms, respectively.

p measured by the DC is around 1 in case of electrons. Therefore E/p is one of the useful variables for the electron identification.

Figure 5.11 shows the E/p distributions in Au+Au collisions and for all charged particles (dashed-dotted line), for the particles with RICH cut ($n1 \geq 4$ solid line) and for the particles with z -flipped RICH cut ($sn1 \geq 4$ dashed line) in left and right, where the p_T range is $0.7 \leq p_T \leq 5$ GeV/c. Shaded histogram in right is the distribution of E/p after the subtraction of z -flipped distribution.

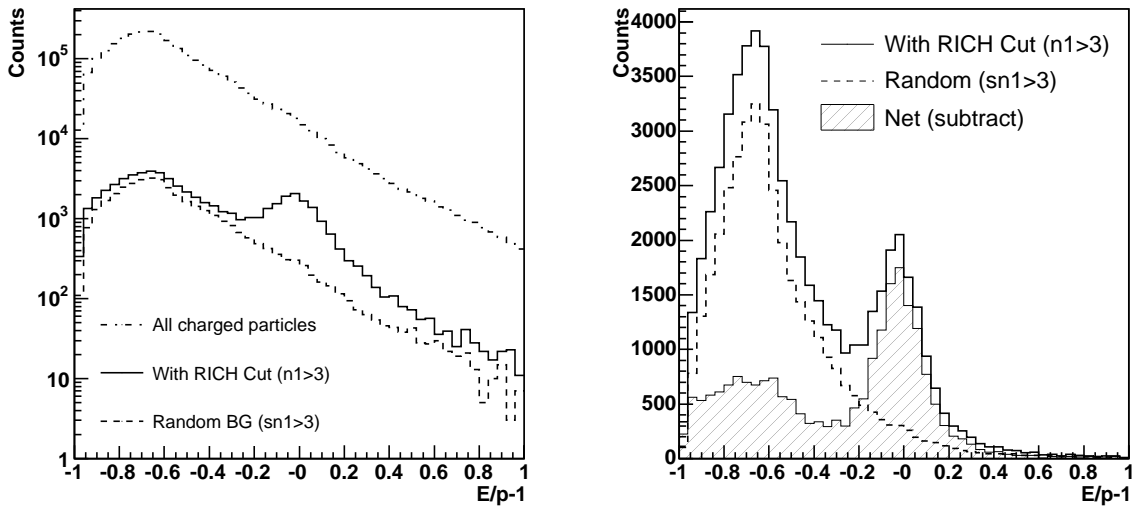


Figure 5.11: Left: E/p distribution for all charged particles (dashed-dotted line), for the particles passed with RICH cut ($n1 \geq 4$) (solid line) and for the particles passed with z -flipped RICH cut ($sn1 \geq 4$) (dashed line), which corresponds to the particles associated to the RICH randomly. Right: E/p distributions for the particles passed with RICH cuts (solid), for the particles with z -flipped RICH cuts (dashed line) and for the net particles of the subtraction of the random association to the RICH (shaded histogram). They are from MB collisions and the momentum range of charged particles are $0.7 \leq p_T \leq 5.0$.

The variable dep is used in this analysis, which is the E/p normalized by the width of E/p distribution $\sigma(E/p)$. As a result, dep does not have momentum dependence. The formula of dep can be written:

$$dep = \frac{E/p - 1}{\sigma_{E/p}(p)}. \quad (5.19)$$

Figure 5.3 shows the $\sigma(E/p)/(E/p)$ as a function of electron momentum. This width $\sigma(E/p)$ was used to calculate dep .

Hit position matching

Distance between the reconstructed track projection point at the surface of the EMCal and the hit position (shower center) of EMCal is expressed by D_ϕ in ϕ direction and D_z in z -direction:

$$D_\phi = \phi_{track} - \phi_{hit}, \quad (5.20)$$

$$D_z = z_{track} - z_{hit}, \quad (5.21)$$

where, z_{track} and ϕ_{track} are the projected z and ϕ position of reconstructed track at EMCAL surface, and z_{hit} and ϕ_{hit} are the hit position in z and ϕ , respectively. Details for the reconstruction of shower center with the EMCAL can be seen in Ref. [113].

The variables $emcsdphi_e$ and $emcsdz_e$ are introduced as follows:

$$emcsdphi_e = D_\phi / \sigma_\phi(p, z) \quad (5.22)$$

$$emcsdz_e = D_z / \sigma_z(p, \theta), \quad (5.23)$$

where $\sigma_\phi(p, z)$ and $\sigma_z(p, \theta)$ are the momentum, z and θ dependent width of D_ϕ and D_z values, respectively.

Calibration for $emcsdphi_e$ and $emcsdz_e$ was done for each EMCAL sector. At first, D_ϕ was checked as functions of momentum, z position of the DC (zed) and ϕ at EMCAL. D_z was also checked as functions of momentum and polar angle of the track θ .

Figure 5.12 shows D_ϕ as a function of zed . Upper (bottom) left and upper (bottom) right are D_ϕ for electrons (positrons) with $0.5 \leq p \leq 0.6$ GeV/ c and $1.4 \leq p \leq 1.6$ GeV/ c , respectively. It is seen that D_ϕ does not distribute around 0 and the dependence of zed is clearly different between electrons and positrons. This is because there is the z dependent residual magnetic field still after DC. Black points in Fig. 5.12 is the mean D_ϕ . D_ϕ as a function of zed was

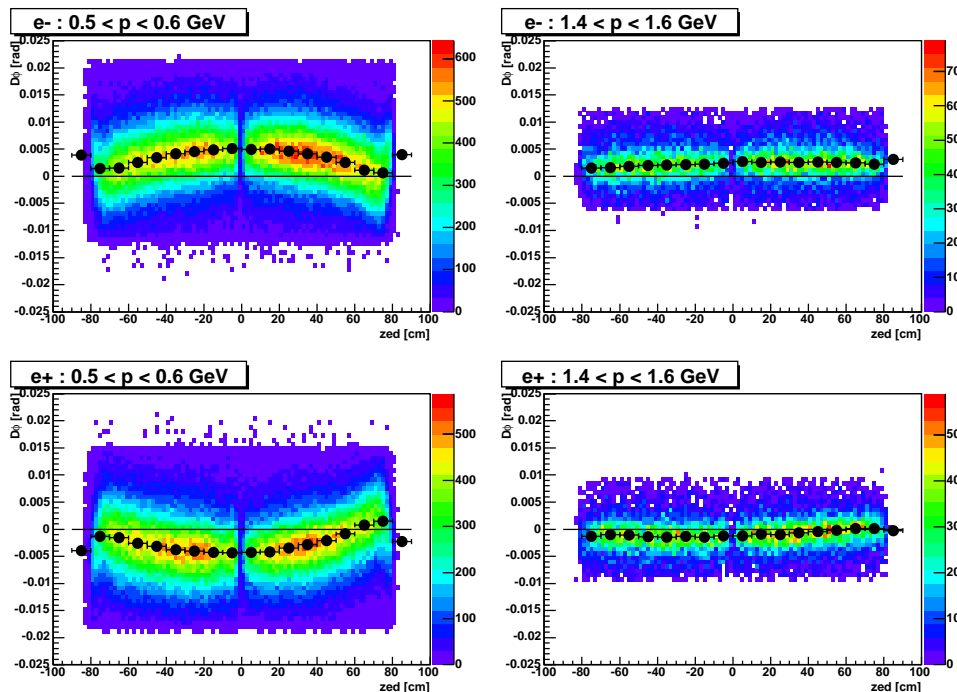


Figure 5.12: D_ϕ as a function of the z position at the DC (zed). Upper (bottom) left and upper (bottom) right are D_ϕ for electrons (positrons) with $0.5 \leq p \leq 0.6$ GeV/ c and $1.4 \leq p \leq 1.6$ GeV/ c , respectively.

fitted with $p_0(p) + p_1(p)zed + p_2(p)zed^2$. Fitting parameters of p_0 , p_1 and p_2 as a function

of momentum for electrons and positrons are shown in Fig. 5.13, where red and blue are for electrons and positrons, respectively. p_0 , p_1 and p_2 were fitted with $c_0 \exp(-c_1 \times p) + c_2$, which were shown as solid lines. After the zed dependence of D_ϕ was corrected, D_ϕ was checked as a

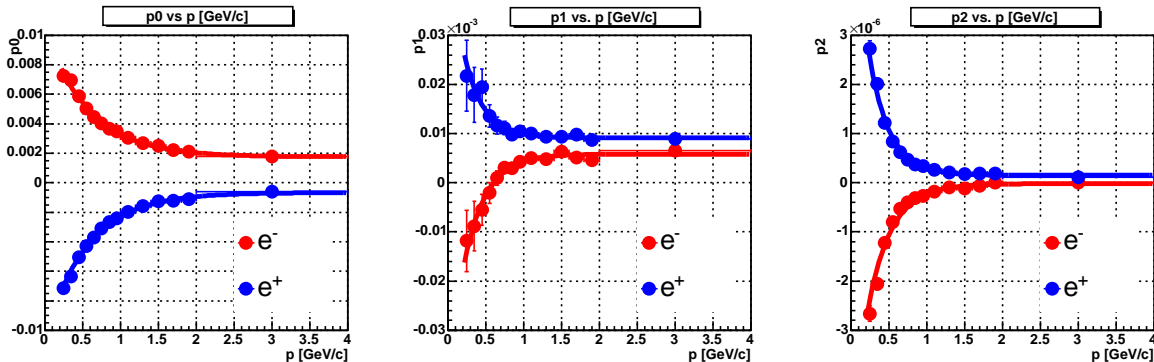


Figure 5.13: Momentum dependence of p_0 , p_1 and p_2 , which were extracted by fitting zed dependence of mean D_ϕ with $p_0(p) + p_1zed + p_2zed^2$. Solid lines were fitting results using $c_0 \exp(-c_1 \times p) + c_2$ function.

function of ϕ at the EMCAL surface to check the incident angle dependence of D_ϕ . Figure 5.14 shows EMCAL ϕ dependence of D_ϕ . Small EMCAL ϕ dependence was observed and that was corrected bin-by-bin for each momentum and EMCAL ϕ .

Figure 5.15 shows D_z as a function of the polar angle θ for electrons. Upper (bottom) left and upper (bottom) right are D_z for electrons (positrons) with $0.5 \leq p \leq 0.6$ GeV/c and $1.4 \leq p \leq 1.6$ GeV/c, respectively. Clear θ dependence can be seen and that is due to the effect of the incident angle. Red and blue points are mean D_z for electrons and positrons, respectively. It is seen that event at $\theta = \pi/2$, which corresponds to the incident angle of 0 degree to the EMCAL surface, D_z does not distribute around 0, which is due to the mis-alignment of the EMCAL. Dependence of D_z on θ was fitted with $p_0(p) \times \tan(\theta - \pi/2) + p_1$ and it was used to correct D_z as a function of momentum and θ .

Width of D_ϕ was checked as functions of momentum and zed and momentum dependence of σ_ϕ at various zed is shown in Fig. 5.16. Left and right of Fig. 5.16 are for electrons and positrons, respectively. In low momentum region ($p \leq 0.5$ GeV/c), σ_ϕ has large z dependence due to the residual magnetic field. Solid lines are the fitting results of momentum dependence of σ_ϕ with $\sqrt{c_0 + c_1/p^{c_2}}$, which was used to calculate $emcsdphi_e$.

Width of D_z was checked as functions of momentum and the polar angle θ of electrons. Momentum dependence of σ_z for various θ is shown in Fig. 5.17. Left and right of Fig. 5.17 are for electrons and positrons, respectively. Solid lines are the fitting results of momentum dependence of σ_z with $\sqrt{c_0 + c_1/p^{c_2}}$, which was used to calculate $emcsdz_e$.

Figure 5.18 shows the dep , $emcsdphi_e$ and $emcsdz_e$ distribution in Au+Au collisions and p_T cut of $0.7 \leq p_T \leq 5$ GeV/c. Solid and dashed lines are the distribution for the particles with RICH cut and with z-flipped RICH cut (random association), respectively. Shaded histograms are the subtracted distributions.

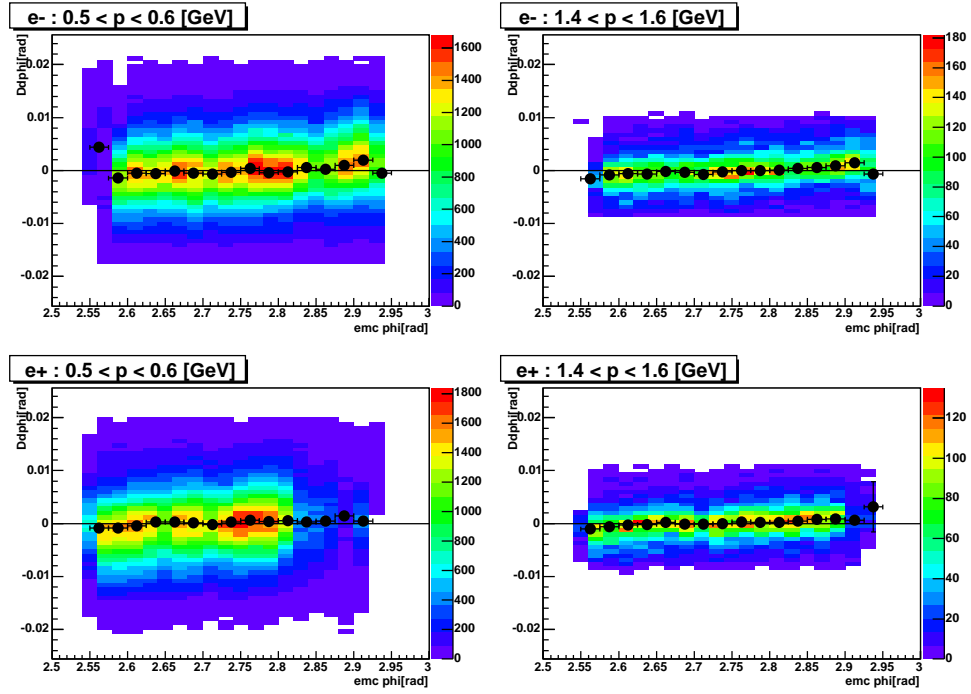


Figure 5.14: EMCAL ϕ dependence of D_ϕ , where the zed dependence of D_ϕ was corrected.

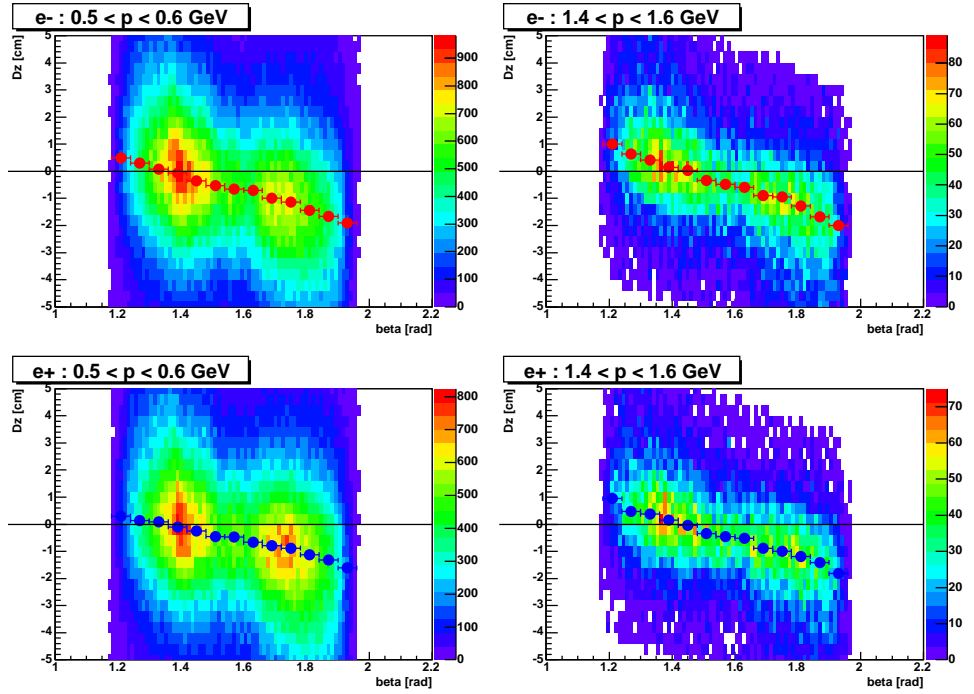


Figure 5.15: D_z as a function of the polar angle θ for electrons. Upper (bottom) left and upper (bottom) right are D_z for electrons (positrons) with $0.5 \leq p \leq 0.6$ GeV/ c and $1.4 \leq p \leq 1.6$ GeV/ c , respectively.

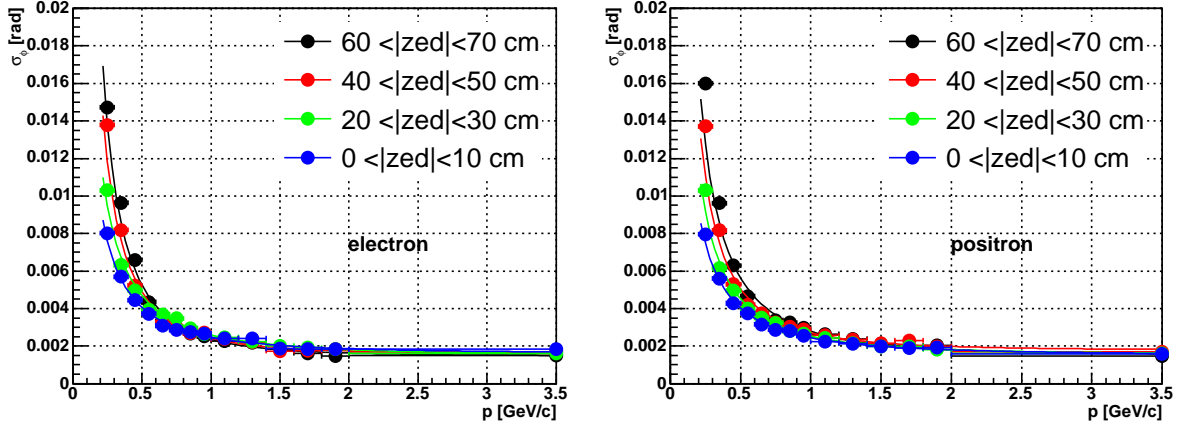


Figure 5.16: Momentum dependence of σ_ϕ at various zed for electrons (left) and positrons (right). Solid lines are the fitting results of momentum dependence of σ_ϕ with $\sqrt{c_0 + c_1/p^{c_2}}$.

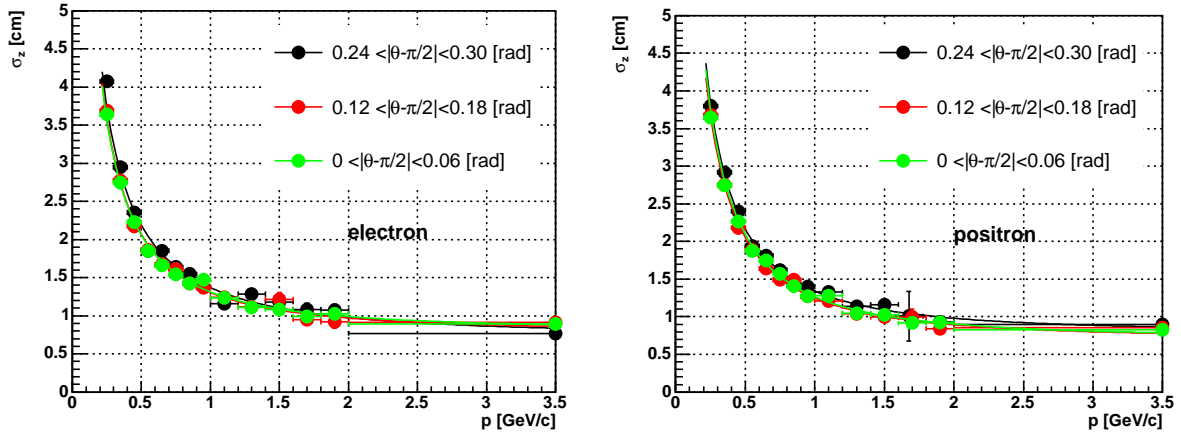


Figure 5.17: Momentum dependence of σ_z for various θ is shown. Solid lines are the fitting results of momentum dependence of σ_z with $\sqrt{c_0 + c_1/p^{c_2}}$.

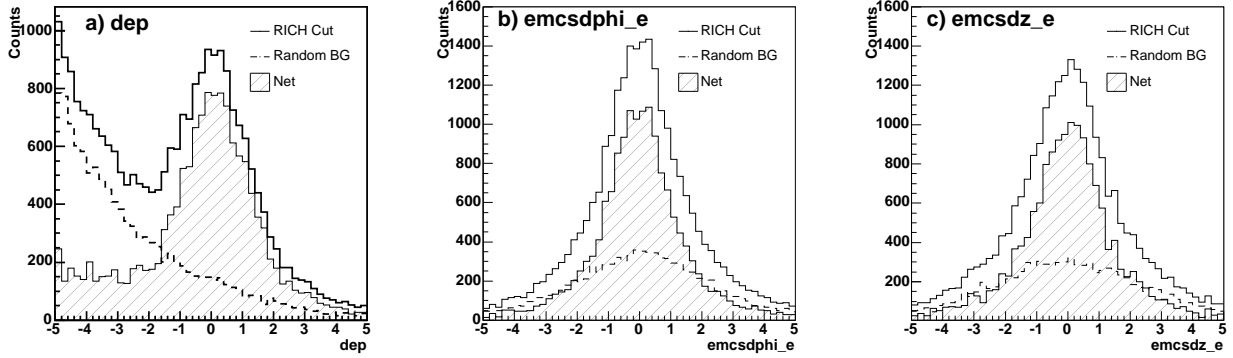


Figure 5.18: a) : *dep* distribution. Solid and dashed lines are the distribution for the particles with RICH cut and with z-flipped RICH cut (random association), respectively. Shaded histogram is the subtracted distribution. b) : *emcsdphi_e* distribution. c) *emcsdz_e* distribution.

5.2.4 Conversion electrons

The reconstructed invariant mass distribution of $e^+ e^-$ pairs have the peak at the low mass region produced by the electron pairs from γ conversion at the beam pipe. This is very useful to check the electron identification parameters and to study the electron identification efficiency.

Since the track reconstruction algorithm assumes that all primary and secondary tracks come from the collision, the electron pairs produced at certain materials are reconstructed such that they have incorrect momentum. This is schematically shown in Fig. 5.19. As a result, the

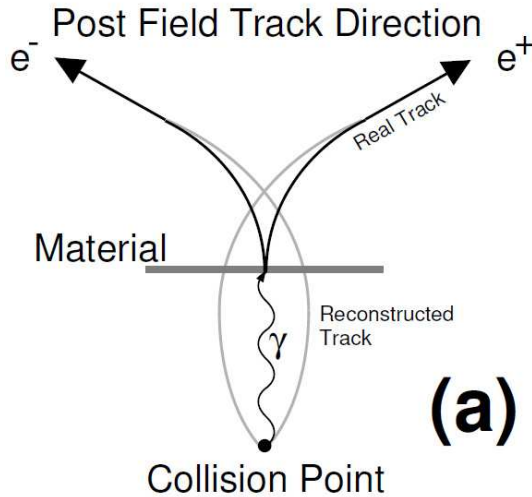


Figure 5.19: (a) The production of conversion electrons.

conversion pairs acquire the fake invariant mass that is proportional to the radial distance of the photon conversion source the beam position.

Left in Fig. 5.20 shows the e^+e^- invariant mass spectrum in low mass region ($M_{e^+e^-} \leq 0.1 \text{ GeV}/c^2$). Black is the invariant mass from e^+e^- pairs, red is the background and the shaded

area is net distribution after the background subtraction. The peak around $0.02 \text{ GeV}/c^2$ is the conversion pairs from the beam pipe and the residual components in the mass spectrum around or less than the conversion pairs are mainly from π^0 Dalitz decay.

Separation of conversion pairs from the Dalitz decay was done by using the angular orientation of the plane defined by the vector product of \mathbf{p}_{e^+} and \mathbf{p}_{e^-} , where \mathbf{p}_{e^+} and \mathbf{p}_{e^-} are the reconstructed momentum vectors of e^+ and e^- of the pair, respectively. The apparent decay plane from conversion pairs (the plane that is parallel to both \mathbf{p}_{e^+} and \mathbf{p}_{e^-}) is perpendicular to the magnetic field. An orientation angle $phiv$ is constructed as follows:

$$\mathbf{u} = \text{unit vector of } (\mathbf{p}_{e^+} + \mathbf{p}_{e^-}), \quad (5.24)$$

$$\mathbf{v} = \text{unit vector of } (\mathbf{p}_{e^+} \times \mathbf{p}_{e^-}), \quad (5.25)$$

$$\mathbf{w} = \mathbf{u} \times \mathbf{v}, \quad (5.26)$$

$$\mathbf{uz} = (0, 0, 1), \quad (5.27)$$

$$\mathbf{ua} = \text{unit vector of } (\mathbf{u} \times \mathbf{uz}), \quad (5.28)$$

$$phiv = \cos^{-1}(\mathbf{w} \cdot \mathbf{ua}), \quad (5.29)$$

where, the symbol “ \times ” shows the vector product and the symbol “ \cdot ” shows the inner products.

Right in Fig. 5.20 shows the conversion pairs extracted by applying the $phiv$ cut ($phiv < 0.015$) to e^+e^- pairs. Clear peak from conversion pairs is seen after $phiv$ cut is applied.

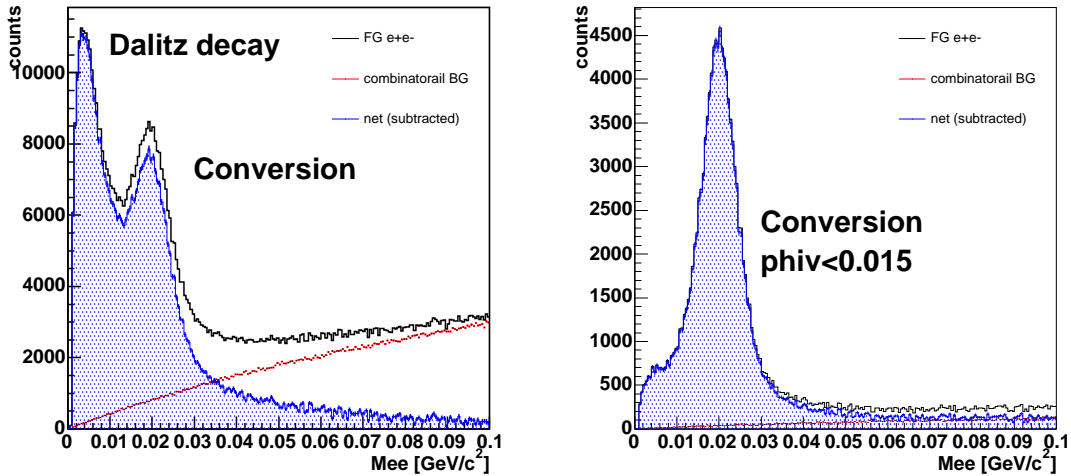


Figure 5.20: Left : invariant mass spectrum in Au+Au collision for lower mass region. without $phiv$ cut. Black is real, red is combinatorial background and blue is the net signal of e^+e^- pairs. Right: invariant mass spectrum after $phiv < 0.015$ cut is applied. Clear peak from conversion pairs is seen.

Figure 5.21 shows the electron identification (eID) parameters of $n0$, $n1$, $npe0$, $npe1$, $disp$, $chi2/npe1$, dep , $emcsdphi_e$ and $emcsdz_e$ for conversion pairs (black). Distributions of these parameters for electrons in Monte Carlo simulation were shown in red, where these parameters in simulation were tuned in the same way to match those in real data.

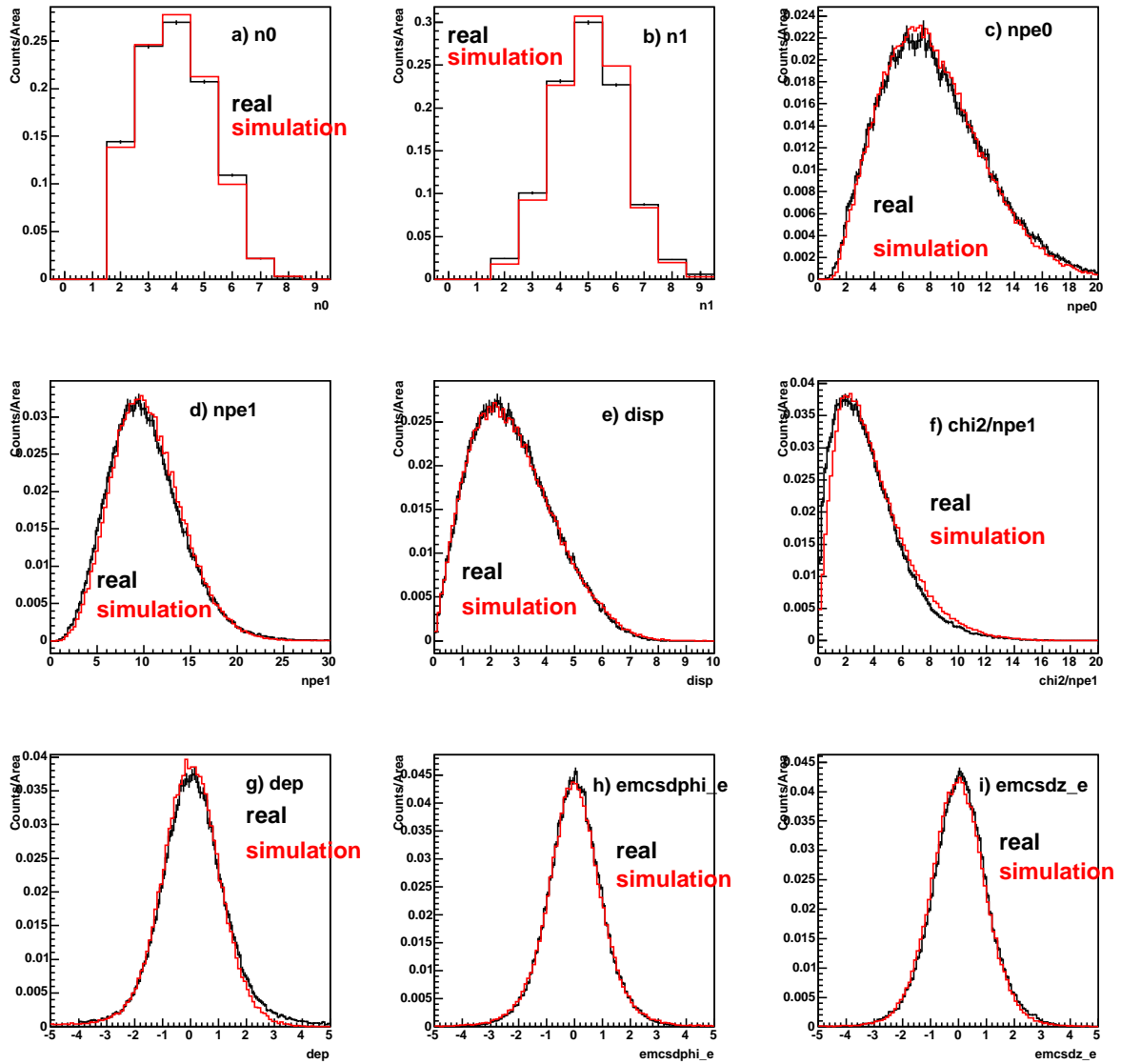


Figure 5.21: eID parameters from conversion pairs (black) and simulation (red). a) n_0 , b) n_1 , c) npe_0 , d) npe_1 , e) $disp$, f) χ^2/npe_1 , g) dep , h) $emcsdphi_e$ and i) $emcsdz_e$.

Chapter 6

Data Analysis 2 - Yield extraction

In this chapter, definition of the invariant yield of J/ψ and nuclear modification factor are described, and the procedures to extract J/ψ yield in Au+Au collisions and the analysis methods are explained. This chapter is organized as follows. Definition of J/ψ yield and nuclear modification factor are described in Sec. 6.1, centrality determination is explained in Sec. 6.2, event selection used in this analysis is described in Sec. 6.3, identification of J/ψ is explained in Sec. 6.4 and the analysis of the correction factors such as detection efficiency of J/ψ is written in Sec. 6.5.

6.1 Invariant Yield and Nuclear Modification Factor

J/ψ is identified using the invariant mass of e^+e^- pairs calculated with the following equation.

$$m_{e^+e^-} = \sqrt{(E_{e^+} + E_{e^-})^2 - (\mathbf{p}_{e^+} + \mathbf{p}_{e^-})^2}, \quad (6.1)$$

where E_{e^-} and E_{e^+} are the total energy and \mathbf{p}_{e^-} and \mathbf{p}_{e^+} are the momentum of electron and positron, respectively.

The invariant cross section of J/ψ as a function of p_T is written as follows.

$$E \frac{d^3\sigma_{J/\psi}}{dp^3} = \frac{d^3\sigma_{J/\psi}}{p_T dy dp_T d\phi} = \frac{1}{2\pi p_T} \frac{d^2\sigma_{J/\psi}}{dp_T dy}, \quad (6.2)$$

where $p_T = \sqrt{p_x^2 + p_y^2}$ is the transverse momentum of J/ψ and y and ϕ is the rapidity and azimuthal angle of J/ψ , respectively.

Invariant cross section of J/ψ decaying to e^+e^- pairs can be extracted experimentally as follows:

$$\frac{1}{2\pi p_T} B \frac{d^2\sigma_{J/\psi}}{dp_T dy} = \frac{1}{2\pi p_T} \frac{N_{J/\psi}(p_T)}{\int L dt \Delta y \Delta p_T \epsilon_{tot}(p_T)}, \quad (6.3)$$

where the $N_{J/\psi}$ is the number of identified J/ψ via e^+e^- decay channel, $\epsilon_{tot}(p_T)$ is the overall detection efficiency for the J/ψ as described in Sec. 6.5, $\int L dt$ is integrated luminosity recorded with the minimum bias trigger, Δy is the rapidity bin and set to $\Delta y = 1$, Δp_T is the p_T bin

width and B is the branching ratio ($5.94 \pm 0.10\%$ from PDG [19]). The integrated luminosity $\int Ldt$ can be expressed as follows:

$$\int Ldt = \frac{N_{evt}}{\sigma_{\text{Au+Au}} \epsilon_{MB-trigger}}, \quad (6.4)$$

where N_{evt} is the number of recorded events, $\sigma_{\text{Au+Au}}$ is the cross section of inelastic Au+Au collisions (6.85 ± 0.54 b [116]) and $\epsilon_{MB-trigger}$ is the minimum bias trigger efficiency ($92.2^{+2.5}_{-3.0}\%$ [118, 119, 120]).

The invariant yield of J/ψ is defined as follows:

$$\frac{1}{2\pi p_T} B \frac{d^2 N_{J/\psi}}{dp_T dy} = \frac{1}{2\pi p_T} \frac{N_{J/\psi}(p_T)}{N_{evt} \Delta y \Delta p_T \epsilon_{tot}(p_T)}, \quad (6.5)$$

$$= \frac{1}{2\pi p_T} \frac{N_{J/\psi}(p_T)}{(\int Ldt \sigma_{\text{Au+Au}} \epsilon_{eff}^{MB-trigger}) \Delta y \Delta p_T \epsilon_{tot}(p_T)}, \quad (6.6)$$

$$= \frac{1}{\sigma_{\text{Au+Au}} \epsilon_{eff}^{MB-trigger}} \times \frac{1}{2\pi p_T} B \frac{d^2 \sigma_{J/\psi}}{dp_T dy}. \quad (6.7)$$

Then the integrated J/ψ yield is calculated as follows:

$$B \frac{dN_{J/\psi}}{dy} = \sum_{p_T} B \frac{d^2 N_{J/\psi}}{dp_T dy} \Delta p_T \quad (6.8)$$

When the statistics of J/ψ is not enough to extract the invariant yield as a function of p_T , the integrated invariant yield can be extracted as follows:

$$B \frac{dN_{J/\psi}}{dy} = \frac{N_{J/\psi}}{N_{evt} \Delta y \langle \epsilon_{tot} \rangle}, \quad (6.9)$$

where the $\langle \epsilon_{tot} \rangle$ is the mean of the overall J/ψ detection efficiency averaged over assumed J/ψ p_T distribution ($d^2 N/dp_T dy$).

Nuclear modification factor (R_{AA}) is widely used to quantify the medium effects in high energy A+A collisions. The definition of R_{AA} is written as follows,

$$R_{AA}(p_T) = \frac{B d^2 N_{J/\psi} / dp_T dy_{\text{Au+Au}}}{B d^2 \sigma_{J/\psi} / dp_T dy_{p+p} \times T_{AB}}, \quad (6.10)$$

$$R_{AA} = \frac{B dN_{J/\psi} / dy_{\text{Au+Au}}}{B d\sigma_{J/\psi} / dy_{p+p} \times T_{AB}}, \quad (6.11)$$

$$T_{AB} = \frac{\langle N_{col} \rangle}{\sigma_{NN}}, \quad (6.12)$$

where T_{AB} is called as nuclear overlap function and is given by the ratio of the number of inelastic nucleon-nucleon collisions N_{col} to the cross section of inelastic nucleon-nucleon collision σ_{NN} . N_{col} is given by the Glauber model calculations as explained Sec. 6.2. R_{AA} is the ratio of the J/ψ yield in Au+Au collisions to the J/ψ yield in $p+p$ collisions scaled by the average number

of nucleon-nucleon collisions. If there is no medium effects on J/ψ production, production of J/ψ in $A + A$ collisions can be described in terms of the incoherent production of J/ψ in independent nucleon-nucleon collisions and R_{AA} is expected to be 1. Since $\langle N_{col} \rangle$ is sensitive to the collision geometry between two colliding nuclei, R_{AA} can be studied as a function of collision geometry, which has important information on the formation of QGP.

The analysis scheme is summarized as follows:

1. Event classification based on collision geometry

This relates to the determination of N_{evt} . Au+Au collision events were classified into some event classes based on the correlation between measured charge with the BBCs and measured energy with the ZDCs. Impact parameter, the number of nucleons participating the collisions and the number of nucleon-nucleon collisions were extracted using Glauber model calculation from the comparison of the correlation between the measured charge with BBCs and measured energy with ZDCs. This is discussed in Sec. 6.2.

2. Run selection for J/ψ analysis

This also relates to the determination of N_{evt} . During the Year-4, there were some runs which had problems on high voltage or front-end electronics in subsystems. These problems led to loss of the acceptance for electrons. These runs were selected by extracting the number of electrons per event for each run and by looking at the hit distributions at each detector as a cross-check. This is described in Sec. 6.3.

3. Identification of J/ψ

This relates to $N_{J/\psi}$. Invariant mass was calculated for any e^+e^- pairs and invariant mass spectrum was obtained. Background in the mass spectrum is composed of two components. One is from uncorrelated e^+e^- pairs and was studied using event mixing method. The other is from correlated e^+e^- pairs such as $D\bar{D}$, $B\bar{B}$ and Drell-Yan pairs and was studied from the lower and higher mass range of J/ψ peak in invariant mass spectrum and from PYTHIA as a cross-check. This is described in Sec. 6.4.

4. Correction factors

This relates to the total detection efficiency of J/ψ ϵ_{tot} . Single $J/\psi \rightarrow e^+e^-$ Monte Carlo simulation was performed to evaluate detection efficiency of J/ψ . Multiplicity dependence of the efficiency was studied by merging simulated e^+e^- tracks from J/ψ into the real data (embedding simulation). In both simulation study, detector response was tuned to match that in the real data and the comparison of J/ψ mass spectrum between real and simulation was done. This is described in Sec. 6.5.

6.2 Event Classification

In this section, a Glauber model and event classification method are described. Impact parameter of two colliding nuclei, the number of participant nucleons and the number of nucleon-nucleon collisions which characterize each event class, are calculated using the Glauber model.

6.2.1 Glauber model

As already described in Sec. 1.3.1, the impact parameter b between two colliding nuclei controls the number of participant nucleons in collisions and the number of inelastic nucleon-nucleon collisions in participant region. The number of participants N_{part} and the number of inelastic nucleon-nucleon collisions N_{col} in a collision with an impact parameter b can be calculated using the Glauber model [121]. The Glauber model is a semi-classical model and describes the dynamics of the nucleus-nucleus collision process based on the geometry of the nucleons inside the colliding nucleus and the geometrical configuration of two colliding nuclei.

The nucleons in each colliding nucleus are distributed according to the Woods-Saxon distribution.

$$\rho(r) = \rho_0 \frac{1}{1 + \exp\left(\frac{r-R}{a}\right)}, \quad (6.13)$$

where ρ_0 is the normal nuclear density, R is the radius and a is diffuseness parameter. For Au nucleus, $R \simeq 6.38$ fm and $a \simeq 0.54$ fm [122]. Probability for the occurrence of nucleon-nucleon collision is calculated as follows, when the nucleus A and nucleus B along the z-axis have the impact parameter b :

$$T(b)\sigma_{NN} = \int \rho_A(b_A, z_A) db_A dz_A \rho_B(b_B, z_B) db_B dz_B \delta(b - b_A - b_B) \sigma_{NN}, \quad (6.14)$$

where $T(b)$ is called as nuclear thickness function and $\rho_{A,B}(b_{A,B}, z_{A,B})$ is the probability function of finding a nucleon in the nucleus A, B at the position $(b_{A,B}, z_{A,B})$. The probability for the occurrence of n inelastic nucleon-nucleon collisions at an impact parameter b is given using $T(b)$ as follows:

$$P(n, b) = \binom{AB}{n} [T(b)\sigma_{NN}]^n [1 - T(b)\sigma_{NN}]^{AB-n}. \quad (6.15)$$

The total probability for the occurrence of at least one inelastic collision at the impact parameter b is

$$\frac{d\sigma_{AB}}{db} = \sum_{n=1}^{AB} P(n, B) = 1 - [1 - T(b)\sigma_{NN}]^{AB}. \quad (6.16)$$

Therefore the total inelastic cross section σ_{AB} can be described as follows:

$$\sigma_{AB} = \int db (1 - [1 - T(b)\sigma_{NN}]^{AB}). \quad (6.17)$$

Taking σ_{NN} as =42 mb, the inelastic cross section σ_{Au+Au} was calculated to be $\simeq 6.9$ barn [19, 116]. The average number of inelastic nucleon-nucleon collisions at the impact parameter b can be expressed as follows:

$$N_{col} = \langle n(b) \rangle = \sum n P(n, b) = AB T(b) \sigma_{NN} \quad (6.18)$$

6.2.2 Centrality determination

Centrality corresponds to the measured fraction of the total inelastic cross section of Au+Au collisions, which has the close relation to the impact parameter of two colliding nuclei. Centrality of 0% and 100% corresponds to the impact parameter of 0 fm (“central collisions”) and $2R$ fm (“peripheral collisions”), respectively, where the R is the radius of Au nuclei.

The total energy measured by the ZDC and the total charge measured by the BBC are sensitive to the impact parameter of the Au+Au collisions. The BBC measures the number of created charged particles at forward rapidity. The number of created charged particles has a positive correlation to the number of participants in the collisions. The ZDC measures the energy from the spectator neutrons that are not bounded in deuterons or heavier fragments, which has a negative correlation to the number of participants.

Figure 6.1 shows the correlation between the total charge measured by BBC and total energy measured by ZDC in Au+Au collisions, where the total charge and total energy are normalized to their maximum value. Centrality of the event, which was defined to be the fraction of the events from most central collision (0%), was determined by “clock-method”. Taking the origin at $(Q_{BBC}/Q_{BBC}^{max}, E_{ZDC}/E_{ZDC}^{max}) = (0.15, 0)$ and the angle of the point from the origin, clock-method categorized the event samples into the groups such that each 1% centrality class had the same number of events with each other. The boundaries of the centrality class of 0-5/5-10/10-15/15-20/20-30/30-40/40-60/60-93% were shown as solid lines in Fig. 6.1.

6.2.3 Glauber simulation

Impact parameter b , N_{col} , N_{part} and the nuclear overlap function T_{AB} in Au+Au collisions were evaluated for each centrality class by using the Glauber model calculation [116]. Glauber model calculation was performed by using the following parameterizations.

- Woods-Saxon nuclear radius $R = 6.38_{-0.13}^{+0.27}$ fm.
- surface thickness $a = 0.54 \pm 0.01$.
- N-N inelastic cross section $\sigma_{NN} = 42 \pm 3$ mb.

Here, the determination of $\langle b \rangle$, $\langle N_{part} \rangle$, $\langle N_{col} \rangle$ and T_{AB} for each centrality class was done by using $R = 6.38$ fm, $a = 0.54$ and $\sigma_{NN} = 42$ mb. The errors of R , a and σ_{NN} were used to estimate the systematic error of these quantities [116].

After the inelastic nucleon-nucleon collisions and the generation of the secondary particles, the total charge by the BBC and the total energy by the ZDC were extracted, where the response of BBC and ZDC were tuned to match them in real data. The correlation between Q_{BBC}/Q_{BBC}^{max} and E_{ZDC}/E_{ZDC}^{max} in Glauber model is shown in Fig. 6.2.

Table 6.1 is the summary of the results from Glauber model calculation for the impact parameter b , $\langle N_{part} \rangle$, $\langle N_{col} \rangle$ and nuclear overlap function T_{AB} in each centrality class.

class [%]	b [fm]	$\langle N_{part} \rangle$	$\langle N_{col} \rangle$	T_{AB} (mb $^{-1}$)
0-5	2.3 ± 0.1	351.4 ± 2.9	1065.4 ± 105.3	25.37 ± 1.77
5-10	4.1 ± 0.2	299.0 ± 3.8	845.4 ± 82.1	20.13 ± 1.36
10-15	5.2 ± 0.3	253.9 ± 4.3	672.4 ± 66.8	16.01 ± 1.15
15-20	6.2 ± 0.2	215.3 ± 5.3	532.7 ± 52.1	12.68 ± 0.86
20-25	7.0 ± 0.4	181.6 ± 5.6	421.8 ± 46.8	10.04 ± 0.85
25-30	7.8 ± 0.3	151.5 ± 4.9	325.6 ± 32.4	7.75 ± 0.58
30-35	8.4 ± 0.4	125.7 ± 4.9	251.0 ± 25.9	5.98 ± 0.48
35-40	9.1 ± 0.4	102.7 ± 4.3	188.6 ± 20.6	4.49 ± 0.43
40-45	9.7 ± 0.4	82.9 ± 4.3	139.4 ± 15.4	3.32 ± 0.31
45-50	10.2 ± 0.4	65.9 ± 3.4	101.3 ± 12.1	2.41 ± 0.25
50-55	10.7 ± 0.4	51.6 ± 3.2	72.1 ± 10.5	1.72 ± 0.23
55-60	11.2 ± 0.4	39.4 ± 3.5	49.9 ± 9.6	1.19 ± 0.23
60-65	11.7 ± 0.5	29.8 ± 4.1	34.4 ± 8.7	0.82 ± 0.21
65-70	12.1 ± 0.5	21.5 ± 3.8	22.6 ± 6.6	0.54 ± 0.16
70-75	12.6 ± 0.5	15.5 ± 3.4	14.8 ± 5.1	0.35 ± 0.12
75-80	13.0 ± 0.6	11.3 ± 2.6	9.9 ± 3.3	0.24 ± 0.08
80-93	14.1 ± 0.6	6.3 ± 1.2	4.9 ± 1.2	0.12 ± 0.03
0-10	3.2 ± 0.2	325.2 ± 3.3	955.4 ± 93.6	22.75 ± 1.56
10-20	5.7 ± 0.3	234.6 ± 4.7	602.6 ± 59.3	14.35 ± 1.00
20-30	7.4 ± 0.3	166.6 ± 5.4	373.8 ± 39.6	8.90 ± 0.72
30-40	8.7 ± 0.4	114.2 ± 4.4	219.8 ± 22.6	5.23 ± 0.44
40-60	10.4 ± 0.4	60.0 ± 4.0	90.6 ± 12.0	2.16 ± 0.26
60-93	13.1 ± 0.6	14.5 ± 2.5	14.5 ± 4.0	0.35 ± 0.10
0-20	4.5 ± 0.3	279.9 ± 4.0	779.0 ± 75.2	18.5 ± 1.27
20-40	8.1 ± 0.4	140.3 ± 3.8	297.0 ± 30.4	7.06 ± 0.58
40-93	12.1 ± 0.5	34.4 ± 1.7	48.1 ± 5.3	1.04 ± 0.16
0-93 (MB)	9.5 ± 0.4	109.1 ± 4.1	257.8 ± 25.4	6.14 ± 0.45

Table 6.1: Results of the Glauber calculation in Au+Au collisions at $\sqrt{s_{NN}} = 200$ GeV showing the average b , N_{part} , N_{col} and T_{AB} for each centrality class. Error is the systematic error [116].

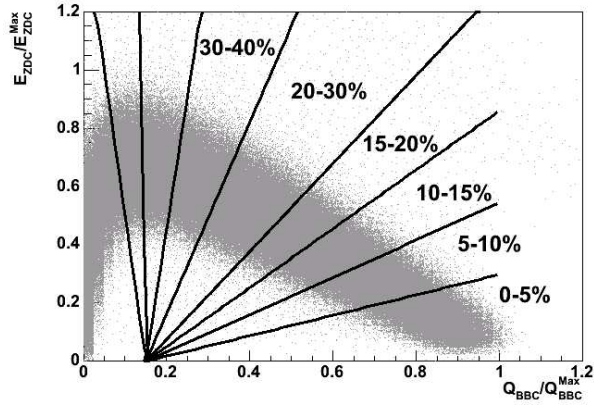


Figure 6.1: The correlation between the fraction of BBC charge Q_{BBC}/Q_{BBC}^{max} and the fraction of ZDC energy E_{ZDC}/E_{ZDC}^{max} . The boundaries for the classification of the event into the centrality class of 0-5/5-10/10-15/15-20/20-30/30-40/40-60/60-93% were shown.

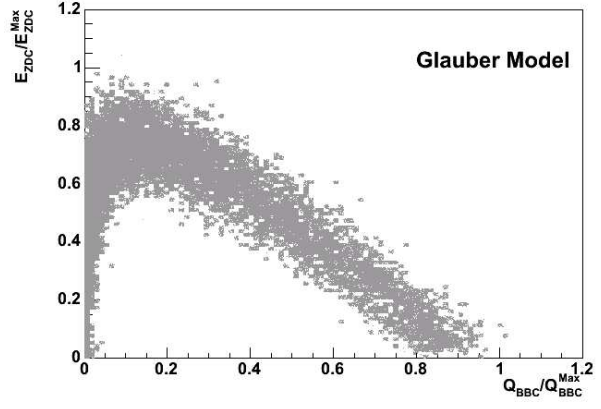


Figure 6.2: The correlation between the fraction of BBC charge Q_{BBC}/Q_{BBC}^{max} and the fraction of ZDC energy E_{ZDC}/E_{ZDC}^{max} in Glauber simulation.

6.3 Run Selection for the J/ψ Analysis

Run selection for $J/\psi \rightarrow e^+e^-$ analysis was done to find out the problematic runs on the detector acceptance, to select the good runs to be analyzed and to avoid the large efficiency fluctuations for the J/ψ over whole Year-4 data.

6.3.1 Fluctuation of the electron yield

To select the good runs, electron yield in each run was checked. Here the electron yield is defined as follows:

$$N_e \times N_p = n_e/N_{evt}(\text{East}) \times n_p/N_{evt}(\text{West}) + n_e/N_{evt}(\text{West}) \times n_p/N_{evt}(\text{East}), \quad (6.19)$$

where n_e , n_p and N_{evt} is the number of electrons, positrons and the number of events, respectively. Since most of an electron and a positron from J/ψ decay fall into the different arm, n_e and n_p in different arm was multiplied to check the run-by-run variation of the electron-positron coincidence yield.

All the runs were classified into 10 groups. Table 6.2 shows the run group, run range, number of runs and number of minimum bias triggered events (“MB events”). In G1 runs, two PbG1 sectors (E0 and E1 sector) were off. In G2 and G3 runs, one PbG1 (E0 sector) was off. The configuration of the central magnetic was “++” from G1 to G6 and “--” from G7 to G10.

Figure 6.3 shows the $N_e \times N_p$ as a function of run number. Closed symbols represent the runs categorized to be the good runs used in this analysis. Open symbols are the bad runs and

run group	run range	number of runs	number of MB events	Note
G1	108280 - 108714	17	10066668	EMCal E0+E1 off
G2	108769 - 110236	103	61165791	EMCal E0 off
G3	111350 - 1113528	48	17550349	EMCal E0 off
G4	111603 - 113528	112	134445218	
G5	113529 - 114330	68	64528590	
G6	114331 - 115780	82	117351255	
G7	115979 - 116691	65	100382161	"- -" field
G8	116701 - 118100	126	172950621	"- -" field
G9	118100 - 120581	157	252565118	"- -" field
G10	121113 - 122223	61	65960535	"- -" field

Table 6.2: run group, run range, number of runs, number of MB events

are not used in this analysis. It was checked that these bad runs were due to the high voltage problems of subsystems (suddenly tripped) or large hot channels in front-end electronics of subsystems. The middle line shown in Fig. 6.3 corresponds to $\langle N_e \times N_p \rangle$ calculated for each run group and the top and bottom lines are the threshold lines to select the good runs, where the threshold lines correspond to $3, 4$ or $5 \times RMS$ of $\langle N_e \times N_p \rangle$ in each run group. Criterion to select $3, 4$ or $5 \times RMS$ of $N_e \times N_p$ was determined iteratively such that the RMS over $\langle N_e \times N_p \rangle$ calculated for selected good runs becomes less than 4%.

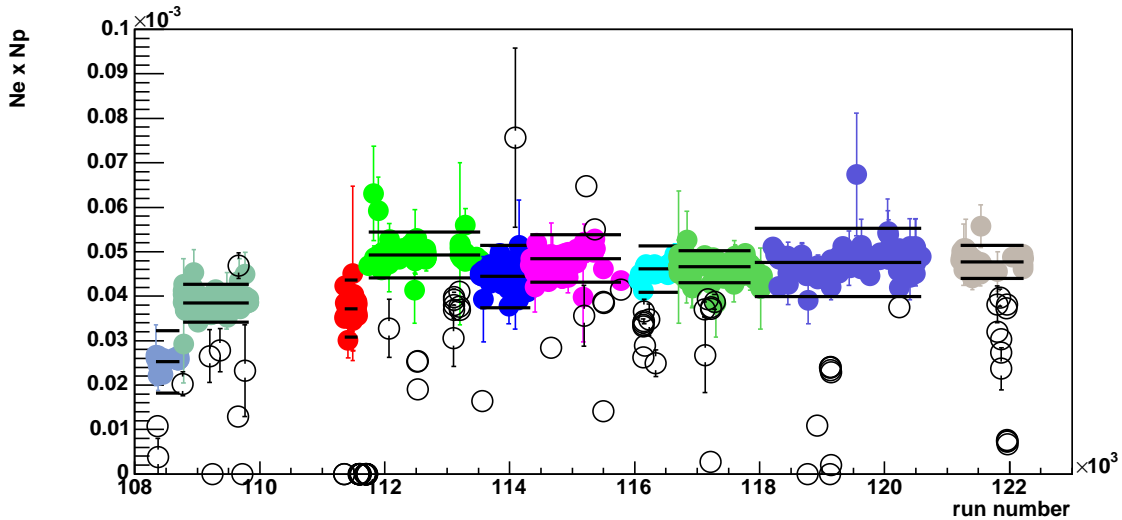


Figure 6.3: $N_e \times N_p$ as a function of run number. Closed symbols are the good runs and open are bad runs. The lines corresponds to $\langle N_e \times N_p \rangle$ and the threshold to select the good runs.

The number of events used in this analysis for each centrality class after the good run selection are summarized in Table 6.3. G1 runs were removed in this analysis since E0 and E1

sector were off during this run period and the statistics in this run period could be negligible.

centrality	E0 off runs (G2-G3)	E0 on runs (G4-G10)
0-93% (minimum bias)	82995530	906992683
0-20%	17977459	195598809
20-40%	17945970	195098190
40-93%	47072101	516295684
0-10%	8970682	97763498
10-20%	9006777	97835311
20-30%	8978735	97570058
30-40%	8967235	97528132
40-60%	17978589	194891662
60-93%	29093512	321404022
0-5%	4471295	48925269
5-10%	4499387	48838229
10-15%	4505641	48936608
15-20%	4501136	48898703

Table 6.3: The number of events used in this analysis after the good run selection.

6.4 Signal Extraction of J/ψ

This chapter describes the pair cuts applied to extract the number of J/ψ s and the method for signal extraction of J/ψ such as background estimation in invariant mass spectrum.

6.4.1 Cut parameters used in signal extraction

Following is the cut parameters used in the J/ψ analysis. One is “standard cuts” used for MB and for centrality up to 40%. The other is “loose cuts” used for the centrality larger than 40%.

Standard cuts

1. Tracks $|z_{vtx}| \leq 30$ cm
2. Tracks $n0 \geq 2$ for the RICH
3. Tracks $n1 \geq 4$ for the RICH
4. Tracks $dep > -2.5$
5. Tracks $\sqrt{emcsdphi_e^2 + emcsdz_e^2} < 2.5$

Loose cuts

1. Tracks $|z_{vtx}| \leq 30$ cm
2. Tracks $n0 \geq 2$ for the RICH
3. Tracks $n1 \geq 2$ for the RICH
4. Tracks $dep > -2.5$
5. Tracks $\sqrt{emcsdphi_e^2 + emcsdz_e^2} < 4$

6.4.2 Additional pair cut

DC ghost tracks

There were many reconstructed tracks which have the almost same DC hit positions. This was due to the fact that some of the hit positions at the DC were participated in the reconstruction of tracks many times, that the tracks were reconstructed multiple times and that there are 7% left-right ambiguity in the hit reconstruction [104].

Figure 6.4 shows the difference in reconstructed DC ϕ position (left) and DC β position (right) between any two same-charge tracks extracted from real data (black) and mixed event background (red), where mixed event was described later and there was no correlation between any two tracks in mixed event. There can be seen a strong peak at $\Delta\phi$ and $\Delta\beta$ of 0 in real event, which means that those two tracks has strong correlation and share the same DC hit region. These tracks is called DC ghost tracks. The additional pair cuts applied to remove

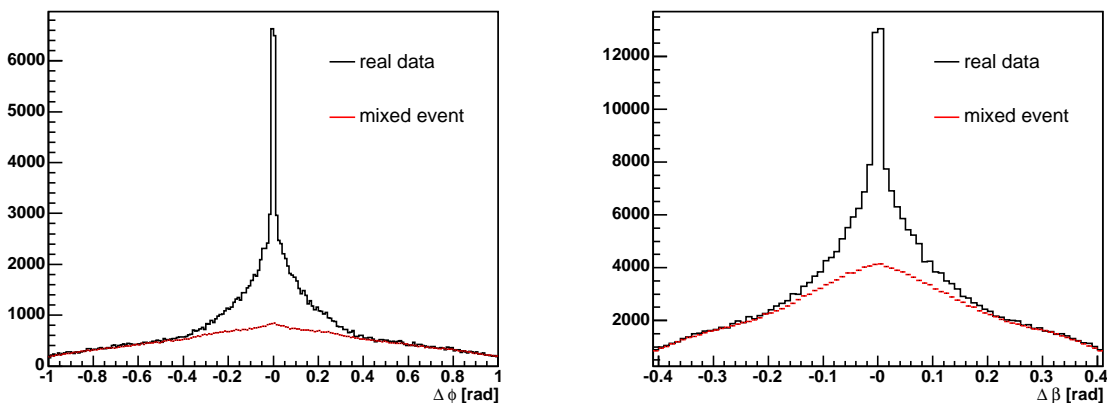


Figure 6.4: Left : Difference in DC ϕ position between any two same-charge tracks. Right : Difference in DC β position between any two same-charge tracks. Black was extracted from each event, while red was extracted from event mixing method as described later and no correlation between any two pairs in event mixing method.

these ghost pairs were as follows:

$$\text{Pair Cut} = \overline{(|\Delta\phi| \leq 0.3 \cap |\Delta\beta| \leq 0.1)}. \quad (6.20)$$

RICH ring sharing

If two tracks outside the DC are parallel each other, the track projection points at RICH PMT plane become close each other. This leads to share the same hit PMTs even if one of the tracks is hadron and the other is electron. This phenomenon is called RICH ring sharing. Post field opening angle $PFOA$ is the variable to quantify how parallel two tracks are with each other and the definition of $PFOA$ is as follows:

$$\vec{A}^{1,2} = (A_x^{1,2}, A_y^{1,2}, A_z^{1,2}) \quad (6.21)$$

$$A_x^{1,2} = \sin(\beta^{1,2}) \times \cos(\phi^{1,2} - \alpha^{1,2}) \quad (6.22)$$

$$A_y^{1,2} = \sin(\beta^{1,2}) \times \sin(\phi^{1,2} - \alpha^{1,2}) \quad (6.23)$$

$$A_z^{1,2} = \cos(\beta^{1,2}) \quad (6.24)$$

$$\cos(PFOA) = \vec{A}^1 \cdot \vec{A}^2, \quad (6.25)$$

where $\beta^{1,2}$, $\phi^{1,2}$ and $\alpha^{1,2}$ are the β position, DC ϕ position and α angle at DC reference radius for the track 1 and 2, respectively.

Figure 6.5 shows the distribution of $\cos(PFOA)$ for the same-charge tracks in each event (black) and mixed event (red). Right in Fig. 6.5 shows the zoom up distribution of $\cos(PFOA)$.

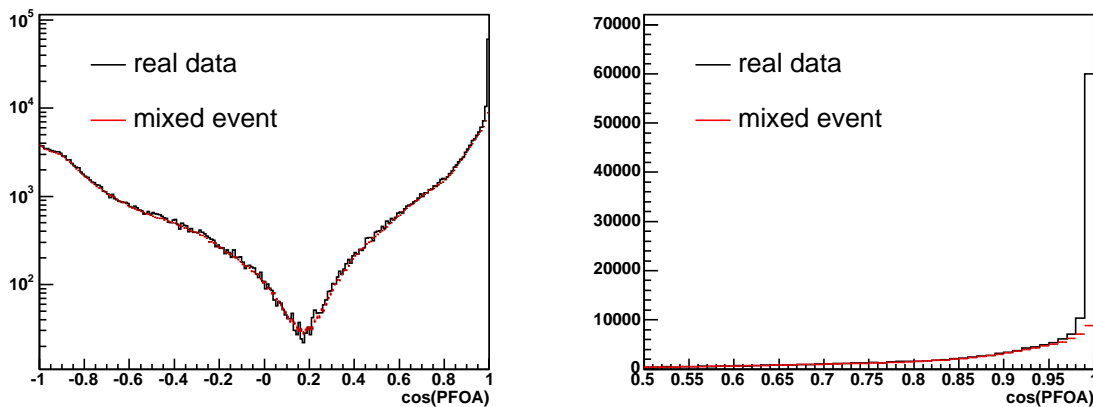


Figure 6.5: Left : The distribution of $\cos(PFOA)$ for the same-charge tracks in each event (black) and mixed event (red). Right : Zoom up distribution of $\cos(PFOA)$.

Strong correlation can be seen in $\cos(PFOA)$ around 1, while such correlation is not seen in mixed event. The additional pair cuts to remove ghost tracks at DC and ring sharing tracks were as follows:

$$\text{Pair Cut (ghost cut)} = \overline{[(|\Delta\phi| \leq 0.3 \cap |\Delta\beta| \leq 0.1) \cup \cos(PFOA) > 0.988]}. \quad (6.26)$$

6.4.3 Invariant mass spectrum

To identify J/ψ , invariant mass between any electron and positron pairs were calculated. Figure 6.6 shows the invariant mass spectrum in minimum bias (MB, 0-93% centrality) collisions. J/ψ peak can be seen clearly.

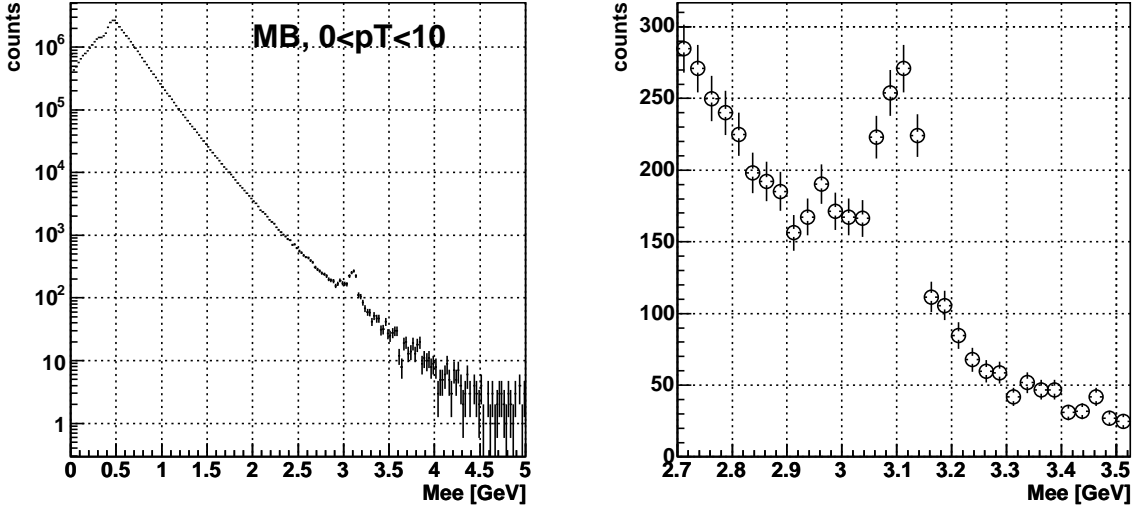


Figure 6.6: Left : Invariant mass spectra of unlike-sign pairs in MB data and all p_T region. Right : Invariant mass spectrum spectrum of unlike-sign pairs between $2.7 \leq M_{ee} \leq 3.5 \text{ GeV}/c^2$

6.4.4 Background evaluation

To calculate the number of J/ψ , it is necessary to subtract background from invariant mass spectrum. Here sources of the background and its evaluation method are listed as follows:

- Uncorrelated electron and positron pairs. (combinatorial background)
This is the background in the invariant mass spectrum derived from the pairs, where sources of electron and positron are independent with each other. Background from these uncorrelated e^+e^- pairs was evaluated using event mixing method.
- Correlated electron and positron pairs from $D\bar{D}$, $B\bar{B}$ and Drell-Yan production (continuum yield)
This is the physics background which exists under J/ψ mass peak and can not be removed by event mixing method. After subtracting the combinatorial background from invariant mass spectrum, contamination of the correlated pairs in the J/ψ mass region was evaluated from the subtracted mass spectrum below and above J/ψ mass region. Cross check of the continuum yield was done using PYTHIA event generator [123].

The number of J/ψ ($N_{J/\psi}$) was defined in terms of the number of e^+e^- pairs in unlike-sign ($N_{pair}^{unlike-sign}$) and mixed unlike-sign invariant mass spectrum ($N_{pair}^{mixed\ unlike-sign}$) and the contamination of the continuum yield (R_{cont}) as follows:

$$N_{pair} = N_{pair}^{unlike-sign} - N_{pair}^{mixed\ unlike-sign}, \quad (6.27)$$

$$R_{cont} = \frac{N_{cont}}{N_{pair}} \quad (6.28)$$

$$N_{J/\psi} = N_{pair}(1 - R_{cont}), \quad (6.29)$$

where N_{cont} is the number of continuum pairs under J/ψ mass region. The mass range used to calculate $N_{J/\psi}$ is $2.9 \leq M_{e^+e^-} \leq 3.3$ GeV/ c^2 , since this mass range gives the best significance of the J/ψ peak.

Event mixing

Event mixing method was used to subtract the uncorrelated combinatorial background, since it enables to keep statistical error of J/ψ from combinatorial background as low as possible.

To perform the event mixing, the events were classified based on the centrality (20 classes), z-vertex (20 classes) and the events were stored in the event buffer with $N_{buffer}(= 20)$ depth. Using the electrons (positrons) in an event and the positrons (electrons) in a different event in the event buffer, uncorrelated e^+e^- pairs were produced. Through this procedure, $2 \times N_{buffer}$ mixed events were produced for one event. Therefore the normalization factor of the mixed event distribution is given by $2 \times N_{buffer}$. However, this normalization factor is diluted since centrality has finite resolution. This dilution can be corrected using like-sign pairs and mixed like-sign pairs. The corrected normalization factor for mixed unlike-sign pairs R_{norm} is as follows:

$$R_{norm} = \frac{1}{2 \times N_{buffer}} \times R(\text{like} - \text{sign}/\text{mixed like} - \text{sign}), \quad (6.30)$$

where $R(\text{like} - \text{sign}/\text{mixed like} - \text{sign})$ is the ratio of like-sign invariant mass spectrum to the mixed like-sign invariant mass spectrum normalized according to $2 \times N_{buffer}$.

Cross check of this normalization factor was studied using toy model simulation, which is described in Appendix C in detail.

Left of Fig. 6.7 shows the invariant mass spectrum in MB collisions for unlike-sign pairs (black) and mixed unlike-sign pairs (red) after the normalization given by Eq. (6.30). Right of Fig. 6.7 shows the invariant mass spectrum after the subtraction of mixed unlike-sign invariant mass spectrum.

Figure 6.8, Figure 6.9, Figure 6.10 and Figure 6.11 show the invariant mass spectra of unlike-sign pairs (black) and mixed unlike-sign pairs (red) after the normalization expressed in Eq. (6.30) for each p_T bin (p_T range is written in the title of the histogram) and for the centrality of 0-93%, 0-20%, 20-40% and 40-93%, respectively. Invariant mass spectra for other centrality classes are shown in Appendix D.

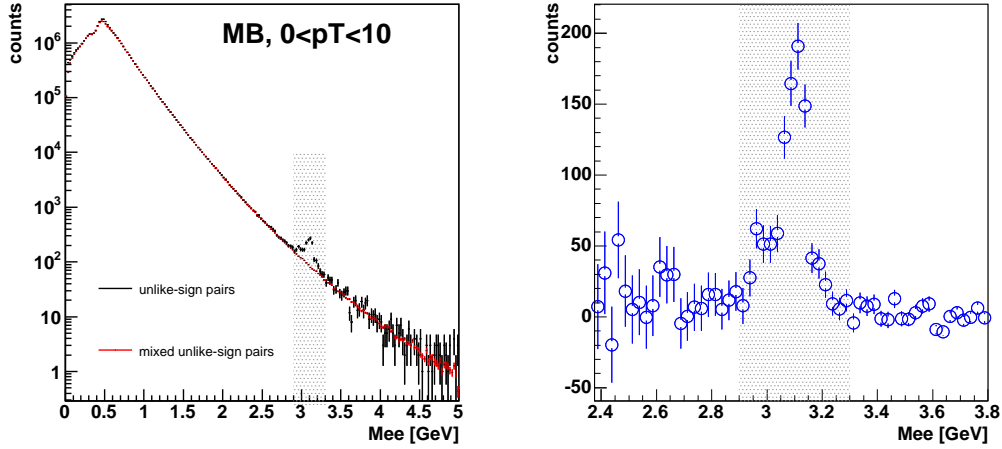


Figure 6.7: Left : Invariant mass spectra of unlike-sign pairs (black) and mixed unlike-sign pairs (red) in MB data and all p_T region. Right : Invariant mass spectrum after the subtraction by mixed unlike-sign pairs. Shaded area corresponds to the mass range for signal counting region, which gives best significance of J/ψ peak.

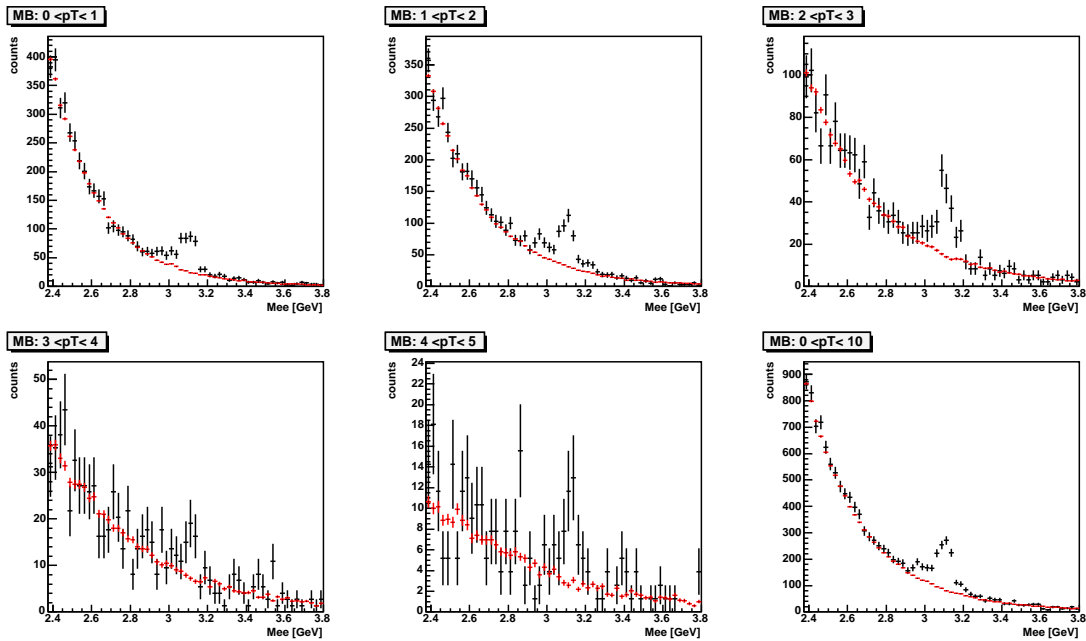


Figure 6.8: Invariant mass spectra of unlike-sign pairs (black) and mixed unlike-sign pairs (red) for 0-1/1-2/2-3/3-4/4-5/0-10 GeV/c p_T bin in MB data sample

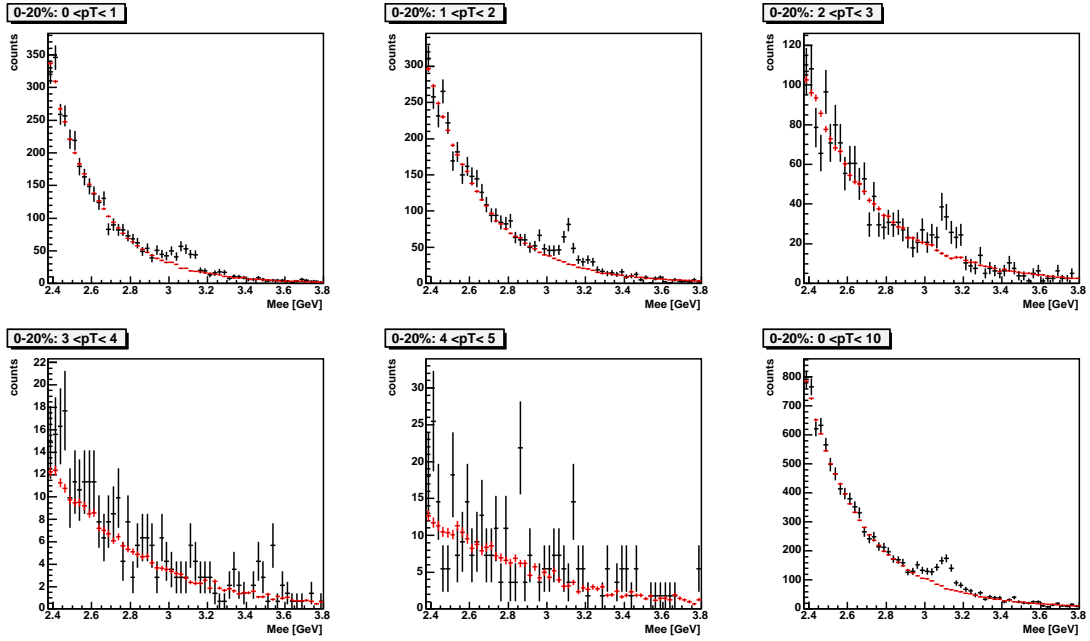


Figure 6.9: Invariant mass spectra of unlike-sign pairs (black) and mixed unlike-sign pairs (red) for 0-1/1-2/2-3/3-4/4-5/0-10 GeV/*c* *p_T* bin in 0-20% data sample

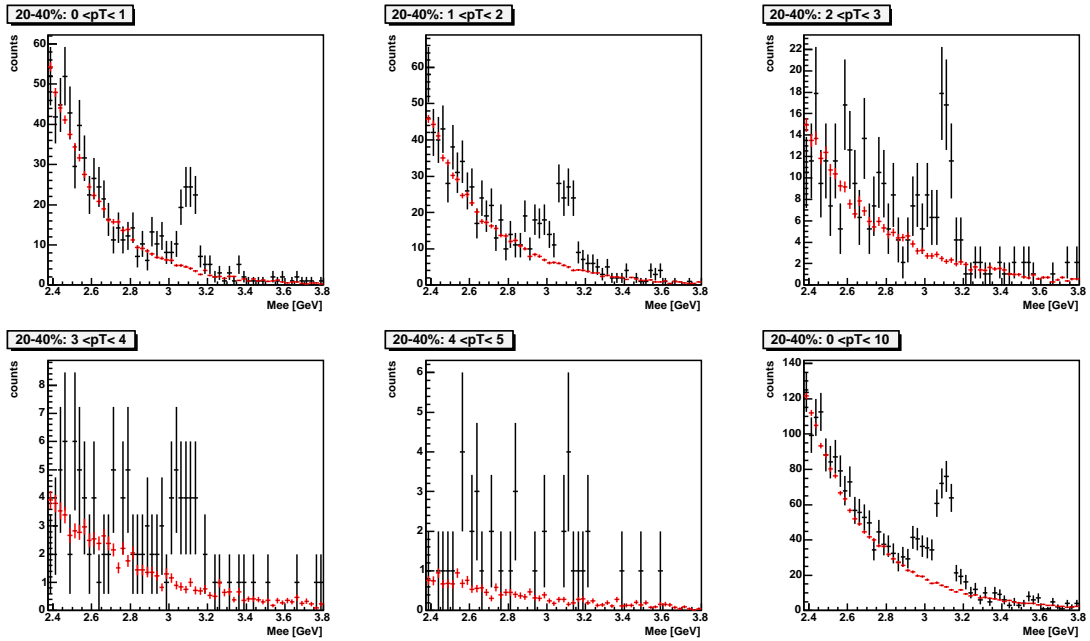


Figure 6.10: Invariant mass spectra of unlike-sign pairs (black) and mixed unlike-sign pairs (red) for 0-1/1-2/2-3/3-4/4-5/0-10 GeV/*c* *p_T* bin in 20-40% data sample

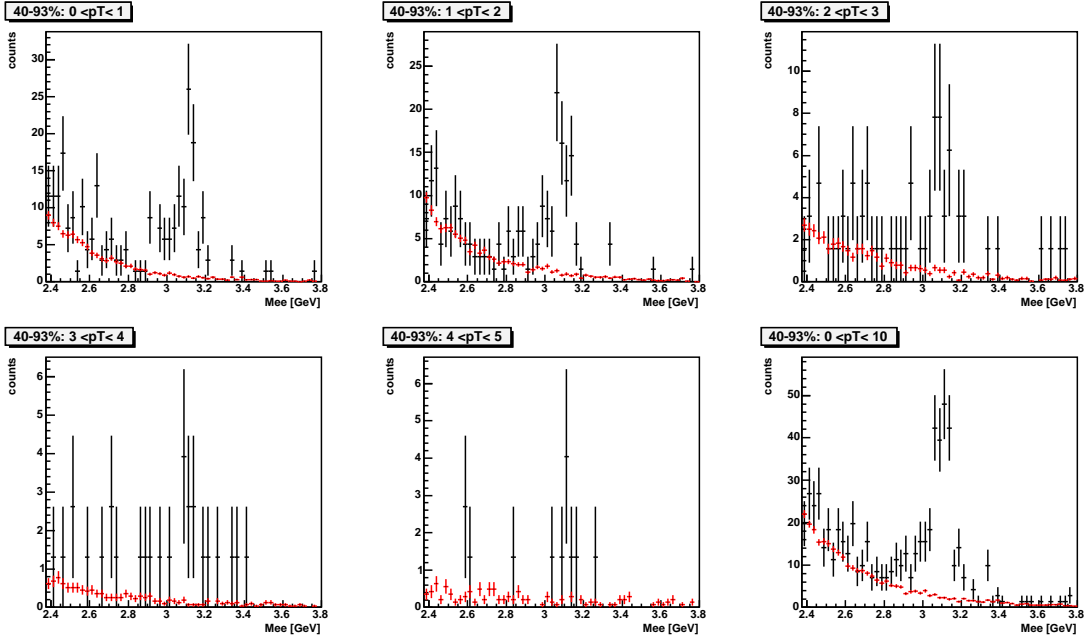


Figure 6.11: Invariant mass spectra of unlike-sign pairs (black) and mixed unlike-sign pairs (red) for 0-1/1-2/2-3/3-4/4-5/0-10 GeV/ c p_T bin in 40-93% data sample

Correction due to the continuum contribution

After the subtraction of combinatorial background, there should remain the residual continuum background from charm, beauty and Drell-Yan pairs. Continuum yield under J/ψ mass region was evaluated by fitting the subtracted invariant mass spectrum with exponential function below and above J/ψ mass region. Then the yield under J/ψ mass region was estimated by interpolating J/ψ mass region. PYTHIA [123] event generator was also used to do the cross-check of the continuum yield under J/ψ mass range. Figure 6.12 shows the e^+e^- invariant mass spectra in MB (Upper Left), 0-20% (Upper Right), 20-40% (Lower left) and 40-93% (Lower right). Black open symbols are from the real data. Blue closed symbols are the invariant mass spectrum from continuum pairs in PYTHIA ($c\bar{c}$ and $b\bar{b}$ events), where the PYTHIA invariant mass spectrum was corrected (1) such that the single electron distribution from heavy quark decays matches to the non-photonic single electron spectrum measured by PHENIX [56, 58] as shown in Fig. 6.13 and Fig. 6.14 and (2) according to the electron identification efficiency and centrality dependent efficiency for pairs. Both invariant mass spectra are in good agreement below and above the J/ψ mass region.

Fitting was performed to the invariant mass spectrum in real data, where the function was the linear combination of double Gaussian and $p_0 \times \exp(-p_1 M - p_2 M^2)$. The fitting results were shown in Fig. 6.12. Green is the fitting result with $p_0 \times \exp(-p_1 M - p_2 M^2)$ and double Gaussian, red and blue are the Gaussian shape. Black solid line is the continuum shape.

From the fitting results, continuum contribution $R_{cont} = N_{cont}/N_{pair}$ was calculated for $2.9 \leq M_{e^+e^-} \leq 3.3$, where N_{pair} corresponds to $N_{pair}^{unlike-sign} - N_{pair}^{mixed\ unlike-sign}$. The results are summarized in Table 6.4. The last error is the deviation of R_{cont} when the fitted parameter

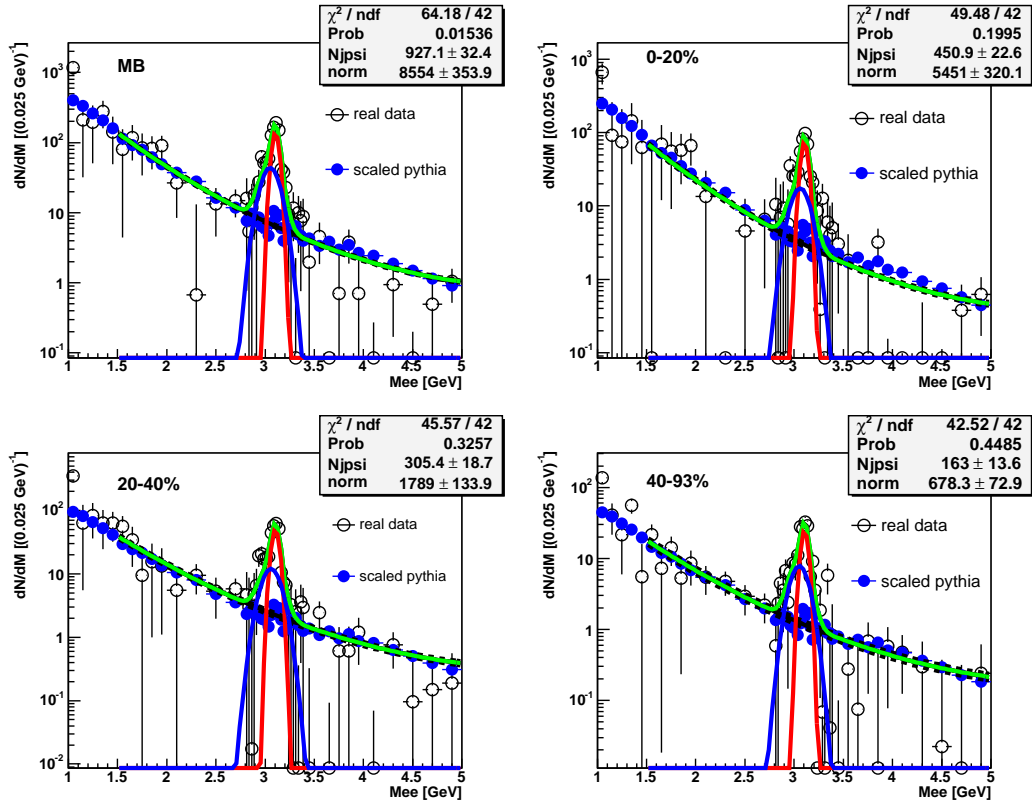


Figure 6.12: Invariant mass spectra in MB (Upper Left), 0-20% (Upper Right), 20-40% (Lower left) and 40-93% (Lower right). Black open symbols are from the real data and blue closed symbols are the mass spectrum from PYTHIA ($c\bar{c}$ and $b\bar{b}$ events). Green is the fitting result with the all the functions, red and blue are the Gaussian shape which correspond to the J/ψ signals, respectively. Black solid line is the continuum shape.

p_0 was moved according to $\pm 1 \sigma$ error.

Centrality	R_{cont} point \pm stat. \pm sys.
MB	$10.3\% \pm 1.1\% \pm 0.4\%$
0-20%	$9.7\% \pm 1.6\% \pm 0.6\%$
20-40%	$10.7\% \pm 1.9\% \pm 0.8\%$
40-93%	$10.8\% \pm 2.6\% \pm 1.1\%$

Table 6.4: R_{cont} for MB/0-20/20-40/40-93% centrality classes. The last error is the deviation of R_{cont} when the fitted parameter p_0 was moved according to $\pm 1 \sigma$ error of p_0 .

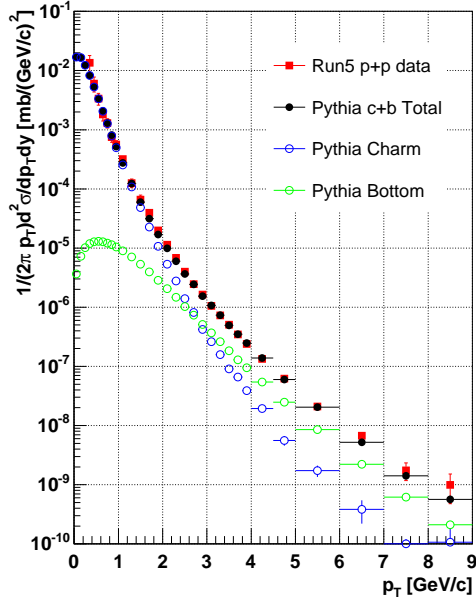


Figure 6.13: The invariant cross section of electrons from heavy quarks as a function of p_T in run5 p+p (red) and PYTHIA events (blue from $c\bar{c}$ events, green from $b\bar{b}$ events and black is summed up between them). The $\sigma_{b\bar{b}}$ is $8.32 \mu\text{b}$ and $\sigma_{c\bar{c}}$ is $567 \mu\text{b}$ [56].

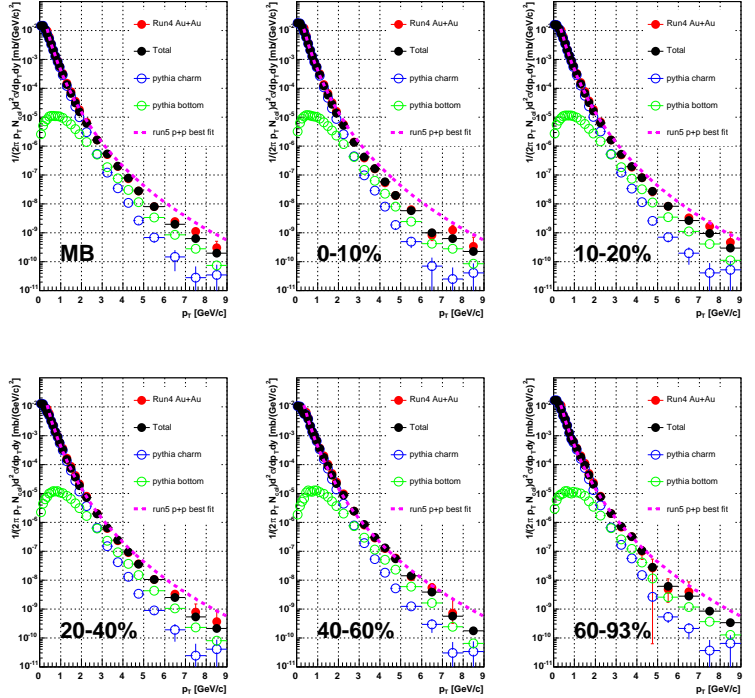


Figure 6.14: single electron spectrum in PYTHIA events for each centrality class. Open blue and open green are the single electron spectrum in $c\bar{c}$ and $b\bar{b}$ events, respectively. Black is the summation between them. Red points are the non-photonic single electron spectrum in Run4 Au+Au. Magenta is the run5 p+p best fit result [58].

6.5 Correction Factors

To obtain the invariant yield of J/ψ , total J/ψ detection efficiency $\epsilon_{tot}(p_T)$ in Eq. (6.5) was evaluated. Total J/ψ detection efficiency $\epsilon_{tot}(p_T)$ is composed as follows:

$$\epsilon_{tot}(p_T) = \epsilon_{det} \times \epsilon_{embed} \times \epsilon_{mass} \times \epsilon_{smearing} \times \epsilon_{run-by-run} \times \epsilon_{bin-width}, \quad (6.31)$$

where ϵ_{det} is the detection efficiency for the single J/ψ including the geometrical acceptance, reconstruction efficiency and electron identification efficiency, ϵ_{embed} is the multiplicity dependent efficiency for the J/ψ detection, ϵ_{mass} is the efficiency for the mass cut ($2.9 \leq M_{e^+e^-} \leq 3.3$ GeV/ c^2), $\epsilon_{smearing}$ is the correction factor of the smearing effect which is due to the momentum resolution, $\epsilon_{run-by-run}$ is the run-by-run efficiency for the J/ψ detection which is due to the fluctuation of the detector acceptance and $\epsilon_{bin-width}$ is the correction factor due to the bin width used in the calculation of the invariant p_T distribution.

To obtain these correction factors, Monte Carlo simulation of $J/\psi \rightarrow e^+e^-$ was performed. Table 6.5 is the summary of the conditions in the generation of J/ψ . The number of generated events were 10 M events.

Variables	Range	Conditions
z - vertex	$-40 \leq z \leq 40$ cm	Flat distribution
J/ψ p_T	$0 \leq p_T \leq 12$ GeV/ c	Flat distribution
rapidity	$-0.5 \leq y \leq 0.5$	Flat distribution
ϕ	$0 \leq \phi \leq 2\pi$	Flat distribution

Table 6.5: Summary of initial conditions for generated J/ψ

In this simulation, same dead channels of DC, PC, RICH and EMCAL in G9 runs were implemented. All the eID parameters were tuned to match the real data and comparison of the fiducial area and electron identification efficiency between real data and simulation were also done. They are described in Appendix E.

6.5.1 Single J/ψ detection efficiency ϵ_{det}

Definition of the single J/ψ detection efficiency is as follows:

$$\epsilon_{det}(p_T) = \frac{N_{J/\psi, reco}(p_T)}{N_{J/\psi, input}(p_T)}, \quad (6.32)$$

where $N_{J/\psi, input}$ is the number of generated J/ψ , and $N_{J/\psi, reco}$ is the number of reconstructed J/ψ , which are the number of e^+e^- pairs from J/ψ falling into the PHENIX acceptance, being reconstructed with the PHENIX reconstruction software and passing the electron identification cuts as used in the real data analysis.

Single J/ψ detection efficiency was calculated for two run groups. One is the efficiency for G2 and G3 groups, where EMCAL E0 sector was off and the other was the efficiency for the run groups from G4 to G10, where all the EMCAL sectors were in good operation.

Single J/ψ detection efficiency was calculated for the two cut sets used in real data analysis. One is for minimum bias (0-93% centrality) and centrality up to 40% (standard cuts) and the other is for the centrality of larger than 40% (loose cuts).

Figure 6.15 shows $\epsilon_{det}(p_T)$ as a function of input J/ψ p_T for two eID cut sets. Left is for standard cuts and right is for loose cuts. $\epsilon_{det}(p_T)$ with and without E0 sector are also shown in the same panel as open and closed symbols, respectively.

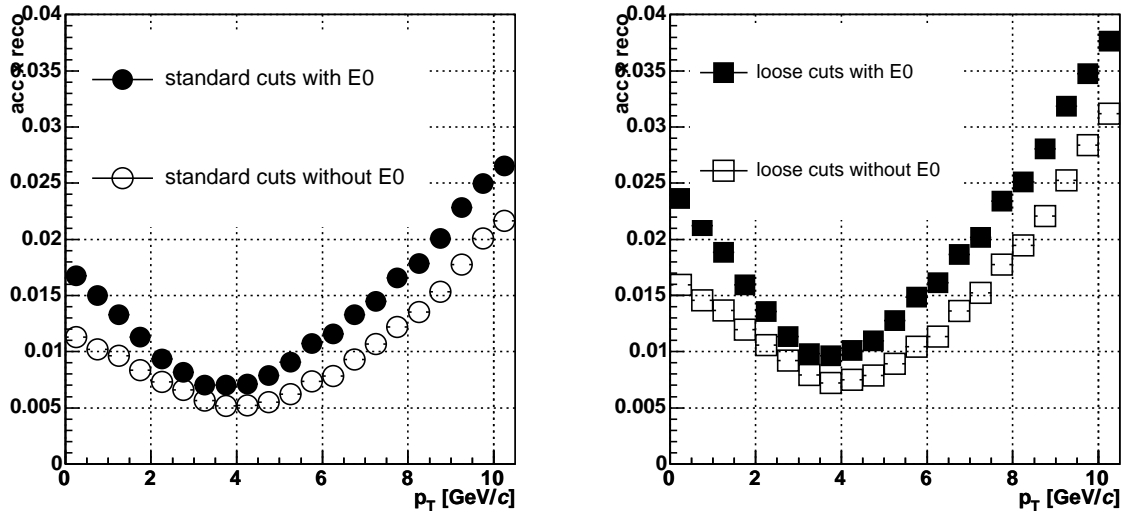


Figure 6.15: acceptance \times efficiency as a function of input J/ψ p_T . Left is for the standard cuts and right is for loose cuts. Open and closed symbols are the results with and without E0 sector, respectively.

6.5.2 Embedding efficiency ϵ_{embed}

In a high multiplicity condition, mis-reconstruction and mis-association of the tracks due to the high hit density in the detectors cause the inefficiency for J/ψ reconstruction. This multiplicity dependent efficiency, called as embedding efficiency, was extracted by embedding simulated tracks of e^+e^- pairs from J/ψ into the real data and by taking the ratio of the number of J/ψ reconstructed after the embedding to that before the embedding, where the same cuts were applied for the tracks before and after the embedding.

The embedding efficiency ϵ_{embed} is expressed as follows:

$$\epsilon_{embed} = \frac{N_{J/\psi}^{embed}}{N_{J/\psi}^{input}} \quad (6.33)$$

Figure 6.16 shows the embedding efficiency ϵ_{embed} as a function of J/ψ p_T for the centrality of 0-5/20-25/40-45/60-65%. It is seen from Fig. 6.16 that ϵ_{embed} have centrality dependence,

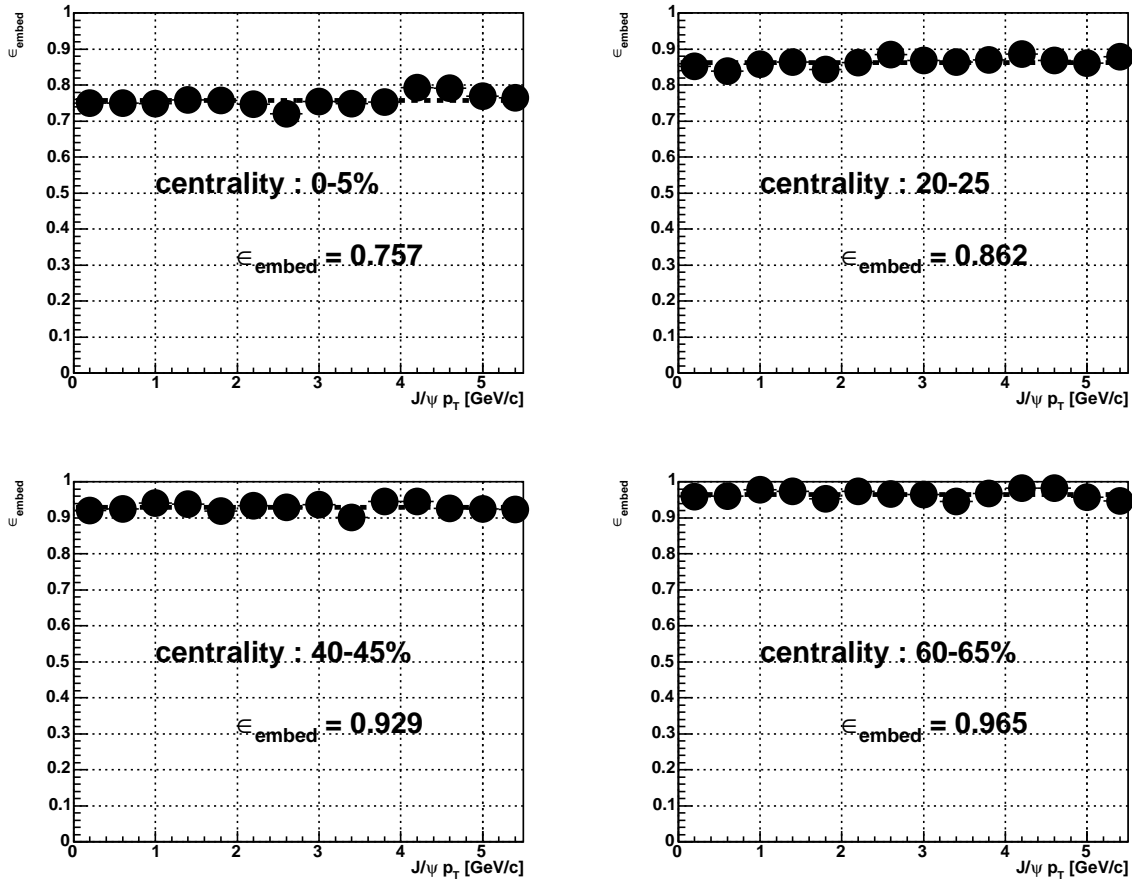


Figure 6.16: Embedding efficiency ϵ_{embed} as a function of J/ψ p_T for the centrality of 0-5/20-25/40-45/60-65%.

but does not have J/ψ p_T dependence. Therefore only efficiency integrated over p_T needs to

be considered. Figure 6.17 shows the embedding efficiency as a function of centrality for the standard eID cuts (Left) and loose eID cuts (Right) and with (closed) and without (open) E0 sector.

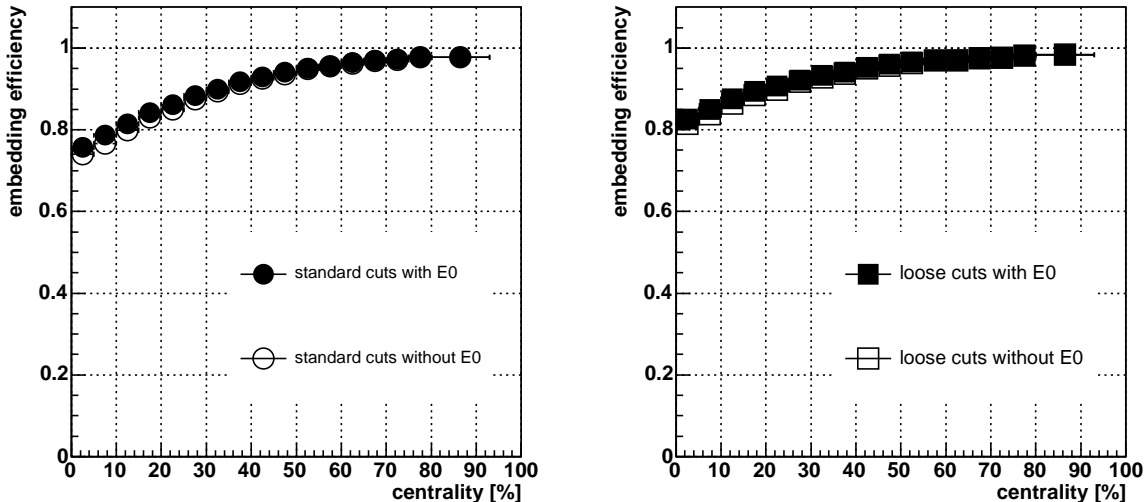


Figure 6.17: Embedding efficiency as a function of centrality. Left is for the standard eID cuts. Right is for the loose eID cuts. Open in both panels are the efficiency without E0 sector and Closed are the efficiency with E0 sector

6.5.3 Internal bremsstrahlung and efficiency for the mass cut ϵ_{mass}

Some fraction of reconstructed J/ψ 's have the mass outside the mass range of $2.9 \leq M_{e^+e^-} \leq 3.3$, because of finite momentum resolution of DC, external bremsstrahlung effect due to the material in the PHENIX and internal bremsstrahlung effect ($J/\psi \rightarrow e^+e^-\gamma$) [124, 125]. Detail of the internal bremsstrahlung effect is described in Appendix F.

Figure 6.18 shows the invariant mass spectrum in $p + p$ (left) and Au+Au collisions (right) and the invariant mass spectrum calculated from simulation study with various mass resolution of J/ψ derived from the momentum resolution of DC (red for 1.0%, green for 1.25% and blue for 1.5% mass resolution), where the external and internal bremsstrahlung effect were taken into account. In the calculation of internal bremsstrahlung of J/ψ , minimum energy of the emitted photon in bremsstrahlung was set to be 10 MeV and the relevant branching ratio was assumed to be 0.324 [125].

The efficiency of the mass cut ϵ_{mass} was extracted by the ratio of the number of J/ψ within mass range of $2.9 \leq M_{e^+e^-} \leq 3.3$ to the number of J/ψ within all mass range. The mass cut efficiency was estimated for each 1 GeV/ c p_T bin by taking into account the mass resolution obtained by Monte Carlo simulation as shown in Fig. 6.19

The results of the mass cut efficiency are summarized in Table 6.6.

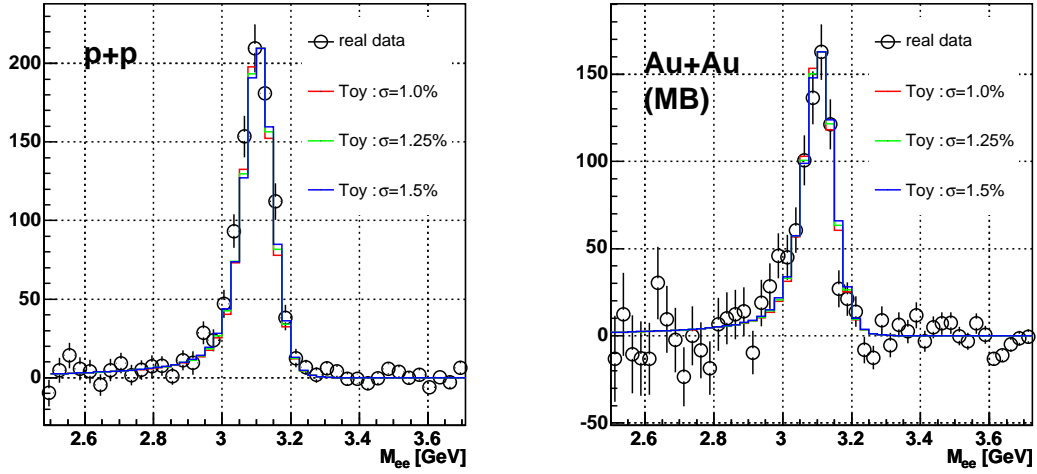


Figure 6.18: Left : Invariant mass spectrum in $p + p$ collisions (black). Right : Invariant mass spectrum in Au+Au collisions (black). Red, green and blue in both panels are the invariant mass spectrum in the simulation study with the internal and external bremsstrahlung effect and with the mass resolution of 1.0%, 1.25% and 1.5%, respectively.

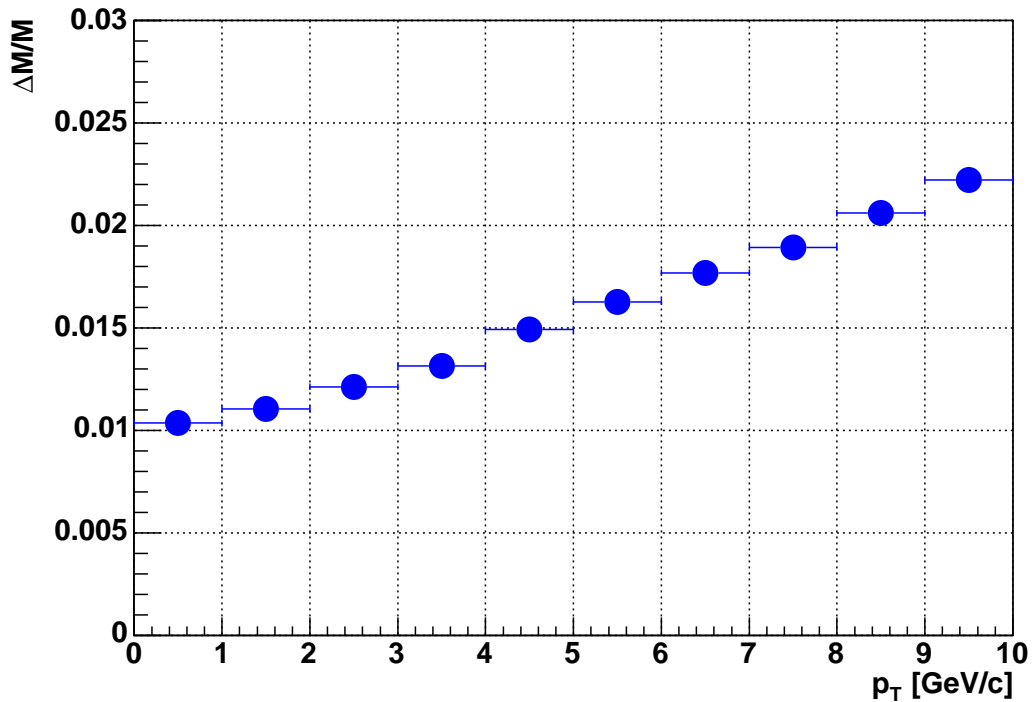


Figure 6.19: p_T dependence of the J/ψ mass resolution

$J/\psi p_T$	Efficiency ϵ_{mass}
0.5	0.880
1.5	0.876
2.5	0.872
3.5	0.872
4.5	0.873
5.5	0.874
6.5	0.873
7.5	0.873
8.5	0.872
9.5	0.870

Table 6.6: efficiency of the mass cut for each 1.0 GeV/ c p_T bin

6.5.4 Smearing effect $\epsilon_{smearing}$

Left in Fig. 6.20 shows the correlation between input $J/\psi p_T$ and reconstructed $J/\psi p_T$ obtained in this simulation study. Right in Fig. 6.20 shows the resolution of reconstructed p_T defined as the width of $p_T^{reco} - p_T^{input}$ as a function of input $J/\psi p_T$. From Fig. 6.20, some J/ψ 's are not reconstructed in the same p_T bin that the J/ψ actually have because of finite resolution in the momentum reconstruction.

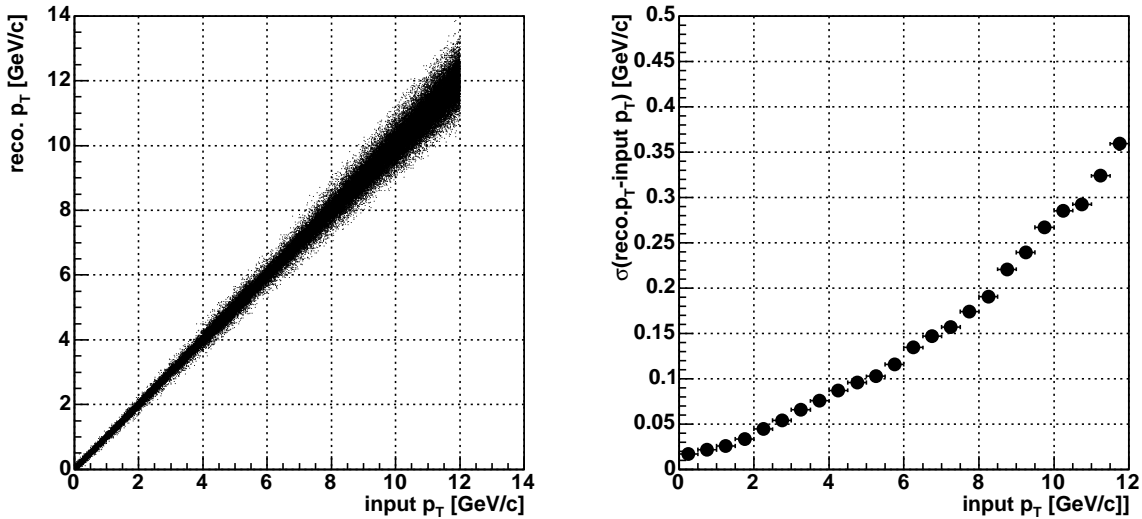


Figure 6.20: Left: Correlation between input and reconstructed $J/\psi p_T$. Right: Resolution of reconstructed $J/\psi p_T$ as a function of input $J/\psi p_T$.

The number of J/ψ 's reconstructed in a p_T bin A ($N_{rec}(A)$) can be expressed by using the probability $P(A, B)$ that a J/ψ actually in the p_T bin B is reconstructed in the p_T bin A and

the number of J/ψ whose input p_T belongs to the p_T bin B ($N_{in}(B)$) as follows.

$$N_{rec}(A) = \sum_B P(A, B) \times N_{in}(B). \quad (6.34)$$

$P(A, B)$ was evaluated for the p_T bin size of 0.25 GeV/ c .

Figure 6.21 shows the $P(A, B)$ as a function of J/ψ p_T , where black, red, green, blue, yellow, magenta, light blue, dark green and purple correspond to the $P(A, B)$ of $A = B$ (diagonal), $A = B + 1$, $A = B - 1$, $A = B + 2$, $A = B - 2$, $A = B + 3$, $A = B - 3$, $A = B + 4$ and $A = B - 4$, respectively. As the p_T becomes larger, $P(A, B)$ of the diagonal ($B = A$) element becomes smaller.

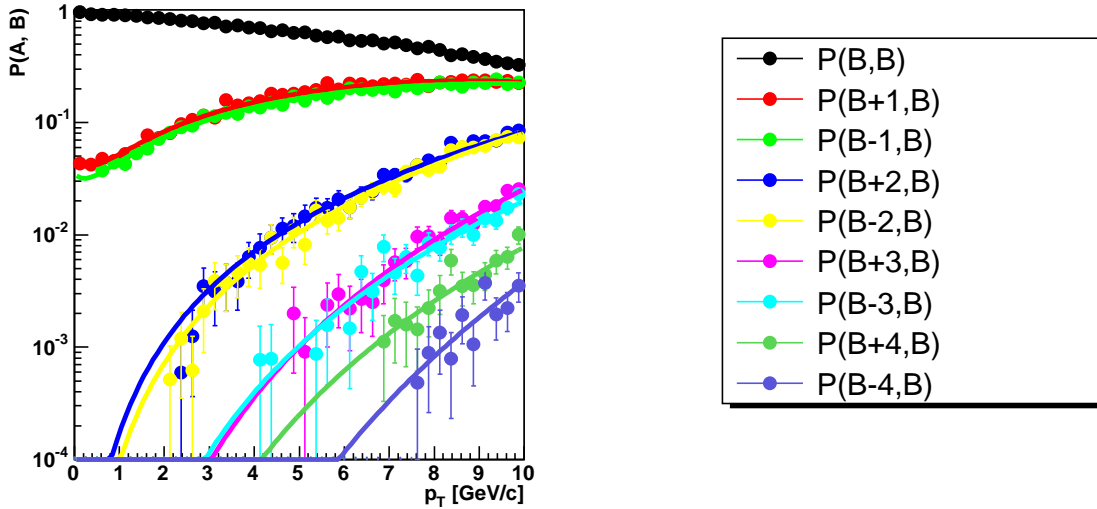


Figure 6.21: $P(A, B)$ as a function of J/ψ p_T . Black, red, green, blue, yellow, magenta, light blue, dark green and purple corresponds to the $P(A, B)$ of $A = B$ (diagonal), $A = B + 1$, $A = B - 1$, $A = B + 2$, $A = B - 2$, $A = B + 3$, $A = B - 3$, $A = B + 4$ and $A = B - 4$, respectively.

Correction factors due to the smearing effect was extracted by taking the following ratio.

$$\begin{aligned} R_{smearing}(A) &= \frac{N_{reco}(A)}{N_{in}(A)}, \\ &= \frac{\sum_B P(A, B) N_{in}(B)}{N_{in}(A)}. \end{aligned} \quad (6.35)$$

Since $P(A, B)$ has J/ψ p_T dependence, the correction factor calculated by Eq. (6.35) is sensitive to the input J/ψ p_T distribution. Here the correction factor was extracted by assuming the invariant J/ψ p_T distribution follows the Kaplan function [126] and has the $\langle p_T^2 \rangle$ of 4.0 [(GeV/ c)²]. As will be discussed in Chapter 7, the p_T distribution of J/ψ was fitted with Kaplan function quite well and the extracted $\langle p_T^2 \rangle$ was 3.77 [(GeV/ c)²] for minimum bias data sample.

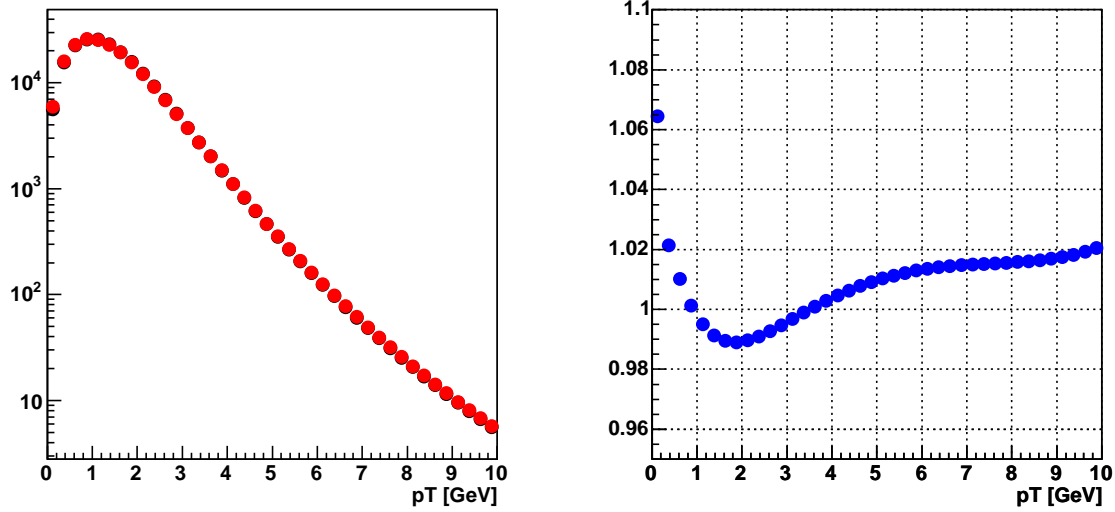


Figure 6.22: Left : Input J/ψ p_T distribution (black) and reconstructed p_T distribution calculated by using $P(A, B)$ and input p_T distribution based on Eq.(6.34).

Left panel in Fig. 6.22 shows the input p_T distribution with the $\langle p_T^2 \rangle$ of 4.0 [(GeV/c)²] (black) and the output p_T distribution (red) which was extracted using $P(A, B)$ shown in Fig. 6.21, input p_T distribution and Eq. (6.34).

Right panel in Fig. 6.22 shows the ratio of the reconstructed J/ψ p_T distribution to the input J/ψ p_T distribution as a function of p_T .

By weighting this ratio (0.25 GeV/c bin) shown in the right in Fig. 6.22 according to the input p_T distribution, the correction factors for each 1 GeV/c bin was obtained and summarized in Table 6.7.

p_T	correction factor ($R_{smearing}(p_T)$)
$0 \leq p_T \leq 1$	1.0138
$1 \leq p_T \leq 2$	0.9916
$2 \leq p_T \leq 3$	0.9914
$3 \leq p_T \leq 4$	0.9991
$4 \leq p_T \leq 5$	1.0064
$5 \leq p_T \leq 6$	1.0114
$6 \leq p_T \leq 7$	1.0141
$7 \leq p_T \leq 8$	1.0153
$8 \leq p_T \leq 9$	1.0162
$9 \leq p_T \leq 10$	1.0187

Table 6.7: Correction factors due to smearing effect for 1 GeV/c bin

6.5.5 Run-by-Run efficiency $\epsilon_{run-by-run}$

The fluctuation of the detector acceptance, primarily due to the instability of the detectors, affects to the detection of the e^+e^- pairs. Since the detector acceptance and dead maps of each detector for G9 runs were implemented in the acceptance calculation in simulation, the fluctuation of detector acceptance were calculated with respect to G9 runs by looking at $\langle N_e \times N_p \rangle$ defined as Eq. (6.19). To reduce the contribution from the statistical fluctuations, the neighboring runs were merged to have the number of MB events larger than $1.0e+06$.

Run-by-Run efficiency from G2-G3 runs

During the runs from G1 to G3, the E0 sector was off. Since the loss of the acceptance due to the E0 sector was taken into account in the acceptance calculation, the run-by-run efficiency was calculated with respect to G9 runs, where $N_e \times N_p$ for G9 runs was obtained without the E0 sector.

Figure 6.23 shows the $\langle N_e \times N_p \rangle$ as a function of run number. Green and Blue line shown for each run group is the mean and RMS of $N_e \times N_p$, respectively. The run-by-run efficiency for each run group was obtained by dividing the mean of $N_e \times N_p$ from each run group by that from G9 runs and the results are summarized in Table 6.8.

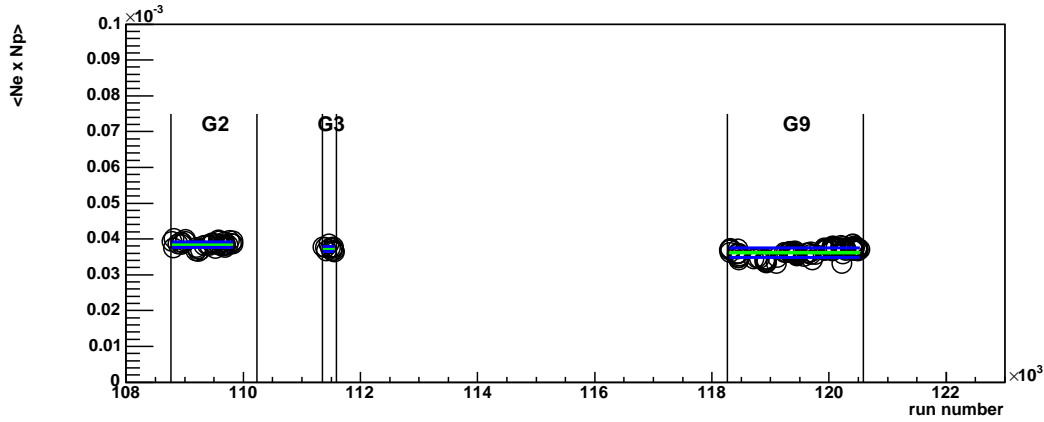


Figure 6.23: $N_e \times N_p$ as a function of run number from G2 to G3 runs. The Green line in each run group is the average of $N_e \times N_p$ per MB event and blue line is its RMS.

run group	run-by-run efficiency (stat \pm RMS)
G2	1.061 ± 0.003 (stat.) ± 0.022
G3	$1.027 \pm 0.003 \pm 0.022$
G9	$1.000 \pm 0.001 \pm 0.036$
G2-G3	$1.055 \pm 0.002 \pm 0.039$

Table 6.8: Run-by-run efficiency from G2 to G3 groups

The total run-by-run efficiency of G2 and G3 runs was calculated from the run-by-run efficiency in each run group weighting according to the number of MB events in G2 and G3 runs.

Run-by-Run efficiency from G4-G10 runs

Figure 6.24 shows $\langle N_e \times N_p \rangle$ as a function of run number. Green and Blue line shown for each run group is the mean and RMS of $\langle N_e \times N_p \rangle$, respectively. The run-by-run efficiency for each run group was obtained by dividing the mean of $N_e \times N_p$ by that from G9 runs and the results are summarized in Table 6.9, where the systematic error of run-by-run efficiency in each run group is the RMS divided by the mean of $N_e \times N_p$ in G9 runs.

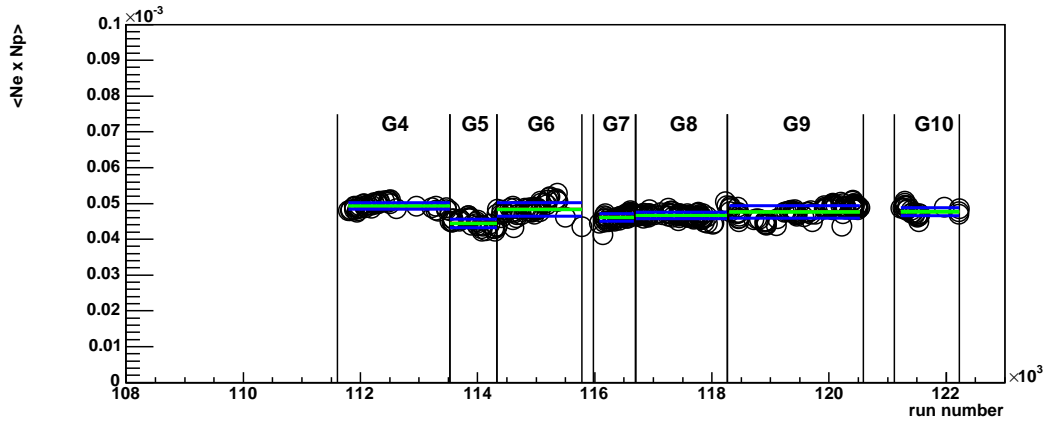


Figure 6.24: $N_e \times N_p$ as a function of run number from G4 to G10 runs. The Green line in each run group is the average of $N_e \times N_p$ and blue line is its RMS.

run group	run-by-run efficiency (stat. \pm RMS)
G4	1.033 ± 0.001 (stat.) ± 0.019
G5	$0.932 \pm 0.002 \pm 0.026$
G6	$1.015 \pm 0.002 \pm 0.038$
G7	$0.966 \pm 0.002 \pm 0.021$
G8	$0.977 \pm 0.001 \pm 0.019$
G9	$1.000 \pm 0.001 \pm 0.036$
G10	$1.000 \pm 0.002 \pm 0.024$
G4-G10	$0.992 \pm 0.001 \pm 0.038$

Table 6.9: Run-by-run efficiency from G4 to G10 groups

The total run-by-run efficiency was calculated from the run-by-run efficiency in each run group weighting according to the number of MB events.

6.5.6 Bin width correction $\epsilon_{bin-width}$

Assumption that the mean p_T of the J/ψ within a bin is the center of the bin is not correct for the falling spectrum. The correction factor due to the finite bin width was extracted as follows. Given that the function $f(p_T)$ is the correct function to describe the spectrum, then the mean p_T , \bar{p}_T , is calculated for a given p_T bin $[a, b]$ by solving the integral equation as follows:

$$f(\bar{p}_T) = \frac{\int_a^b f(p_T) dp_T}{b - a}. \quad (6.36)$$

Then the data point is moved from the bin center to \bar{p}_T .

The other way to take into account this effect is to move the points vertically. This correction is also done by calculating the following quantities $\epsilon_{bin-width}$:

$$\epsilon_{bin-width} = \frac{\frac{1}{b-a} \int_a^b f(p_T) dp_T}{f\left(\frac{b+a}{2}\right)}, \quad (6.37)$$

$$\left(\frac{1}{2\pi p_T} \frac{d^2 N}{dy dp_T}\right)_{cor} = \frac{\left(\frac{1}{2\pi p_T} \frac{d^2 N}{dy dp_T}\right)_{uncor}}{\epsilon_{bin-width}}. \quad (6.38)$$

Given that the invariant p_T distribution is described by $\frac{1}{2\pi p_T} \frac{d^2 N}{dy dp_T} \propto (1 + (p_T/p_0)^2)^{-6}$ with $p_0 = \sqrt{4\langle p_T^2 \rangle} = 4.17$, which is from Year-5 $p + p$ result [86] (See Appendix H), $\epsilon_{bin-width}$ in Eq. (6.37) for 1 GeV/ c p_T bin was calculated and is summarized in Table 6.5.6.

p_T [GeV/ c]	correction factor ($\epsilon_{bin-width}$)
0.5	0.927
1.5	0.964
2.5	1.011
3.5	1.043
4.5	1.057
5.5	1.062
6.5	1.060
7.5	1.045
8.5	1.049
9.5	1.031

Table 6.10: Bin shift correction factors

6.5.7 Overall J/ψ detection efficiency ϵ_{tot}

Overall efficiency ϵ_{tot} in Eq. (6.5) was extracted based on Eq. (6.31), where the correction factors for each run group were combined by weighting according to the number of events in each run group. Figure 6.25 shows the ϵ_{tot} as a function of J/ψ p_T for MB/0-20/20-40/40-93 centrality classes (Left) and for 0-10/10-20/20-30/30-40/40-60/60-93 centrality classes (Right).

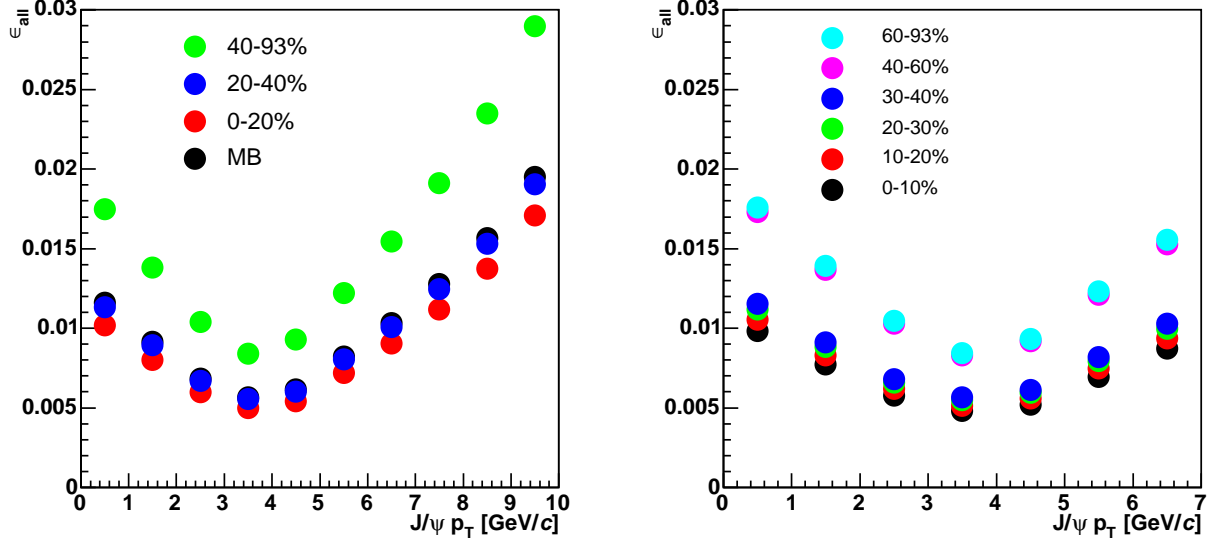


Figure 6.25: Left: ϵ_{tot} as a function of p_T for MB/0-20/20-40/40-93. Right : ϵ_{tot} as a function of p_T for 0-10/10-20/20-30/30-40/40-60/60-93.

Table 6.11 and Table 6.12 are the summary of combined overall efficiency ϵ_{tot} .

p_T	ϵ_{tot} (MB)	ϵ_{tot} (0-20%)	ϵ_{tot} (20-40%)	ϵ_{tot} (40-93%)
0.5	0.0116	0.0102	0.0113	0.0175
1.5	0.00915	0.00802	0.00893	0.0138
2.5	0.00683	0.00599	0.00668	0.0104
3.5	0.00567	0.00497	0.00554	0.00838
4.5	0.00617	0.00540	0.00602	0.00927
5.5	0.00822	0.00721	0.00803	0.0122
6.5	0.0103	0.00905	0.0101	0.0154
7.5	0.0128	0.0112	0.0125	0.0191
8.5	0.0157	0.0137	0.0153	0.0235
9.5	0.0195	0.0171	0.0190	0.0290

Table 6.11: ϵ_{tot} as a function of p_T and for each centrality class (MB/0-20/20-40/40-93%)

p_T	ϵ_{tot} (0-10%)	ϵ_{tot} (10-20%)	ϵ_{tot} (20-30%)	ϵ_{tot} (30-40%)	ϵ_{tot} (40-60%)	ϵ_{tot} (60-93%)
0.5	0.00981	0.0105	0.0112	0.0115	0.0173	0.0176
1.5	0.00773	0.0083	0.00883	0.00911	0.0137	0.0139
2.5	0.00578	0.0062	0.0066	0.00681	0.0103	0.0105
3.5	0.00479	0.00514	0.00547	0.00564	0.00829	0.00844
4.5	0.00521	0.00559	0.00595	0.00614	0.00917	0.00934
5.5	0.00695	0.00746	0.00793	0.00819	0.0121	0.0123
6.5	0.00873	0.00937	0.00996	0.0103	0.0153	0.0155

Table 6.12: ϵ_{tot} as a function of p_T and for each centrality class (0-10/10-20/20-30/30-40/40-60/60-93%)

6.5.8 Mean overall efficiency

For wider than 10% centrality bins, invariant p_T distribution of J/ψ was extracted and the integrated yield was calculated by integrating the invariant p_T distribution. For 5% centrality bins, there is not enough statistics to extract the invariant p_T distribution. The integrated yield was calculated by extracting the mean acceptance and using it as the p_T independent correction factor as expressed in Eq. (6.9).

The mean acceptance was calculated as follows:

$$\langle \epsilon_{tot} \rangle = \frac{\int \frac{dN(J/\psi)}{dp_T \epsilon_{tot}(p_T)} \times \epsilon_{tot}(p_T) \times dp_T}{\int \frac{dN(J/\psi)}{dp_T \epsilon_{tot}(p_T)} dp_T}, \quad (6.39)$$

This calculation was done for 0-5/5-10/10-15/15-20% centrality bins using the shape of the p_T distribution of $\frac{dN(J/\psi)}{dp_T \epsilon_{tot}(p_T)} \propto p_T(1 + (p_T/c_1)^2)^{-6}$. Here c_1 was determined from J/ψ p_T distribution in 0-20% centrality bin, which was $c_1 = \sqrt{4\langle p_T^2 \rangle} = 3.4$. Details on the J/ψ p_T distributions are discussed in Chapter 7. The results of the mean overall efficiency $\langle \epsilon_{tot} \rangle$ for 0-5/5-10/10-15/15-20% centrality bins are summarized in Table 6.13.

centrality	$\langle \epsilon_{tot} \rangle$
0-5%	0.00775
5-10%	0.00806
10-15%	0.00835
15-20%	0.00863

Table 6.13: $\langle \epsilon_{tot} \rangle$ for 0-5/5-10/10-15/15-20% centrality calculated from the J/ψ p_T distribution for 0-20% centrality

6.6 Systematic Error Evaluation

6.6.1 Signal extraction of J/ψ

This systematic uncertainty relates to the number of J/ψ s. This uncertainty is composed to two components. One is the normalization of mixed event distribution for the subtraction of combinatorial background, and the other is the continuum contribution.

Normalization of mixed event invariant mass spectrum

Normalization factor for mixed event invariant mass distribution was given by Eq. (6.30). Systematic uncertainty of normalization factor was estimated using toy model simulation and described in detail in Appendix C. Deviation of the normalization factor from $2 \times N_{buffer}$ is partially due to the effect of the finite centrality resolution. There are still difference in the normalization factor between real data and toy model calculations by 1~3% even if the centrality resolution is taken into account. Therefore 3% was assigned as the systematic uncertainty for the normalization of mixed event invariant mass spectrum. Statistical error of like-sign and mixed like-sign ratio, which is used to extract the normalization factor, is also assigned as the systematic errors of the normalization factor. Ratio of the like-sign distribution to the mixed like-sign distribution is shown in Appendix C. Statistical errors are less than 1% for the centrality of less than 40% and 1-2% for the centrality of larger than 40%.

Continuum contribution

Correction factors due to the continuum contribution ($D\bar{D}$, $B\bar{B}$ and DY) are summarized in Table 6.4. Systematic uncertainty of the continuum correction was estimated from the statistic error and systematic error, which was due to the normalization of continuum yield. From Table 6.4, maximum difference in the correction was $(10.8 - \sqrt{2.6^2 + 1.1^2}) - (9.7 - \sqrt{1.6^2 + 0.6^2})\% = 5\%$. 5% was assigned as the systematic uncertainty from continuum correction.

6.6.2 Corrections

Single J/ψ detection efficiency

At first, statistic error in the simulation study was 1% and 1% was assigned as the systematic uncertainty.

- **acceptance difference between real and simulation**

Same detector dead maps as observed in real data for DC, PC, RICH and EMCAL were implemented in simulation. Detail is described in Appendix E. ϕ and zed distributions for electrons were checked for both real data and simulation and are shown in Fig. E.6.

Systematic error of the acceptance difference between simulation and real data was estimated by evaluating following ratio R_{acc} for each DC side.

$$R_{acc} = \left\langle \frac{\frac{dN^{East}}{d\phi^{sim}}}{\frac{dN^{East}}{d\phi^{real}}} \right\rangle \times \left\langle \frac{\frac{dN^{West}}{d\phi^{sim}}}{\frac{dN^{West}}{d\phi^{real}}} \right\rangle, \quad (6.40)$$

where $\frac{dN^{East}}{d\phi_{sim}}$, $\frac{dN^{East}}{d\phi_{real}}$, $\frac{dN^{West}}{d\phi_{sim}}$, $\frac{dN^{West}}{d\phi_{real}}$ are the $dN/d\phi$ in East in simulation, in East in real data, in West in simulation and in West in real data. R_{acc} was found to be 0.967 for DC south side and 0.972 for DC north side. 3% difference was assigned as the systematic error of acceptance difference for single electrons in real and simulation, which leads to the systematic error of 6% for pairs.

- **eID efficiency difference between real and simulation**

Comparison of electron identification efficiency in real data and simulation is described in Appendix E. Here conversion and Dalitz pairs were used to evaluate eID efficiency in real data. The difference in eID efficiency between real data and simulation for each DC sector (East South, East North, West South and West North) is summarized in Table E.2. The difference in eID efficiency was found to be 1.5% for single electrons, which leads to 3% difference in eID efficiency for pairs. This 3% was assigned as the systematic uncertainty of eID efficiency in simulation.

- **z vertex effect**

In the calculation of ϵ_{det} , the z vertex distribution of J/ψ was generated to be flat between $-40 \leq z \leq 40$ cm. The systematic error due to the uncertainty of z vertex distribution of J/ψ was estimated from the difference in ϵ_{det} extracted from the z vertex distribution inferred from the real data. Left in Fig. 6.26 shows the z vertex distribution in MB Au+Au collisions. Right in Fig. 6.26 shows ϵ_{det} as a function of J/ψ p_T with flat z vertex distribution (closed) and the z vertex distribution inferred from in the real data (open). The different in ϵ_{det} is 2% with small

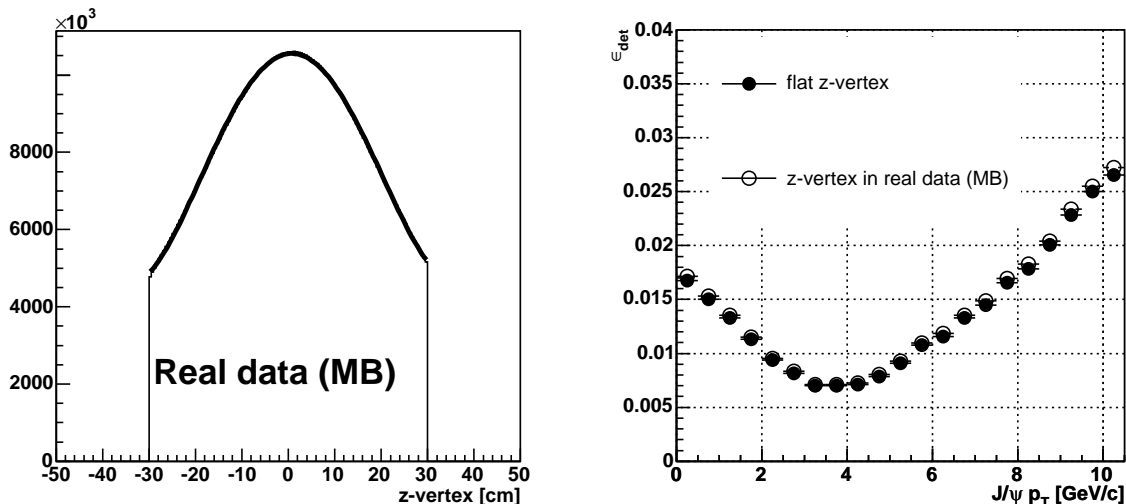


Figure 6.26: Left : z vertex distribution in Au+Au collisions (MB). Right : ϵ_{det} as a function of J/ψ p_T with flat z vertex distribution (closed) and the z vertex distribution in real data (open).

J/ψ p_T dependence and 2% is assigned as systematic uncertainty.

- **Rapidity shape**

Since ϵ_{det} was calculated with flat rapidity distribution, the systematic error due to the uncertainty of rapidity distribution of J/ψ was evaluated. In this evaluation, 4 types of the J/ψ rapidity distribution were assumed, which were extracted by PYTHIA with 4 kinds of parton distribution functions GRV94LO (red), GRV94HO (green), MRSTHO (blue) and CTEQ5M (yellow). Left 2×2 panels of Fig. 6.27 show the 4 types of the rapidity distribution of J/ψ and right 2×2 panels show ϵ_{det} as a function of J/ψ p_T with these 4 types J/ψ rapidity distribution. The difference in ϵ_{det} due to the rapidity shape is very small from Fig. 6.27 and was found to be 0.7%. 0.7% was assigned as the systematic error due to the rapidity distribution of J/ψ .

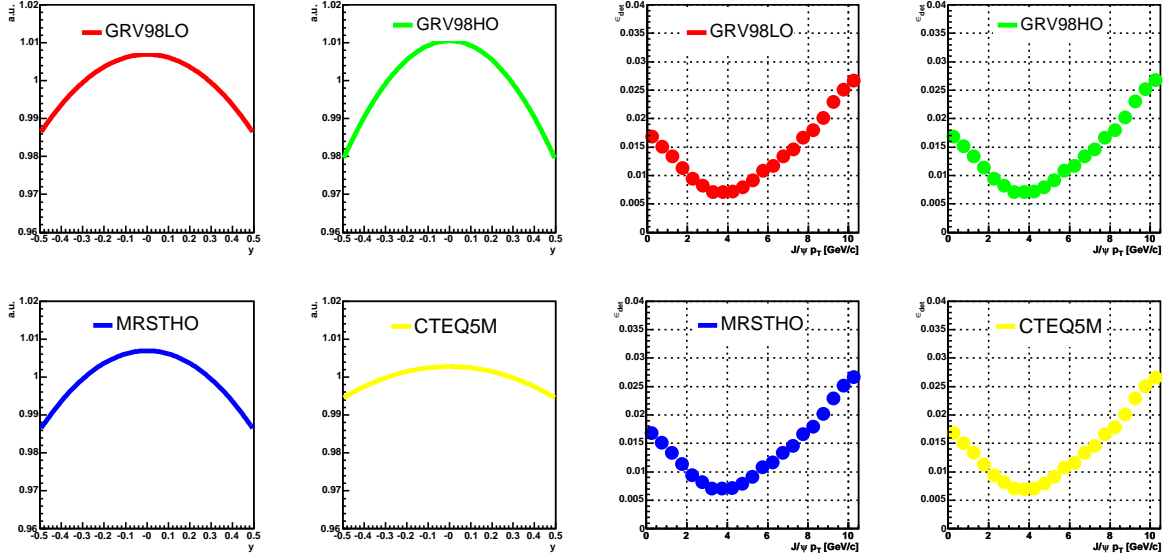


Figure 6.27: Left 2×2 : 4 types of the J/ψ rapidity distribution extracted by PYTHIA with GRV94LO (red), GRV94HO (green), MRSTHO (blue) and CTEQ5M (yellow) PDF. Right 2×2 : ϵ_{det} as a function of J/ψ p_T for these 4 rapidity distribution of J/ψ with GRV94LO (red), GRV94HO (green), MRSTHO (blue) and CTEQ5M (yellow) PDF. The difference from different PDFs is very small.

Systematic error of embedding efficiency

Systematic error of embedding efficiency was estimated by comparing the centrality dependence of eID efficiency for single electrons in real data and the embedding efficiency for single electrons in this simulation [58].

Since the embedding efficiency for pairs almost equals to the square of the embedding efficiency for single electrons and positrons, the systematic error of embedding efficiency for pairs can be estimated by using the following relation.

$$\begin{aligned}
 \delta\epsilon_{embed} &= \delta(\epsilon_{embed,1} \times \epsilon_{embed,2}) \\
 &= \epsilon_{embed} \times \sqrt{(\delta\epsilon_{embed,1}/\epsilon_{embed,1})^2 + (\delta\epsilon_{embed,2}/\epsilon_{embed,2})^2} \\
 &= \epsilon_{embed} \times \sqrt{2} \times \delta\epsilon_{embed,1}/\epsilon_{embed,1},
 \end{aligned} \tag{6.41}$$

where ϵ_{embed} , $\epsilon_{embed,i=1,2}$ are the embedding efficiency for pairs, single electrons and positrons, respectively. Results of systematic errors of embedding efficiency for each 5% centrality class are 6.60% (0-5% centrality), 5.85% (5-10% centrality), 5.22% (10-15% centrality) and 4.65% (15-20% centrality). Systematic errors for each 10% centrality class are 6.26% (0-10% centrality), 4.91% (10-20% centrality), 3.94% (20-30% centrality) and 3.20% (30-40% centrality). Systematic errors for larger than 40% centrality class are 2.43% (40-60% centrality), 1.78% (60-93% centrality), and 2.01 (40-93% centrality). Systematic errors for 0-20%, 20-40% and MB are 5.56%, 3.54% and 4.55%, respectively.

Smearing correction

The systematic error of smearing effect was estimated by changing the $\langle p_T^2 \rangle$ of input p_T distribution. Table 6.14 shows the correction factors of smearing effect for 1 GeV/ c bin with $\langle p_T^2 \rangle = 3.0$ and 5.0. From the difference in the correction factors with the different $\langle p_T^2 \rangle$, 1% is assigned

p_T	correction factors $\langle p_T^2 \rangle = 3.0$	correction factors $\langle p_T^2 \rangle = 5.0$
$0 \leq p_T \leq 1$	1.0130	1.0146
$1 \leq p_T \leq 2$	0.9926	0.9910
$2 \leq p_T \leq 3$	0.9952	0.9887
$3 \leq p_T \leq 4$	1.0044	0.9955
$4 \leq p_T \leq 5$	1.0121	1.0030
$5 \leq p_T \leq 6$	1.0169	1.0085
$6 \leq p_T \leq 7$	1.0194	1.0117
$7 \leq p_T \leq 8$	1.0204	1.0133
$8 \leq p_T \leq 9$	1.0212	1.0145
$9 \leq p_T \leq 10$	1.0237	1.0172

Table 6.14: Correction factors due to smearing effect for 1 GeV/ c bin with the input $\langle p_T^2 \rangle = 3.0$ and 5.0 [(GeV/ c)²]

as the systematic error due to the smearing effect.

Run-by-Run efficiency

Run-by-run efficiency was calculated by dividing $\langle N_e \times N_p \rangle$ for each run group by that for G9 runs. Systematic error of run-by-run efficiency was taken to be *RMS* of $N_e \times N_p$ for each run group divided by $\langle N_e \times N_p \rangle$ for G9 runs. *RMS* for G2-G3 runs and G4-G10 runs divided by $\langle N_e \times N_p \rangle$ for G9 runs were summarized in Table 6.8 and Table 6.9, respectively. 3.8% and 3.9% were assigned as systematic error of run-by-run efficiency.

Bin width correction

Systematic error was estimated for various $\langle p_T^2 \rangle$ of J/ψ p_T distribution. Systematic error of 2% is assigned from the variation of $\epsilon_{bin-width}$ with the different $\langle p_T^2 \rangle$ values (=3.0 and 5.0).

Mean overall efficiency

Systematic error of the mean overall efficiency estimated by changing $\langle p_T^2 \rangle$ of J/ψ p_T distribution. Table 6.15 is the mean overall efficiency with $\langle p_T^2 \rangle = 3.7 \pm 0.5$ (GeV/c)² for 0-5% centrality bin. The $\langle p_T^2 \rangle$ was shifted by ± 0.5 (GeV/c)² here since the quadratic sum of stat. error and sys. error of $\langle p_T^2 \rangle$ in 0-20% centrality bin is ~ 0.5 (GeV/c)², which is discussed later.

The deviation of $\langle \epsilon_{tot} \rangle$ from different $\langle p_T^2 \rangle$ is assigned as the systematic error, which is 3%.

$\langle p_T^2 \rangle$ [(GeV/c) ²]	$\langle \epsilon_{tot} \rangle$
3.7-0.5	0.00795 (+2.7%)
3.7	0.00775
3.7+0.5	0.00756 (-2.4%)

Table 6.15: $\langle \epsilon_{tot} \rangle$ with different p_T distribution

6.6.3 Summary of the systematic errors

The systematic errors are summarized in Table 6.16. The evaluation method of the mass cut

list of sys error	systematic errors	Type
Background normalization	3-5% (central-peripheral)	A
Continuum correction	5%	A
run-by-run efficiency	3.9% (G2-G3) and 3.8% (G4-G10)	B
Statistics from simulation	1%	B
Acceptance variation between simulation and real data	6%	B
eID efficiency variation between simulation and real data	3%	B
Unknown z vertex and rapidity of J/ψ distribution	2.7%	B
embedding efficiency	6.3%/4.9%/3.9% in 0-10/10-20/20-30%	B
embedding efficiency	3.2%/2.4%/1.8% in 30-40/40-60/60-93%	B
embedding efficiency	5.6%/3.5%/2.0% in 0-20/20-40/40-93%	B
embedding efficiency	4.6% in MB	B
embedding efficiency	6.6%/5.9%/5.2%/4.7% in 0-5/5-10/10-15/15-20%	B
mean acceptance calculation	3% (R_{AA} in 0-5/5-10/10-15/15-20% centrality)	B
momentum smearing	1%	B
bin shift correction error	2%	B
mass cut efficiency	1%	B

Table 6.16: summary of the systematic error

efficiency was same as used in the J/ψ analysis in Year-5 $p + p$ collisions. Therefore systematic error from radiation tail is canceled out and it is not shown up in the systematic error of R_{AA} . Other systematic errors were summed up quadratically in the invariant p_T yield calculation and R_{AA} calculation. The systematic errors were classified into two groups here. One “Type A” is the point-to-point uncorrelated systematic error, which is independent for centrality and p_T . The other “Type B” is the point-to-point correlated systematic errors with respect to the centrality and/or p_T for which the points can move coherently by the same amount.

Chapter 7

Experimental Results

In this chapter, the transverse momentum distribution of J/ψ and integrated yeild in Au+Au collisions for various centrality classes are shown. Also $\langle p_T^2 \rangle$ of J/ψ and R_{AA} as a function of centrality are presented.

7.1 Transverse Momentum Distributions

Invariant p_T distribution was obtained for MB/0-20/20-40/40-93 and 0-10/10-20/20-30/30-40/40-60/60-93% centrality bins based on Eq. (6.5). Figure 7.1 shows the invariant p_T distribution for MB (black, $\times 100$ scale up), 0-20% (red, $\times 10$ scale up), 20-40% (blue), 40-93% (green, $\times 10$ scale down). Figure 7.2 shows the invariant p_T distribution for 0-10% (black, $\times 10^5$ scale up), 10-20% (red, $\times 10^4$ scale up), 20-30% (green, $\times 10^3$ scale up), 30-40% (green, $\times 10^2$ scale up), 40-60% (magenta, $\times 10^1$ scale up), 60-93% (light blue). The values of each point, statistic error, uncorrelated systematic error (Type A) and correlated systematic error (Type B) are summarized in Table G.1, Table G.2 and Table G.3 in Appendix G.

7.2 Extraction of $\langle p_T^2 \rangle$ and Centrality Dependence of $\langle p_T^2 \rangle$

Two methods were used to calculate $\langle p_T^2 \rangle$ for each centrality class. One method was using the data points of invariant p_T distribution directly, and the other was by fitting the data points with the Kaplan function, which is defined as follows:

$$f_{Kaplan}(p_T) \equiv \left(1 + \frac{p_T^2}{B^2}\right)^n, \quad (7.1)$$

where the exponent n was fixed to 6 which can describe J/ψ distribution at CDF experiment [126]. $\langle p_T^2 \rangle$ was calculated as follows:

$$\langle p_T^2 \rangle_{data} = \frac{\sum_{p_T} p_T^2 d^2 N / dp_T dy \Delta p_T}{\sum_{p_T} d^2 N / dp_T dy \Delta p_T}, \quad (7.2)$$

$$\langle p_T^2 \rangle_{fit} = \frac{\int_{p_T} p_T^3 f_{Kaplan}(p_T) dp_T}{\int_{p_T} p_T f_{Kaplan}(p_T) dp_T}, \quad (7.3)$$

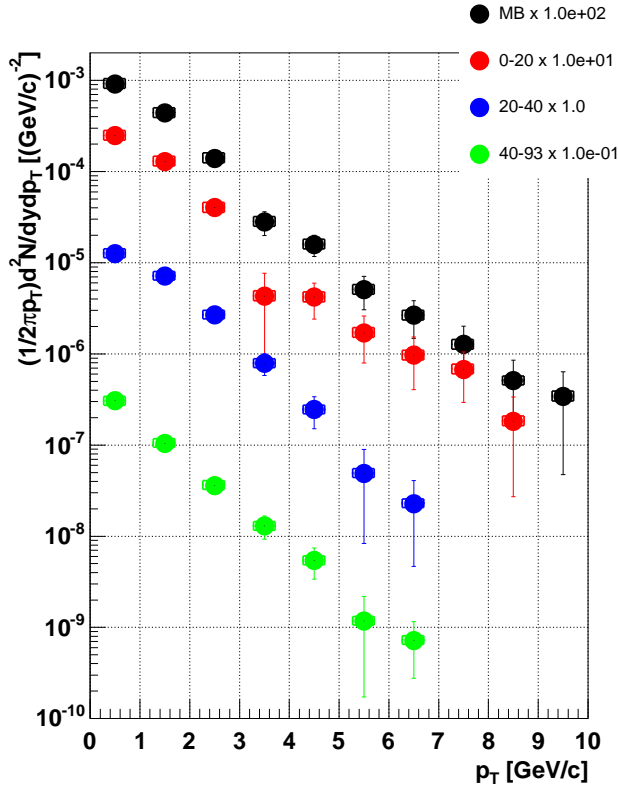


Figure 7.1: Invariant p_T distribution for MB, 0-20%, 20-40% and 40-93%. Bars are the stat. error and the brackets are the total sys. errors calculated by the quadratic summation of uncorrelated and correlated sys. errors.

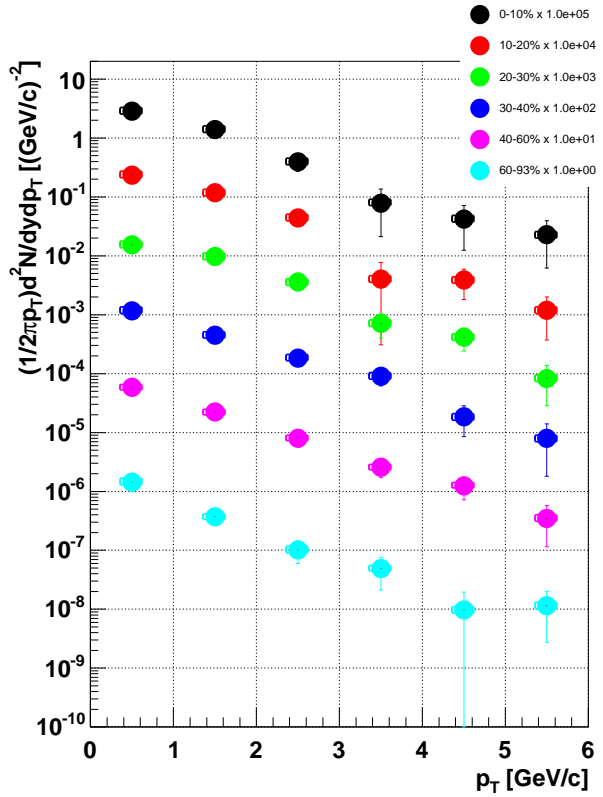


Figure 7.2: Invariant p_T distribution for 0-10%, 10-20%, 20-30%, 30-40%, 40-60% and 60-93%. Bars are the stat. error and the brackets are the total sys. error.

where the data points up to 5 GeV/c was used in $\langle p_T^2 \rangle_{data}$ and the integration was performed up to 5 GeV/c in $\langle p_T^2 \rangle_{fit}$. Figure 7.3 shows the invariant p_T distributions and the Kaplan functions obtained after fitting invariant p_T distribution in $p+p$ collisions and in Au+Au collisions for each centrality class (MB/0-20/20-40/40-93% in left and 0-10/10-20/20-30/30-40/40-60/60-93% in right) of Au+Au collisions.

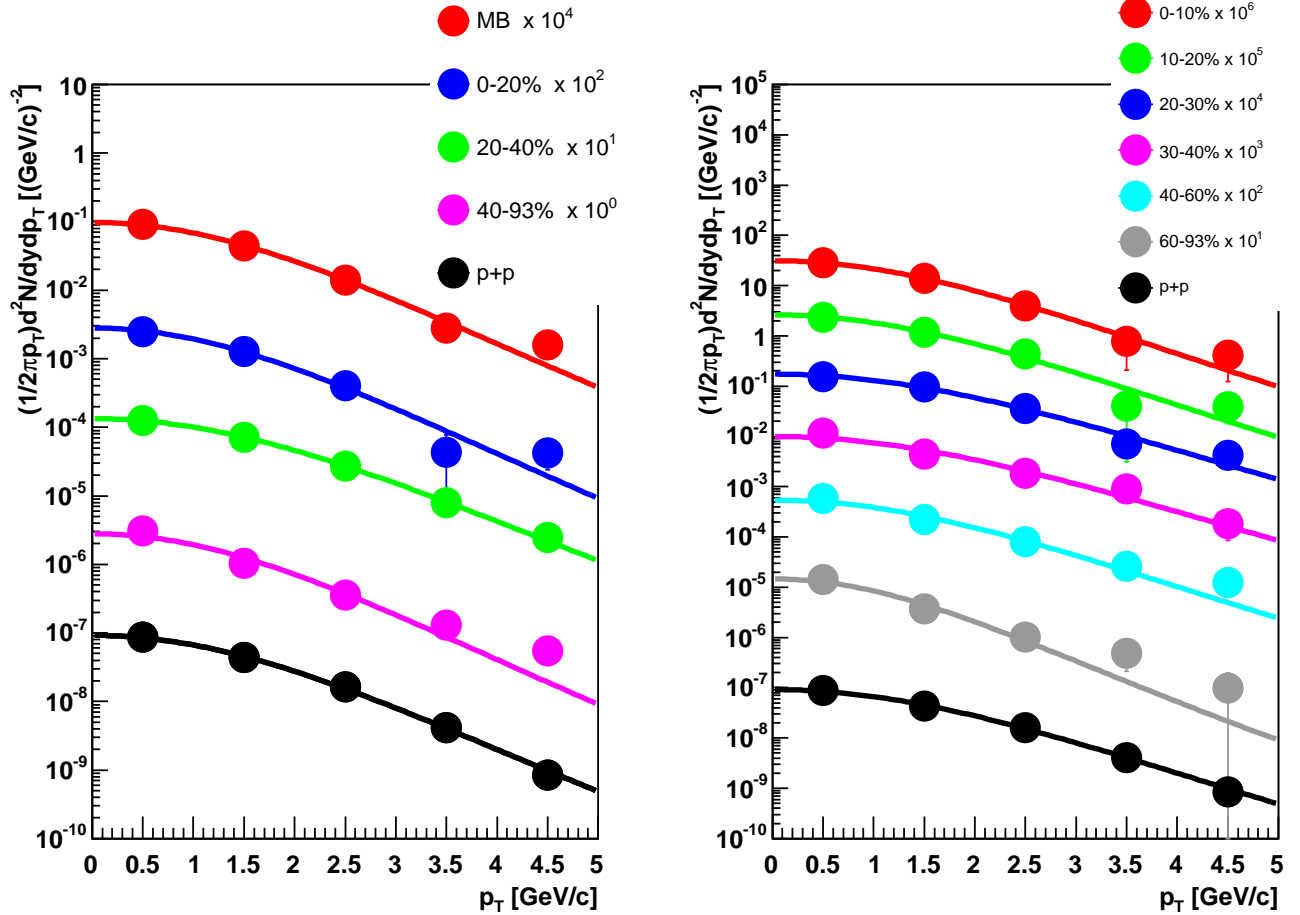


Figure 7.3: Left : Invariant p_T distributions in MB/0-20/20-40/40-93% centrality and in $p+p$ collisions. Right : Invariant p_T distributions in 0-10/10-20/20-30/30-40/40-60/60-93% centrality and in $p+p$ collisions. Error shown in this figure is only statistic error.

The statistic error was calculated numerically as follows.

$$\langle p_T^2 \rangle = \frac{\sum_i w_i x_i}{\sum_i x_i}, \quad (7.4)$$

$$\begin{aligned} \sigma^2 &= \sum_i \sigma_{x_i}^2 (\partial / \partial x_i (\sum_i w_i x_i / \sum_i x_i))^2, \\ &= \sum_i \sigma_{x_i}^2 ((w_i \sum_j x_j - \sum_j w_j x_j) / (\sum_j x_j)^2)^2, \end{aligned} \quad (7.5)$$

where $w_i \equiv p_T^2$ and $x_i \equiv d^2N/dydp_T \times \Delta p_T$. The similar error propagation was performed to calculate statistical error of $\langle p_T^2 \rangle$ for the fitting method.

Systematic error was evaluated from maximum deviation of $\langle p_T^2 \rangle$ when each data point was moved up/down independently according to $\pm 1 \sigma$ error of uncorrelated systematic errors.

Figure 7.4 shows $\langle p_T^2 \rangle$ as a function of N_{col} in $p + p$ (black) $d+Au$ MB (green) and Au+Au collisions (MB/0-20/20-40/40-93% in left and 0-10/10-20/20-30/30-40/40-60/60-93% in right).

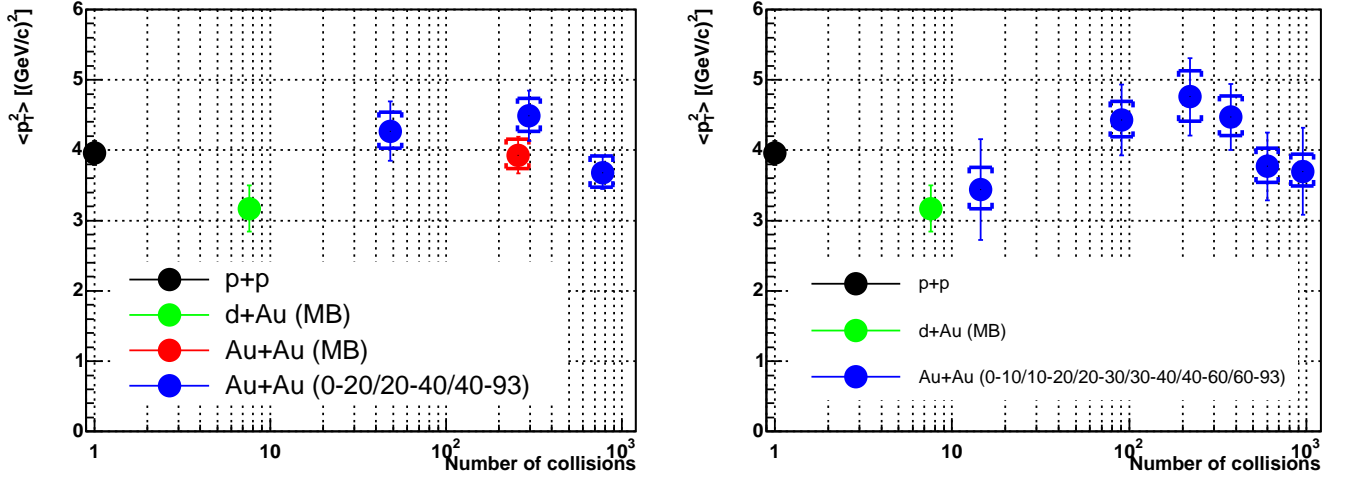


Figure 7.4: $\langle p_T^2 \rangle$ as a function of N_{col} in $p + p$ (black) $d+Au$ MB (green) and Au+Au (MB/0-20/20-40/40-93% in left and 0-10/10-20/20-30/30-40/40-60/60-93% in right) collisions.

$\langle p_T^2 \rangle$ for each centrality class is summarized in Table G.4.

$\langle p_T^2 \rangle$ shows the little dependence of the number of collisions, which suggests that the Cronin effect at RHIC energy is smaller compared to at SPS energies.

7.3 R_{AA} as a function of p_T

R_{AA} as a function of p_T was extracted using the Year-5 $p + p$ J/ψ results as reference [86]. The invariant cross section in $p + p$ collisions for each p_T bin is summarized in Appendix. H.

Figure 7.5 shows the R_{AA} as a function of p_T for MB, 0-20%, 20-40% and 40-93% centrality. Shaded area on each point corresponds to the statistical and systematic errors of the invariant cross section in $p + p$ collisions and band corresponds to the systematic error from T_{AB} , which is 7%, 7%, 8% and 15% for MB, 0-20%, 20-40% and 40-93% centrality, respectively. The calculation was done up to 5 GeV/c .

Figure 7.6 shows the R_{AA} as a function of p_T for 0-10, 10-20%, 20-30% 30-40, 40-60 and 60-93% centrality bins. Shaded area on each point corresponds to the statistical and systematic errors of the invariant cross section in $p + p$ collisions and band corresponds to the systematic error from T_{AB} , which is 7%, 7%, 8%, 8%, 12% and 29% for 0-10%, 10-20%, 20-30%, 30-40%, 40-60% and 60-93% centrality, respectively. The calculation was done up to 5 GeV/c . The values of each point, statistic error, uncorrelated systematic error (Type A) and correlated systematic error (Type B) are summarized in Table G.5 and Table G.6 in Appendix G.

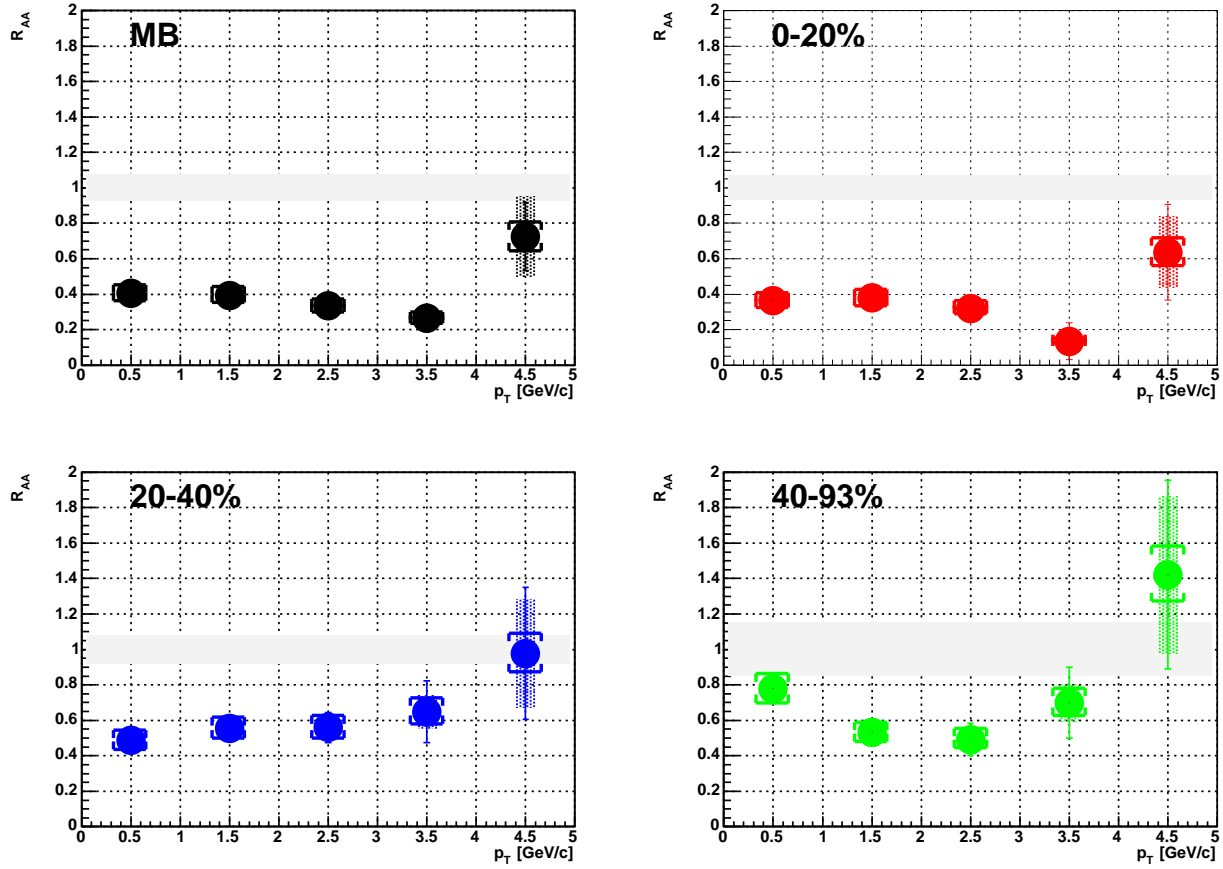


Figure 7.5: R_{AA} as a function of p_T for MB, 0-20%, 20-40% and 40-93% centrality. Bars are the stat. error and the brackets are the total sys. error. Shaded area on each point corresponds to the $p + p$ stat. and sys. error and band corresponds to the systematic error from T_{AB} .

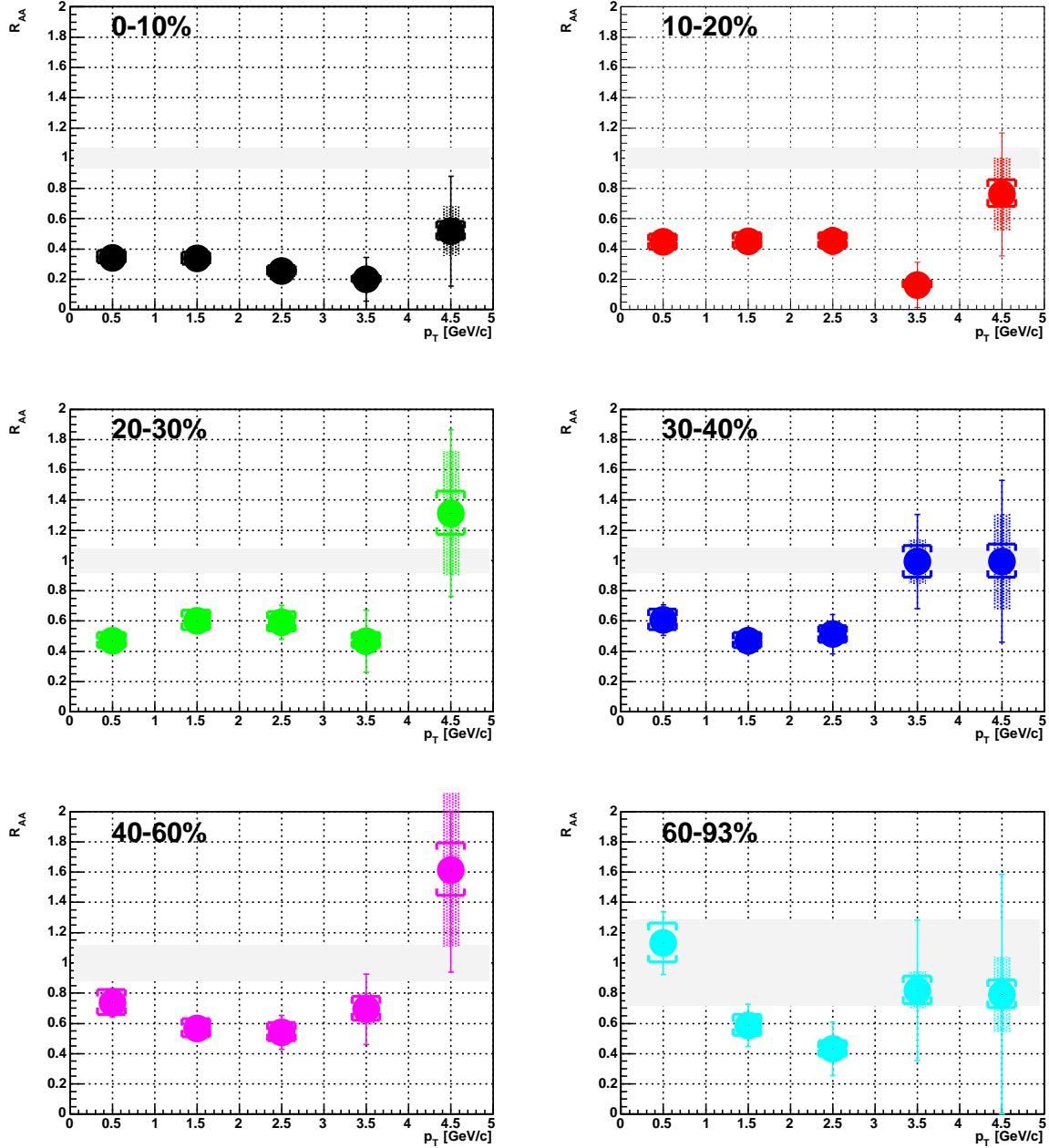


Figure 7.6: R_{AA} as a function of p_T for 0-10, 10-20%, 20-30% 30-40, 40-60 and 60-93% centrality bins. Bars are the stat. error and the brackets are the total sys. error. Shaded area on each point corresponds to the $p + p$ stat. and sys. error. Band corresponds to the systematic error from T_{AB} .

For the central collisions, J/ψ suppression is found to be ~ 0.4 and the suppression doesn't depend on J/ψ p_T .

7.4 Integrated Invariant Yield

Integrated invariant yield defined as Eq. (6.8) was obtained by integrating the invariant p_T distribution shown in Fig. 7.2. In case for 5% centrality bin, Eq. (6.9) was used to extract the integrated invariant yield.

Table 7.1 shows the $BdN/dy/N_{col}$ of J/ψ for each centrality classes. The first error is the statistical error and the second one is the total systematic error, which is the quadratic sum between uncorrelated and correlated systematic error.

centrality	N_{part}	N_{col}	$BdN/dy/N_{col} \pm \text{stat.} \pm \text{total sys. error}$
MB	109	258	$4.14\text{e-}07 \pm 2.03\text{e-}08 \pm 4.70\text{e-}08$
0-20%	280	779	$3.82\text{e-}07 \pm 2.93\text{e-}08 \pm 4.50\text{e-}08$
20-40%	140	296	$5.94\text{e-}07 \pm 4.11\text{e-}08 \pm 6.51\text{e-}08$
40-93%	34	45	$6.69\text{e-}07 \pm 4.82\text{e-}08 \pm 7.29\text{e-}08$
0-10%	325	955	$3.35\text{e-}07 \pm 3.91\text{e-}08 \pm 4.07\text{e-}08$
10-20%	235	603	$4.62\text{e-}07 \pm 4.4\text{e-}08 \pm 5.30\text{e-}08$
20-30%	167	374	$6.08\text{e-}07 \pm 5.31\text{e-}08 \pm 6.74\text{e-}08$
30-40%	114	220	$6.17\text{e-}07 \pm 6.46\text{e-}08 \pm 6.70\text{e-}08$
40-60%	58.4	90.6	$6.86\text{e-}07 \pm 5.73\text{e-}08 \pm 7.54\text{e-}08$
60-93%	14.5	14.5	$7.81\text{e-}07 \pm 1.05\text{e-}07 \pm 8.80\text{e-}08$
0-5%	351	1065	$2.65\text{e-}07 \pm 5.14\text{e-}08 \pm 3.35\text{e-}08$
5-10%	299	845	$3.45\text{e-}07 \pm 5.44\text{e-}08 \pm 4.24\text{e-}08$
10-15%	254	672	$3.75\text{e-}07 \pm 5.67\text{e-}08 \pm 4.49\text{e-}08$
15-20%	215	533	$4.58\text{e-}07 \pm 6.05\text{e-}08 \pm 5.39\text{e-}08$

Table 7.1: $BdN/dy/N_{col}$ of J/ψ for MB, 0-20/20-40/40-93%, 0-10/10-20/20-30/30-40/40-60/60-93% and 0-5/5-10/10-15/15-20% centrality classes. The first error in the last column is stat. error and second is total sys. errors.

7.5 Centrality Dependence of R_{AA}

Year-5 $p+p$ result was used as the baseline for R_{AA} calculation [86]. The J/ψ production cross section in $p+p$ collisions is as follows:

$$B \frac{d\sigma}{dy} = 44.3 \pm 1.4 (\text{stat.}) \pm 5.1 (\text{sys.}) \pm 4.5 (\text{lumi.bias}) \text{ nb.} \quad (7.6)$$

Figure. 7.7 shows the nuclear modification factor (R_{AA}) as a function of the number of participants. Centrality classes are 0-5%, 5-10%, 10-15%, 15-20%, 20-30%, 30-40%, 40-60%

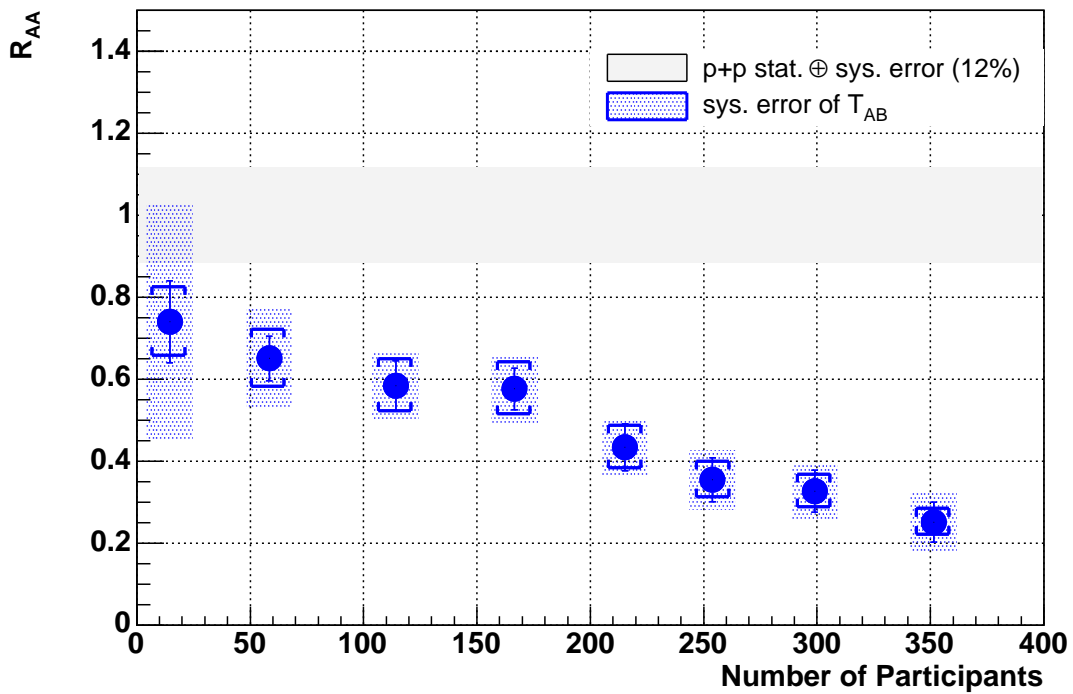


Figure 7.7: R_{AA} as a function of the number of participants. The centrality binning is 0-5/5-10/10-15/15-20/20-30/30-40/40-60/60-93. The band corresponds to the quadratic sum of statistic error and systematic error from Year-5 $p + p$ J/ψ results. The shaded area in each point is the systematic error of T_{AB} .

and 60-93%. The shaded area in each point is the systematic error of T_{AB} . Table 7.2 is the summary of the R_{AA} for each centrality class, where the first error is the stat. error and the second is the total sys. error. It is seen that strong suppression of J/ψ production by a factor

centrality	N_{part}	$R_{AA} \pm \text{stat.} \pm \text{total sys. error}$
0-5%	351	$0.251 \pm 0.0488 \pm 0.0317$
5-10%	299	$0.327 \pm 0.0516 \pm 0.0401$
10-15%	254	$0.355 \pm 0.0538 \pm 0.0425$
15-20%	215	$0.434 \pm 0.0574 \pm 0.0509$
20-30%	167	$0.576 \pm 0.0503 \pm 0.0636$
30-40%	114	$0.585 \pm 0.0613 \pm 0.0632$
40-60%	58.4	$0.651 \pm 0.0544 \pm 0.0711$
60-93%	14.5	$0.74 \pm 0.0997 \pm 0.0831$

Table 7.2: R_{AA} as a function of the number of participants

of ~ 4 is observed in central Au+Au collisions.

Chapter 8

Discussion

J/ψ production in Au+Au collisions is discussed in this chapter. The experimental results of the nuclear modification factor (R_{AA}) as a function of centrality and p_T at RHIC energies are compared to the results observed at SPS energies and compared to the theoretical models to understand the fate of J/ψ in hot and dense medium created at RHIC.

8.1 Comparison of R_{AA} to SPS Energy Results

The NA50 experiment at CERN SPS measured the $J/\psi \rightarrow \mu^+\mu^-$ in Pb+Pb collisions at 158 GeV per nucleon in the target rest frame, which corresponds to $\sqrt{s_{NN}} = 17.3$ GeV in center of mass frame, with the rapidity coverage of $0 \leq y \leq 1$ in center of mass frame. The NA50 experiment measured the ratio of the cross section of J/ψ to the cross section of Drell-Yan pairs, $B\sigma(J/\psi)/\sigma(DY)$, as a function of centrality, where the production of Drell-Yan pairs is found to be scaled to the number of binary nucleon-nucleon collisions [77]. To calculate R_{AA} for NA50 Pb+Pb collisions, $B\sigma(J/\psi)/\sigma(DY)$ from NA51 $p + p$ collisions were used. Since NA51 $p + p$ collisions were performed at 450 GeV in the target rest frame, NA51 had different kinematic domain such as x_F , and the isospin combination for Drell-Yan production is different in case of $p + p$ collisions and Pb+Pb collisions, those corrections were done based on Ref. [82].

Figure 8.1 shows R_{AA} as a function of the number of participants in Au+Au collisions at $\sqrt{s_{NN}} = 200$ GeV (red) and in Pb+Pb collisions at $\sqrt{s_{NN}} = 17.3$ GeV (black). Bars in Au+Au data at RHIC correspond to the quadratic summation of statistical error and uncorrelated systematic error. Brackets in Au+Au data correspond to the correlated systematic error, where systematic error from T_{AB} is included. Bars and brackets for NA50 data correspond to statistical and total systematic errors, respectively.

The J/ψ suppression relative to the inelastic nucleon-nucleon collisions observed at RHIC is found to be compatible to that observed at SPS.

8.2 Comparison of R_{AA} to the Theoretical Models

To understand the J/ψ production in heavy-ion collisions and its modification in the medium, R_{AA} of J/ψ was compared to various theoretical models. Following models were compared and

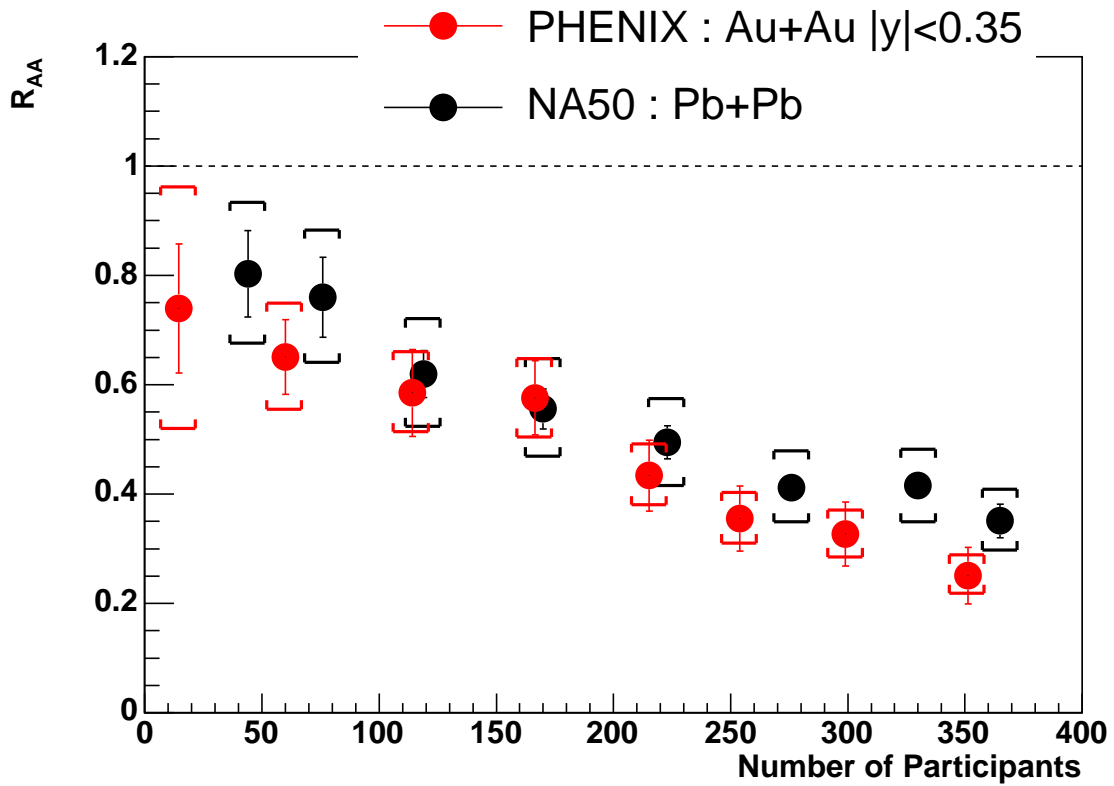


Figure 8.1: R_{AA} as a function of the number of participants from PHENIX data (red) and NA50 data (black). Bar in PHENIX data corresponds to the quadratic summation of stat. error and uncorrelated sys. error. Bracket in PHENIX data corresponds to the correlated sys. error, where T_{AB} error is included.

brief description of them are described in each subsection.

1. Cold nuclear matter effects (nuclear absorption and gluon shadowing)
2. Dissociation by comovers
3. Dissociation by thermal gluons in QGP
4. Dissociation \oplus recombination of J/ψ
5. Sequential melting
6. Threshold model

8.2.1 Cold nuclear matter effects

Cold nuclear matter effects such as nuclear absorption of J/ψ in the nuclear environments and gluon shadowing, which is due to the different gluon distribution in heavy nuclei compared to that in proton, lead to modify the J/ψ yield. They were observed in $p+A$ collisions by the NA38/NA50/NA51 experiments at CERN SPS [128, 129, 130] and by the E772/E866 experiments at FNAL Tevatron [131, 132].

Cold nuclear matter effects to the J/ψ production at RHIC energy was extracted from the J/ψ measurement in $d+Au$ collisions performed in 2003 at RHIC. PHENIX measured J/ψ yield as a function of rapidity [87]. Figure 8.2 shows the R_{dAu} as a function of rapidity. Here definition of R_{dAu} is as follows:

$$R_{dAu} = \frac{d\sigma_{dAu}^{J/\psi}/dy}{\langle N_{col} \rangle \times d\sigma_{pp}^{J/\psi}/dy}, \quad (8.1)$$

where $\langle N_{col} \rangle$ is the average number of inelastic nucleon-nucleon interactions calculated based on Glauber model.

Rapidity and momentum fraction of partons are closely related with each other as described in Eq. (2.20) and Eq. (2.21). Since deuteron is going from negative z to positive z , J/ψ going to positive (negative) rapidity is coming from small (large) x parton in Au nuclei. As shown in Fig. 2.12, depletion of gluon PDF is occurred for small x partons, which leads to suppression of J/ψ production at positive rapidity. Tendency of R_{dAu} as a function of rapidity shown in Fig. 8.2 is consistent with this gluon shadowing picture. Quantitative analysis of gluon shadowing and nuclear absorption was done by R. Vogt [90]. Solid and dashed lines shown in Fig. 8.2 are the prediction of R_{dAu} with Eskola-Klein-Salgado (EKS) gluon shadowing and the nuclear absorption cross section of 1 mb and 3 mb.

From Fig. 8.2, EKS parameterization of PDF [68] can reproduce the observed rapidity dependence of R_{dAu} and the nuclear absorption cross section was limited to be 0-2 mb at mid-rapidity. The cold nuclear matter effects extracted from $d+Au$ collisions were extrapolated to Au+Au collisions [133].

Figure 8.3 shows R_{AA} as a function of the number of participants with the comparison to the predictions from cold nuclear matter effects, where solid, dashed and dotted lines are the

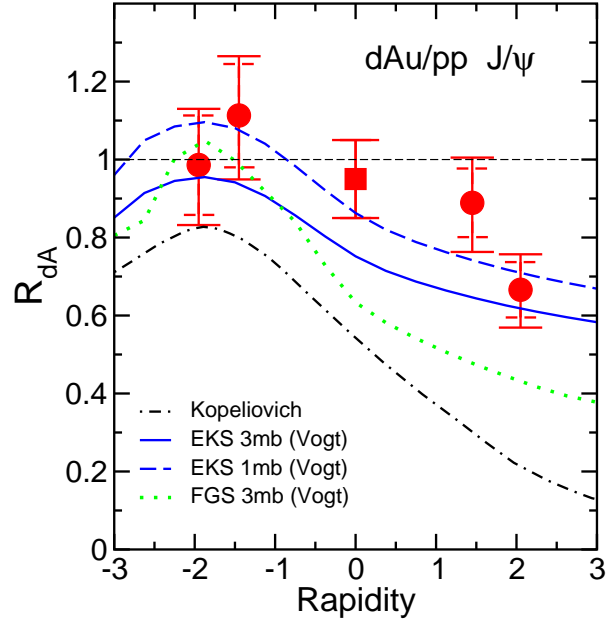


Figure 8.2: R_{dAu} as a function of rapidity. 12% overall normalization uncertainty is not shown here. The theoretical curves are described in text.

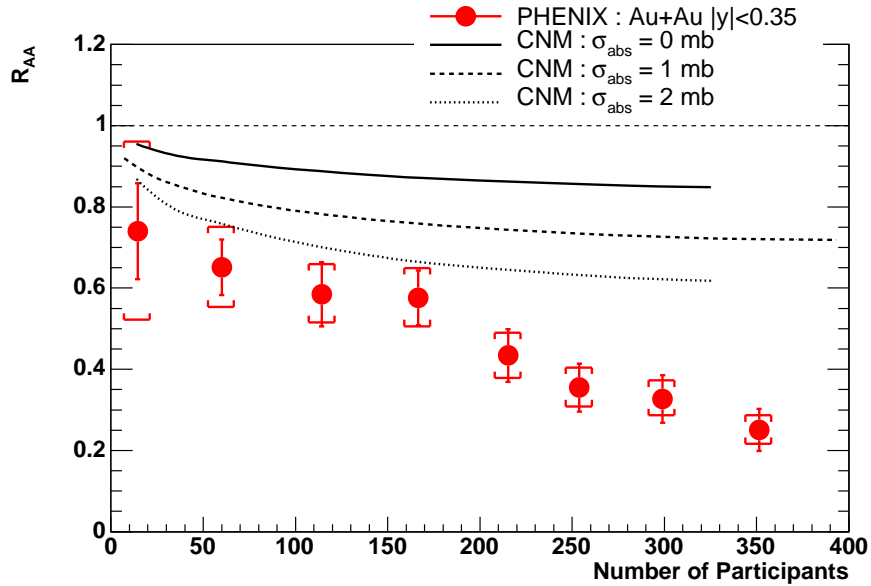


Figure 8.3: R_{AA} as a function of the number of participants. Bar corresponds to the quadratic summation of stat. error and uncorrelated sys. error. Bracket corresponds to the correlated sys. error, where T_{AB} error is included. Solid, dashed and dotted lines are the prediction of R_{AA} from cold nuclear matter effects with EKS shadowing and the nuclear absorption cross section of 0, 1 and 2 mb, respectively.

calculations based on EKS gluon shadowing and nuclear absorption cross section of 0, 1 and 2 mb, respectively [133].

The observed J/ψ suppression at RHIC is stronger by a factor of 2~3 relative to the cold nuclear matter effects in central Au+Au collisions.

8.2.2 Dissociation by comovers

After the nuclear absorption in the nuclear environment, the survived J/ψ interacts with secondary comoving hadrons ($J/\psi + h \rightarrow D + \bar{D}$) if QGP state isn't formed. The cross section of J/ψ with comovers, σ_{co} , of 0.65 mb can reproduce the observed J/ψ suppression at SPS [59, 63, 64]. The density of comovers was extrapolated from SPS to RHIC energy from the measurement of charged particle multiplicity, which was parameterized as a function of N_{part} and N_{col} [134].

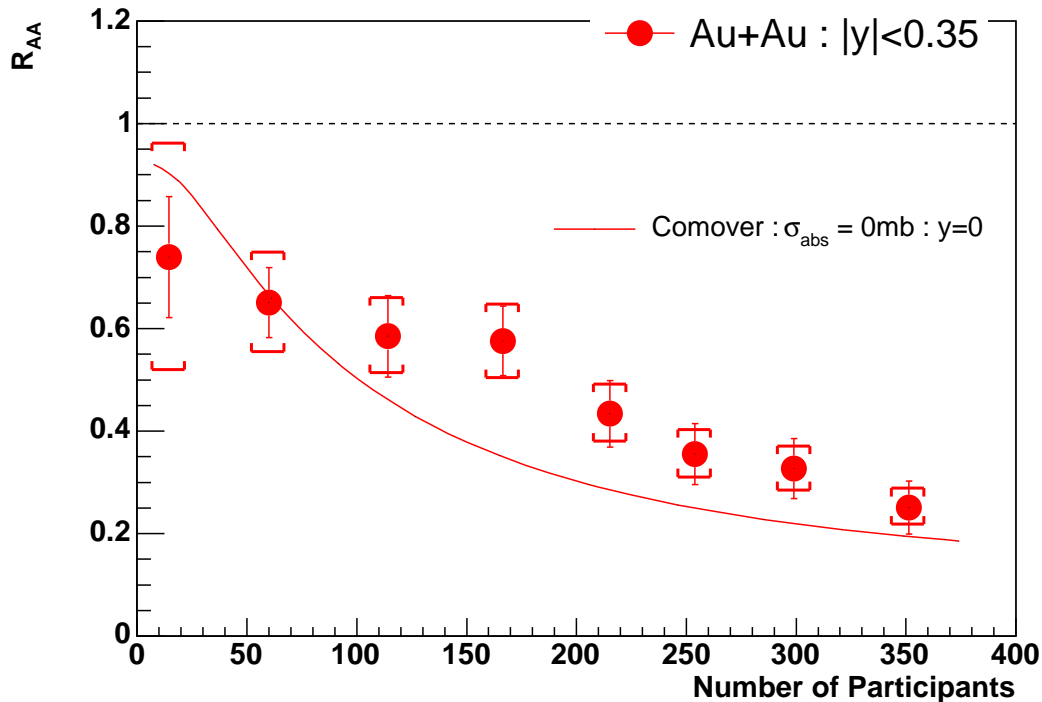


Figure 8.4: R_{AA} as a function of the number of participants. Bar corresponds to the quadratic summation of stat. error and uncorrelated sys. error. Bracket corresponds to the correlated sys. error, where T_{AB} error is included. Solid line is the prediction of R_{AA} from comover dissociation model, where the cold matter effects were taken into account (shadowing and the absorption cross section of 0 mb).

Figure 8.4 shows R_{AA} as a function of the number of participants with the comparison to the prediction from comover dissociation model, where comover interaction cross section was assumed to be same as SPS ($\sigma_{co} = 0.65$ mb) and cold nuclear matter effects (shadowing and 0 mb absorption cross section) were taken into account.

Suppression by comovers cannot reproduce the suppression pattern of J/ψ and it overestimates the J/ψ suppression at RHIC energy.

There should be noted that comover model could reproduce J/ψ suppression in Pb+Pb collisions at SPS, while it failed to describe the ψ' suppression in Pb+Pb collisions and J/ψ suppression in In+In collisions at SPS [135]. One of the interesting observations at SPS is that J/ψ suppression in S+U collisions is quite compatible to the nuclear absorption as shown in Fig. 2.13, while the comover density seems to be much larger in S+U collisions than that in p +A collisions.

8.2.3 Dissociation by thermal gluons in QGP

After the nuclear absorption in the nuclear environment, the survived J/ψ interacts with the thermal gluons in dense gluon field ($J/\psi + g \rightarrow c + \bar{c} + g$) The inelastic width (or dissociation rate) between J/ψ and gluons can be written as follows [51]:

$$\Gamma_\psi(T) = (\tau_{J/\psi})^{-1} = \sum_i \int \frac{d^3k}{(2\pi)^3} f^i(k; T) \sigma_\psi^{diss} v_{rel}, \quad (8.2)$$

where i runs over all matter constituents (q, \bar{q}, g), $f^i(k; T)$ is the (thermal) parton distribution function, σ_ψ^{diss} is parton-induced break up cross section and v_{rel} is the relative velocity between J/ψ and partons. σ_ψ^{diss} was calculated by the leading order diagram [48] and break up cross section by quark (anti-quark) can be negligible compared the break up cross section by gluons [136]. Thermal gluon distribution was assumed to be written as Bose distribution, $f^i(k; T) \propto [\exp(k/T) - 1]^{-1}$ [137].

There are two independent model predictions based on this dynamical dissociation picture. One takes into account the in-medium binding energy of J/ψ inferred from recent quenched lattice QCD calculations [138, 139]. The J/ψ yield in this model can be obtained by solving:

$$\frac{dN_\psi}{dt} = -\Gamma_\psi N_\psi \quad (8.3)$$

The result of R_{AA} as a function of the number of participants in this model was shown as the solid line in Fig. 8.5, where the shadowing and nuclear absorption (1.5 mb cross section) were taken into account.

The other model takes into account the transportation of J/ψ in the medium [52, 140]. J/ψ motion in QGP is described by a transport approach with continuous suppression controlled by the pQCD processes ($J/\psi + g \rightarrow c + \bar{c}$). The distribution function of J/ψ $f_{J/\psi}(\mathbf{p}_T, \mathbf{x}, \tau | \mathbf{b})$ in the transverse phase space $(\mathbf{p}_T, \mathbf{x})$ at fixed impact parameter \mathbf{b} is controlled by the transport equation:

$$\frac{\partial f_{J/\psi}}{\partial \tau} + \mathbf{v}_{J/\psi} \cdot \nabla f_{J/\psi} = -\alpha_{J/\psi} f_{J/\psi}, \quad (8.4)$$

where the second term in l.h.s arises from the free streaming of J/ψ with the transverse velocity $\mathbf{v}_{J/\psi}$ and suppression is reflected in the loss term α in r.h.s. Eq. (8.4) can be solved analytically with the result:

$$f_{J/\psi}(\mathbf{p}_T, \mathbf{x}, \tau | \mathbf{b}) = f_{J/\psi}(\mathbf{p}_T, \mathbf{x} - \mathbf{v}_{J/\psi}(\tau - \tau_0), \tau_0 | \mathbf{b}) \times \exp\left(-\int_{\tau_0}^{\tau} d\tau' \alpha_{J/\psi}(\mathbf{p}_T, \mathbf{x} - \mathbf{v}_{J/\psi}(\tau - \tau'), \tau' | \mathbf{b})\right), \quad (8.5)$$

where τ_0 is the formation time of QGP from when the suppression by thermal gluons sets in. The loss term α can be expressed as follows [140]:

$$\alpha_{J/\psi}(\mathbf{p}_T, \mathbf{x}, \tau | \mathbf{b}) = \frac{1}{2E_{J/\psi}} \int \frac{d^3k}{(2\pi)^3 2E_g} W_{gJ/\psi}^{c\bar{c}}(s) f_g(k, \mathbf{x}, \tau) \times \Theta(T(\mathbf{x}, \tau | \mathbf{b}) - T_c) \quad (8.6)$$

where the step function Θ corresponds to the onset of suppression by thermal gluons above T_c , the local temperature $T(\mathbf{x}, \tau | \mathbf{b})$ was determined by the hydrodynamics of the QGP and $W_{gJ/\psi}^{c\bar{c}}(s)$ is the pQCD calculated transport probability of the gluon dissociation as a function of the colliding energy \sqrt{s} . The final state J/ψ number and momentum distribution at fixed impact parameter $|\mathbf{b}|$ can be extracted by integrating the distribution function in Eq. (8.6) at time $\tau \rightarrow \infty$ over the transverse momentum and coordinate. The result of R_{AA} as a function of the number of participants in this model was shown as the dashed line in Fig. 8.5, where nuclear absorption (3 mb cross section assumed in this model) was taken into account.

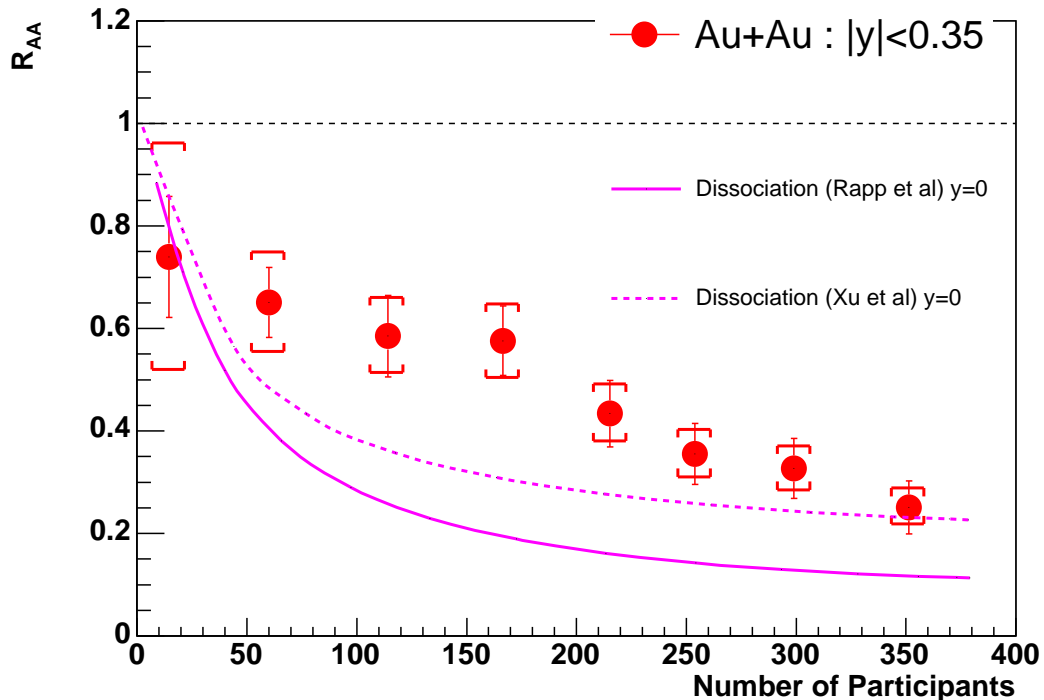


Figure 8.5: R_{AA} as a function of the number of participants. Bar corresponds to the quadratic summation of stat. error and uncorrelated sys. error. Bracket corresponds to the correlated sys. error, where T_{AB} error is included. The solid and dashed lines are explained in text.

Both models can reproduce observed J/ψ suppression at SPS [51, 140]. However the J/ψ suppression observed at RHIC is not so strong as expected by these models extrapolated from SPS to RHIC.

One of the questionable points in these models is that it is not sure that the break up process of J/ψ by gluons can be described perturbative QCD process. Although the radius

of J/ψ is small and binding energy is large compared to typical QCD scale in vacuum, lattice QCD calculations and potential model analyses show that the binding energy decreases as temperature goes high, which indicates that the process may be more complicated and higher order diagram may contribute in high temperature environment [136]. For the small binding energy, the validity of the perturbative calculations for gluonic dissociation cross section might be questionable. The same point is raised for the dissociation of ψ' and χ_c by gluons, since their binding energy is compatible or less than typical QCD scale. Treatment of the feed-down fraction is also questionable.

8.2.4 Dissociation \oplus recombination of J/ψ

Recombination of J/ψ from uncorrelated $c\bar{c}$ pairs has been expected at RHIC energy since the charm quark pairs are created more abundantly, a factor of ~ 100 , in central A+A collisions at RHIC energy compared to SPS energy. The approach for the J/ψ production from recombination in A+A collisions has been discussed widely and various recombination models have been emerged such as kinetic models and transport models which assume the continuous destruction and formation of J/ψ in QGP and/or later stage [146, 147, 51, 138, 139, 140, 52] and the statistic coalescence models which assumes the creation of J/ψ around the phase boundary between QGP and hadron phase according to statistical law [54, 141, 142, 144, 55, 145].

Kinetic formation

In this model, the conditions for J/ψ recombination are assessed in terms of a simple rate equation for the time evolution of the number of J/ψ 's:

$$\frac{dN_\psi}{dt} = -\Gamma_\psi(N_\psi - N_\psi^{eq}), \quad (8.7)$$

where Γ_ψ is given by Eq. (8.2) and $N_\psi^{eq}(T; \gamma_c)$ is J/ψ number in thermal equilibrium, which determines the J/ψ recombination and can be expressed as follows [51]:

$$N_\psi^{eq}(T; \gamma_c) = V_{FB} n_\psi^{eq}(T; \gamma_c) \quad (8.8)$$

$$n_\psi^{eq}(T; \gamma_c) = 3\gamma_c^2 \int \frac{d^3q}{(2\pi)^3} f^\psi(m_\psi, T), \quad (8.9)$$

where V_{FB} is fireball 3-volume [148], $n_\psi^{eq}(T; \gamma_c)$ is the density and γ_c is the charm quark fugacity which is adjusted to the total number of $c\bar{c}$ pairs $N_{c\bar{c}}$ in the system via [143, 144]:

$$N_{c\bar{c}} = \frac{1}{2}\gamma_c N_{op} \frac{I_1(\gamma_c N_{op})}{I_0(\gamma_c N_{op})} + V_{FB} \Sigma_\psi n_\psi^{eq}(T; \gamma_c), \quad (8.10)$$

where $N_{op} = V_{FB} n_{op}(m_{c,D}; T)$ denotes the total equilibrium number of open-charm states (c quark and charmed meson). As a results, $N_\psi^{eq}(T; \gamma_c)$ is sensitive to the open charm yield (cross section), open-charm spectrum and in-medium masses of c quarks.

The results of R_{AA} in this model are shown in the panel “a)” and “b)” in Fig. 8.6. The result shown in the panel “a)” takes into account the in-medium modification of charm quark

mass, charm thermalization (relaxation time of charm quarks in medium) and binding energy of charmonium states [138] in the medium. The result shown in the panel “b)” does not take into account these in-medium effects at all [147].

Transport model

This model is extension of the model associated to J/ψ suppression in transport approach [52]. The distribution function $f_{J/\psi}$ can be expressed in this model by adding the gain term in r.h.s in Eq. (8.4):

$$\frac{\partial f_{J/\psi}}{\partial \tau} + \mathbf{v}_{J/\psi} \cdot \nabla f_{J/\psi} = -\alpha_{J/\psi} f_{J/\psi} + \beta_{J/\psi}. \quad (8.11)$$

The distribution function $f_{J/\psi}$ in Eq. (8.11) can be obtained analytically as follows:

$$f_{J/\psi}(\mathbf{p}_T, \mathbf{x}, \tau | \mathbf{b}) = f_{J/\psi}(\mathbf{p}_T, \mathbf{x} - \mathbf{v}_{J/\psi}(\tau - \tau_0), \tau_0 | \mathbf{b}) \times e^{-\int_{\tau_0}^{\tau} d\tau' \alpha_{J/\psi}(\mathbf{p}_T, \mathbf{x} - \mathbf{v}_{J/\psi}(\tau - \tau'), \tau' | \mathbf{b})} \\ + \int_{\tau_0}^{\tau} d\tau' \beta_{J/\psi}(\mathbf{p}_T, \mathbf{x} - \mathbf{v}_{J/\psi}(\tau - \tau'), \tau' | \mathbf{b}) \times e^{-\int_{\tau'}^{\tau} d\tau'' \alpha_{J/\psi}(\mathbf{p}_T, \mathbf{x} - \mathbf{v}_{J/\psi}(\tau - \tau''), \tau'' | \mathbf{b})} \quad (8.12)$$

The gain term is related to the inverse process of the gluon dissociation and β can be written as:

$$\beta_{J/\psi}(\mathbf{p}_T, \mathbf{x}, \tau | \mathbf{b}) = \frac{1}{2E_{J/\psi}} \int \frac{d^3k}{(2\pi)^3 2E_g} \frac{d^3q}{(2\pi)^3 2E_c} d^3q' (2\pi)^3 2E_{\bar{c}} \\ \times W_{c\bar{c}}^{gJ/\psi}(s) f_c(\mathbf{q}, \mathbf{x}, \tau | \mathbf{b}) f_{\bar{c}}(\mathbf{q}', \mathbf{x}, \tau | \mathbf{b}) \\ \times (2\pi)^4 \delta^4(p + k - q - q') \times \Theta(T(\mathbf{x}, \tau | \mathbf{b}) - T_c), \quad (8.13)$$

where there is again a step function controlling the recombination region in the coordinate space, $E_g = \sqrt{\mathbf{k}^2 + m_g^2}$, $E_{J/\psi} = \sqrt{\mathbf{p}_T^2 + m_{J/\psi}^2}$, $E_c = \sqrt{\mathbf{q}^2 + m_c^2}$, $E_{\bar{c}} = \sqrt{\mathbf{q}'^2 + m_{\bar{c}}^2}$ are the gluon, J/ψ and charm quark energies and $W_{c\bar{c}}^{gJ/\psi}$ is the transition probability of $c\bar{c}$ recombination and can be expressed in terms of $W_{gJ/\psi}^{c\bar{c}}$ from the detailed balance requirement. The charm quark distribution $f_c(\mathbf{q}, \mathbf{x}, \tau | \mathbf{b})$ in QGP is not well understood since the charm quarks are heavy and may not be fully thermalized. For simplicity, two kinds of charm quark distribution functions (f_c and $f_{\bar{c}}$) were assumed [52]. In the weak interaction limit of charm quarks in QGP, the charm quarks are expected to keep their original momentum distribution $g_c(\mathbf{q})$ derived directly by pQCD calculation [146] and their initial space distribution determined by nuclear geometry,

$$f_{c,\bar{c}}(\mathbf{q}, \mathbf{x} | \mathbf{b}) = \sigma_{pp}^{c\bar{c}} T_A(\mathbf{x}) T_B(\mathbf{x} - \mathbf{b}) g_{c,\bar{c}}(\mathbf{q}), \quad (8.14)$$

where $\sigma_{pp}^{c\bar{c}} = 622 \mu\text{b}$ is the cross section for initial charm production at RHIC energy [149]. In the strong interaction limit, where c and \bar{c} are strongly correlated to the medium, they are thermalized and distributed in the phase space according to the statistic law,

$$f_{c,\bar{c}}(\mathbf{q}, \mathbf{x} | \mathbf{b}) \sim \frac{1}{e^{p_\mu u^\mu/T} + 1}, \quad (8.15)$$

where $u_\mu(\mathbf{x}, \tau | \mathbf{b})$ is the medium velocity.

The result of R_{AA} in this model is shown in the panel “c)” in Fig. 8.6, where solid line is the calculation with pQCD charm quark distribution and dashed line is the calculation with thermal charm quark distribution.

Statistic coalescence model

This model assumes that all heavy quarks are created in primary hard collisions and that their abundance stays constant until hadronization. For the charmonia state, this model assumes that no charmonia production takes place before the formation time τ_0 of the QGP or that all charmonia formed before τ_0 are melted in the initial hot QGP phase and that all the charmonia are produced when the system hadronizes. The number of directly produced $c\bar{c}$ pairs $N_{c\bar{c}}^{dir}$ can be expressed in this framework as follows [54]:

$$N_{c\bar{c}}^{dir} = \frac{1}{2}\gamma_c N_{oc}^{th} \frac{I_1(\gamma N_{oc}^{th})}{I_0(\gamma N_{oc}^{th})} + \gamma_c^2 N_{c\bar{c}}^{th}, \quad (8.16)$$

where I_n is modified Bessel function, γ_c is fugacity parameter that takes into account the deviations of heavy quark multiplicity from the value expected in complete chemical equilibrium and N_{oc}^{th} and $N_{c\bar{c}}^{th}$ are the total number of open and hidden charm hadrons, respectively. In the fireball volume V , N_{oc}^{th} and $N_{c\bar{c}}^{th}$ can be written as $N_{oc}^{th} = n_{oc}^{th}V$ and $N_{c\bar{c}}^{th} = n_{c\bar{c}}^{th}V$, where n_{oc}^{th} and $n_{c\bar{c}}^{th}$ are the grand-canonical densities, respectively. The open charm and hidden charm densities can be expressed in the grand-canonical ensemble as follows [144]:

$$\begin{aligned} N_j &= \frac{d_j e^{\mu_j/T}}{2\pi^2} T m_j^2 I_2(m_j/T) \\ &\simeq d_j e^{\mu_j/T} \left(\frac{m_j T}{2\pi}\right)^{3/2} \exp\left(-\frac{m_j}{T}\right), \end{aligned} \quad (8.17)$$

where T is the temperature of the system, m_j and d_j denote the particle mass and degeneracy factors and I_2 is the modified Bessel function. The particle chemical potential μ_j in Eq. (8.17) is defined as:

$$\mu_j = b_j \mu_B + s_j \mu_s + c_j \mu_c, \quad (8.18)$$

where b_j , s_j and c_j are the baryonic number, strangeness and charm number of particle j , respectively. The baryonic chemical potential μ_B regulates the baryonic density at the phase boundary, while the strange and charm chemical potentials μ_s and μ_c should be found from the requirement of zero value for the total strangeness and charm in the system. The second term in r.h.s in Eq. (8.16) is the expected charmonia yield in this model. The input parameters of this model are the temperature T and baryochemical potential μ_b for statistical model calculations, the heavy quark production cross section $\sigma_{pp}^{c\bar{c}}$ in nucleon-nucleon collisions and the volume of one unit rapidity, V at chemical freeze-out. (T, μ_b) of (161, 22.4) MeV was used [150] and $\sigma_{pp}^{c\bar{c}}$ was taken from recent pQCD calculations [151], where the number of produced charm quark pairs in A+A collisions was calculated by using nuclear overlap function T_{AA} as $N_{c\bar{c}} = \sigma_{pp}^{c\bar{c}} \times T_{AA}$. The volume V was estimated from the following relation:

$$dN_{ch}/dy = n_{ch}^{th} V, \quad (8.19)$$

where dN_{ch}/dy was measured charged particle multiplicity per unit rapidity [152] and n_{ch}^{th} is the charged particle density computed within thermal model. Resulting charm canonical suppression factor I_1/I_0 and fugacity γ_c as a function of the number of participants at RHIC Au+Au collisions are shown in Ref. [142]. The result of R_{AA} in this model is shown in the panel “d)” in Fig. 8.6.

Hadron-String Dynamics

Hadron-String-Dynamics (HSD) transport is one of the models to describe the nuclear dynamics and to understand the creation of hot and dense hadronic matter and modification of hadron properties in a hot and dense medium. For each particle species i ($i = N, \pi, \rho, K$ and so on), the phase space density f_i follows the transport equation [153].

$$\left(\frac{\partial}{\partial t} + \left(\frac{\partial}{\partial \mathbf{p}} H\right) \cdot \frac{\partial}{\partial \mathbf{r}} - \left(\frac{\partial}{\partial \mathbf{r}} H\right) \cdot \frac{\partial}{\partial \mathbf{p}}\right) f_i(\mathbf{r}, \mathbf{p}, t) = I_{coll}(f_1, f_2, \dots, f_N), \quad (8.20)$$

where I_{coll} is the collision term describing elastic and inelastic hadronic reactions such as baryon-baryon, baryon-meson and meson-meson, formation and decay of baryonic and mesonic resonances and detail balance on the level of $1 \leftrightarrow 2$ and $2 \leftrightarrow 2$ ($2 \leftrightarrow n$) reactions. The collisional term I_{coll} can be expressed as follows [153]:

$$\begin{aligned} I_{coll} = & \Sigma_{h_2, h_3, h_4 \dots} \int d_2 d_3 d_4 \dots \delta^4(E + E_2 - E_3 - E_4 \dots) \\ & \times \left(f_{h_3}(x, p_3) f_{h_4}(x, p_4) | M |_{34 \rightarrow 12 \dots}^2 \bar{f}(x, p) \bar{f}_2(x, p_2) \right. \\ & \left. - f_h(x, p) f_{h_2}(x, p_2) | M |_{12 \rightarrow 34 \dots}^2 \bar{f}_3(x, p_3) \bar{f}_4(x, p_4) \right) \dots, \end{aligned} \quad (8.21)$$

where $| M |_{12 \leftrightarrow 34 \dots}^2 \delta^4(E + E_2 - E_3 - E_4 \dots)$ is the transition rate for the process $1+2 \leftrightarrow 3+4 \dots$ and $\bar{f}(x, p) = 1 \pm f(x, p)$ is the phase-space factors which are responsible for fermion Pauli-blocking or Bose enhancement depending on the type of hadron in the final/initial channel [153].

For the description of J/ψ production in A+A collisions, this model takes into account the destruction of J/ψ by secondary hadrons (π, ρ, K and baryons) and their backward reactions to form J/ψ [55]. Also nuclear absorption of J/ψ with the cross section of 4.4 mb inferred from SPS energies and feed-down contribution of ψ' and χ_c are taken into account.

The result of R_{AA} in this model is shown in the panel “e)” in Fig. 8.6.

From Fig. 8.6, J/ψ suppression can be described much better by the models with the recombination scenario. However, the centrality dependence of J/ψ suppression, in particular, the trend of J/ψ suppression falling down above the number of participant nucleons of ~ 160 , cannot be well described with these results.

There are some questionable points in these models. First, the dissociation cross section of J/ψ by gluons is not well understood at higher temperature regime, as mentioned previously. Second, the charm quarks are expected to be created only at the initial stage of collisions and the abundance will be fixed then, which means that the production of charmed hadrons doesn't follow the statistical law. Application of statistical law for the production of charmed hadrons seems to be questionable.

As pointed out in Sec. 2.4.1, the charm production such as cross section as functions of charm p_T and rapidity and its modification in hot and dense medium need to be understood quantitatively since they are the input parameters for the recombination of J/ψ . At RHIC energy, charm production seems to be flatter as a function of rapidity than the pQCD expectations [57]. Moreover, charm quarks suffer significant energy loss in hot and dense medium and participate in the partonic flow [58]. The mechanisms to explain those observations simultaneously are still open questions.

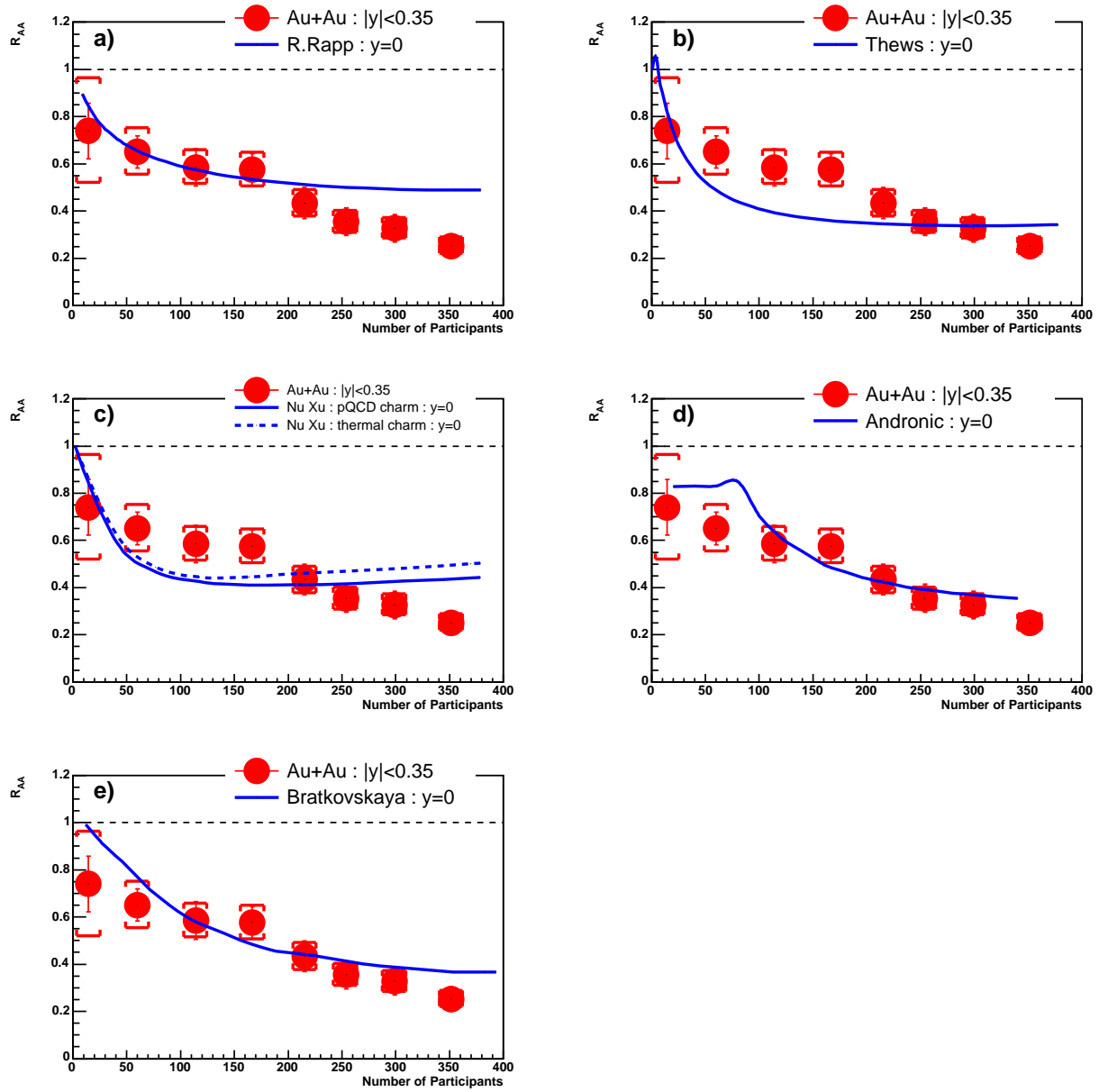


Figure 8.6: R_{AA} as a function of the number of participants. Bar corresponds to the quadratic summation of stat. error and uncorrelated sys. error. Bracket corresponds to the correlated sys. error, where T_{AB} error is included. Solid lines in “a)” and “b)” are the calculation from kinetic formation model described in text. Solid and dashed lines in “c)” are from transport model, where charm quark distribution was taken from pQCD or thermal one, respectively. Solid lines in “d)” and “e)” are from statistical hadronization model and HSD model, respectively.

8.2.5 Sequential melting

Finite temperature (quenched) lattice QCD calculations and potential model calculations predict that the J/ψ can survive in QGP up to $\sim 2 T_c$, while excite states χ_c and ψ' are dissociated just above T_c [42, 43, 44, 46, 47].

In hadron-hadron collisions, it is found that about 60% of the observed J/ψ 's are directly produced as (1S) states and other $\sim 35\%$ are coming from χ_c and $\sim 5\%$ from ψ' decay [36]. The difference in the dissociation temperatures of these charmonia states thus leads to a sequential melting of J/ψ , where suppression of J/ψ from χ_c and ψ' decay occurred at lower temperature and “directly” produced J/ψ is suppressed at higher temperature [154, 155].

Survive probability of J/ψ $S_{J/\psi}$ in A+A collisions is defined as the ratio of the nuclear modification factor R_{AA} to that expected from the cold nuclear matter effects. This gives the quantitative information on the J/ψ suppression due to the final state effects. It is assumed that $S_{J/\psi}$ consists of two terms: one term $S_{J/\psi}^{dir}$ which corresponds to the survival probability of directly produced J/ψ and a second term S_χ which corresponds to the survival probability of J/ψ decayed from χ_c and ψ' . By taking into account the feed-down contribution from ψ' and χ_c (total $\sim 40\%$) [36], $S_{J/\psi}$ can be written as follows:

$$S_{J/\psi} = 0.6S_{J/\psi}^{dir} + 0.4S_\chi. \quad (8.22)$$

Figure 8.7 shows $S_{J/\psi}$ as a function of energy density at SPS energies (Upper) [155] and at SPS and RHIC energies (Bottom). Here, energy density was estimated using Bjorken's formula [13]:

$$\epsilon_{bj} = \frac{1}{A_\perp \tau_0} \frac{dE_T}{dy}, \quad (8.23)$$

where A_\perp is the transverse area, τ_0 is the formation time of QGP and dE_T/dy is the transverse energy density per unit rapidity. For the PHENIX data points, A_\perp and $\frac{dE_T}{dy}$ were taken from Ref. [15]. For the formation time τ_0 , $\tau_0 = 1$ fm/c was taken at both SPS and RHIC energies here. This formation time τ_0 of 1 fm/c seems under-estimated at SPS energies since the crossing time of the nuclei is ~ 1.6 fm/c, while it seems over-estimated at RHIC energies. Measurement of particle azimuthal anisotropy and comparison to thermo-hydrodynamics calculations show that the formation time is ~ 0.6 fm/c [157]. The other estimation of τ_0 at RHIC was done in Ref. [158]. The average transverse mass $\langle m_T \rangle$, which can be extracted by $\langle m_T \rangle = (dE_T/dy)/(dN/dy)$, is $\simeq 0.57$ GeV, which gives the formation time of $t \simeq \hbar/m_T \simeq 0.35$ fm/c.

Results of $S_{J/\psi}$ in NA50 Pb+Pb collisions and NA60 In+In collisions are shown in both panels, where the systematic error due to the uncertainty of cold nuclear matter effects ($\sim 10\%$) are not shown. $S_{\psi'}$ in NA50 Pb+Pb collisions is available in Ref. [156] and $0.6+0.4S_{\psi'}$ is also shown in the upper panel in Fig. 8.7. Bottom shows the $S_{J/\psi}$ as a function of energy density in NA50 Pb+Pb, NA60 In+In and PHENIX Au+Au collisions. Here the cold nuclear matter effects at RHIC were taken from Ref. [133], which is shown as a dashed-line in Fig. 8.3 ($\sigma_{abs} = 1.0$ mb). Additional systematic errors due to the uncertainties in cold nuclear matter effects were evaluated using $\sigma_{abs} = 0$ mb and 2 mb, which were shown as boxes on PHENIX data points. Table 8.1 is the summary of $S_{J/\psi}$ as a function of centrality in Au+Au collisions at RHIC.

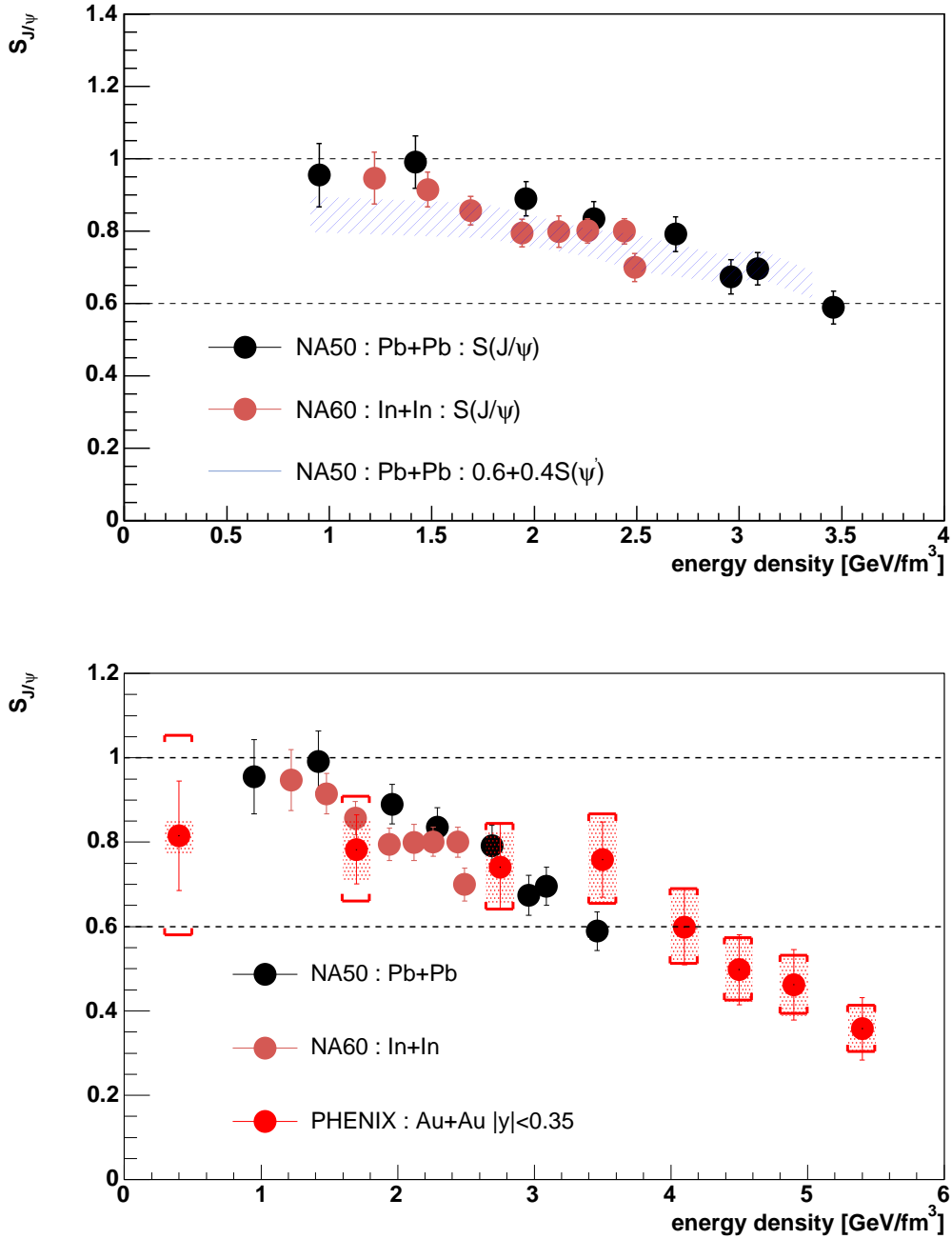


Figure 8.7: Upper : $S_{J/\psi}$ as a function of energy density in NA50 Pb+Pb collisions (Black), NA60 In+In collisions (Brown) and calculated probability $0.6+0.4S_{\psi'}$ by using ψ' measurement in NA50 Pb+Pb collisions [156]. Systematic error approximately 16% shown in Fig. 8.1 are not shown here. Bottom : $S_{J/\psi}$ as a function of energy density in NA50 Pb+Pb (black), NA60 In+In (brown) and PHENIX Au+Au collisions (red). Additional systematic error due to the uncertainty in cold nuclear matter effects are shown as box on PHENIX data points.

centrality	N_{part}	ϵ_{bj} [GeV/fm ³]	$S_{J/\psi} \pm \text{uncor. sys.} \pm \text{cor. sys.} \pm \text{CNM sys}$
0-5%	351.4	5.40	$0.358 \pm 0.073 \pm 0.055 \pm 0.057$
5-10%	299	4.90	$0.462 \pm 0.078 \pm 0.070 \pm 0.073$
10-15%	253.9	4.50	$0.498 \pm 0.081 \pm 0.074 \pm 0.075$
15-20%	215.3	4.10	$0.599 \pm 0.087 \pm 0.088 \pm 0.087$
20-30%	166.6	3.50	$0.759 \pm 0.080 \pm 0.107 \pm 0.103$
30-40%	114.2	2.75	$0.741 \pm 0.090 \pm 0.102 \pm 0.087$
40-60%	60.0	1.70	$0.783 \pm 0.082 \pm 0.125 \pm 0.072$
60-93%	14.5	0.40	$0.815 \pm 0.123 \pm 0.236 \pm 0.040$

Table 8.1: $S_{J/\psi}$ in Au+Au collisions as a function of centrality.

$S_{J/\psi}$ at SPS and RHIC from peripheral to mid-central Au+Au collisions ($\epsilon_{bj} \leq 4$) seem to be consistent with the melting of χ_c and ψ' , where $S_{J/\psi}$ is in good agreement with $0.6 + 0.4S_{\psi'}$. For more central collisions, survival probability of J/ψ is below 0.6, which means that direct J/ψ might be suppressed. However, systematic error due to the uncertainty of cold nuclear matter effects are large and more precise data for d +Au collisions is urgently needed. Also feed-down fraction from χ_c and ψ' needs to be measured at RHIC energy.

8.2.6 Threshold model

This model is motivated by the color screening scenario in QGP, where all charmonia are destroyed in the medium above the threshold energy density [159, 160, 161].

This model assumes that the fate of J/ψ depends on the local energy density where J/ψ is formed. Local energy density is proportional to the participant density. If the energy density or participant density exceeds a critical or threshold value, all the J/ψ 's are completely destroyed. Transverse expansion of the system is neglected in this model. In the collisions, where the energy density is below threshold, J/ψ is absorbed only due to J/ψ -nucleon interaction.

The production cross section of J/ψ in A+A collisions at the impact parameter \mathbf{b} can be expressed as follows:

$$\sigma_{AA}^{J/\psi}(\mathbf{b}) = \sigma_{NN}^{J/\psi} \int d^2\mathbf{s} T_A^{eff}(\mathbf{s}) T_B^{eff}(\mathbf{b} - \mathbf{s}) \times S_{anom}(\mathbf{b}, \mathbf{s}), \quad (8.24)$$

where S_{anom} is the suppression factor, $T^{eff}(\mathbf{b})$ is the effective nuclear overlap function and \mathbf{s} is the transverse position. S_{anom} and $T^{eff}(\mathbf{b})$ can be written as follows:

$$S_{anom}(\mathbf{b}, \mathbf{s}) = \Theta(n(\mathbf{b}, \mathbf{s}) - n_c) \quad (8.25)$$

$$T^{eff}(\mathbf{b}) = \int_{-\infty}^{\infty} dz \rho(\mathbf{b}, z) \exp\left(-\sigma_{abs} \int_z^{\infty} dz' \rho(\mathbf{b}, z')\right), \quad (8.26)$$

where $n(\mathbf{b}, \mathbf{s})$ is the local participant transverse density, n_c is the threshold density, σ_{abs} is the J/ψ -nucleon absorption cross section and ρ is the nuclear density function which can be described by Woods-Saxon form. It was realized that if the theta function is smeared such that the

suppression is gradual rather than abrupt, the quality of fit to data improves considerably [159]. Therefore S_{anom} is re-written as follows:

$$S_{anom}(\mathbf{b}, \mathbf{s}) = 0.5[1 - \tanh(\lambda(n(\mathbf{b}, \mathbf{s}) - n_c))]. \quad (8.27)$$

Local participant transverse density $n(\mathbf{b}, \mathbf{s})$ at the impact parameter \mathbf{b} and the transverse position \mathbf{s} can be written as follows:

$$n(\mathbf{b}, \mathbf{s}) = T_A(\mathbf{s})[1 - \exp(-\sigma_{NN}T_B(\mathbf{s} - \mathbf{b}))] + T_B(\mathbf{b} - \mathbf{s})[1 - \exp(-\sigma_{NN}T_A(\mathbf{s}))]. \quad (8.28)$$

Figure 8.8 shows the transverse participants density in Cu+Cu (left) and Au+Au (right) collisions for various values of the impact parameter, $b=0, 2, 4, \dots$ (from top to bottom). The x axis is the distance of from the center of two colliding nuclei, where $x = 0$ corresponds to the $b/(1 + R_A/R_B)$ from the center of the nucleus A [161]. For the most central Au+Au collisions,

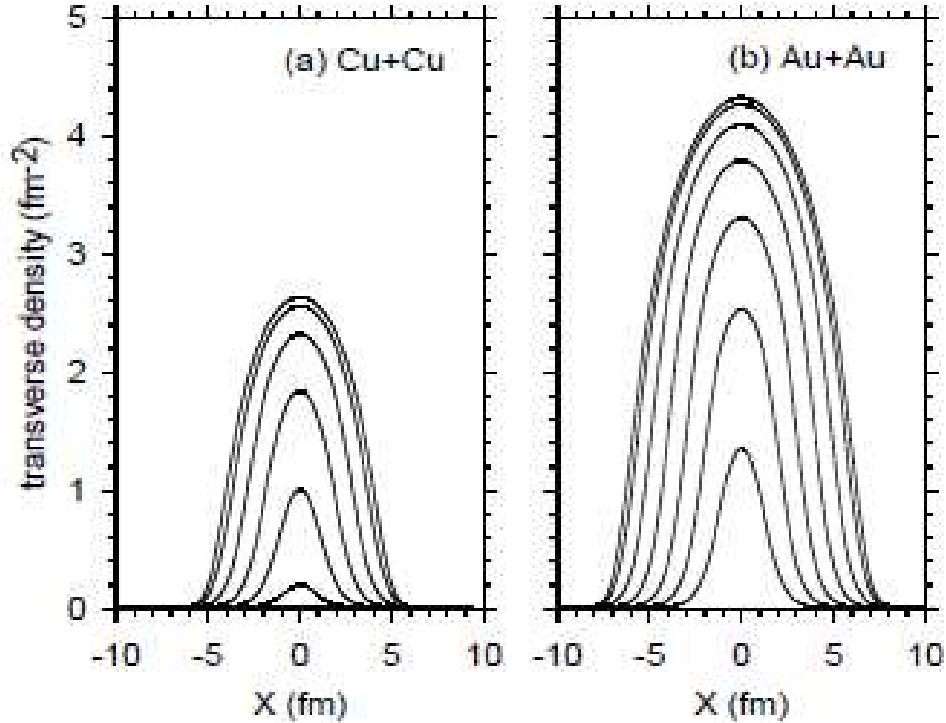


Figure 8.8: Transverse participants density in Cu+Cu (left) and Au+Au (right) collisions for various values of the impact parameter, $b=0, 2, 4, \dots$ (from top to bottom). The origin is at a distance, $d = b/(1 + R_A/R_B)$ from the center of the nucleus A [161].

maximum transverse participant density is $\sim 4.32 \text{ fm}^{-2}$.

The results of R_{AA} in this model is shown in Fig. 8.9 for various threshold parameters $n_c = 3.6$ (blue), 3.8 (green), 4.0 (red) and ∞ (black) fm^{-2} . The cross section of nuclear absorption is taken to be 3 mb. Since this model does not take into account the feed-down contribution from ψ' and χ_c , such feed-down effect is practically taken over by the larger nuclear absorption cross section of 3 mb. However, this model can describe observed J/ψ suppression at RHIC, which means that J/ψ is dissolved in QGP.

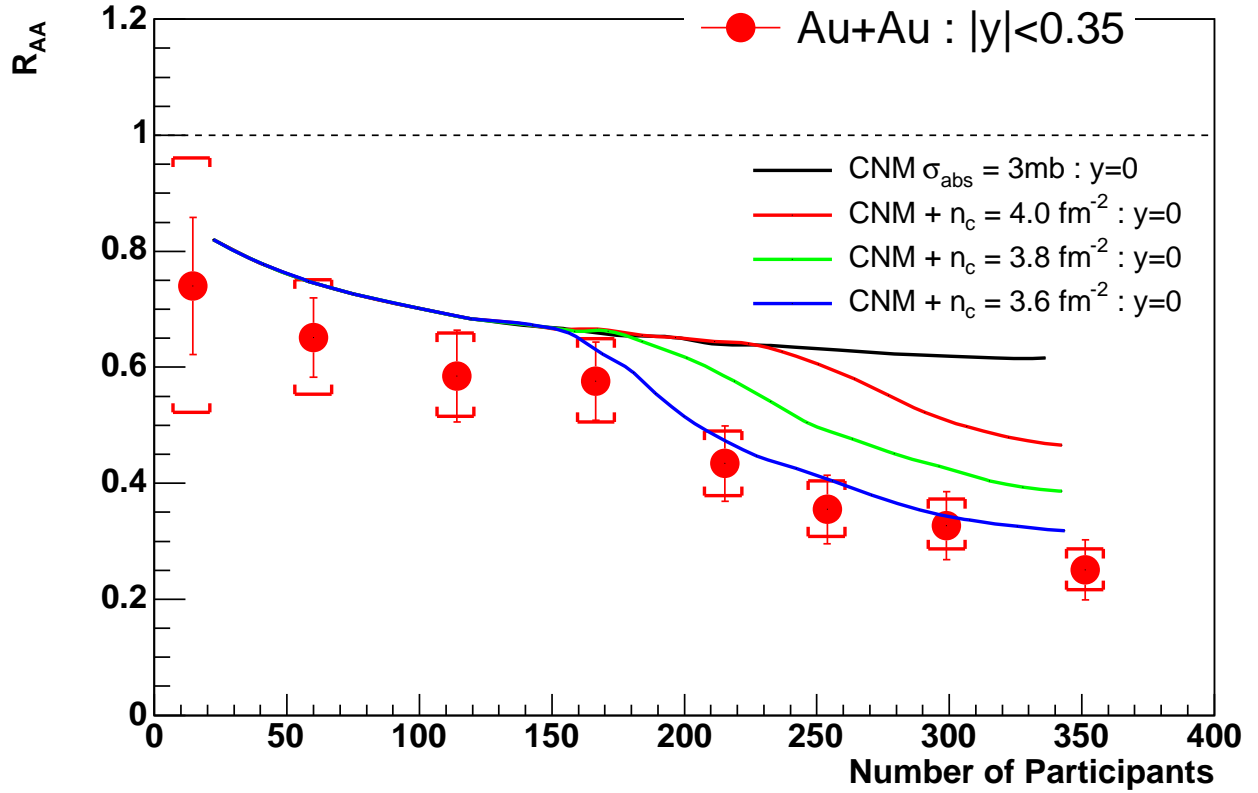


Figure 8.9: R_{AA} as a function of the number of participants. Bar corresponds to the quadratic summation of stat. error and uncorrelated sys. error. Bracket corresponds to the correlated sys. error, where T_{AB} error is included. Red, green and blue lines are the calculations of this model with the threshold density of $n_c = 4.0, 3.8, 3.6 \text{ fm}^{-2}$, respectively. Black line is the calculation, where only the nuclear absorption is taken into account.

8.2.7 χ^2 test for the theoretical models

Quantitative check was done to investigate how the theoretical models support the observed J/ψ suppression well. The average difference D and the dispersion χ^2 between data points and the theoretical models were calculated based on the following equation.

$$D(\text{data} - \text{theory}) = \frac{\sum_i (R_{AA}^{data}(i) - R_{AA}^{theory}(i))/\sigma^2(i)}{\sum_i 1/\sigma^2(i)}, \quad (8.29)$$

$$\chi^2(\text{data} - \text{theory}) = \sum_i \left(\frac{R_{AA}^{data}(i) - R_{AA}^{theory}(i)}{\sigma(i)} \right)^2 \quad (8.30)$$

where summation was taken over all centrality bins i and the quadratic sum between statistical error and systematic errors were used as the weight for $\sigma^2(i)$.

Table 8.2 is the summary of the D and χ^2 between data points and theoretical models.

Model	D	$\chi^2/\text{n.d.f}$	Ref.
CNM effects ($\sigma_{abs}=1\text{mb}$)	-0.35	16.92	Fig. 8.3
comover model	0.10	1.93	Fig. 8.4
gluon dissociation (Xu)	0.11	2.49	Fig. 8.5
gluon dissociation (Rapp)	0.22	7.29	Fig. 8.5
kinetic formation (Rapp)	-0.12	2.90	Fig. 8.6
kinetic formation (Thews)	0.04	1.70	Fig. 8.6
transport model (Xu)	-0.03	2.20	Fig. 8.6
statistic coalescence model (Anton)	-0.04	0.77	Fig. 8.6
hadron-string-dynamics	-0.05	0.88	Fig. 8.6
threshold model ($n_c = 3.6$)	-0.05	0.44	Fig. 8.9

Table 8.2: Summary of D and χ^2 between data points and various theoretical models.

Conclusion from model comparison

From these comparison, J/ψ production in Au+Au collisions at RHIC can be concluded:

- **J/ψ is stronger suppressed relative to cold nuclear matter effects**
However, the CNM effects at RHIC is large uncertainties due to the small statistics of J/ψ in d +Au collisions. More precise measurements will be needed in future.
- **J/ψ suppression is not so strong as expected from dissociation scenario extrapolated from SPS to RHIC.**
However, dissociation of J/ψ , χ and ψ' with gluons and comovers in pQCD approach is questionable in higher temperature environment, where the binding energy is compatible to or less than the typical QCD scale.

- **J/ψ suppression can be described better with dissociation and recombination.** Recombination of J/ψ seems to compensate the stronger J/ψ suppression at RHIC. However, charm production at RHIC energy and its modification of medium such as large energy loss and thermalization of charm quarks in medium are still poorly known.
- **Suppression from peripheral to mid-central collisions can be interpreted by the melting of only χ_c and ψ' .** Direct J/ψ seems to be suppressed for most central collisions.

8.3 Model Calculation for J/ψ Suppression

The evolution of the medium is described by the hydrodynamics. Hydrodynamics calculations reproduce the observed particle spectra in low p_T region, azimuthal anisotropy of particles and particle multiplicity for wide pseudo-rapidity region very well [162, 163]. Another theoretical model was constructed by the author. This model copes with the evolution of the medium and the fate of J/ψ in the medium, simultaneously. The evolution of the medium is characterized by the temperature $T(\mathbf{x}, t)$, parton density $\rho(\mathbf{x}, t)$ and the transverse flow $\beta(\mathbf{x}, t)$ of the medium as a function of space-time point (\mathbf{x}, t) . In this model, $T(\mathbf{x}, t)$, $\rho(\mathbf{x}, t)$ and $\beta(\mathbf{x}, t)$ in Ref. [164] were used and were provided by T. Hirano and Y. Nara. The strategy to study of the J/ψ suppression (including feed-down effect) is as follows:

- Determination of the trajectory of J/ψ inside QGP

The production points of J/ψ (\mathbf{x}_0), p_T of J/ψ and the azimuthal angle of J/ψ ($\phi_{J/\psi} = \arctan(y, x)$) are the input parameters and the rapidity of J/ψ is set to be 0 ($p_z = 0$) in this calculation. Inside the QGP, J/ψ is assumed to be moved as

$$\mathbf{x}_{J/\psi}(t) = \boldsymbol{\beta}_{J/\psi} t + \mathbf{x}_0, \quad (8.31)$$

where $\boldsymbol{\beta}_{J/\psi}$ is the velocity vector of J/ψ and the trajectory was extracted for each $\Delta t = 0.2$ fm/ c . The formation time of J/ψ is not taken into account. The values of the input parameters are described later.

- Determination of the $T(\mathbf{x}, t)$, $\rho(\mathbf{x}, t)$ and $\beta(\mathbf{x}, t)$ along the trajectory of J/ψ
 $T(\mathbf{x}, t)$, $\rho(\mathbf{x}, t)$ and $\beta(\mathbf{x}, t)$ were obtained for each space-time point with the width of $\Delta x = 0.2$ fm, $\Delta y = 0.2$ fm and $\Delta t = 0.2$ fm using hydrodynamical calculation.
- If the temperature at the certain space-time point where J/ψ is exceeds the dissociation temperature, J/ψ is melt. This means that the survival probability of J/ψ becomes zero. No recombination of J/ψ is taken into account.
- Similar study was done for χ_c and ψ' , where the dissociation temperature was assumed to be lower than that of J/ψ . In this model, suppression of χ_c and ψ' is assumed to be same since the dissociation temperatures of them are expected to be almost same in lattice QCD calculations.

8.3.1 Picture of the evolution of the medium

The thermalization of the medium is assumed to happen at $\tau_0 = 0.6 \text{ fm}/c$ in this hydrodynamical calculation [164]. Figure 8.10 and Figure 8.11 show the temperature (left) and parton density (right) in transverse plane for various time, where the impact parameter is $b = 3.1 \text{ fm}$ (0-10% centrality) and $b = 10.8 \text{ fm}$ (50-60% centrality), respectively. Here the center of two colliding nuclei in transverse plane are taken to be $(x, y) = (-b/2, 0)$ and $(x, y) = (b/2, 0)$, where b is the impact parameter.

8.3.2 Definition of the survival probability

Figure 8.12 shows the temperature (left) and the parton density (right) as a function of t along the trajectory of J/ψ for various impact parameters, where J/ψ p_T is $0.5 \text{ GeV}/c$, azimuthal angle $\phi_{J/\psi}$ is $\pi/4$ and the production point of J/ψ is $\mathbf{x}_0 = (0, 0)$. For more central collisions, the achieved temperature is larger and duration time of QGP is longer. The relation between temperature and time as shown in Fig. 8.12 was used to calculate the survival probability of J/ψ and $\chi(=\psi', \chi_c)$. The survival probability $S_\psi(\psi = J/\psi, \chi)$ is defined as follows:

$$S_\psi = \prod_i S_\psi(t_i), \quad (8.32)$$

where $S_\psi(t_i)$ is the survival probability in each Δt bin width and i runs over until the temperature drops below the critical temperature of 170 MeV . Here $t(i)$ can be written as $t(i) = t_0 + \Delta t \times i = 0.6 + 0.2 \times i$. The survival probability at the time bin i is defined using Θ function as follows:

$$S_\psi(t_i) = \left(1 - \Theta(T(\mathbf{x}(i), t(i))/T_c - T_d/T_c)\right), \quad (8.33)$$

where $T(\mathbf{x}(i), t(i)) \equiv T(i)$ is the temperature where J/ψ is at the time of $t(i)$, T_c and T_d are the critical temperature (170 MeV) and the dissociation temperature, respectively. Here the $\mathbf{x}(i)$ is expressed as follows:

$$\mathbf{x}(i) = \beta_\psi \times (0.6 + 0.2 \times i) + \mathbf{x}_0. \quad (8.34)$$

This means that temperature $T(\mathbf{x}(i), t(i))$ depends on J/ψ p_T , azimuthal angle $\phi_{J/\psi, \chi}$ and production point \mathbf{x}_0 .

In this calculation, J/ψ , ψ' and χ_c suppression were studied with following input parameters of p_T , production points \mathbf{x}_0 and azimuthal angle $\phi_{J/\psi, \chi_c}$.

- p_T
 p_T of J/ψ and χ_c was set to 0.5, 1.5, 2.5, 3.5, 4.5 GeV/c .
- Production points \mathbf{x}_0
 Production points \mathbf{x}_0 can be written as $\mathbf{x}_0 = (R \cos \phi_{prod}, R \sin \phi_{prod})$, where R is the radial position and ϕ_{prod} is the azimuthal angle of the production points. R was set from 0 fm to 6 fm to have the interval of 0.5 fm. Therefore,
 $R = 0.0, 0.5, 1.0, 1.5, 2.0, 2.5, 3.0, 3.5, 4.0, 4.5, 5.0, 5.5, 6.0 \text{ fm}$.
 Azimuthal angle ϕ_{prod} was set to $0, \pi/8, \pi/4, 3\pi/8$ and $\pi/2$.
 Therefore, the number of production points defined in this model was $13 \times 5 = 65$.

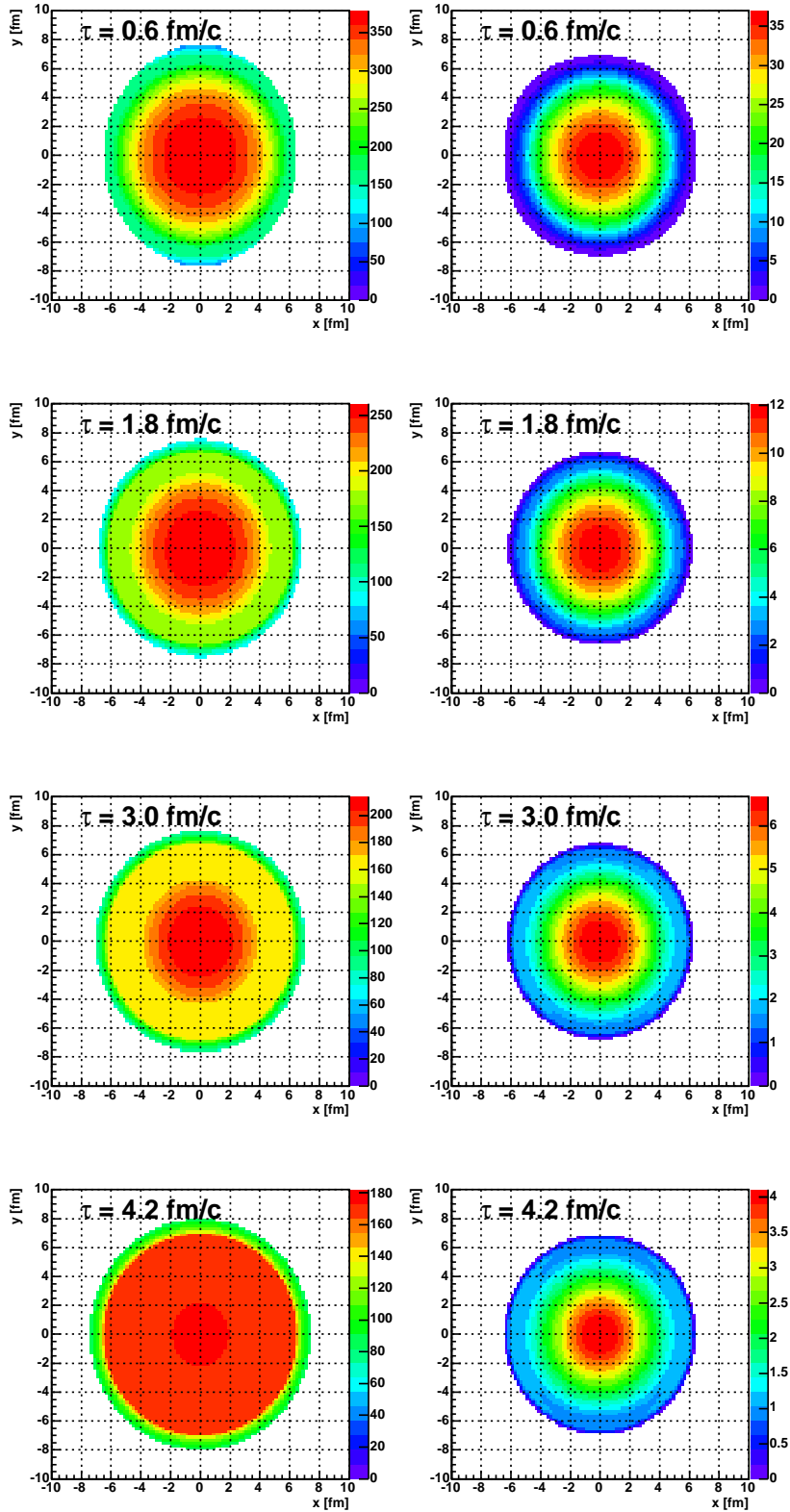


Figure 8.10: Left : Temperature at each space-time points with $b = 3.1$ fm/c. Right : Parton density at each space-time points with $b = 3.1$ fm/c, where the temperature is above 170 MeV.

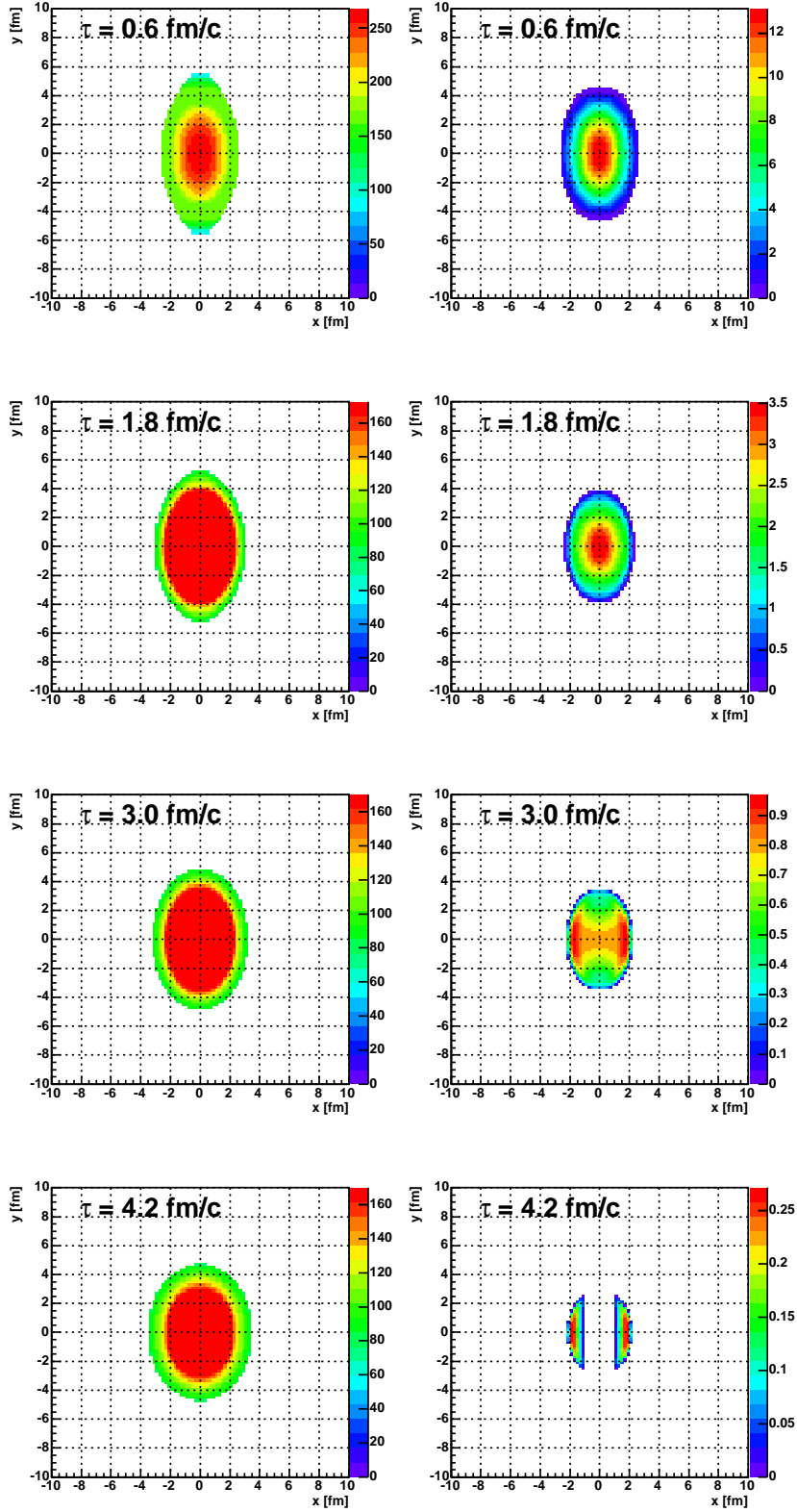


Figure 8.11: Left : Temperature at each space-time points with $b = 10.8$ fm/c. Right : Parton density at each space-time points with $b = 10.8$ fm/c, where the temperature is above 170 MeV.

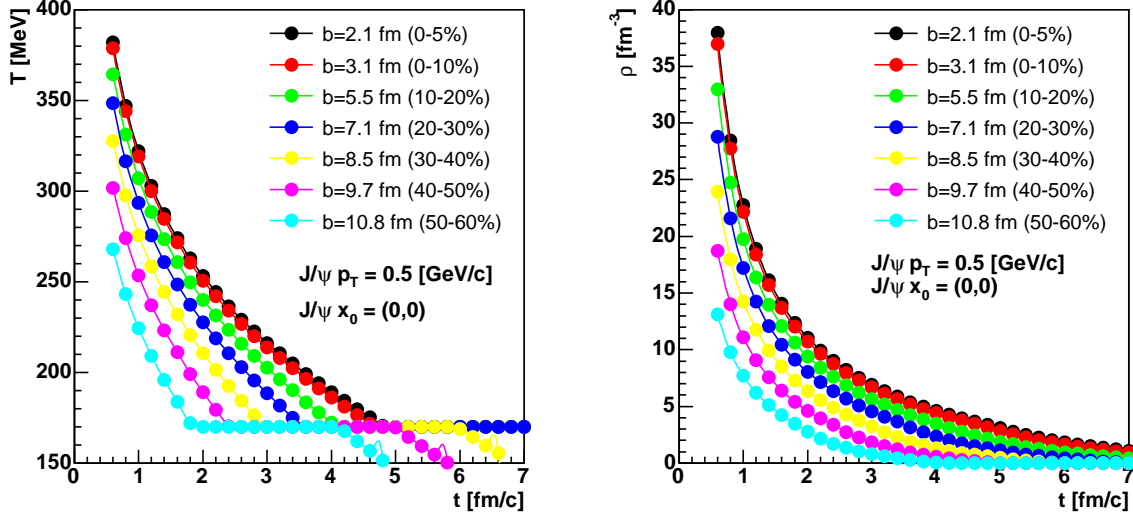


Figure 8.12: Temperature (left) and the parton density (right) as a function of t along the trajectory of J/ψ for various impact parameters (centrality), where J/ψ p_T is 0.5 GeV/ c and the production of J/ψ is set to $\mathbf{x}_0 = (0, 0)$.

- Azimuthal angle $\phi_{J/\psi, \chi}$

This azimuthal angle defines the moving direction of J/ψ and χ . This was varied from 0 to 2π with the span of $1/8\pi$. Therefore, $\phi_{J/\psi, \chi} = 1/8\pi \times i$ ($0 \leq i \leq 15$).

The strategy to obtain the survival probability of J/ψ and χ over $\phi_{J/\psi, \chi}$, \mathbf{x}_0 and p_T is summarized as follows:

1. Extract the survival probability S_ψ defined as Eq. (8.32) for various azimuthal angle, various production points and various p_T .
2. Take the average survival probability over production points and azimuthal angle
First, survival probability for each production point was extracted by taking the average of survival probability over the azimuthal angle $\phi_{J/\psi, \chi}$.

In this model, formation time of J/ψ is not taken into account. This means that the production point \mathbf{x}_0 should be inside the participant region. Since the production probability depends on the nucleon density of two colliding nuclei, the average survival probability over the production points is obtained by taking the average of the survival probability for various production points according to the nuclear thickness function. This is written as follows:

$$S_\psi = \frac{\sum_{\mathbf{x}_0} S_\psi(\mathbf{x}_0) T_A(\mathbf{x}_0 - \mathbf{b}/2) T_B(\mathbf{x}_0 + \mathbf{b}/2)}{\sum_{\mathbf{x}_0} T_A(\mathbf{x}_0 - \mathbf{b}/2) T_B(\mathbf{x}_0 + \mathbf{b}/2)}, \quad (8.35)$$

where $T_{A,B}(\mathbf{x})$ is the nuclear thickness function and defined as follows:

$$T_{A,B}(\mathbf{x}) = \int \rho(\mathbf{x}, z) dz, \quad (8.36)$$

where $\rho(\mathbf{x}, z)$ is the nucleon density at (\mathbf{x}, z) and Woods-Saxon distribution is used.

3. Extract the average survival probability over all p_T range

This was done by weighting the survival probability for various p_T according to invariant p_T distribution as follows:

$$S_\psi = \frac{\sum_{p_T} S_\psi(p_T) \frac{d^2 N}{dy dp_T}}{\sum_{p_T} \frac{d^2 N}{dy dp_T}}. \quad (8.37)$$

Finally, the survival probability, which should be compared to real data, was calculated using the survival probability of J/ψ and χ as follows:

$$S_{J/\psi}^{all} = (1 - f_{FD})S_{J/\psi} + f_{FD}S_\chi, \quad (8.38)$$

where f_{FD} corresponds to the feed-down contribution from χ_c and J/ψ decay to J/ψ .

Since the feed down contribution at RHIC energy has not been measured, feed down contribution factor f_{FD} as well as the dissociation temperatures of J/ψ and χ are treated as free parameters in this model. Quantitative estimation of dissociation temperatures of J/ψ and χ and feed down contribution was performed by comparing the observed J/ψ suppression with the calculations from this model. Parameters concerning the feed down contribution f and the dissociation temperatures of J/ψ ($T_{diss}(J/\psi)$) and χ ($T_{diss}(\chi)$) used in the calculation are listed as follows:

- $f_{FD} = 0, 0.05, 0.10, 0.15, 0.20, 0.25, 0.30, 0.35, 0.40, 0.45, 0.50, 0.55, 0.60, 0.70$
- $T_{diss}(J/\psi) = (1.9 + 0.01 \times i)T_c \quad (0 \leq i \leq 40)$
- $T_{diss}(\chi) = (1.0 + 0.03 \times i)T_c \quad (0 \leq i \leq 36)$

χ^2 test was performed for the result of the survival probability obtained with each set of the parameters ($T_{diss}(J/\psi), T_{diss}(\chi), f_{FD}$) as listed above. Definition of χ^2 was same as Eq. (8.30), where $\sigma(i)$ is taken to be uncorrelated errors in real data. Correlated systematic errors were used to investigate how the dissociation temperatures changed by moving the points of $S_{J/\psi}$. Extraction of ($T_{diss}(J/\psi), T_{diss}(\chi), f_{FD}$) was done by minimizing χ^2 , and χ^2 contour for 1σ was extracted to estimate the systematic errors of ($T_{diss}(J/\psi), T_{diss}(\chi), f_{FD}$).

8.3.3 Result of model calculations

Figure 8.13 shows the survival probability $S^{all}(J/\psi)$, $S(J/\psi)$ and $S(\chi)$ as a function of the number of participants with $(T_{diss}(J/\psi), T_{diss}(\chi), f_{FD}) = (2.12T_c, 1.34T_c, 0.25)$, which gives the best χ^2 between real data and model calculations. Red points are the real data as shown in Fig. 8.7. Blue and green lines are the survival probability for direct J/ψ and χ , respectively, and black line is the survival probability of J/ψ , which was extracted based on Eq. (8.38). The suppression pattern above $N_{part} \sim 160$ reflects increase of the transverse area above $T \sim 2.12T_c$ with a decrease of the impact parameter.

Figure 8.14, Figure 8.15, Figure 8.16 and Figure 8.17 show the example of the survival probability of J/ψ $S^{all}(J/\psi)$ as a function of the number of participants for the feed down

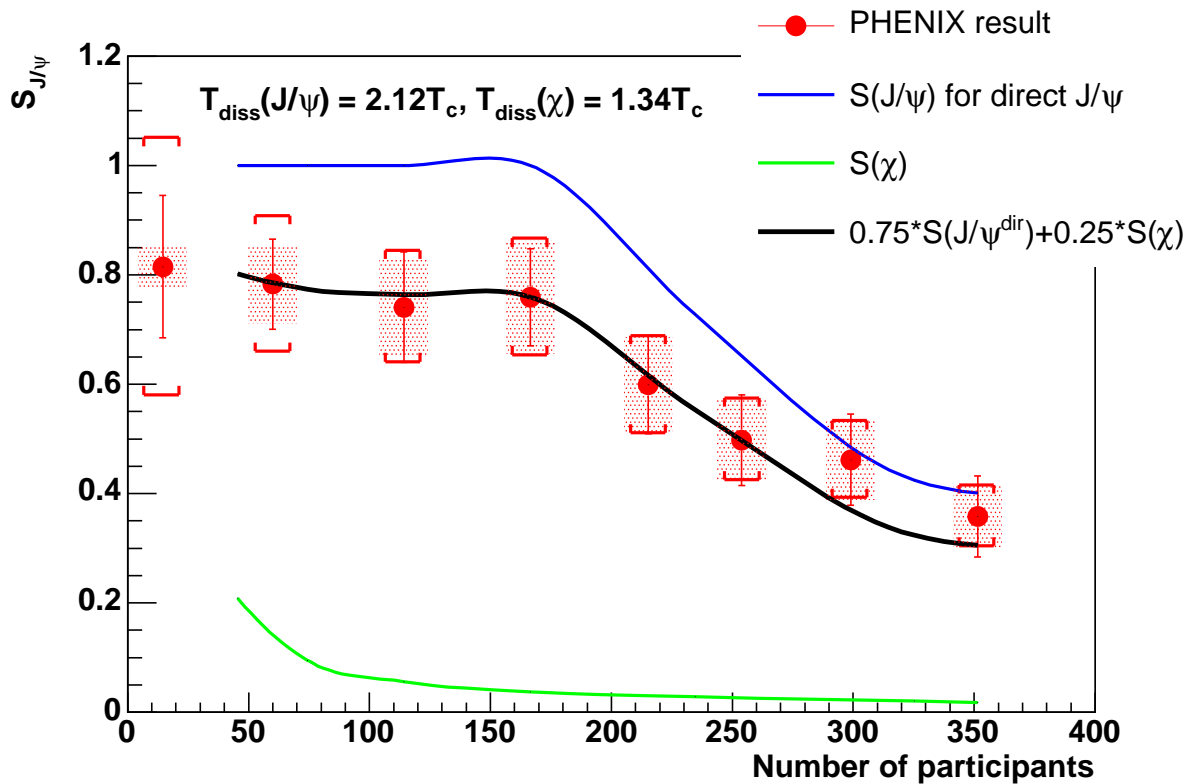


Figure 8.13: Survival probability of J/ψ as a function of the number of participants. Red points are the real data as shown in Fig. 8.7. Blue and green lines are the survival probability for direct J/ψ and χ , respectively, and black line is the survival probability of J/ψ , which was extracted based on Eq. (8.38) with $(T_{\text{diss}}(J/\psi), T_{\text{diss}}(\chi), f_{FD}) = (2.12T_c, 1.34T_c, 0.25)$.

contribution $f_{FD}=0.1, 0.25, 0.40$ and 0.6 , respectively. Dotted lines in figure a), b), c), d), e), f), g) and h) are the survival probability of direct J/ψ $S(J/\psi)$ with the dissociation temperatures of $T_{diss}(J/\psi)=1.9, 2.0, 2.05, 2.12, 2.15, 2.20$ and $2.25T_c$, respectively. Dashed lines correspond to the survival probability of χ_c $S(\chi)$ for various dissociation temperatures of χ , where black, red, green, blue, magenta and light blue are for $T_{diss}(\chi_c)=1.04, 1.10, 1.19, 1.31, 1.40$ and $1.52T_c$, respectively. Solid lines in each figure correspond to the survival probability of J/ψ with feed down contribution $S^{all}(J/\psi)$. Different colors of solid lines correspond to different dissociation temperature of χ_c as explained above.

Figure 8.18, shows the comparison of the survival probability between real data and model calculations, where the data points in real data were moved up according to correlated systematic errors. Feed down contributions, dissociation temperatures of J/ψ and χ_c shown here are same as shown in Fig. 8.14.

Figure 8.19 shows the comparison of the survival probability between real data and toy model calculation, where the data points in real data were moved down according to correlated systematic errors. Feed down contributions, dissociation temperatures of J/ψ and χ_c shown here are the same as shown in Fig. 8.16.

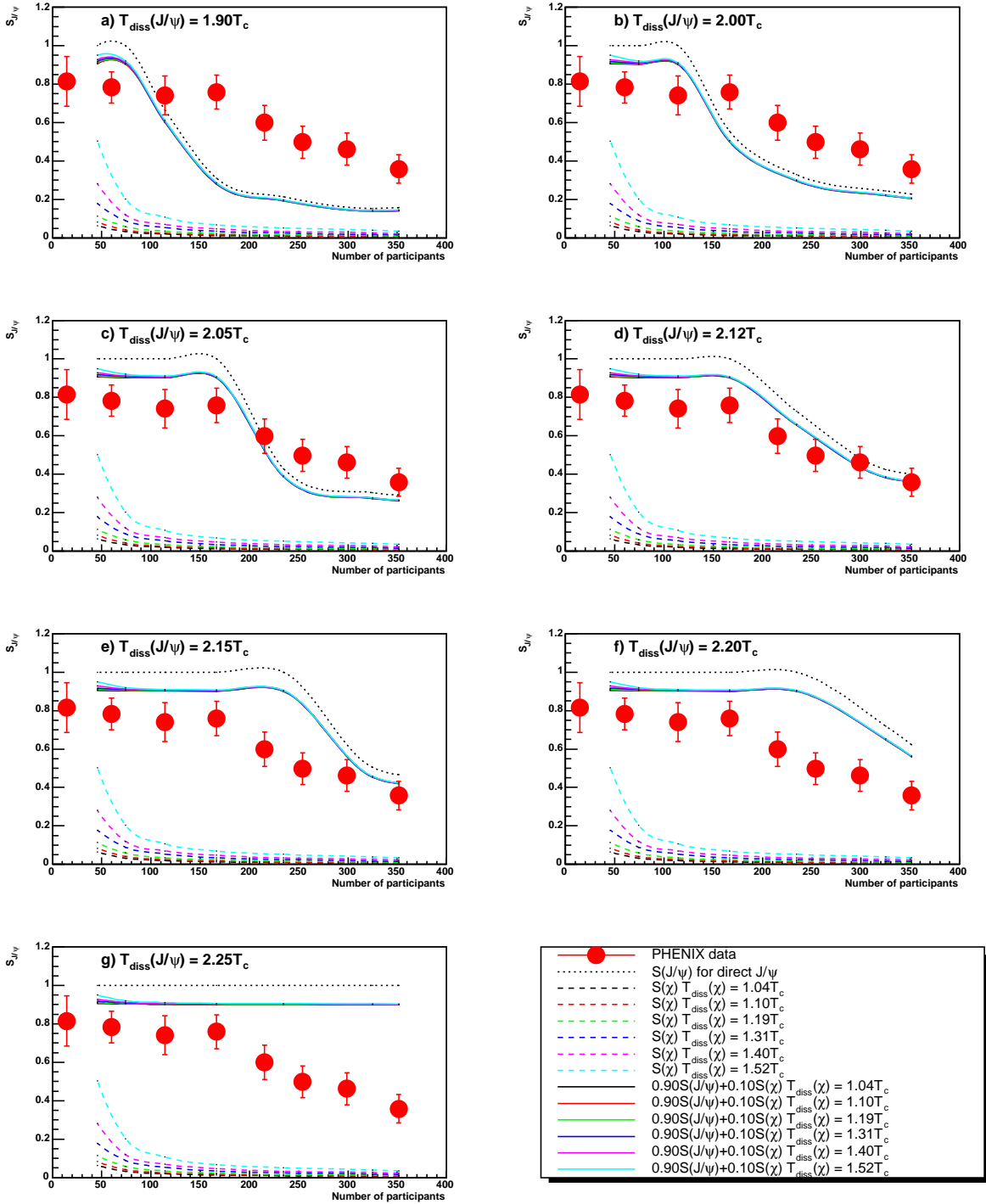


Figure 8.14: Survival probability of J/ψ as a function of the number of participants, where red points are from real data and solid lines are the results from model calculations with $T_{diss}(J/\psi)/T_c = 1.9$ (a), 2.0 (b), 2.05 (c), 2.12 (d), 2.15 (e), 2.2 (f) and 2.15 (g) and with feed down contribution of 10%. Different colors correspond to different $T_{diss}(\chi_c)$ explained in text.

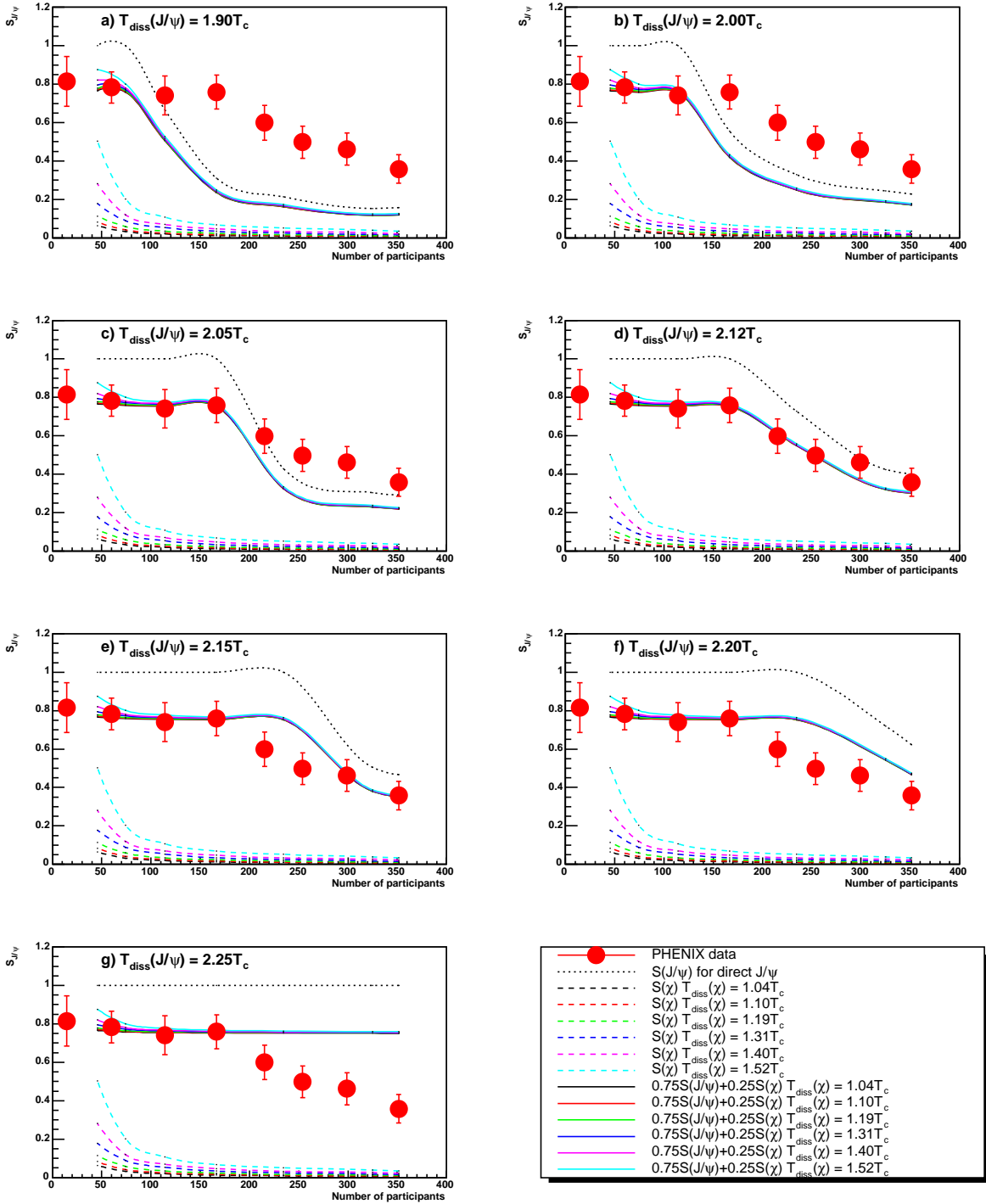


Figure 8.15: Survival probability of J/ψ as a function of the number of participants, where red points are from real data and solid lines are the results from toy model calculations with $T_{diss}(J/\psi)/T_c = 1.9$ (a), 2.0 (b), 2.05 (c), 2.12 (d), 2.15 (e), 2.2 (f) and 2.15 (g) and with feed down contribution of 25%. Different colors correspond to different $T_{diss}(\chi_c)$ explained in text.

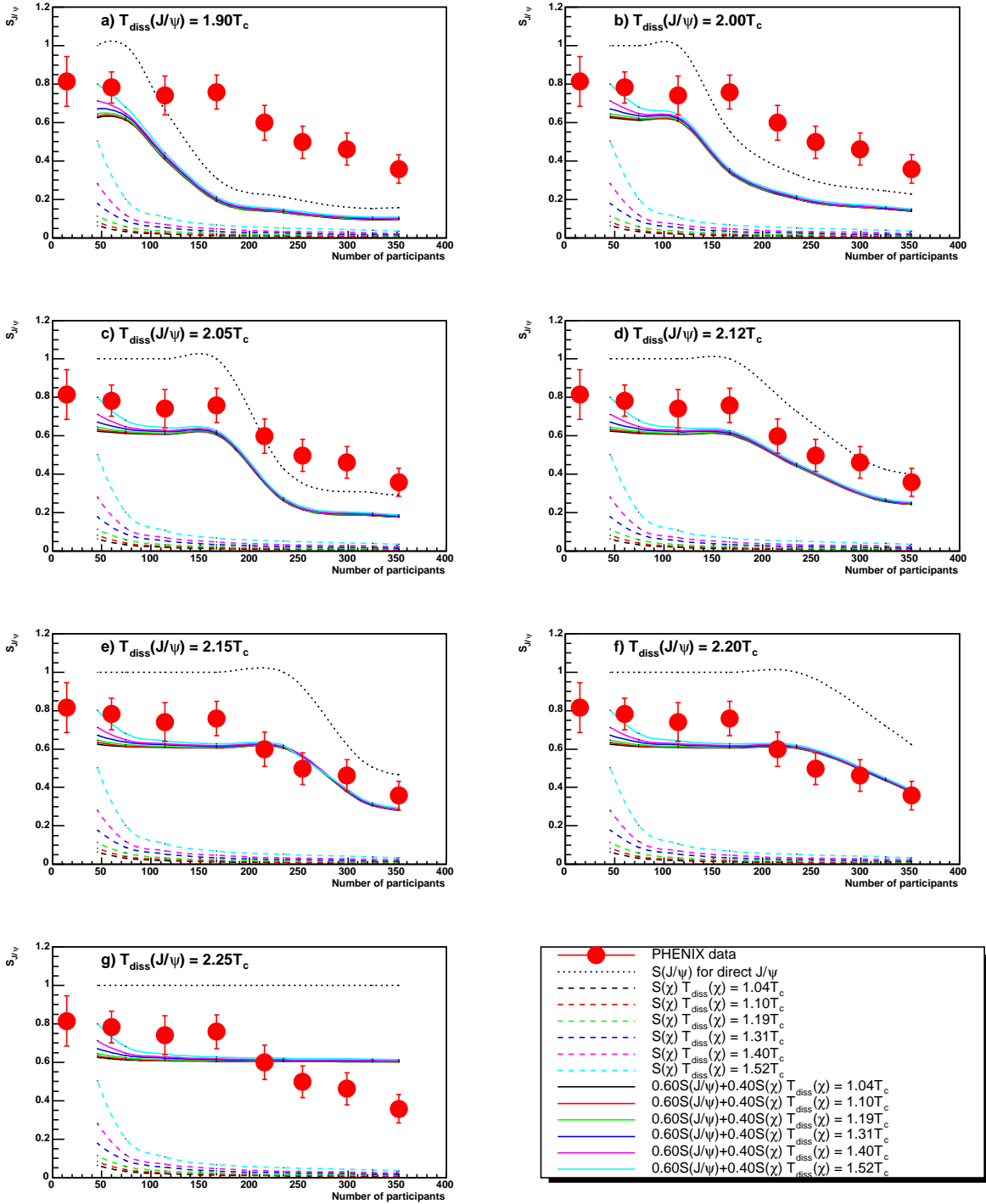


Figure 8.16: Survival probability of J/ψ as a function of the number of participants, where red points are from real data and solid lines are the results from toy model calculations with $T_{diss}(J/\psi)/T_c = 1.9$ (a), 2.0 (b), 2.05 (c), 2.12 (d), 2.15 (e), 2.2 (f) and 2.15 (g) and with feed down contribution of 40%. Different colors correspond to different $T_{diss}(\chi)$ explained in text.

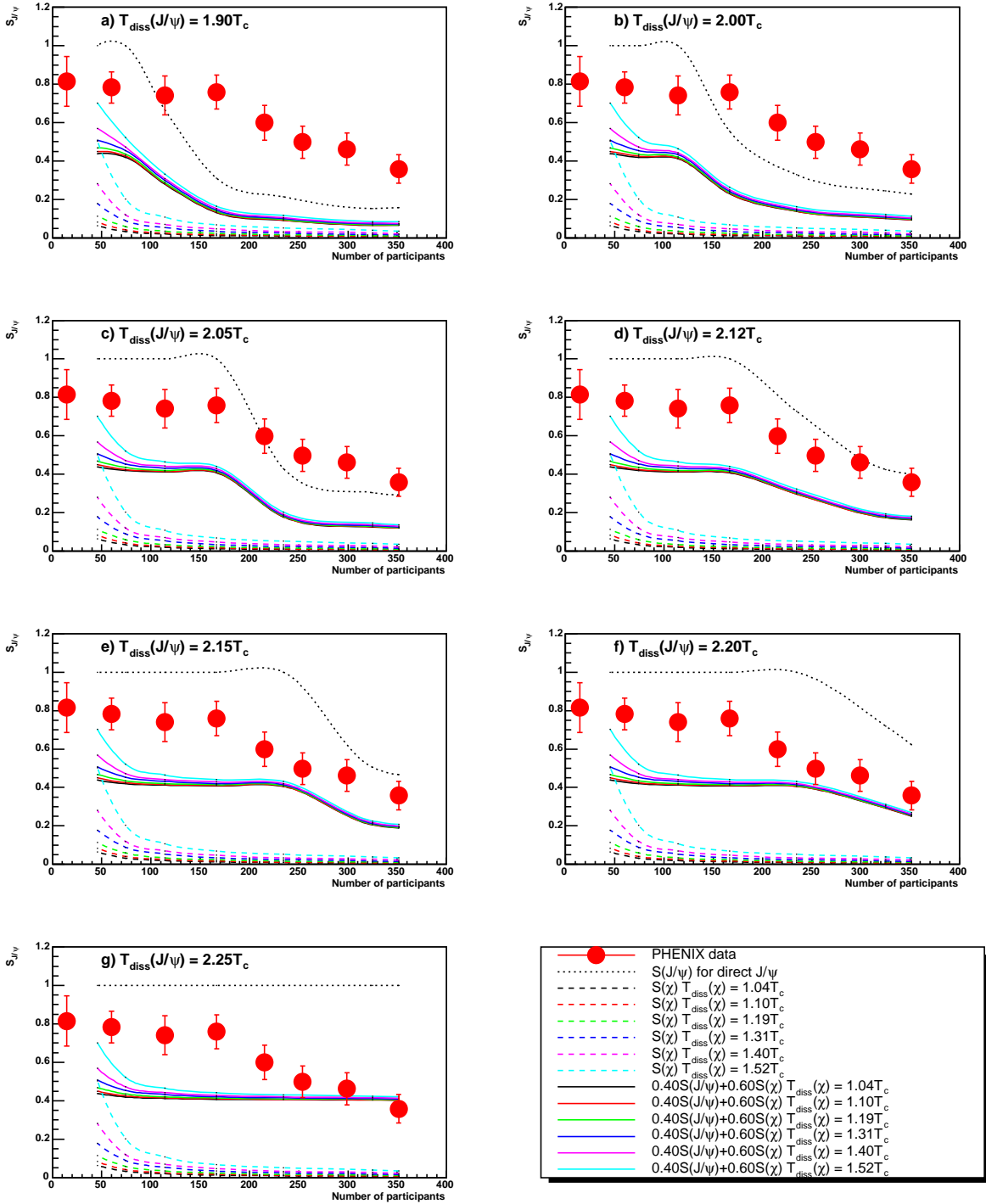


Figure 8.17: Survival probability of J/ψ as a function of the number of participants, where red points are from real data and solid lines are the results from toy model calculations with $T_{diss}(J/\psi)/T_c = 1.9$ (a), 2.0 (b), 2.05 (c), 2.12 (d), 2.15 (e), 2.2 (f) and 2.15 (g) and with feed down contribution of 60%. Different colors correspond to different $T_{diss}(\chi)$ explained in text.

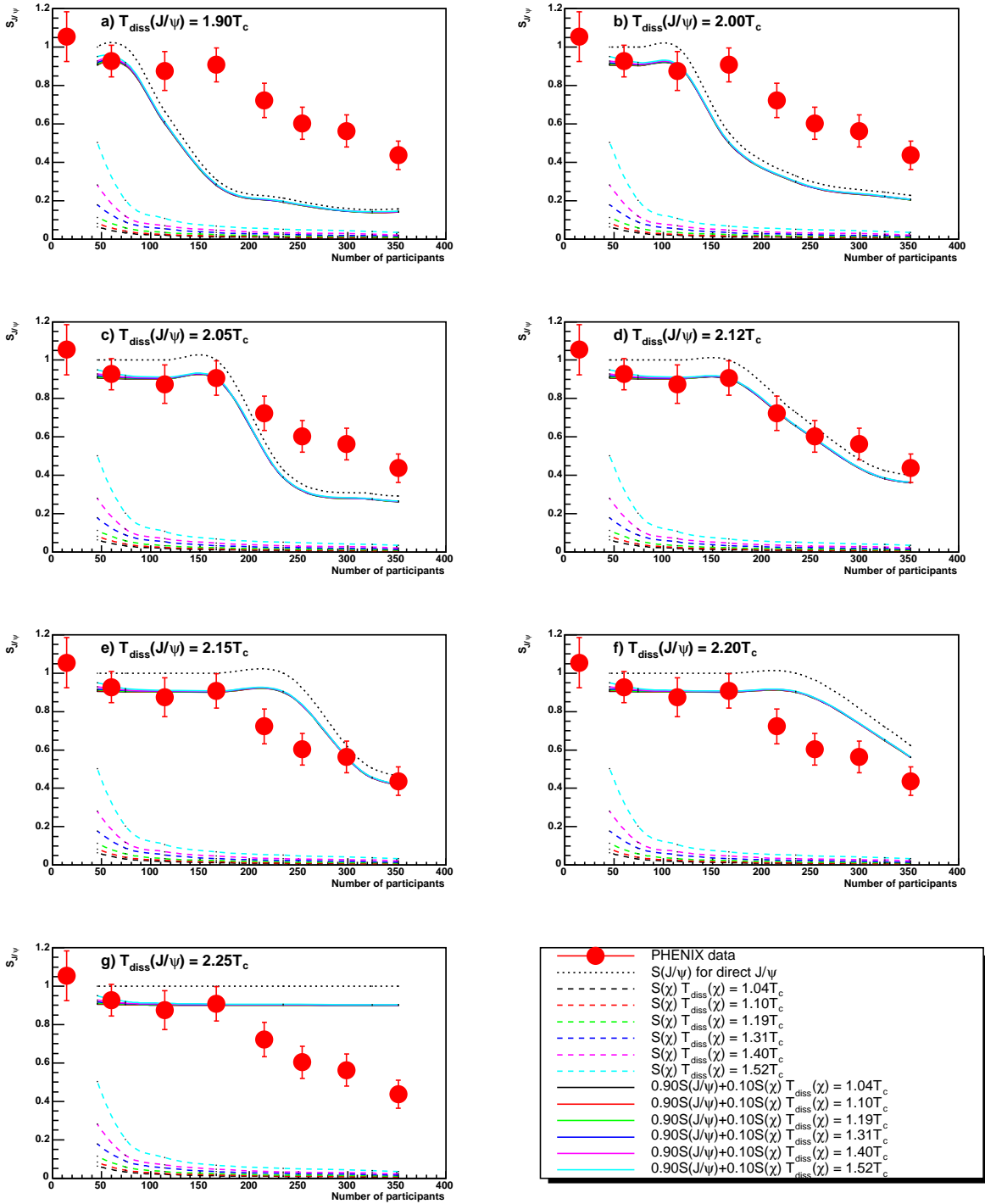


Figure 8.18: Same figure as shown in Fig. 8.14. Difference is that the real data points are moved up according to point-to-point correlated systematic errors. Feed down contribution is assumed to be 10%.

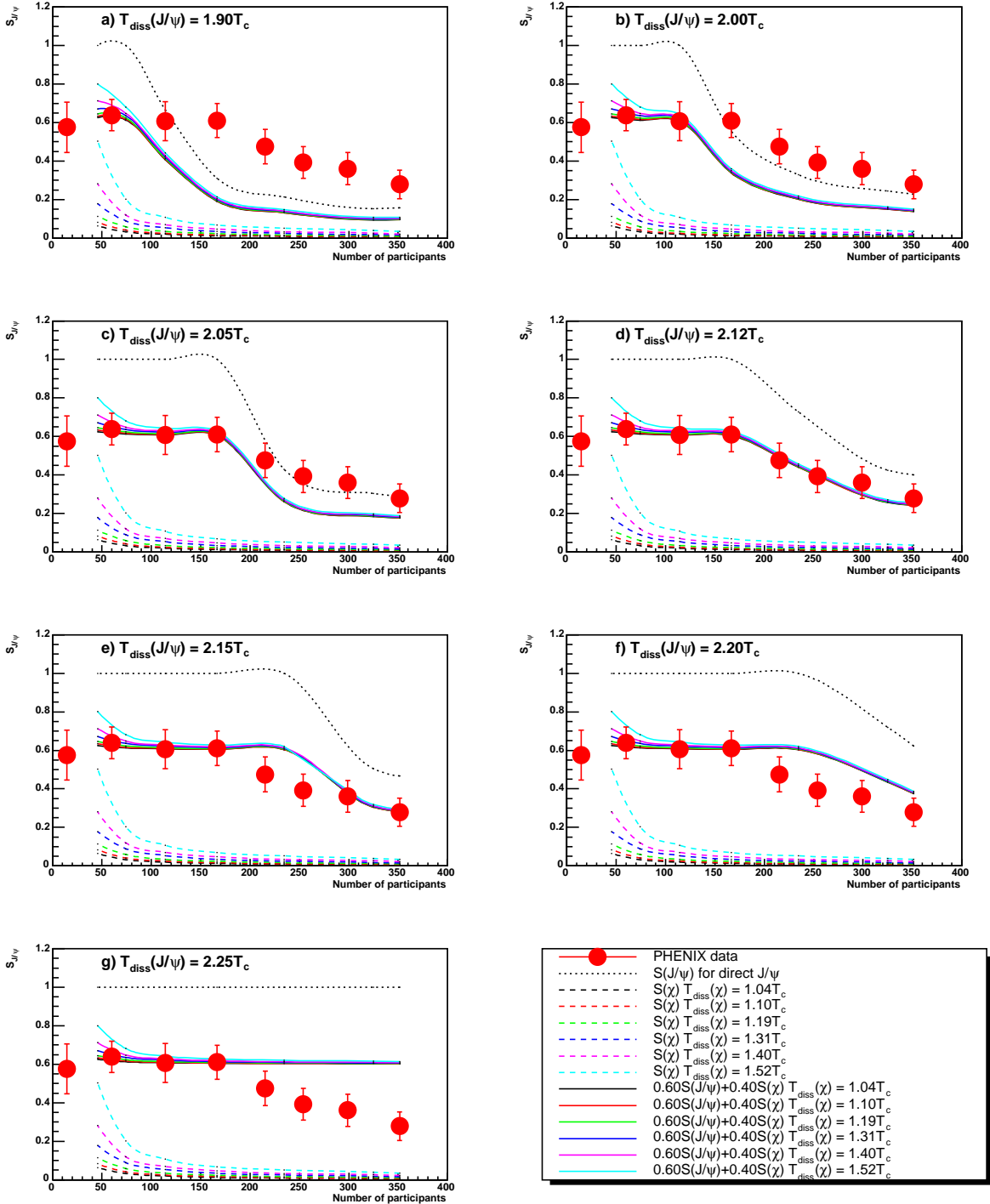


Figure 8.19: Same figure as shown in Fig. 8.16. Difference is that the real data points are moved down according to point-to-point correlated systematic errors. Feed down contribution is assumed to be 40%.

χ^2 TEST and Results of $T_{diss}(J/\psi)$, $T_{diss}(\chi)$ and f_{FD}

χ^2 test was performed for each set of the parameters $(T_{diss}(J/\psi), T_{diss}(\chi), f_{FD})$ and minimum χ^2 was extracted. Then χ^2 contour levels for 1σ and 2σ were extracted to estimate the associated errors for $(T_{diss}(J/\psi), T_{diss}(\chi_c), f_{FD})$.

Figure 8.20 shows χ^2 contour as a function of $(T_{diss}(J/\psi), T_{diss}(\chi_c))$ for various feed down contribution f_{FD} , where the 1σ and 2σ contours are shown as solid and dashed lines, respectively. Here the results are shown for the feed down contribution of 15%, 20%, 25%, 30%, 35% and 40%. For other values of feed down contribution, there is no 1σ contours observed. The minimum χ^2 was achieved at $(T_{diss}(J/\psi), T_{diss}(\chi_c), f_{FD}) = (2.12T_c, 1.34T_c, 0.25)$, which is shown as cross symbol in Fig. 8.20. When 1σ contour is taken to be the error of $(T_{diss}(J/\psi), T_{diss}(\chi_c), f_{FD})$, each of them becomes:

$$T_{diss}(J/\psi) = (2.12^{+0.08}_{-0.03})T_c \quad (8.39)$$

$$T_{diss}(\chi_c) = (1.34^{+0.44}_{-0.34})T_c \quad (8.40)$$

$$f_{FD} = 0.25^{+0.15}_{-0.10} \quad (8.41)$$

Figure 8.21 shows χ^2 as a function of $(T_{diss}(J/\psi), T_{diss}(\chi_c))$ for various feed down contribution f_{FD} , where the 1σ and 2σ contours are shown as solid and dashed lines, respectively. Here the results are shown for the feed down contribution of 0%, 5%, 10%, 15%, 20%, 25%, 30%, 35% and 40%. Here, survival probability of J/ψ in real data were moved up according to correlated systematic errors. The minimum χ^2 was achieved for $(T_{diss}(J/\psi), T_{diss}(\chi_c), f) = (2.12T_c, 1.52T_c, 0.10)$, which is shown as cross symbol in Fig. 8.21. When 1σ contour is taken to be the error of $(T_{diss}(J/\psi), T_{diss}(\chi_c), f)$, each of them becomes:

$$T_{diss}(J/\psi) = (2.12^{+0.09}_{-0.02})T_c \quad (8.42)$$

$$T_{diss}(\chi_c) = (1.52 \pm 0.5)T_c \quad (8.43)$$

$$f_{FD} = 0.10^{+0.25}_{-0.10} \quad (8.44)$$

Figure 8.22 shows χ^2 as a function of $(T_{diss}(J/\psi), T_{diss}(\chi_c))$ for various feed down contribution f_{FD} , where the 1σ and 2σ contours are shown as solid and dashed lines, respectively. Here the results are shown for the feed down contribution of 30%, 35%, 40%, 45%, 50% and 55%. Here, survival probability of J/ψ in real data were moved down according to correlated systematic errors. The minimum χ^2 was achieved for $(T_{diss}(J/\psi), T_{diss}(\chi_c), f) = (2.12T_c, 1.22T_c, 0.40)$, which is shown as cross symbol in Fig. 8.22. When 1σ contour is taken to be the error of $(T_{diss}(J/\psi), T_{diss}(\chi_c), f)$, each of them becomes:

$$T_{diss}(J/\psi) = (2.12^{+0.09}_{-0.05})T_c \quad (8.45)$$

$$T_{diss}(\chi_c) = (1.22^{+0.38}_{-0.22})T_c \quad (8.46)$$

$$f_{FD} = 0.40^{+0.15}_{-0.10} \quad (8.47)$$

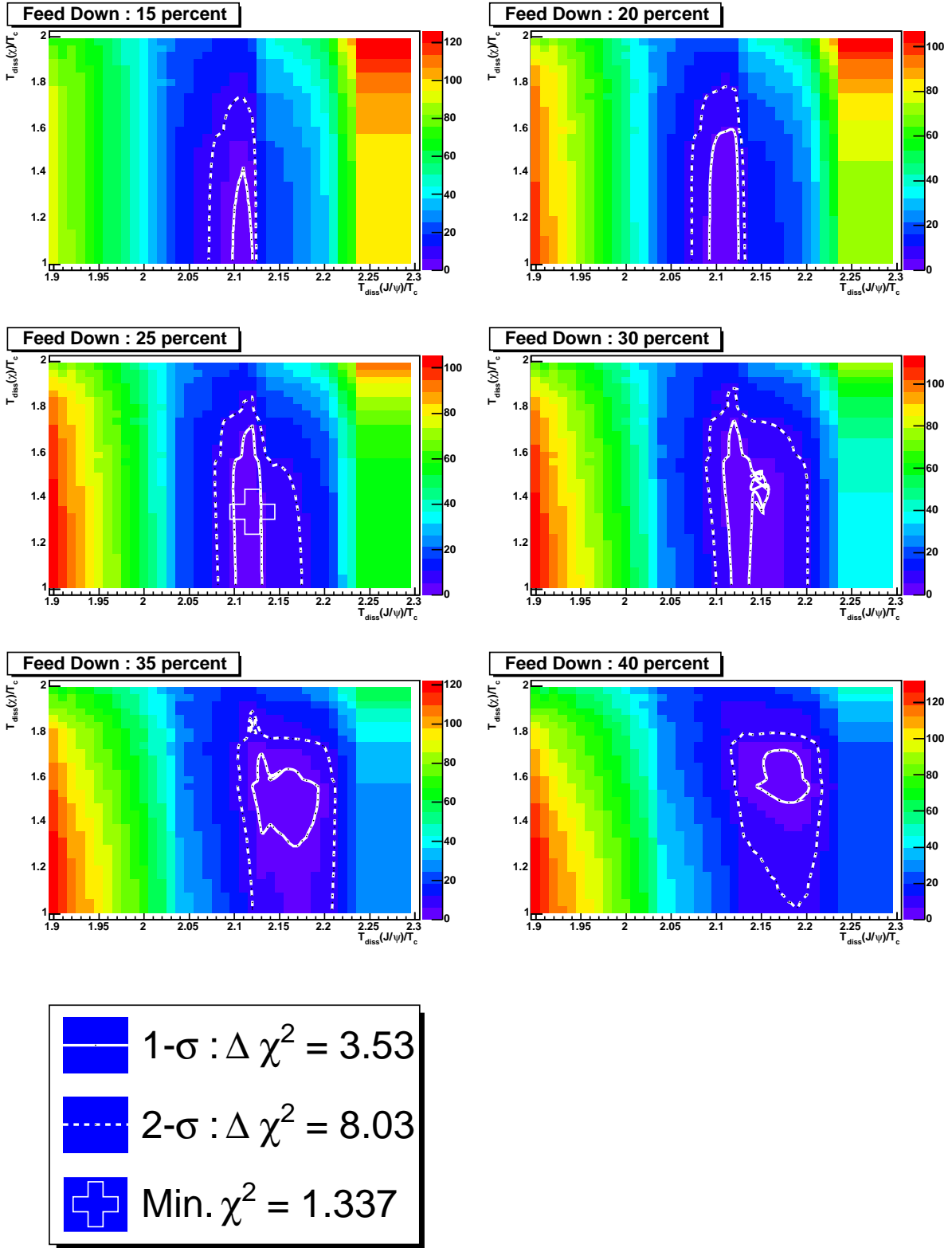


Figure 8.20: χ^2 as a function of $(T_{diss}(J/\psi), T_{diss}(\chi_c))$ for various feed down contribution f . χ^2 contours for 1σ and 2σ are shown as solid and dashed lines, respectively. Feed down contribution is written in each title box.

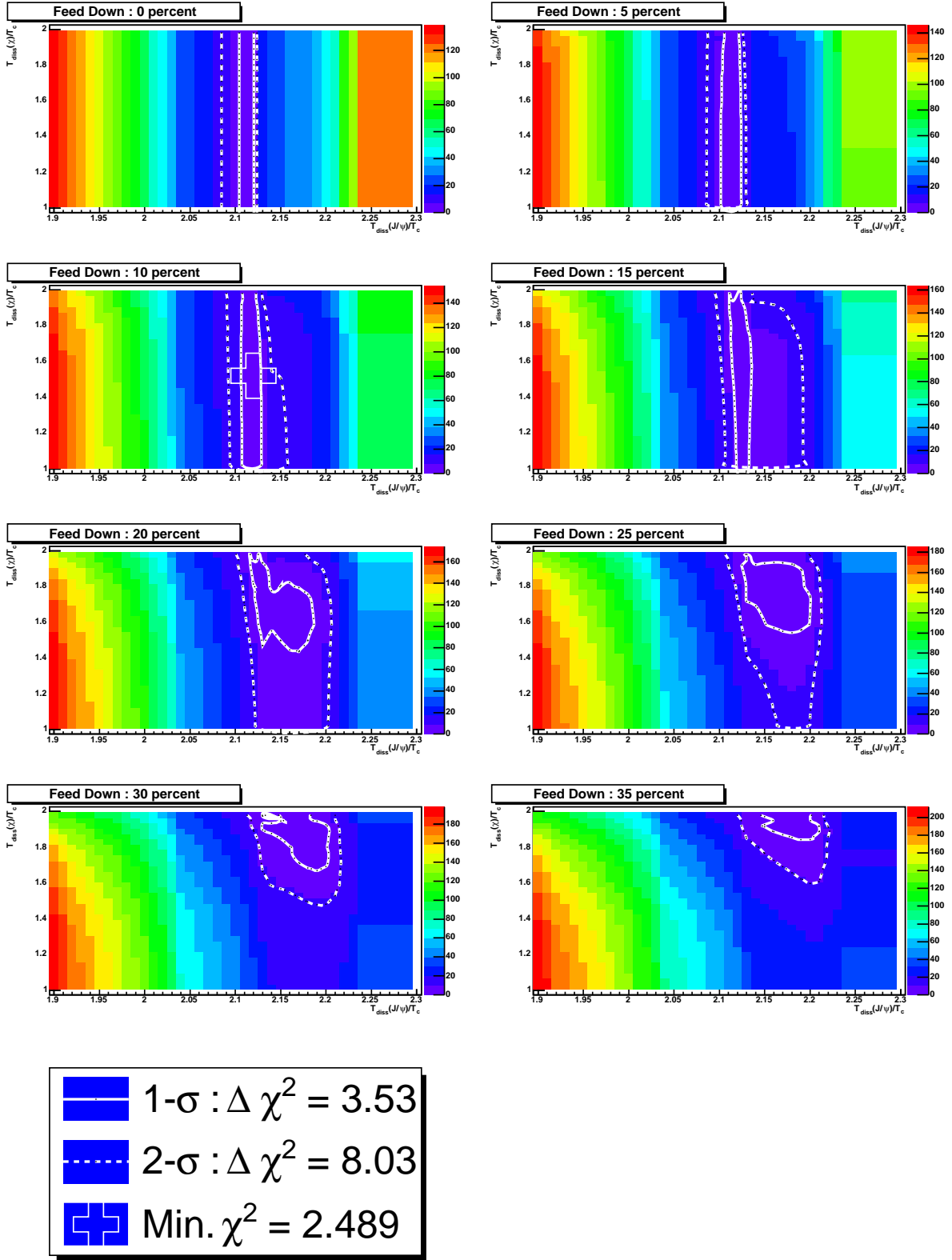


Figure 8.21: Contour plots on $(T_{diss}(J/\psi), T_{diss}(\chi_c))$ plane for various feed down contribution f . Solid and dotted lines are 1σ and 2σ contour levels, respectively. data points are moved up according to correlated errors.

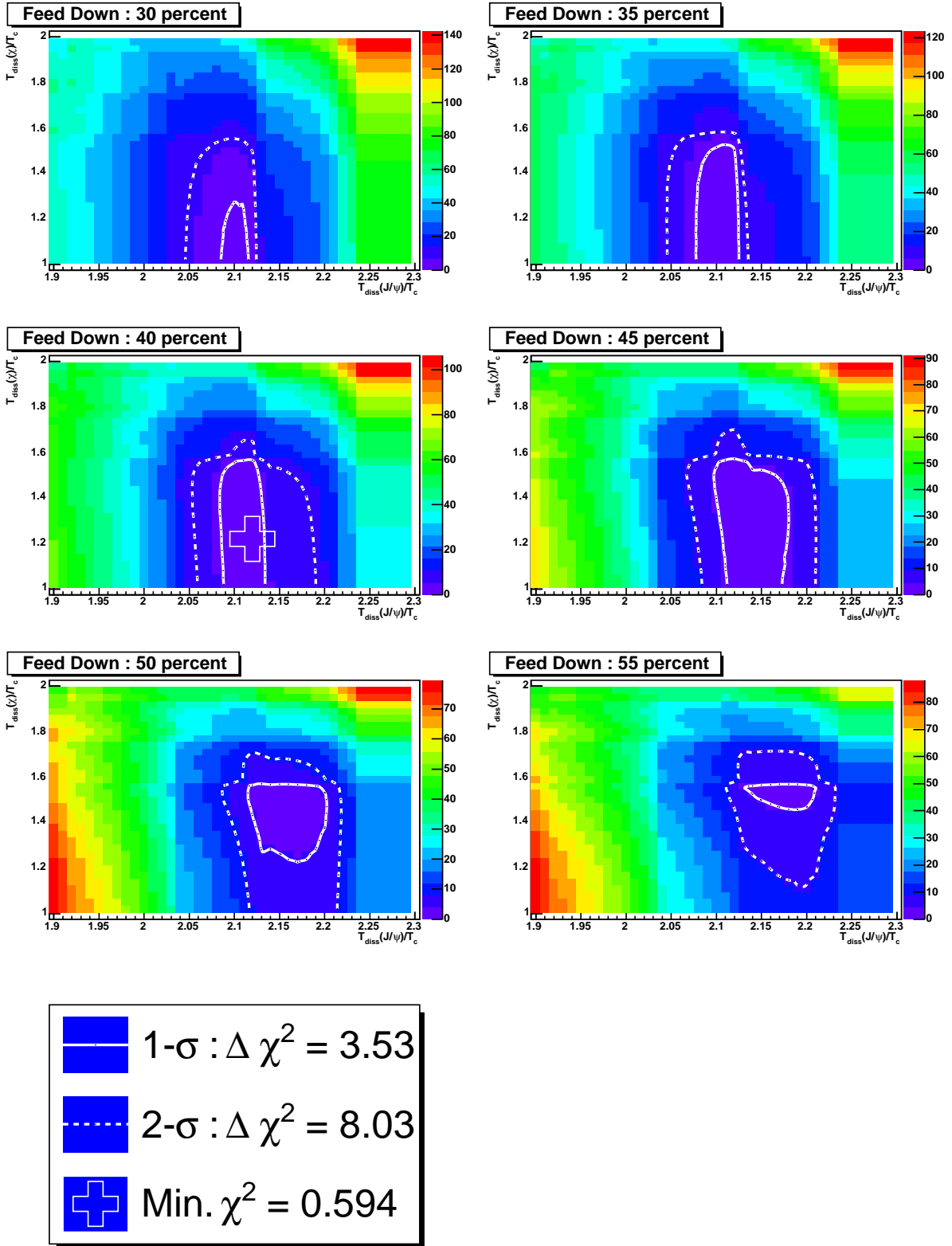


Figure 8.22: Contour plots on $(T_{diss}(J/\psi), T_{diss}(\chi_c))$ plane for various feed down contribution f , where the 1σ χ^2 region exist on the plane. Solid and dotted lines are 1σ and 2σ contour levels, respectively. data points are moved down according to correlated errors.

By taking the average between Eq. (8.39), Eq. (8.42) and Eq. (8.45), dissociation temperature of J/ψ was obtained:

$$T_{diss}(J/\psi) = (2.12^{+0.09}_{-0.03})T_c. \quad (8.48)$$

The dissociation temperature of χ_c and ψ' was obtained as follows:

$$T_{diss}(\chi_c) = (1.36^{+0.44}_{-0.36})T_c. \quad (8.49)$$

The feed down contribution was estimated as follows:

$$f_{FD} = 0.25^{+0.18}_{-0.10} \quad (8.50)$$

Figure 8.23 shows the survival probability as a function of the number of participants. Red points are real data, blue solid lines are best fit results and shaded area corresponds to the 1σ deviation of the survival probability. Middle and bottom of Fig. 8.23 are the results where the survival probability in real data were moved up and down according to correlated systematic errors, respectively.

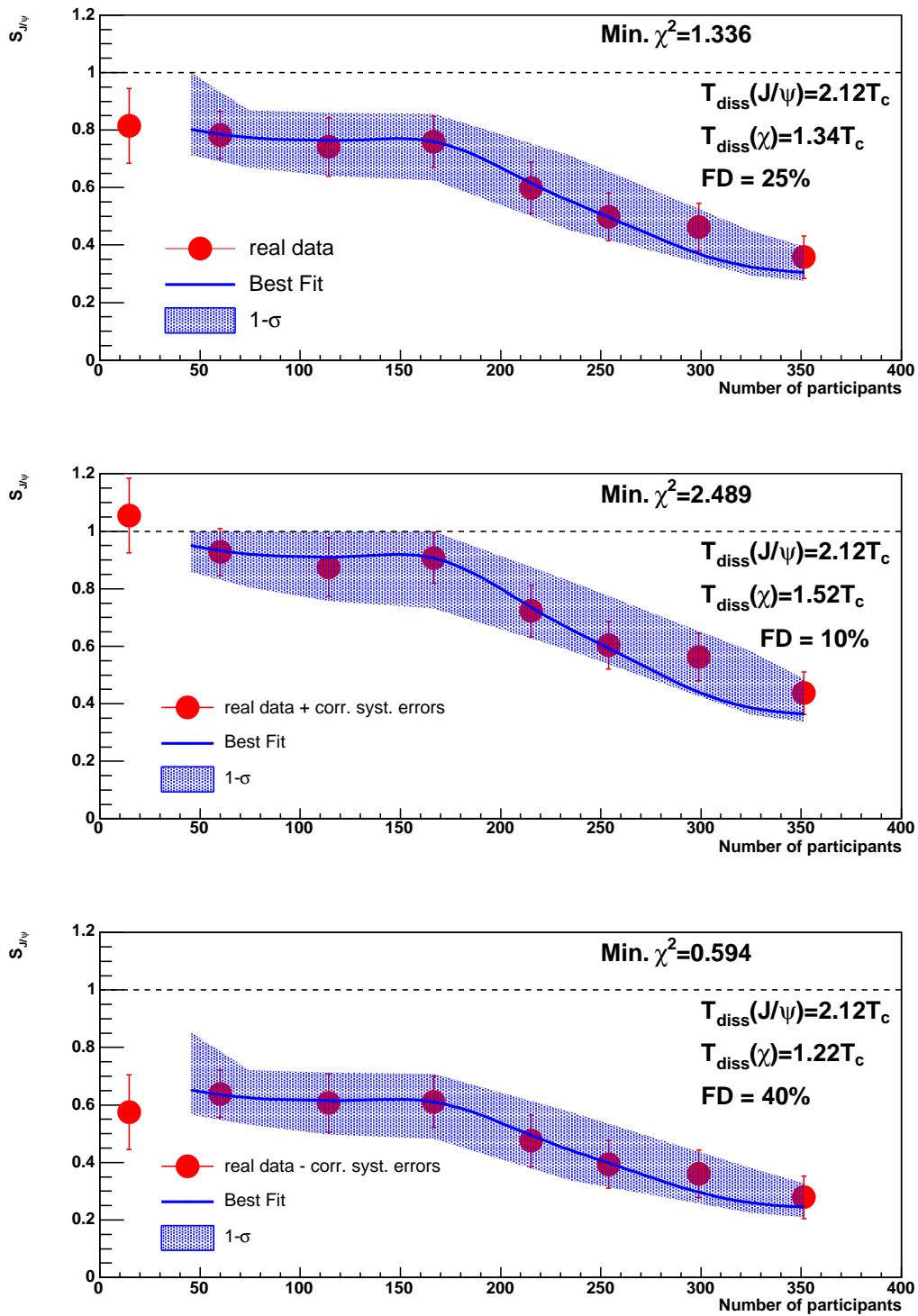


Figure 8.23: The survival probability as a function of the number of participants. Red points are real data, blue solid lines are best fit results and shaded area corresponds to the 1σ deviation of survival probability. Real data in middle and bottom are moved up and down according to correlated systematic errors.

Current experimental $S_{J/\psi}$ results suggest that the survival probability obtained from real data can be described well by this model with $(T_{diss}(J/\psi), T_{diss}(\chi), f_{FD}) \simeq (2.12T_c, 1.34T_c, 0.25)$, $(2.12T_c, 1.52T_c, 0.10)$ and $(2.12T_c, 1.22T_c, 0.40)$. χ^2 analysis gives the quantitative estimation of $(T_{diss}(J/\psi), T_{diss}(\chi), f_{FD})$ and their errors, which result in as follows:

$$T_{diss}(J/\psi) = (2.12^{+0.09}_{-0.03})T_c \quad (8.51)$$

$$T_{diss}(\chi_c) = (1.36^{+0.44}_{-0.36})T_c \quad (8.52)$$

$$f_{FD} = 0.25^{+0.18}_{-0.10} \quad (8.53)$$

It is noted that the systematic uncertainties from hydrodynamics calculation are not included in these results.

These results indicate that the observed J/ψ suppression is due to the sequential melting of J/ψ , first from χ_c and ψ' decay in mid-central Au+Au collisions and second from “directly” produced J/ψ . Also these results suggest that the dissociation temperature of J/ψ is higher than the original expectation ($\sim 1.1T_c$, see Chap. 2) and is in quite good agreement with the expectation from lattice QCD calculations and potential model analyses.

p_T dependence of J/ψ suppression

Survival probability was extracted for each p_T bin with this model and the survival probability as a function of p_T was compared to the results in Au+Au collisions. Figure 7.6 shows R_{AA} as a function of p_T for the centrality of 0-10/10-20/20-30/30-40/40-60/60-93%. CNM effects were taken out by assuming that the CNM effects don't have J/ψ p_T dependence.

Figure 8.24 shows the survival probability $S_{J/\psi}$ as a function of J/ψ p_T for 0-10% (upper left), 10-20% (upper right), 20-30% (lower left) and 30-40% (lower right). Red points are the survival probability extracted from real data, where R_{AA} was divided by that from CNM effects (1 mb absorption cross section). Bracket corresponds to the total systematic uncertainties and box corresponds to the stat. and sys. errors in the invariant p_T distribution in $p + p$ collisions. Band corresponds to the systematic uncertainties of T_{AB} . Blue lines correspond to the expected survival probability obtained from this model calculation, where the dissociation temperatures and feed down contribution were set to $(T_{diss}(J/\psi), T_{diss}(\chi), f_{FD}) = (2.12T_c, 1.36T_c, 0.25)$. The shaded area corresponds to the survival probabilities of J/ψ from model calculations, which satisfy within the 1σ contour of the survival probability.

From Fig. 8.24, J/ψ suppression is expected to be flat up to at least 5 GeV/ c . The observed J/ψ suppression seems to be flat and that is in agreement with the J/ψ suppression expected using this model calculations.

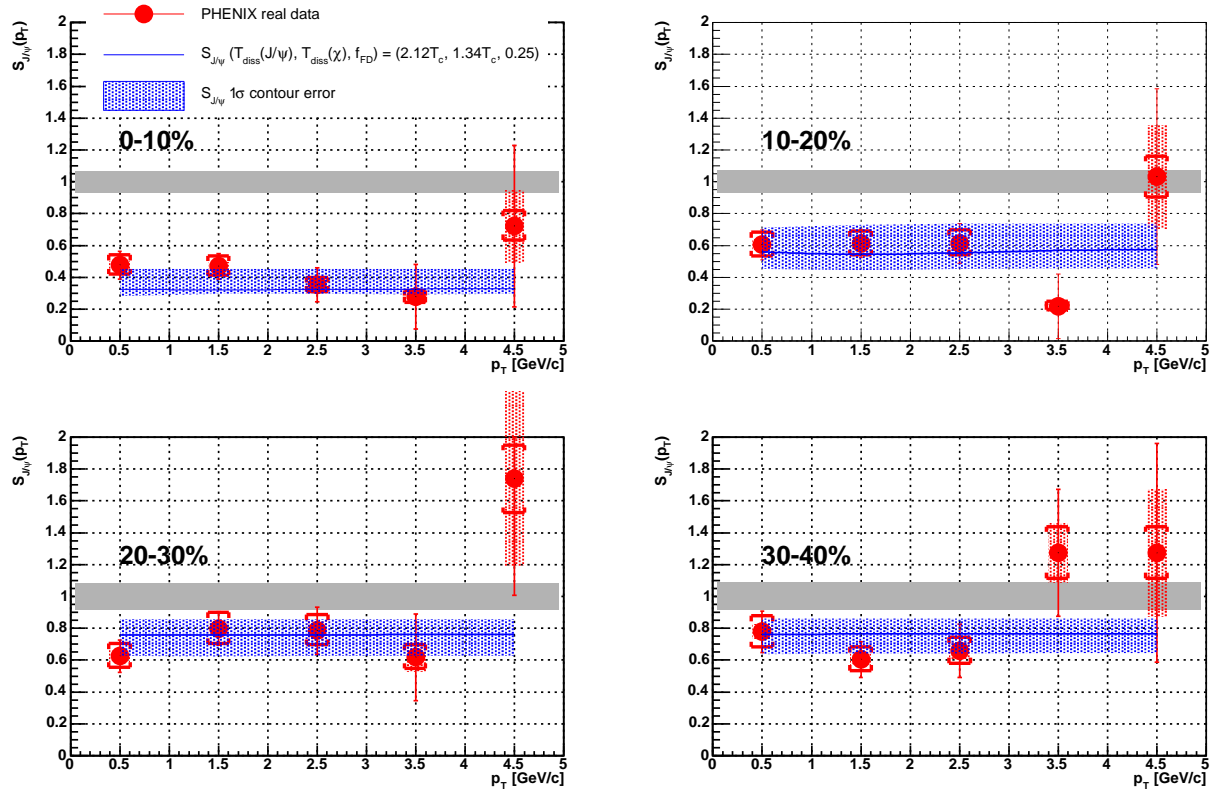


Figure 8.24: Survival probability $S_{J/\psi}$ as a function of J/ψ p_T for 0-10% (upper left), 10-20% (upper right), 20-30% (lower left) and 30-40% (lower right). Data points are explained in text.

Conclusion from this model calculation

From this toy model calculations, J/ψ suppression at RHIC can be concluded as follow:

- **Stronger suppression at more central collisions can be interpreted as the melt of directly produced J/ψ .**
- **The dissociation temperatures of J/ψ and χ_c are extracted to be $(2.12_{-0.03}^{+0.09})T_c$ and $(1.36_{-0.36}^{+0.44})T_c$, respectively, which are in agreement in recent lattice QCD calculations and potential model analyses.**
- **Feed down contribution is estimated from observed J/ψ suppression, which results in $25_{-10}^{+18}\%$.**
- **The suppression seems to be flat as a function of p_T ($p_T \leq 5$ GeV/c), which reproduces the observed suppression as a function of p_T .**

There are remaining issues to be considered in this model calculation, which are listed as follows:

- Θ function as the survival probability.
In this model calculation, survival probability of J/ψ is assumed to be Θ function. Lattice QCD calculations and potential model analyses suggest that the dissociation of J/ψ occurs gradually rather than stepwise as a function of temperature. This indicates that the survival probability $\Theta(T - T_{diss})$ needs to be smeared.
- Transportation of J/ψ in QGP
In this model calculation, J/ψ is assumed to move freely in QGP and to be destroyed if the local temperature exceeds the dissociation temperature. At RHIC energy, charm quarks suffer large energy loss and participate in the partonic flow. This indicates that the charm quarks interact the medium strongly and move diffusively rather than freely in QGP. The fate of J/ψ should be considered in more dynamical framework such as transport description.

8.4 Toward the Future Experiments

Following lists are the issues to be solved to understand J/ψ production in A+A collisions in more detail.

- Need to measure CNM effects more precisely
Initial state effects such as CNM effects are one of the key issues to be understood to extract the final state effects on J/ψ production. Due to the small statistics of J/ψ in Year-3 d +Au collisions, it is difficult to determine the CNM effects quantitatively at RHIC energy.

- Need to measure feed-down contribution at RHIC energy
It is important to measure how fraction of χ_c and ψ' decay to J/ψ at RHIC energy. It gives valuable information to determine the survival probability of χ and directly produced J/ψ . Measurement of χ_c in 200 GeV $p + p$ collisions is under way in PHENIX and the feed-down fraction at RHIC energy will be provided in near future.
- High statistics data in A+A collisions
Au+Au collisions will be held in Year-8 RHIC physics running. $4 \times$ larger statistics is expected in Year-8 Au+Au collisions compared to in Year-4 Au+Au collisions. This will enable for us to reduce the statistical errors.
- Need to measure J/ψ suppression in various collision systems and at various collision energies
Since the dissociation of J/ψ depends on the temperature achieved in the system, measurement of J/ψ in various collision systems at various collision energies will give the unique information of the J/ψ suppression pattern. Cu+Cu collisions were performed in Year-5 RHIC physics running. The analysis is on going and the final results will be provided soon. In 2008, LHC will start its operation. Pb+Pb collisions at $\sqrt{s_{NN}} = 5.5$ TeV will be performed at LHC. Since the energy density and the temperature are expected to be achieved ~ 15 and ~ 2 times larger at RHIC, respectively, primordial J/ψ 's are expected to be completely dissolved in central Pb+Pb collisions. Another importance of the high-energy heavy-ion collisions at LHC is that Υ family can be measured at these energies. Simultaneous measurement of J/ψ and Υ will provide the important insights of the properties of the color screening and the modifications of quarkonia potential in QGP. While the primordial J/ψ 's are expected to be completely dissolved at LHC, the strong enhancement of final J/ψ yield due to the recombination of $c\bar{c}$ pairs is predicted [142]. Therefore J/ψ measurement at LHC will be valuable to understand the J/ψ production mechanism in high-energy heavy-ion collisions, especially, the recombination of J/ψ .

Chapter 9

Conclusion

The measurement of J/ψ yield in Au+Au collisions at the center of mass energy per nucleon ($\sqrt{s_{NN}}$) of 200 GeV has been performed at mid-rapidity region ($|\eta| \leq 0.5$) in order to understand the J/ψ production in A+A collisions and to study the properties of hot and dense medium created at RHIC energy. J/ψ measurement was performed via e^+e^- decay channel with the PHENIX detector and ~ 1000 J/ψ was obtained in Year4 Au+Au collisions.

It is seen that J/ψ yield is strongly suppressed by a factor of ~ 4 in central Au+Au collisions with respect to that in $p + p$ collisions scaled by the average number of nucleon-nucleon collisions. J/ψ suppression in Au+Au collisions is found to be stronger by a factor of $2\sim 3$ than the expectation from cold nuclear matter effects such as nuclear absorption of J/ψ in nuclear environment and gluon shadowing.

Model calculations involving the destruction of J/ψ by thermal gluons and comoving hadrons, which were successful for the SPS results, underpredict the J/ψ suppression at RHIC energy, when the gluon density and comover density are extrapolated from SPS to RHIC energy. The magnitude of J/ψ suppression at RHIC energy is reproduced better with inclusion of the recombination process, while the centrality dependence of J/ψ suppression, in particular, the trend of J/ψ suppression falling down above the number of participant nucleons of ~ 160 , cannot be well described with these results.

Survival probability of J/ψ , which is due to the final state effects in hot and dense medium, was calculated by dividing J/ψ yield in Au+Au collisions by the expectation of J/ψ yield from cold nuclear matter effects. The survival probability of J/ψ at RHIC energy is ~ 0.35 in most central Au+Au collisions and the magnitude is quite similar to that observed at SPS energies from peripheral to mid-central Au+Au collisions and stronger in central Au+Au collisions.

The author constructed the model to study J/ψ suppression at RHIC energy, which incorporated the recent lattice QCD result for J/ψ melting and feed down effect from χ_c and ψ' decay to J/ψ , into the hydrodynamical space-time evolution of the colliding system based on the assumption that J/ψ and $\chi(= \chi_c, \psi')$ production are completely suppressed in the deconfined medium above the melting temperature of them. With this model, J/ψ suppression at RHIC can be reproduced quite well as a result of sequential melting of J/ψ , first from χ_c and ψ' decay started from mid-central Au+Au collisions and second from “directly” produced J/ψ occurred in central Au+Au collisions. Dissociation temperature of “directly” produced J/ψ is estimated to be $(2.12^{+0.09}_{-0.03})T_c$ with this model, which does not depend on cold nuclear matter effects and

suggests that “directly” produced J/ψ is dissolved in the medium at RHIC energy. Occurrence of the suppression of directly produced J/ψ around $2.12T_c$ is consistent with the predictions of the melting temperature of J/ψ by lattice QCD calculations.

Acknowledgment

First and foremost, I would like to express my deep gratitude to Prof. H. Hamagaki for introducing me to the exciting field of high-energy heavy-ion physics and for leading me to the PHENIX experiment. His abundant knowledge and many pieces of valuable advice have always guided me. I couldn't accomplish this work at all without the discussion with him. I would like to express my sincere thanks to Dr. K. Ozawa for giving me a great deal of advice, comments, encouragements and helps on my study. I could learn the physics of this field, experimental techniques, data analysis and so on a lot from them as an experimentalist.

I wish to acknowledge all the collaborators of the PHENIX experiment. I am grateful to the previous spokesperson Prof. W. A. Zajc for his encouragement to my work. I specially wish to thank Dr. T. Sakaguchi, Mr. T. Matsumoto, Dr. S. Kametani, Mr. K. Kato and Dr. F. Kajihara for giving me abundant knowledge of the RICH detector and a great deal of advice on the data analysis. I wish to acknowledge the Heavy/Light Physics Working Group people of the PHENIX for their helps, valuable discussion and friendship. I'm grateful to Dr. Y. Akiba for his comments, many pieces of advice and the useful discussions in the data analysis. I appreciate Dr. X. Wei, Prof. T. Frawley, Prof. M. Rosati, Prof. T. K. Hemmick, Dr. A. Lebedev, Mr. C. L. Silva, Prof. J. L. Nagel, Dr. H. Pereira, Dr. G. de Cassagnac and Dr. M. Leitch for the valuable discussion in the data analysis and the physics results of J/ψ production. I thank Dr. T. Hirano for providing the data sets of the hydrodynamics calculations, which is very valuable and useful in my study, and for giving me the fruitful discussions and comments.

I would like to express my warm appreciation to all the present past members of our group, Dr. T. Horaguchi, Mr. T. Isobe, Mr. N. Kurihara, Mr. S. X. Oda, Mr. Y. Morino, Mr. S. Saito, Mr. Y. L. Yamaguchi and Mr. Y. Aramaki for their kind helps, discussion and friendship at the CNS and BNL.

I thank Mr. T. Nakamura, Mr. H. Masui, Dr. S. Sakai, Mr. M. Konno, Ms. M. Shimomura, Mr. M. Togawa, Mr. Y. Fukao and Dr. K. Okada for their helps and friendship at BNL.

I wish to acknowledge all the members of the Center for Nuclear Study, University of Tokyo. I express my special thanks to institute secretaries, Ms. H. Hirano, Ms. I. Yamamoto, Ms. T. Endo, Ms. Y. Kishi, Ms. K. Takeuchi and Ms. T. Itagaki for their daily helps and encouragements.

I wish to express my thanks to all the staff of the RHIC project, Collider-Accelerator and Physics Department at BNL. The PHENIX experiment is supported by the U. S. Department of Energy under contracts to U. S.-Japan High Energy Physics Collaboration Treaty.

This analysis was supported by the RIKEN PHENIX Computing Center in Japan (CCJ). I appreciate all the staff of the CCJ.

I am grateful to Prof. M. Fukushima, Prof. S. Komamiya, Prof. T. Nagae and Prof. T. Uesaka for their valuable comments and important advice. I would like to express my appreciation to Prof. S. Yamashita for his truly relevant advice and proof-readings.

I wish to acknowledge one of the best friends of mine, Mr. D. Iwamoto. Without meeting with him, I couldn't have discovered such this beautiful world of science (mathematics and physics). I really wish that he is pleased at my success from heaven.

At last but not the least, I would like to express my deepest appreciation to my parents, Kazuaki Gunji and Mayumi Gunji, and my sisters, Waka Gunji and Maki Gunji, for their continuous encouragements and supports. I owe it to them that I could accomplish my study and have such precious experiences in my life.

I am deliriously happy to have been surrounded by such excellent advisers, collaborators, friends and family members. My work would never be completed without their supports and encouragements.

Appendix A

Kinematic Variables

A.1 Transverse momentum

In this analysis, z axis is chosen as the beam going direction. The transverse momentum and the transverse mass are defined in terms of two momentum components of a particle:

$$p_T^2 \equiv p_x^2 + p_y^2, \quad (\text{A.1})$$

$$m_T^2 \equiv m^2 + p_x^2 + p_y^2 = E^2 - p_z^2, \quad (\text{A.2})$$

where E , p_x , p_y , p_z and m are the total energy, x , y and z component of the momentum and the rest mass of a particle, respectively.

A.2 Rapidity and pseudo-rapidity

Choosing the beam going direction as the z axis, the rapidity y of a particle is defined as

$$y \equiv \frac{1}{2} \ln\left(\frac{E + p_z}{E - p_z}\right), \quad (\text{A.3})$$

where E is the total energy of the particle and p_z is the z component of the momentum. The rapidity is transformed under the Lorentz boost in the z direction with the velocity β as follows:

$$y \rightarrow y + \tanh^{-1} \beta \quad (\text{A.4})$$

The particle total energy E and z component momentum p_z can be written in terms of rapidity y and transverse mass m_T as follows:

$$E = m_T \cosh y, \quad (\text{A.5})$$

$$p_z = m_T \sinh y. \quad (\text{A.6})$$

Pseudo-Rapidity η can be expressed in terms of the angle θ between the particle momentum and \vec{p} and z axis as follows:

$$\eta \equiv \frac{1}{2} \ln\left(\frac{|\vec{p}| + p_z}{|\vec{p}| - p_z}\right) = -\ln\left(\tan\left(\frac{\theta}{2}\right)\right) \quad (\text{A.7})$$

A.3 Relation to the space-time coordinate

The proper time τ is defined as follows:

$$\tau = \sqrt{t^2 - z^2}, \quad (\text{A.8})$$

where z is the spatial coordinate and t is the time coordinate. From the analogy of the relation between m_T , p_z , E and y , the space-time (t, z) position of the particle can be related to the rapidity y as follows:

$$t = \tau \cosh y \quad (\text{A.9})$$

$$z = \tau \sinh y \quad (\text{A.10})$$

Appendix B

Performance of the Drift Chamber

B.1 Single wire resolution

Three point method was used to evaluate position resolution in ϕ direction using zero field data [104]. This method is based on the fact that a track is straight line within the DC and the distance calculated from drift time should lineally depend on the wire number, which is assigned from inner to outer detector. This idea is illustrated in Fig. B.1. Residual distribution

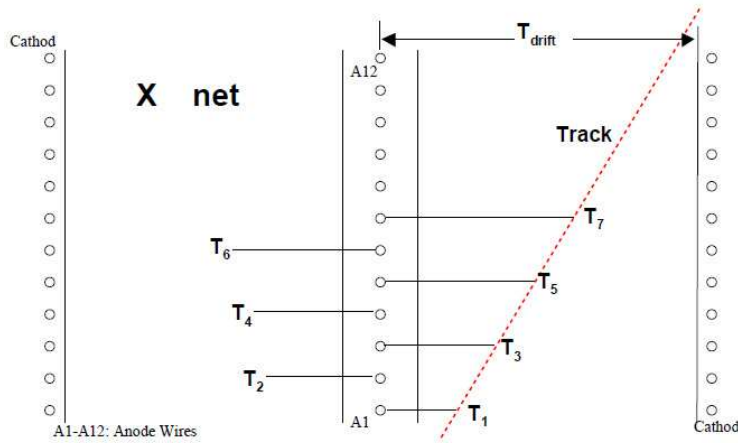


Figure B.1: Illustration of three point method. T_i corresponds to the drift time for the anode wire i .

$v_{drift}\Delta T = v_{drift}[(T_1+T_5)/2-T_3]$ are shown in Fig. B.2, where the calibration of v_{drift} (typically $52 \mu/\text{sec}$) and time zero are already performed. The measured single hit resolution is close to or better than the design resolution of $150 \mu\text{m}$.

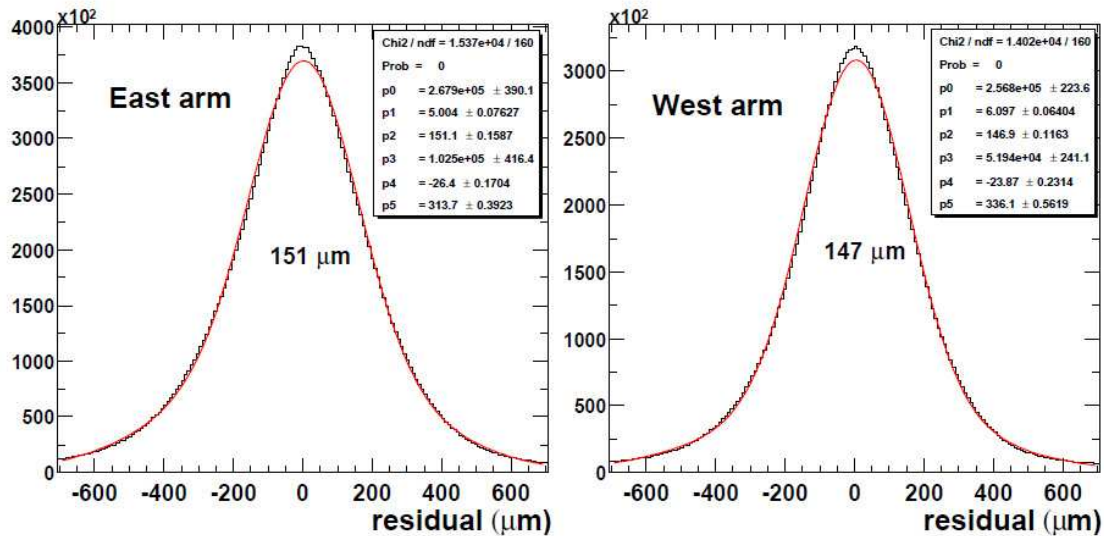


Figure B.2: Residual distribution of the tracks for the each arm (left) and west arm (right).

B.2 Single wire efficiency and tracking efficiency

Three point method was used to study the single wire efficiency [104]. If a hit is found in each of the two neighboring drift region and they belong to the same track, this track can be fixed by a straight line connecting these two hits. Then it is expected to find a hit where the track crosses the current drift region. By counting the fraction of missing hits, the single wire efficiency can be determined. Figure B.3 shows the DC single wire efficiency averaged over 4 neighboring wires for X1 and X2 wire nets. The blank areas are due to inactive regions in the DC. It is seen that most of wires have above 90% efficiency in the active detector area.

Tracking efficiency in low multiplicity environments can be calculated directly from the single wire efficiency shown in Fig. B.3 based on a binomial statistics. If a track requires minimum 8 hits found out of 12 possible hits, this gives more than 99% tracking efficiency in the active area of the DC.

Figure B.4 shows the tracking efficiency of the DC extracted in GEANT simulation [115]. Efficiency in this study was taken to the ratio of the number of tracks reconstructed by DC to the number of input GEANT tracks. The average efficiency in simulation is 98.5%.

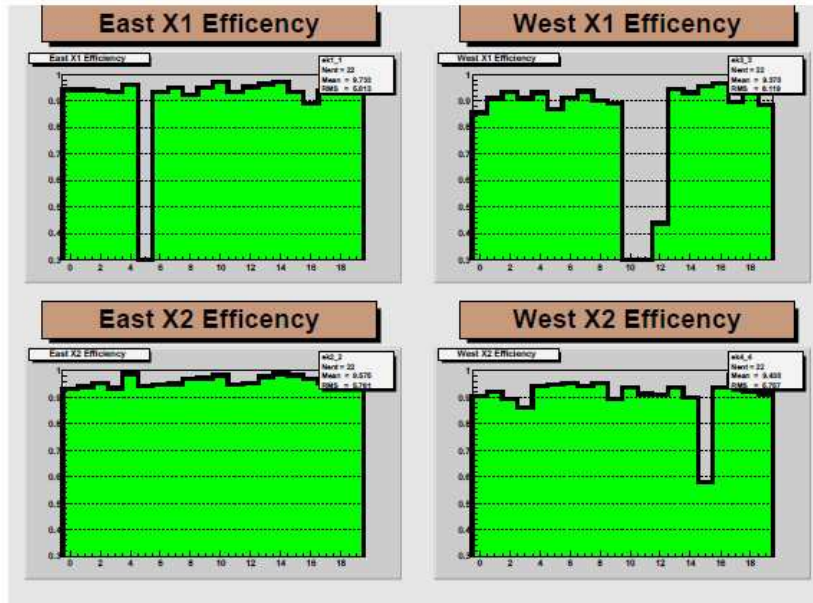


Figure B.3: The single wire efficiency calculated by three point method.

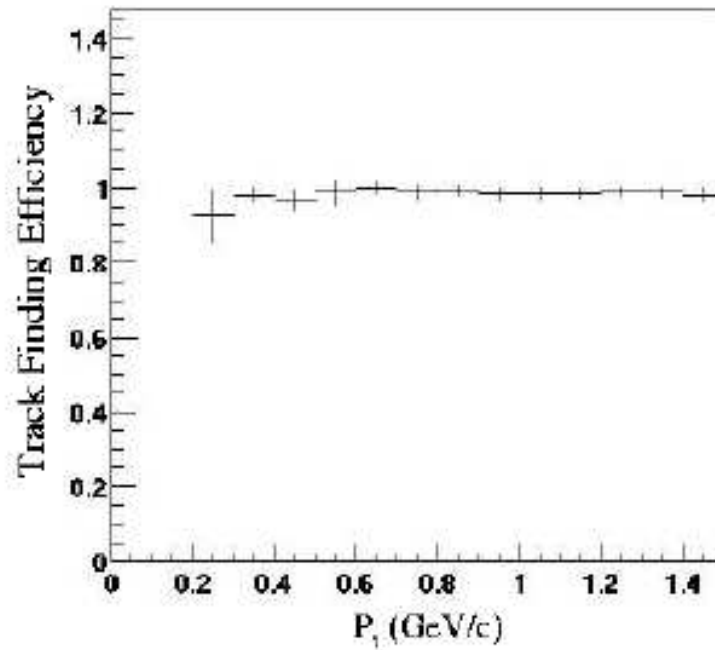


Figure B.4: Tracking efficiency of the DC as a function of input momentum.

Appendix C

Background Normalization for Mixed Event

Event mixing method was used to subtract the uncorrelated combinatorial background from unlike-sign invariant mass distribution.

To perform the event mixing, the events were classified based on the centrality (20 classes) and z-vertex (20 classes). The events were stored in the event buffer with $N_{buffer}(= 20)$ depth. Using the electrons (positrons) in an event and the positrons (electrons) in a different event in the event buffer, uncorrelated e^+e^- pairs were produced. Through this procedure, $2 \times N_{buffer}$ mixed events were produced for one event. Therefore the normalization factor of the mixed event distribution is given by $2 \times N_{buffer}$. However, this normalization factor is diluted since centrality has finite resolution. This dilution can be corrected using like-sign pairs and mixed like-sign pairs. The corrected normalization factor for mixed unlike-sign pairs R_{norm} is as follows:

$$R_{norm} = \frac{1}{2 \times N_{buffer}} \times R(\text{like} - \text{sign}/\text{mixed like} - \text{sign}). \quad (\text{C.1})$$

Validity of R_{norm} as the normalization factor was checked using toy model simulations and described in this chapter.

C.1 Ratio of like-sign and mixed like-sign spectra in real data

Figure C.1, Figure C.2 and Figure C.3 show the invariant mass spectrum of like-sign pairs (black in the left panel) and mixed like-sign pairs (red in the left panel). Ratio of the mass spectrum between like-sign and mixed like-sign spectrum for each 5% centrality bins up to 50% centrality, 50-60% and 60-93% were shown in right of Fig. C.1, Fig. C.2 and Fig. C.3. Here the mixed like-sign distribution was normalized according to the ideal normalization factor $2 \times N_{buffer}$. Therefore the ratio shown in right would be 1 in the ideal case. The ratio was fitted with constant and the result was shown in each panel.

The ratio between like-sign pairs and mixed like-sign pairs for each centrality obtained from real data is summarized in Table C.1. It is seen that the ratio between like-sign and mixed

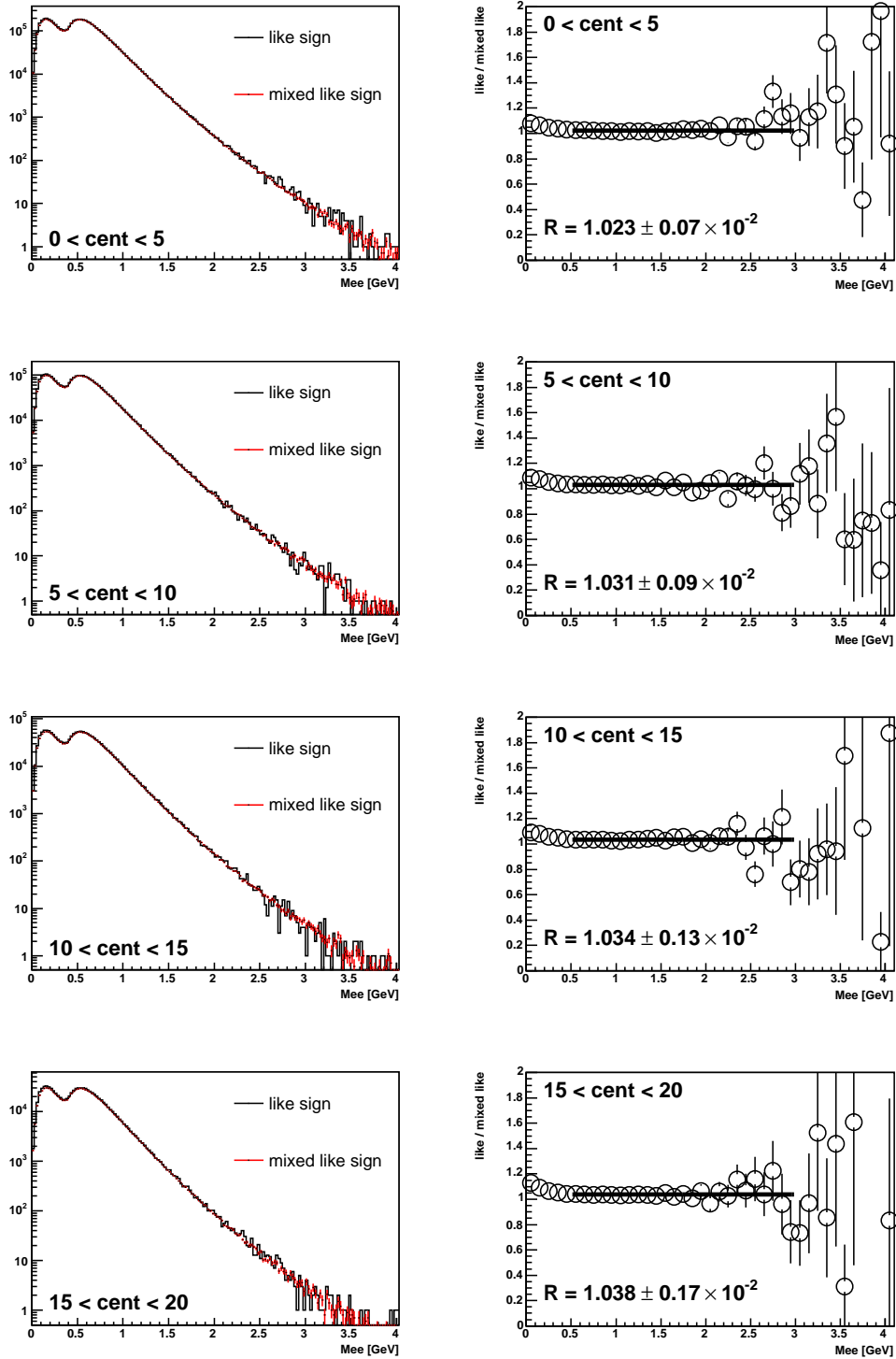


Figure C.1: Left : Invariant mass spectrum of like-sign pairs (black) and mixed like-sign pairs (red). Right : The ratio of the invariant mass spectrum between like-sign pairs and mixed like-sign pairs. The centrality shown in this figure is 0-5/5-10/10-15/15-20% centrality.

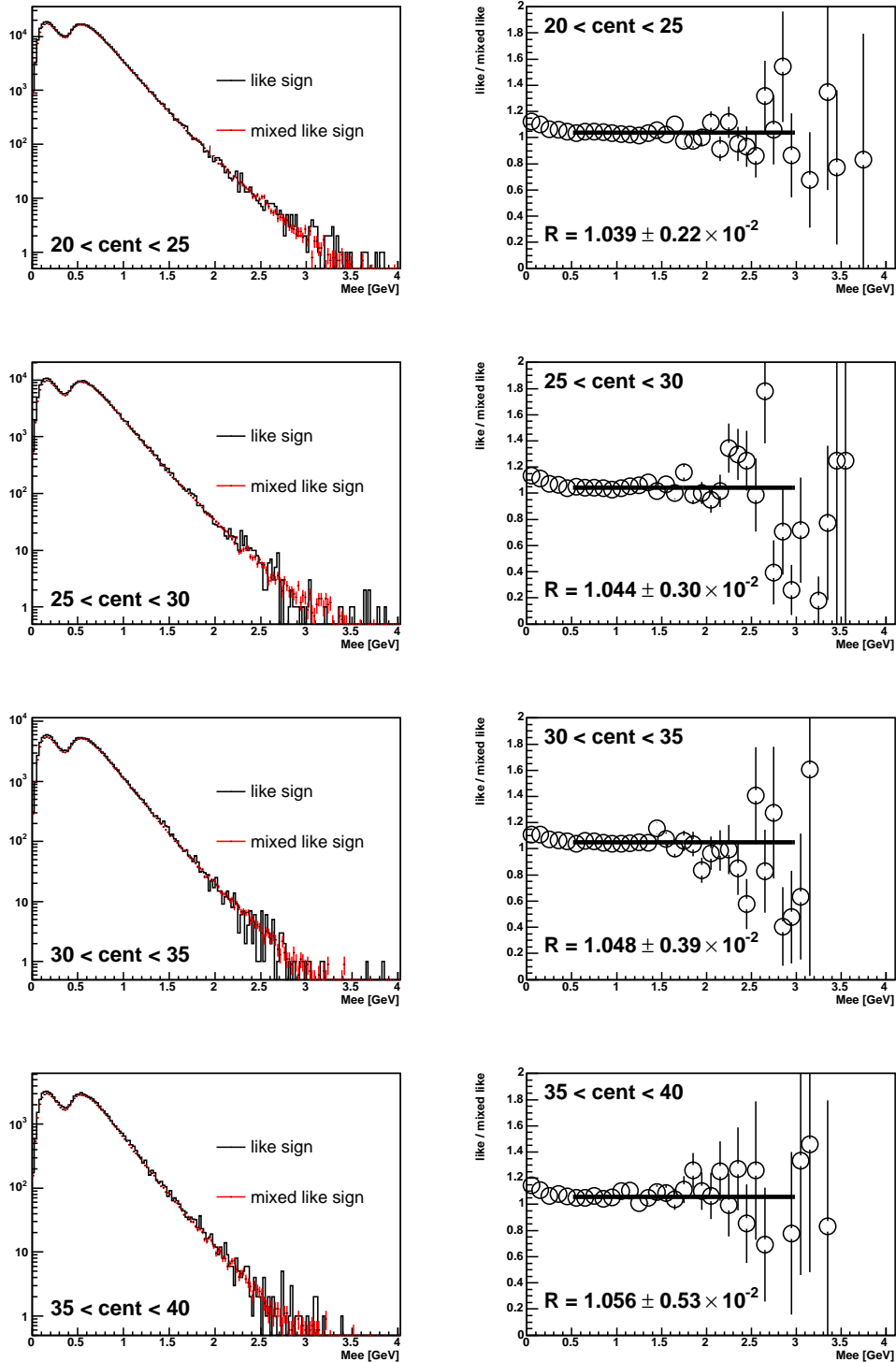


Figure C.2: Left : Invariant mass spectrum of like-sign pairs (black) and mixed like-sign pairs (red). Right : The ratio of the invariant mass spectrum between like-sign pairs and mixed like-sign pairs. The centrality shown in this figure is 20-25/25-30/30-35/35-40% centrality.

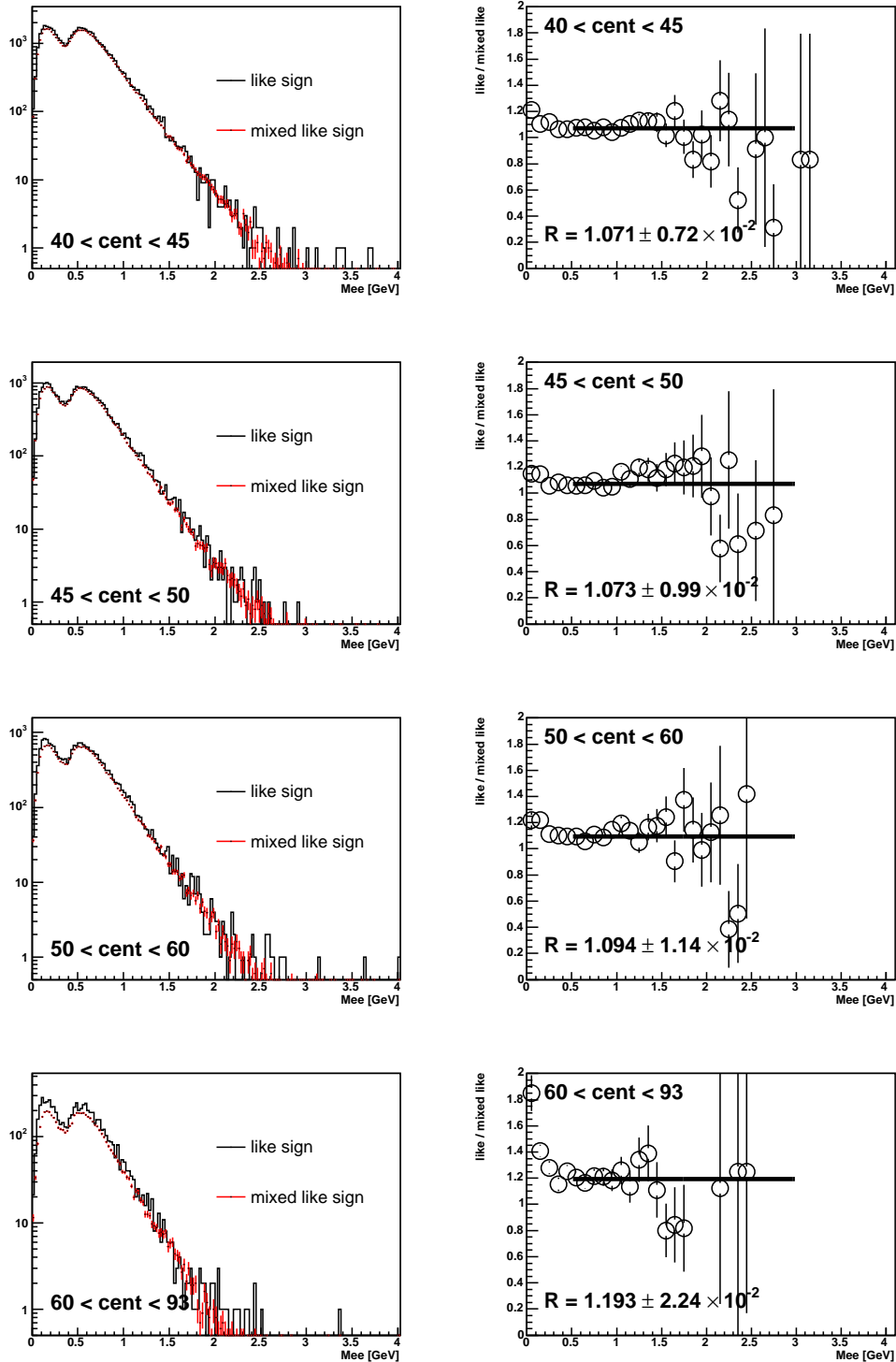


Figure C.3: Left : Invariant mass spectrum of like-sign pairs (black) and mixed like-sign pairs (red). Right : The ratio of the invariant mass spectrum between like-sign pairs and mixed like-sign pairs. The centrality shown in this figure is 40-45/45-50/50-60/60-93% centrality.

Centrality	$\langle N_{part} \rangle$	Ratio (like-sign/mixed like-sign) in real data
0-5%	351.4	1.023 ± 0.001
5-10%	299.0	1.031 ± 0.001
10-15%	253.9	1.034 ± 0.001
15-20%	215.3	1.038 ± 0.002
20-25%	181.6	1.039 ± 0.002
25-30%	151.5	1.044 ± 0.003
30-35%	125.7	1.048 ± 0.004
35-40%	102.7	1.056 ± 0.005
40-45%	82.9	1.071 ± 0.007
45-50%	65.9	1.073 ± 0.010
50-60%	45.5	1.094 ± 0.011
60-93%	14.5	1.193 ± 0.022

Table C.1: Ratio of like-sign to the mixed like-sign for each centrality class in real data. In real data, statistical error is negligible up to 60% and is $\sim 2\%$ in 60-93% bin.

like-sign in real data is not 1, which has clear centrality dependence.

C.2 Toy model simulation

This dilution can be described by the effect of finite centrality resolution. This was checked using toy model simulation. The strategy to study the effect of finite centrality resolution on the ratio is summarized as follows:

1. **Generate the centrality randomly and extract the corresponding average number of the participants $\langle N_{part} \rangle$ using the Glauber model calculation.**
2. **The number of participants N_{part} is determined by smearing it around the average number of participants ($\langle N_{part} \rangle$) according to Gaussian distribution, where the Gaussian *RMS* is extracted from Glauber model calculation. From this smearing, the number of participants is fixed.**

In this stage, the resolution of the centrality is transformed into the resolution of the number of participants. Here RMS/N_{part} was extracted using Glauber model calculations and is shown in Fig. C.4.

3. **Construct uncorrelated pairs from e^+ and e^- distributions, where e^+ and e^- distributions follow Poisson distribution and mean of Poisson distribution was fixed from the centrality dependence of electron multiplicity distributions.**

Electron multiplicity distributions and centrality dependence are discussed in Sec. C.2.1.

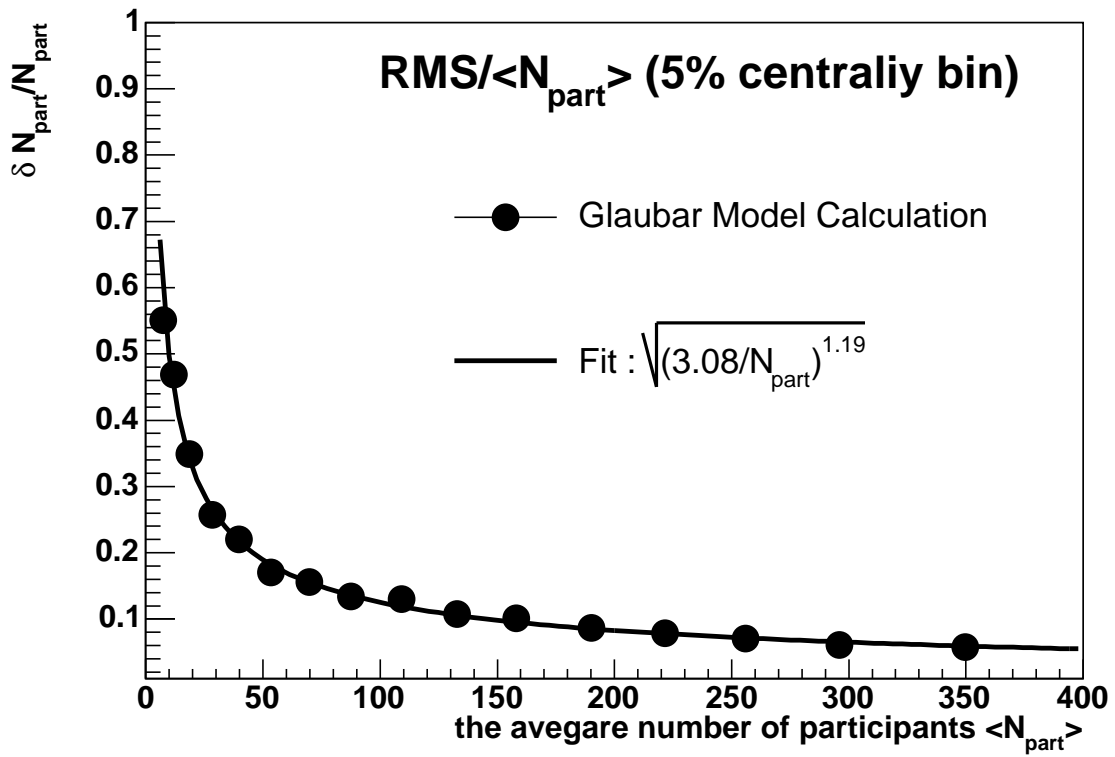


Figure C.4: The resolution of the average number of participants ($\delta \langle N_{part} \rangle / \langle N_{part} \rangle$) as a function of the number of participants (black closed points). Black line is the fitting result and the function was written in this plot.

C.2.1 Electron multiplicity distribution

Figure C.5 shows the multiplicity distribution of electrons (open circle) and positrons (closed circle) in each centrality class (0-5/5-10/10-15/15-20/20-25/25-30/30-35/35-40/40-45/45-50/50-60/60-93% centrality classes), where the electrons and positrons which didn't pass the ghost cut were rejected. Each distribution was fitted with Poisson distribution $P(N; \mu) = (\mu^N / N!) \exp(-\mu)$ and the results were shown as dashed-line and solid line for electrons and positrons, respectively.

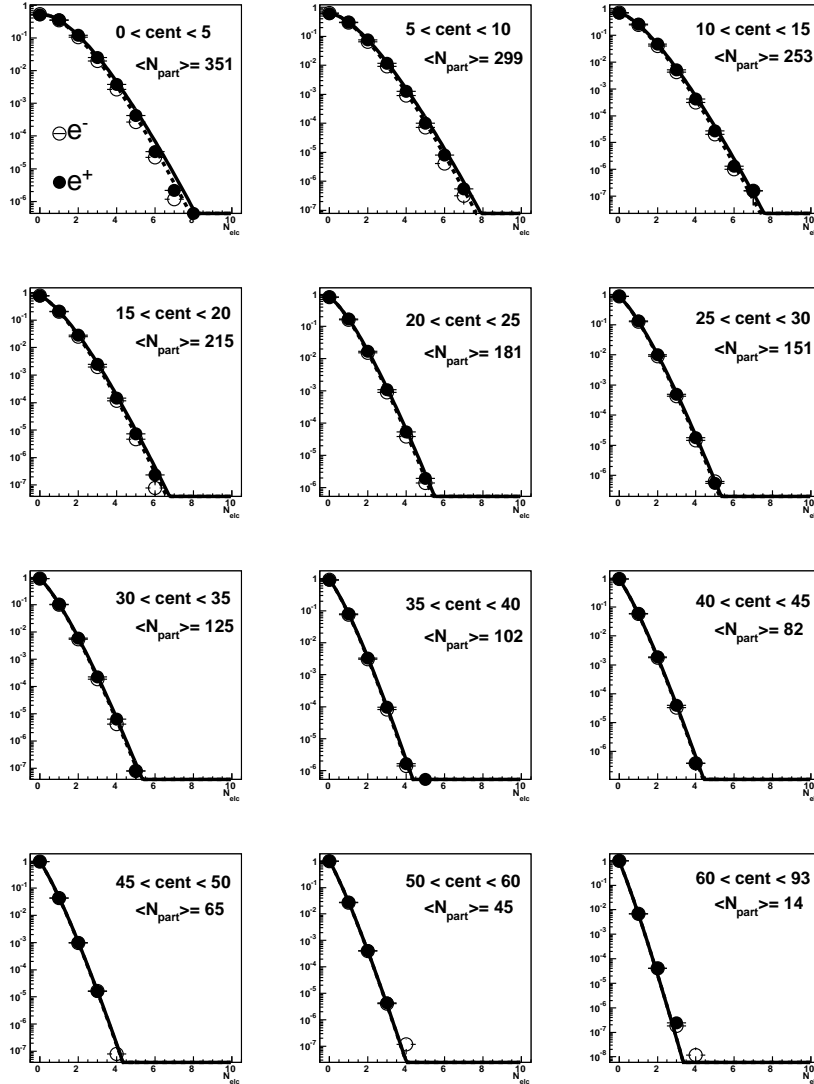


Figure C.5: Multiplicity distribution of electrons (open circle) and positrons (closed circle) in each centrality class (0-5/5-10/10-15/15-20/20-25/25-30/30-35/35-40/40-45/45-50/50-60/60-93% centrality classes). Dashed-lines and Solid lines are the Poisson distributions for electrons and positrons, respectively.

Figure C.6 shows μ of the Poisson distribution as a function of the number of participants

for positrons (Left) and electrons (Right). Solid lines are the fitting results of μ as a function of the number of participants. Fitting functions and results are as follows:

$$\mu_{e^+} = (2.85 \pm 0.01) \times 10^{-4} \times N_{part}^{1.161 \pm 0.001} + (5.078 \pm 0.09) \times 10^{-7} \times N_{part}^{2 \times (1.161 \pm 0.001)} \quad (C.2)$$

$$\mu_{e^-} = (3.04 \pm 0.01) \times 10^{-4} \times N_{part}^{1.141 \pm 0.001} + (5.666 \pm 0.11) \times 10^{-7} \times N_{part}^{2 \times (1.141 \pm 0.001)} \quad (C.3)$$

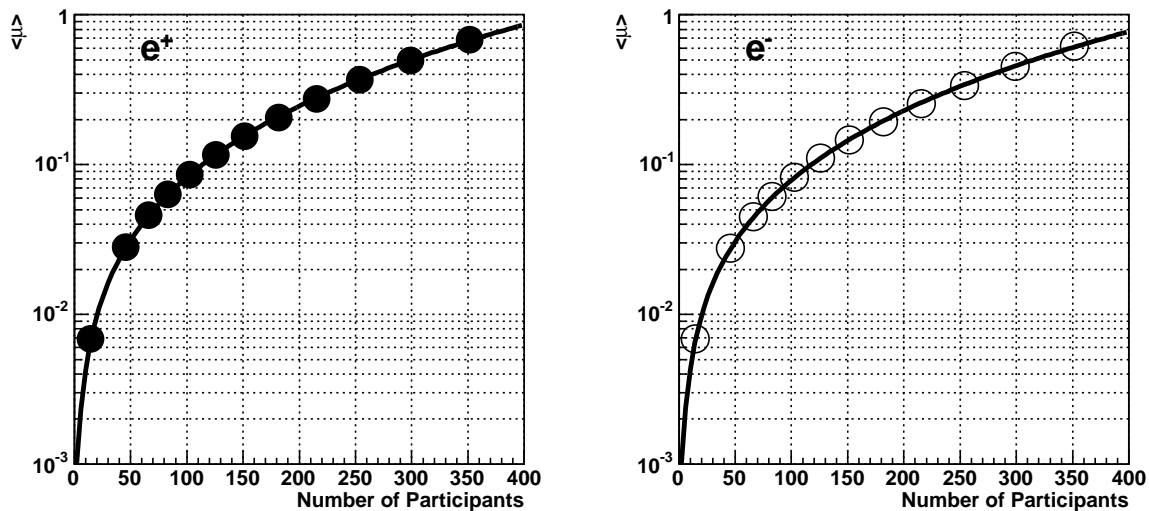


Figure C.6: μ of the Poisson distribution as a function of the number of participants for positrons (Left) and electrons (Right). Solid lines are the fitting results as described in Eq. (C.2) and Eq. (C.3).

C.3 Results of toy model simulations

C.3.1 Case of zero centrality resolution

Figure C.7 shows the ratio of the invariant mass from like-sign pairs to that from mixed like-sign pairs (left) and ratio of the invariant mass from unlike-sign pairs to that from mixed unlike-sign pair (right), where no smearing for N_{part} was applied and the ideal normalization $2 \times N_{buffer}$ was applied to mixed like-sign and mixed unlike-sign spectrum. The ratio of like-sign spectrum over mixed like-sign spectrum and the ratio of unlike-sign spectrum over mixed unlike-sign spectrum are equal to 1, which means that the ideal normalization $2 \times N_{buffer}$ is the correct normalization factor if the resolution of the centrality or the number of participants are set to zero.

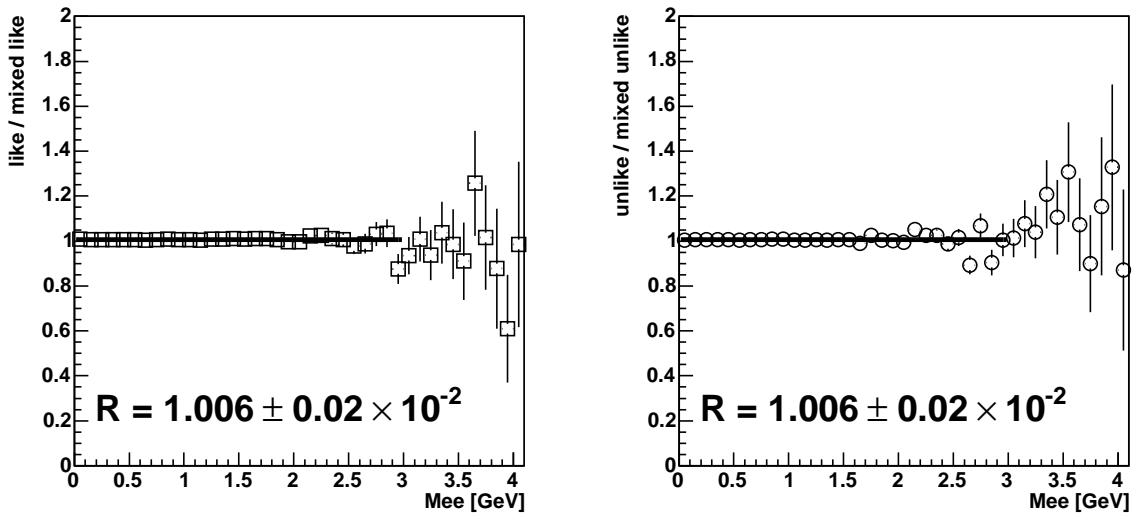


Figure C.7: Left : Ratio of the like-sign spectrum over the mixed like-sign spectrum. Right : Ratio of the unlike-sign spectrum over the mixed unlike-sign spectrum. Centrality range is 0-5/5-10/10-15/15-20% from upper to lower. No smearing of the number of participants was taken into account.

C.3.2 Case of finite centrality resolution

Figure C.8, Figure C.9 and Figure C.10 show the ratio of the invariant mass from like-sign pairs to that from mixed like-sign pairs (left) and ratio of the invariant mass from unlike-sign pairs to that from mixed unlike-sign pairs (right) for each centrality class obtained by this toy model, where the ideal normalization $2 \times N_{buffer}$ is applied to mixed like-sign and unlike-sign spectrum.

Table C.2 is the summary of the ratio of like-sign to the mixed like-sign and the ratio of the unlike-sign to mixed unlike-sign spectrum for each centrality class with the smearing for the number of participants. By comparing the ratio obtained from real data, which is summarized

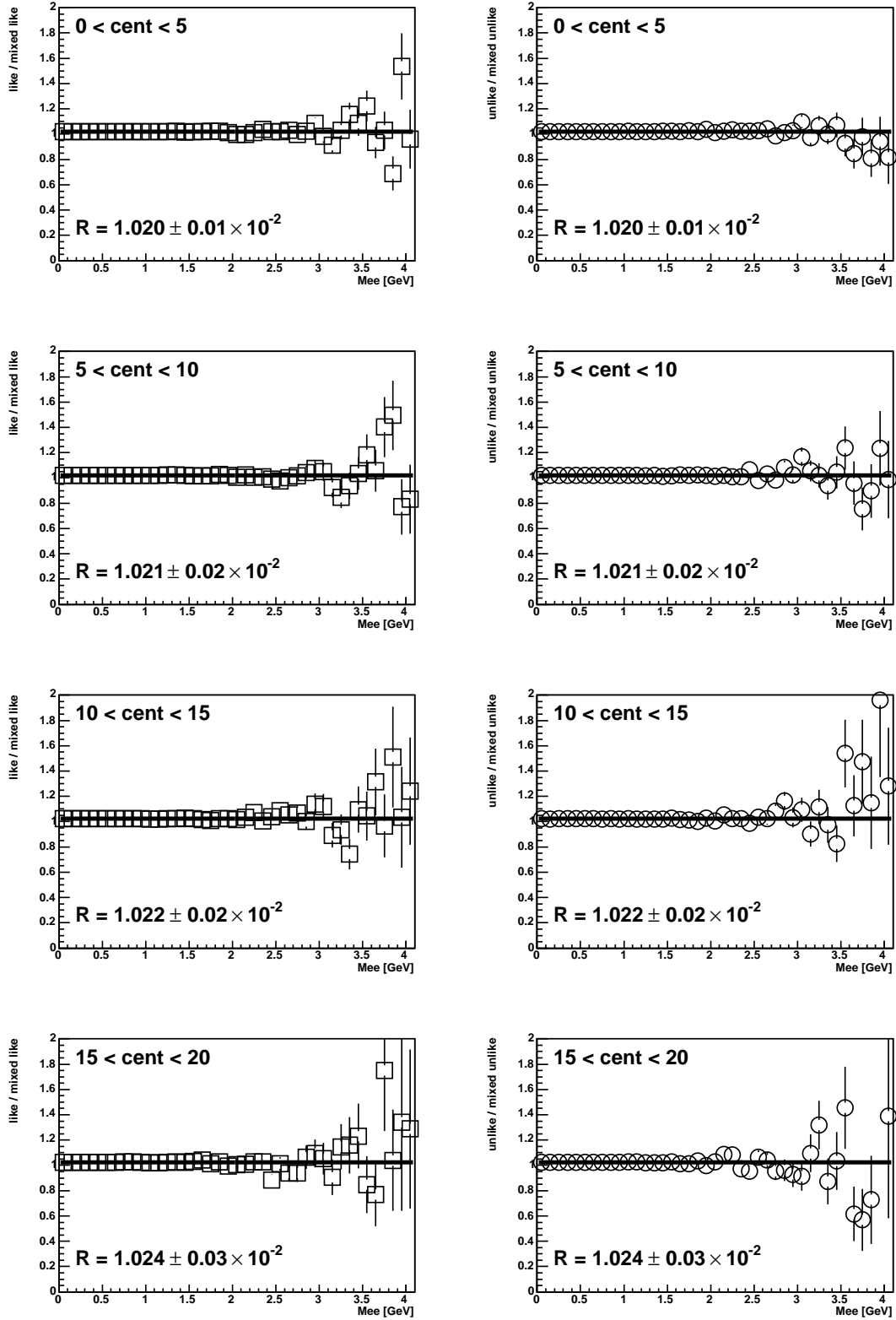


Figure C.8: Left : Ratio of the like-sign spectrum over the mixed like-sign spectrum. Right : Ratio of the unlike-sign spectrum over the mixed unlike-sign spectrum. Centrality range is 0-5/5-10/10-15/15-20% from uppper to lower.

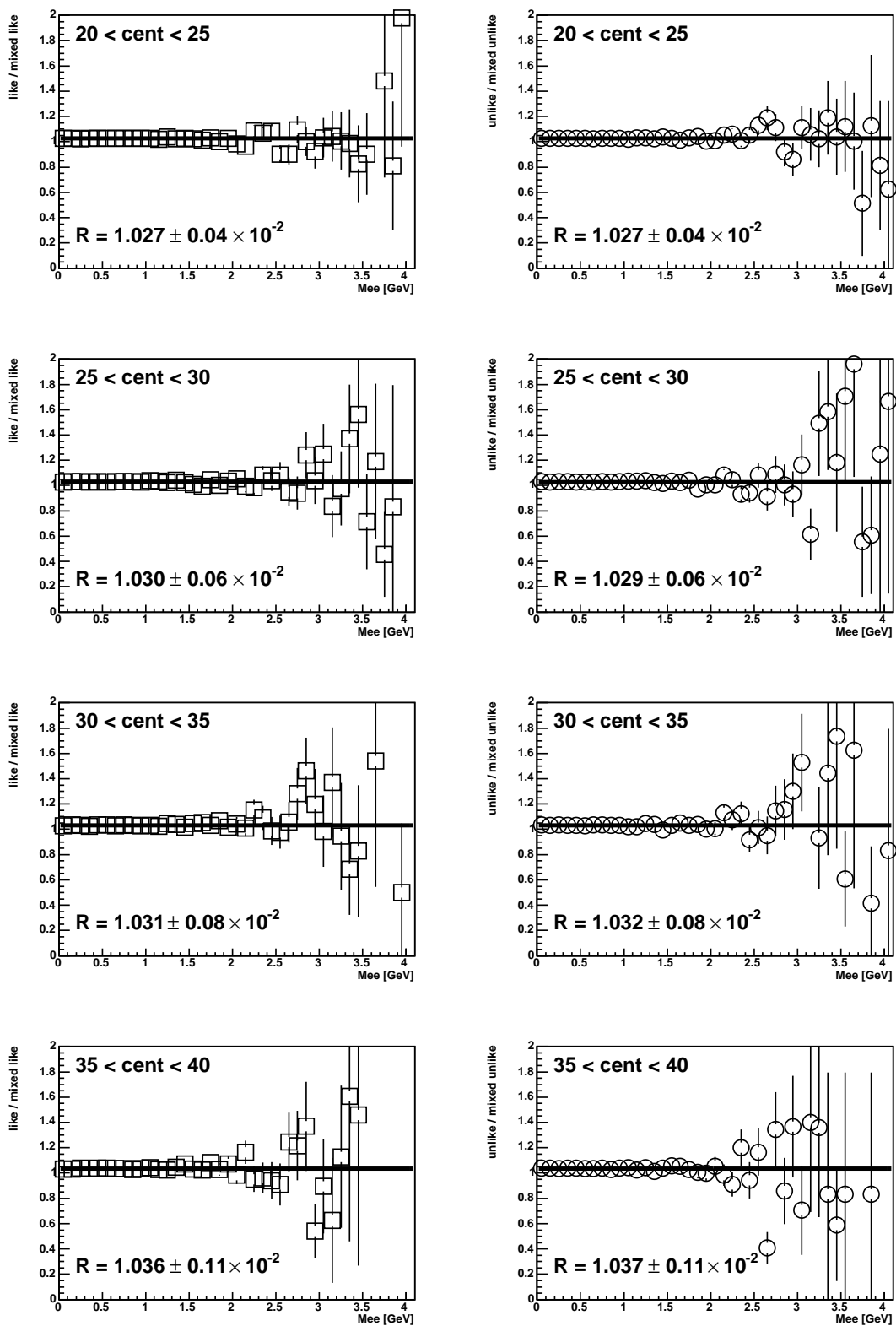


Figure C.9: Left : Ratio of the like-sign spectrum over the mixed like-sign spectrum. Right : Ratio of the unlike-sign spectrum over the mixed unlike-sign spectrum. Centrality range is 20-25/25-30/30-35/35-40% from upper to lower.

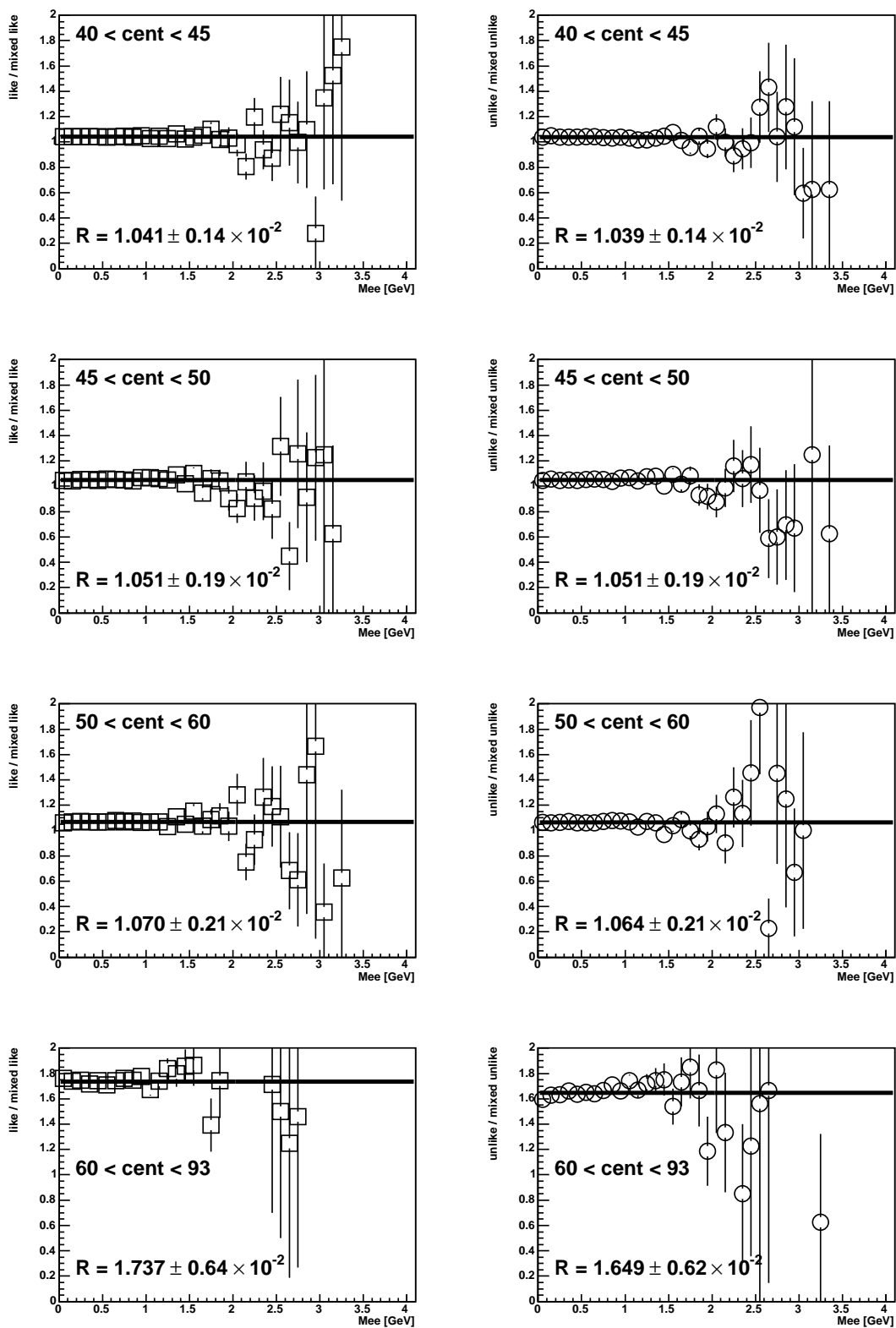


Figure C.10: Left : Ratio of the like-sign spectrum over the mixed like-sign spectrum. Right : Ratio of the unlike-sign spectrum over the mixed unlike-sign spectrum. Centrality range is 40-45/45-50/50-60/60-93% from upper to lower.

Centrality	$\langle N_{part} \rangle$	R (like-sign/mixed like-sign)	R (unlike-sign/mixed unlike-sign)
0-5%	351.4	1.020	1.020
5-10%	299.0	1.021	1.021
10-15%	253.9	1.022	1.022
15-20%	215.3	1.024	1.024
20-25%	181.6	1.027	1.027
25-30%	151.5	1.030	1.029
30-35%	125.7	1.031	1.032
35-40%	102.7	1.036	1.037
40-45%	82.9	1.041	1.039
45-50%	65.9	1.061	1.061
50-60%	45.5	1.070	1.064
60-93%	14.5	1.737	1.649

Table C.2: Ratio of like-sign to the mixed like-sign and the ratio of the unlike-sign and mixed unlike-sign spectrum for each centrality class with the smearing effect for the number of participants.

in Table C.1, the centrality dependence of the ratio between like-sign and mixed like-sign is reproduced well except 60-93% centrality bin. However, there is still 1~3% difference in normalization factor. This 3% difference was taken to be the systematic uncertainties of the normalization for the mixed event distributions.

For 60-93% centrality bin, ratio of like-sign to mixed like-sign R is greatly different between real data and toy model calculation. One of the possible reason is that N_{part} for larger than 60% centrality has large systematic uncertainties (larger than 14%) in Glauber model calculation based on Table 6.1 and that the N_{part} resolution as shown in Fig. C.4 and Poisson μ parameter as shown in Fig. C.6 change dramatically when N_{part} varies $\pm 14\%$. These two coincident effects lead the large uncertainties on the determination of R in toy model calculation. For instance, the resolution of N_{part} for 60-65% centrality bin shown in Fig. C.4 is $\sim 25\%$ and it varies from 22% to 28% when the systematic uncertainties of N_{part} are taken into account from Table 6.1. When the N_{part} resolution is 22% and 28%, R becomes ~ 1.1 and ~ 8 , respectively, which indicates that R has large uncertainty and that R is difficult to be determined for this centrality region.

Appendix D

Invariant Mass Distributions

Figure D.1, Figure D.2, Figure D.3, Figure D.4, Figure D.5, Figure D.6 show the invariant mass spectra of unlike-sign pairs (black) and mixed unlike-sign pairs (red) after the normalization expressed in Eq. (6.30) for each p_T bin (p_T range is written in the title of the histogram) and for 0-10%, 10-20%, 20-30%, 30-40%, 40-60%, 60-93% centrality, respectively.

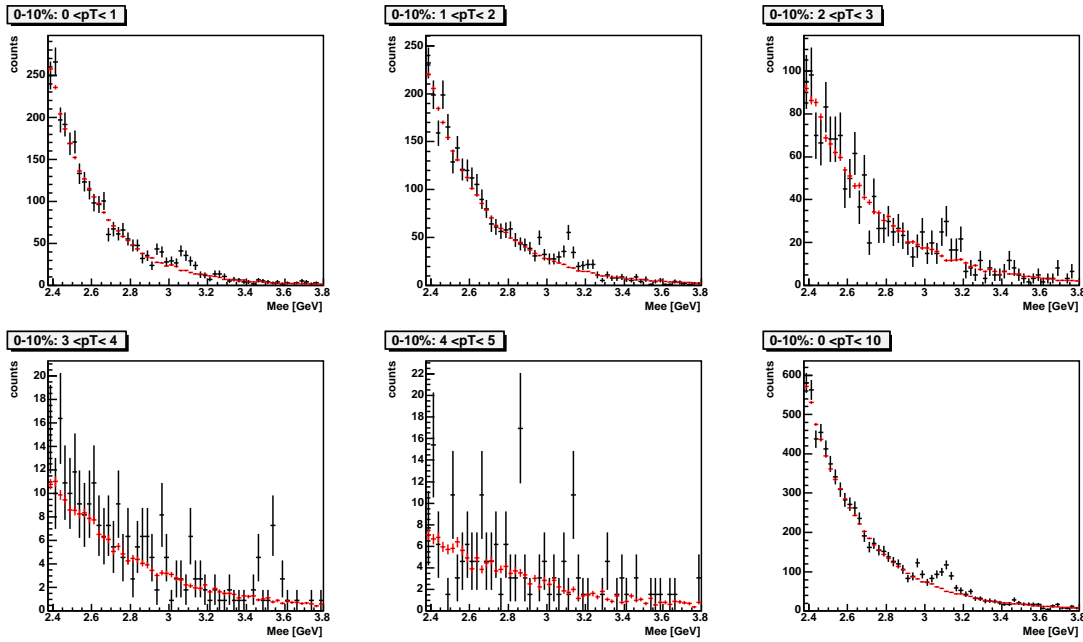


Figure D.1: Invariant mass spectra of unlike-sign pairs (black) and mixed unlike-sign pairs (red) for 0-1/1-2/2-3/3-4/4-5/0-10 GeV/ c p_T bin in 0-10% data sample

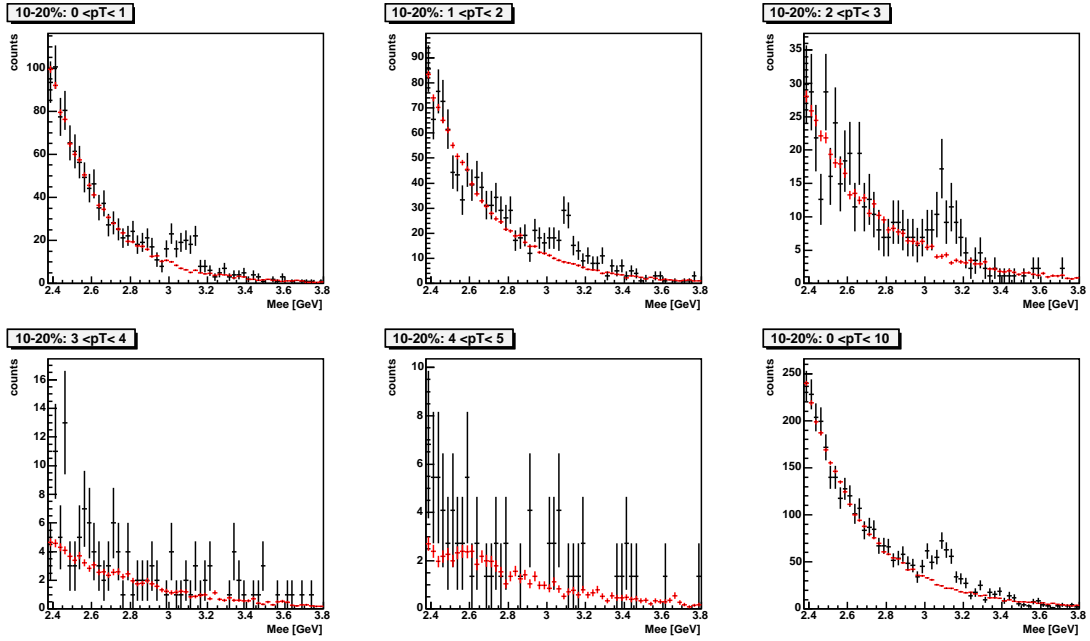


Figure D.2: Invariant mass spectra of unlike-sign pairs (black) and mixed unlike-sign pairs (red) for 0-1/1-2/2-3/3-4/4-5/0-10 GeV/ c p_T bin in 10-20% data sample

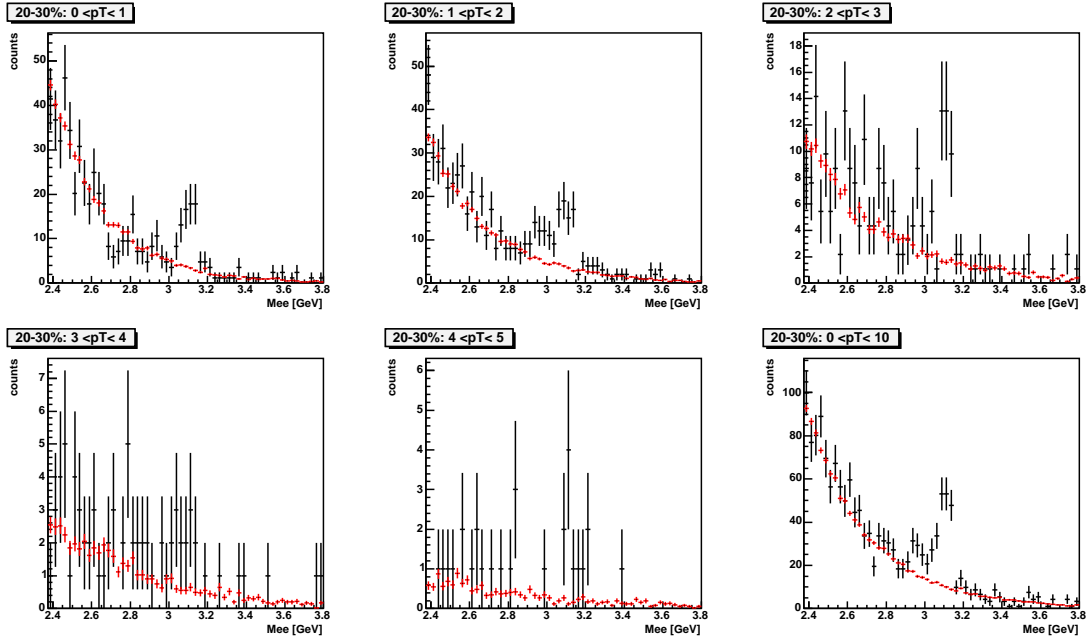


Figure D.3: Invariant mass spectra of unlike-sign pairs (black) and mixed unlike-sign pairs (red) for 0-1/1-2/2-3/3-4/4-5/0-10 GeV/ c p_T bin in 20-30% data sample

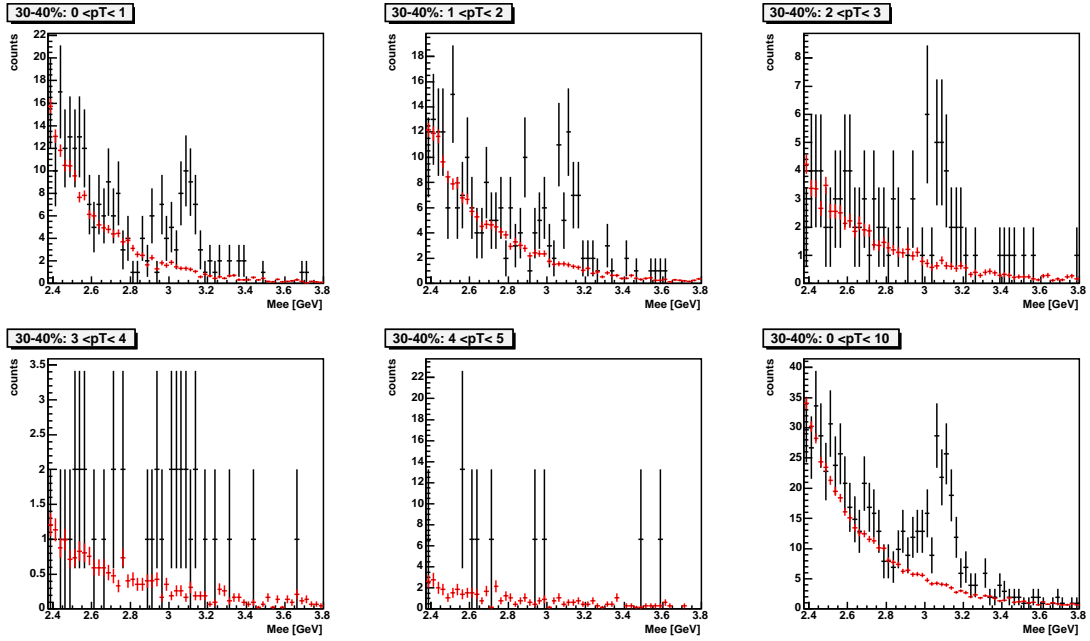


Figure D.4: Invariant mass spectra of unlike-sign pairs (black) and mixed unlike-sign pairs (red) for 0-1/1-2/2-3/3-4/4-5/0-10 GeV/ c p_T bin in 30-40% data sample

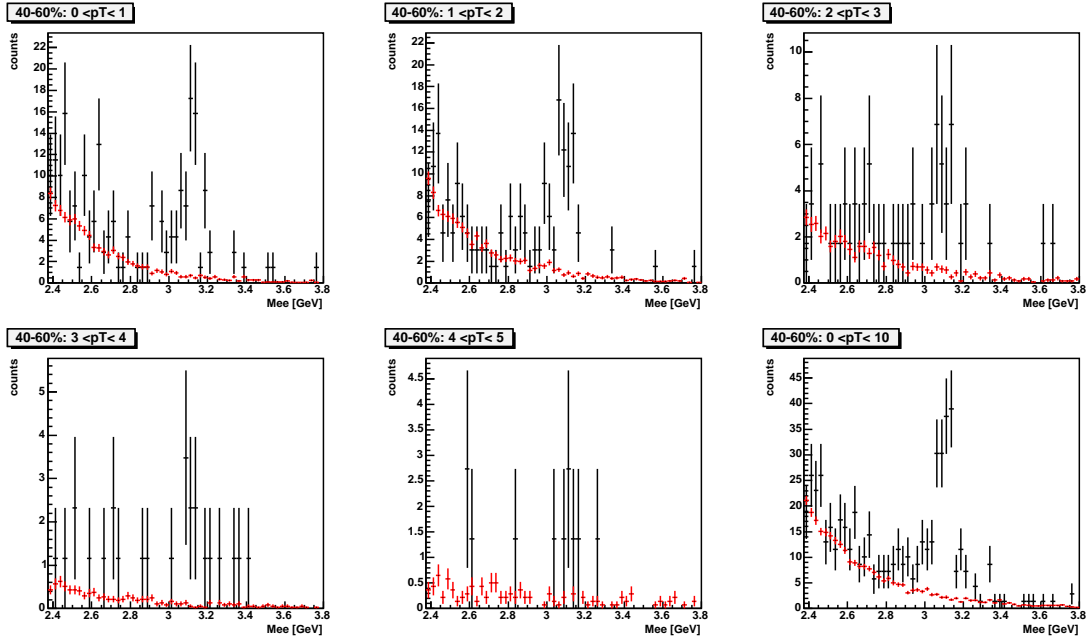


Figure D.5: Invariant mass spectra of unlike-sign pairs (black) and mixed unlike-sign pairs (red) for 0-1/1-2/2-3/3-4/4-5/0-10 GeV/ c p_T bin in 40-60% data sample

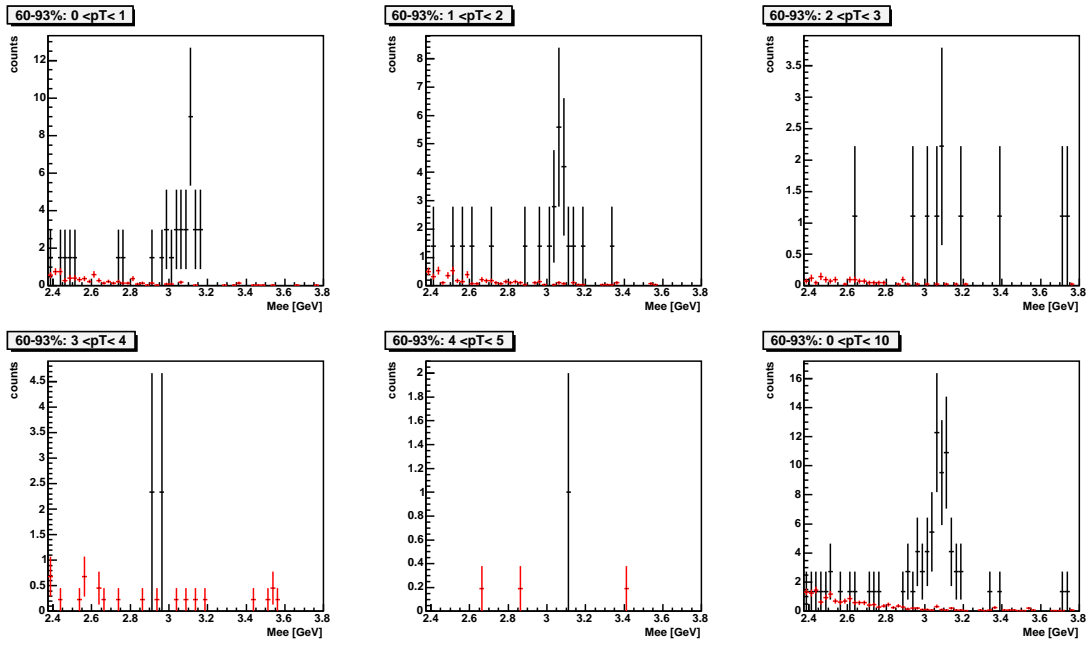


Figure D.6: Invariant mass spectra of unlike-sign pairs (black) and mixed unlike-sign pairs (red) for 0-1/1-2/2-3/3-4/4-5/0-10 GeV/ c p_T bin in 60-93% data sample

Appendix E

Comparison of Simulation with Real Data

E.1 Comparison of momentum resolution

Momentum resolution in simulation was checked by taking the difference in momentum between input GEANT momentum and reconstructed momentum. Symbols in Fig. E.1 are the difference in the momentum ($\Delta p = p_{reco} - p_{GEANT}$) as a function of reconstructed momentum. Solid line corresponds to the momentum resolution extracted in real data. It is seen that the momentum resolution in real data and simulation is in good agreement.

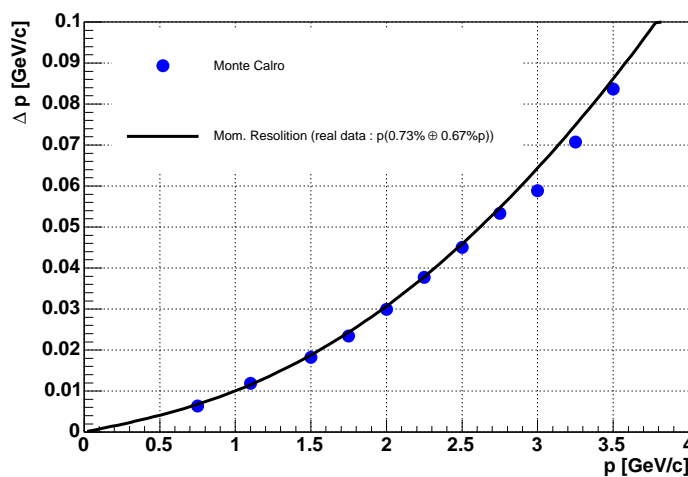


Figure E.1: Momentum difference between input GEANT momentum and reconstructed momentum (symbols) and momentum difference extracted from real data (solid line).

E.2 Comparison of the eID parameters

Electron identification (eID) parameters such as $n0$, $npe0$, $n1$, $npe1$, $disp$, $chi2$, dep , $emcsdphi_e$ and $emcsdz_e$ were tuned to reproduce those in real data. Figure E.2 shows the eID parameters in real data (black) and simulation (red) for $n0$, $n1$, $npe0$, $npe1$, $disp$, $chi2/npe1$, dep , $emcsdphi_e$ and $emcsdz_e$. These parameters in simulation are in agreement with real data.

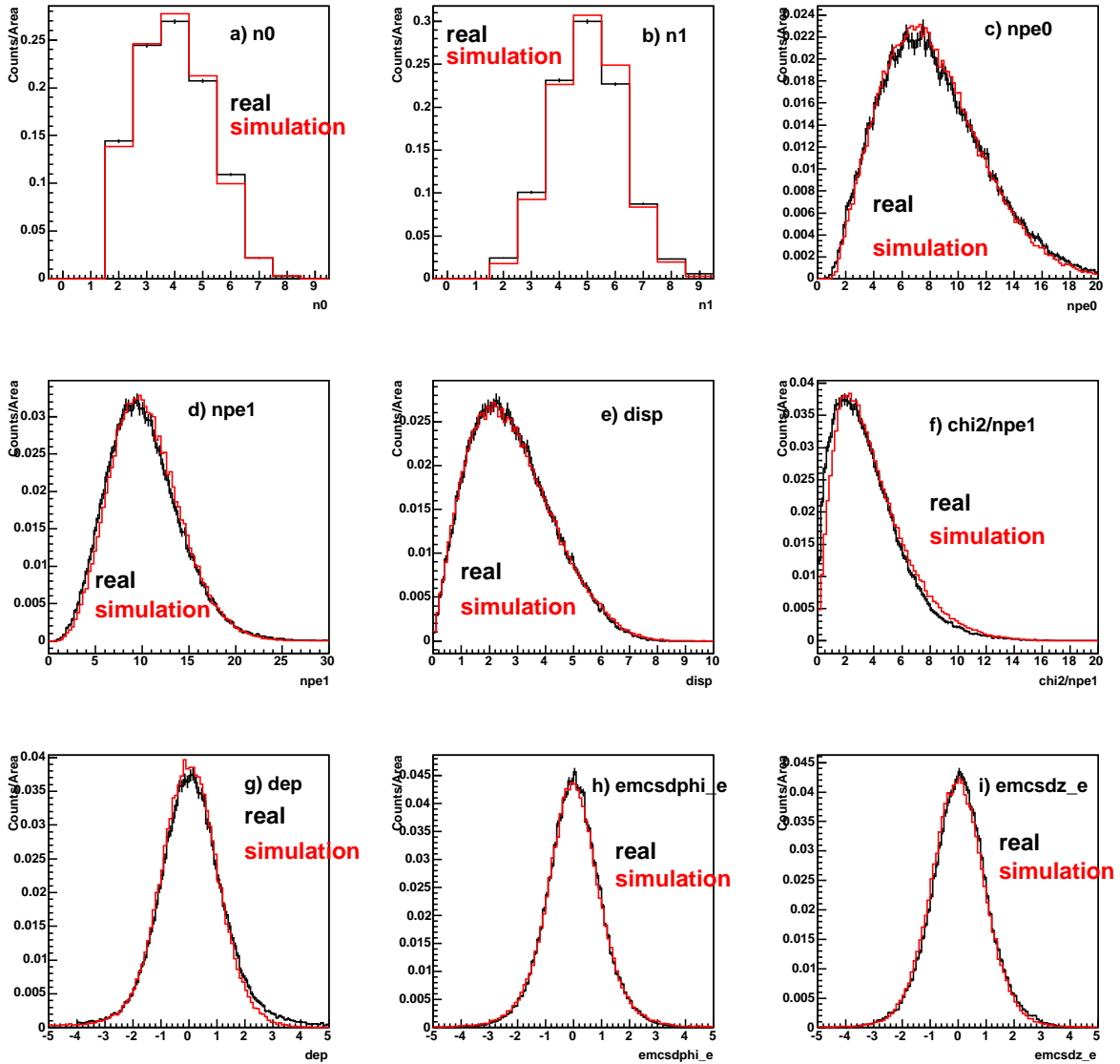


Figure E.2: Comparison of eID parameters in real (black) and simulation (red). a) $n0$, b) $n1$, c) $npe0$, d) $npe1$, e) $disp$, f) $chi2/npe1$, g) dep , h) $emcsdphi_e$ and i) $emcsdz_e$.

E.3 Comparison of the detector acceptance

Detector dead maps were searched for the real data in G9 run groups and the same dead maps of DC, RICH, EMCal and PC were implemented in this simulation. Figure E.3, Figure E.4 and Figure E.5 show the hit map of DC, PC1-PC3 and EMCal in real data (left column) and in simulation (right column). Since the same dead channels are implemented in simulation, the inactive area are similar between real data and simulation. In Fig. E.3, cell and panel correspond to ϕ and r coordinates, respectively. In Fig. E.4, x-axis and y-axis correspond to z and y coordinates, respectively. In Fig. E.5, x-axis and y-axis correspond to z and y coordinates, respectively.

Figure E.6 shows the ϕ and zed distributions for single electrons at the each DC sector in real data (black) and simulation (red). Upper left, upper right, lower left and lower right are the ϕ distribution at the DC south, ϕ distribution at the DC north, zed distribution at the East DC and zed distribution at the West DC, respectively. The acceptance in ϕ and zed in simulation is in good agreement with real data.

Systematic error of the acceptance difference between simulation and real data was estimated by evaluating following ratio R_{acc} for each DC side.

$$R_{acc} = \left\langle \frac{\frac{dN^{East}}{d\phi_{sim}}}{\frac{dN^{East}}{d\phi_{real}}} \right\rangle \times \left\langle \frac{\frac{dN^{West}}{d\phi_{sim}}}{\frac{dN^{West}}{d\phi_{real}}} \right\rangle, \quad (\text{E.1})$$

where $\frac{dN^{East}}{d\phi_{sim}}$, $\frac{dN^{East}}{d\phi_{real}}$, $\frac{dN^{West}}{d\phi_{sim}}$, $\frac{dN^{West}}{d\phi_{real}}$ are the $dN/d\phi$ in East in simulation, in East in real data, in West in simulation, in West in real data as shown in Fig. E.6, respectively.

Table E.1 is the summary of R_{acc} for each DC side. The deviation of R_{acc} from 1 was assigned as the systematic error of the acceptance for single electrons and the systematic error is 3%, which corresponds to the systematic error for pairs of 6%.

DC Side	R_{acc}
South	0.967
North	0.972

Table E.1: R_{acc} for DC south and north.

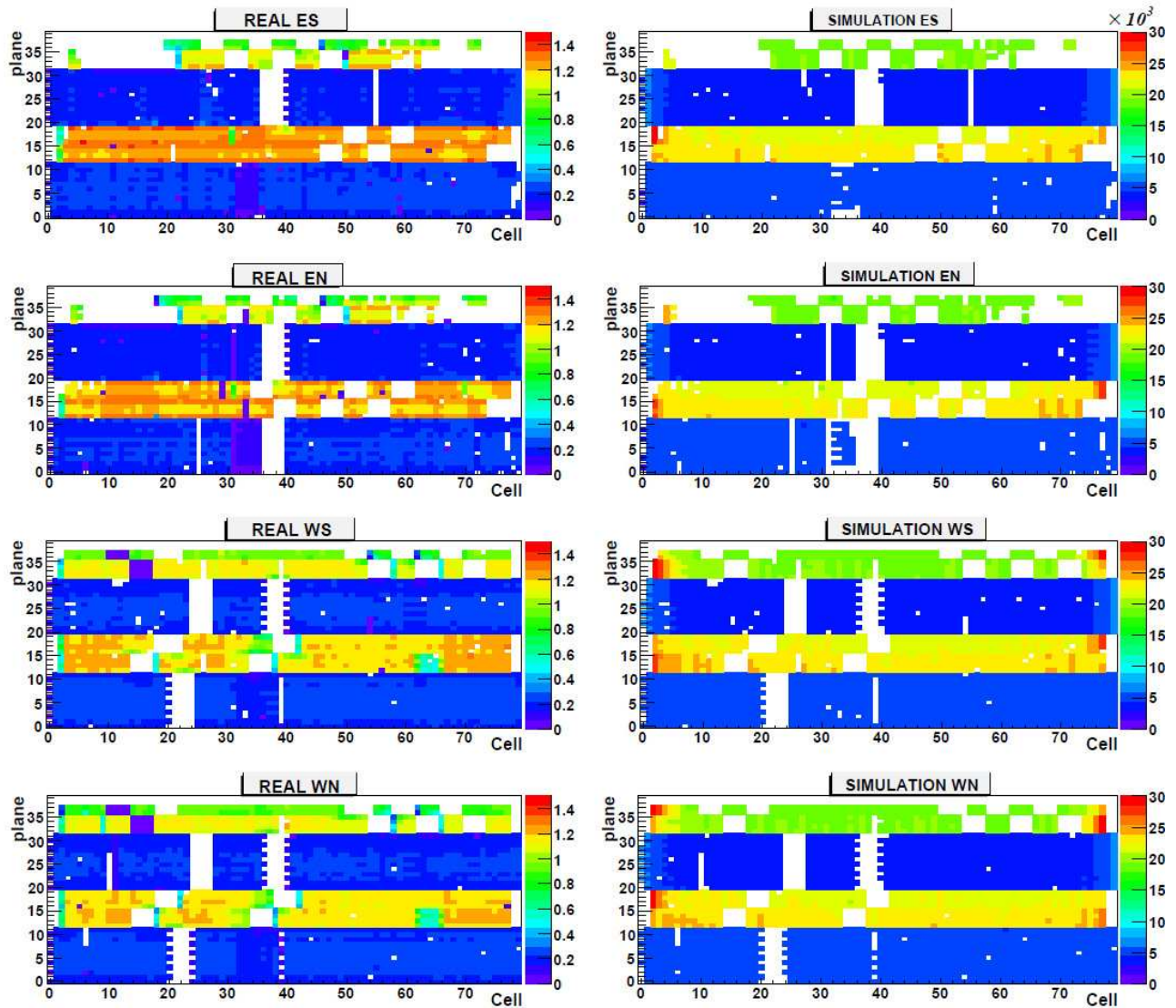


Figure E.3: Left : DC dead maps for each sector (East South, East North, West South and West North). Right : DC dead maps in simulation. X1 and X2 wires corresponds to the plane of 0-11 and 20-31, respectively. UV1 and UV2 wires corresponds to the plane number of 12-19 and 32-39, respectively.

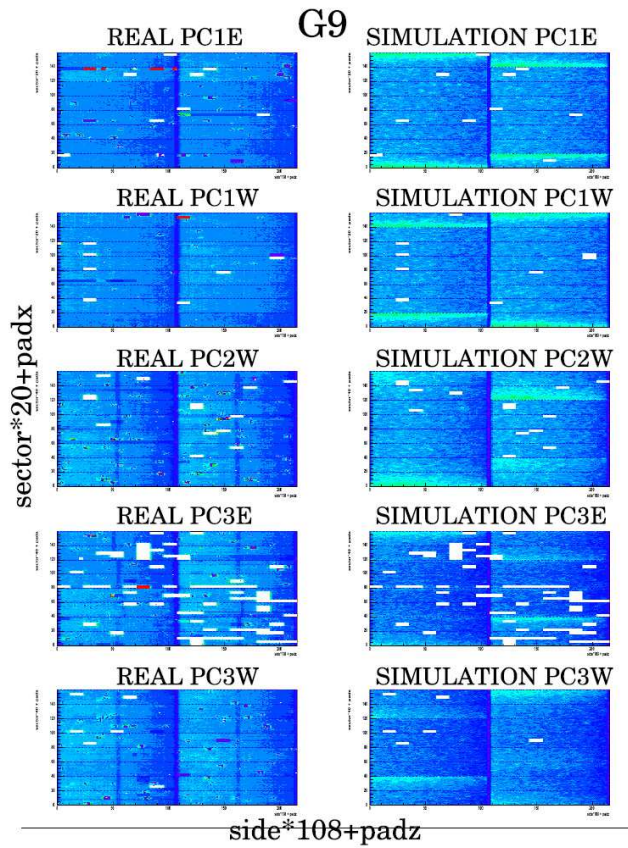


Figure E.4: Left from up to bottom: PC1 East, PC1 West, PC2 West, PC3 East, PC3 West dead maps. Right : Pad Chamber dead maps in simulation.

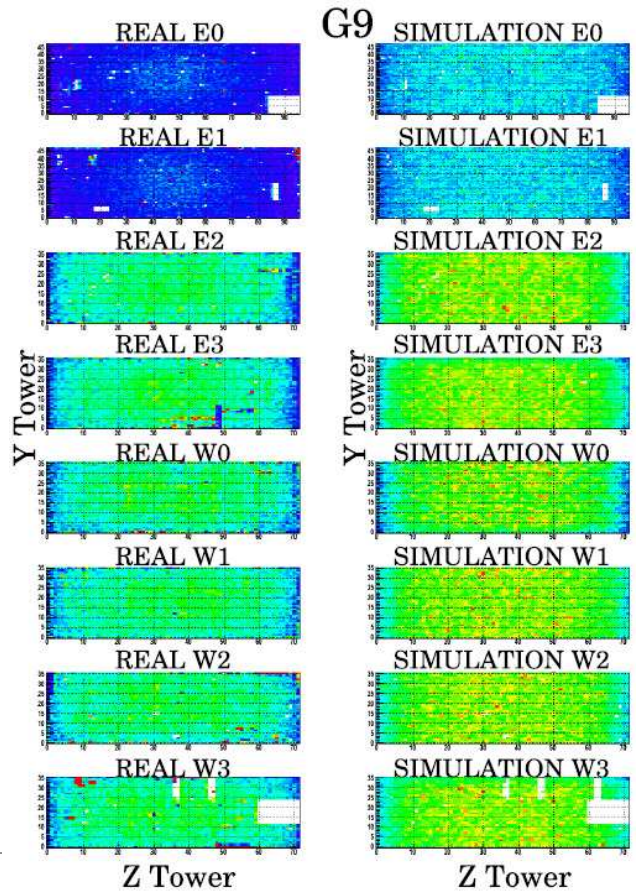


Figure E.5: Left from up to bottom: EMCAL E0, E1, E2, E3, W0, W1, W2 and W3 dead maps. Right : EMCAL dead maps in simulation.

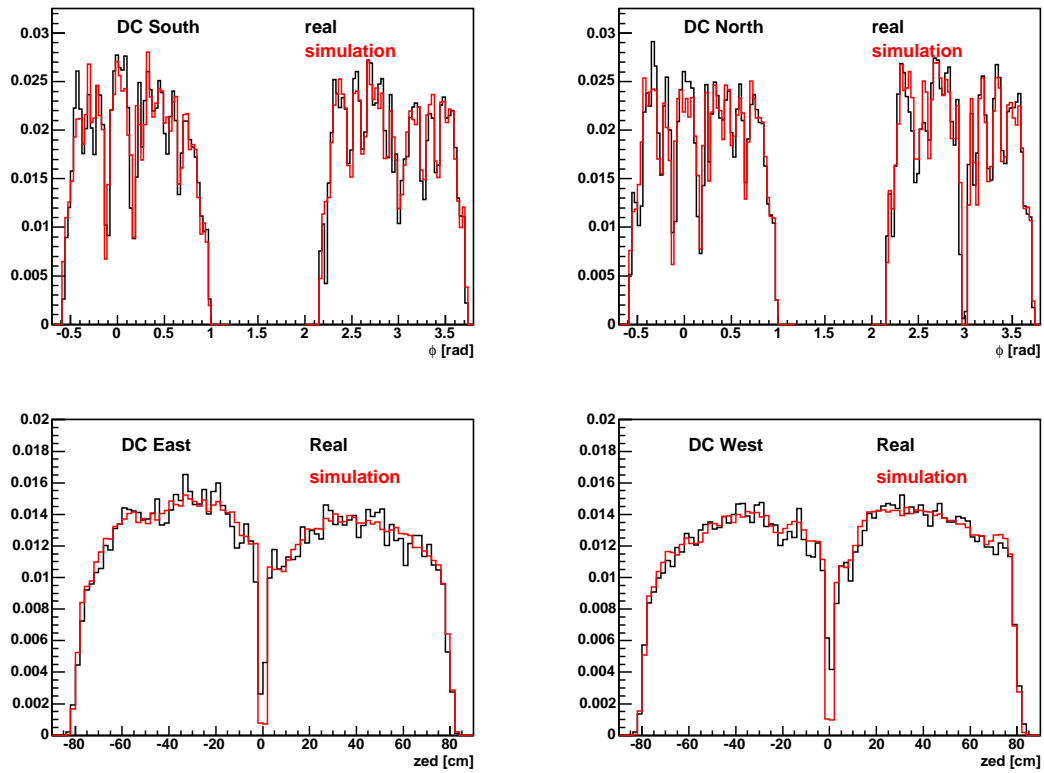


Figure E.6: Upper left, upper right, lower left and lower right are the ϕ distribution at the DC south, ϕ distribution at the DC north, zed distribution at the East DC and zed distribution at the West DC, respectively. Black is for real data and red for simulation.

E.4 Comparison of the eID efficiency

Electron identification efficiency for the standard eID cuts was checked between real data and simulation. Conversion and Dalitz pairs were used to calculate electron identification efficiency in real data. The eID efficiency for standard eID cuts were compared between real and simulation. This work was done for East South (ES), East North (EN), West South (WS) and West North (WN), separately. Figure E.7 shows the eID efficiency as a function of electron p_T from real (Red) and Simulation (Blue) for ES (Upper-Left), EN (Upper-Right), WS (Lower-Left) and WN (Lower-Right). The blue and red dotted line are the results of fitting with a constant. The efficiency in real and simulation were summarized in Table E.2. Electron identification efficiency in real and simulation was in good agreement.

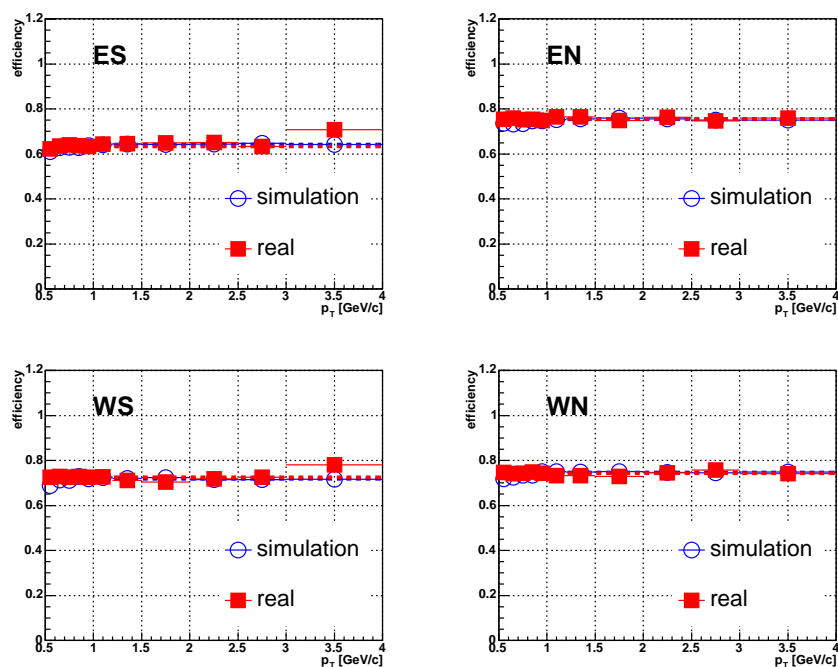


Figure E.7: eID efficiency as a function electron p_T from real (Red) and Simulation (Blue) for ES (Upper-Left), EN (Upper-Right), WS (Lower-Left) nd WN (Lower-Right).

sector	Efficiency (real)	Efficiency (simulation)	difference (real/sim)
ES	0.633	0.642	0.986
EN	0.756	0.754	1.002
WS	0.726	0.718	1.011
WN	0.743	0.747	0.994

Table E.2: eID efficiency for real and simulation for each sector

The pair efficiency for J/ψ was $0.695 \times 0.734 = 0.510$ (east average \times west average) in real and $0.698 \times 0.732 = 0.511$ in simulation, which are in good agreement each other. From

Table E.2, systematic error due to the difference in eID efficiency was 1.5% for single and 3% for pairs in this analysis.

The eID efficiency was 10% lower at ES than at others, which was due to the insufficient calibration of the RICH mirror alignment.

E.5 Centrality dependence of eID parameters

Parameters of dep , $emcsdphi_e$ and $emcsdz_e$ from conversion pairs and from embedding simulation were compared for 0-20%, 20-40% and 40-93% centrality classes. Figure E.8 shows eID parameters of dep (left column), $emcsdphi_e$ (middle column) and $emcsdz_e$ (right column) for 0-20% (upper), 20-40% (middle) and 40-93% (bottom) centrality classes. Black is from conversion pairs and red is from embedding simulation. These eID Parameters in embedding simulation are in good agreement with those in conversion pairs.

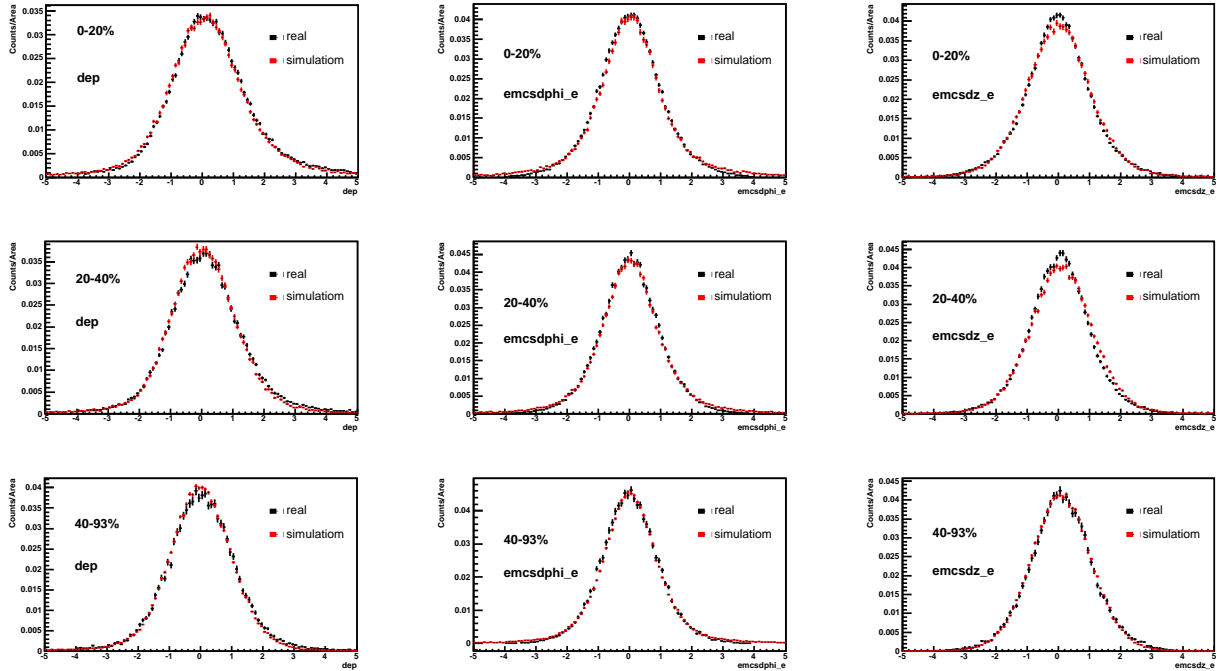


Figure E.8: eID parameters of dep (left column), $emcsdphi_e$ (middle column) and $emcsdz_e$ (right column) for 0-20% (upper), 20-40% (middle) and 40-93% (bottom) centrality classes. Black is from conversion pairs and red is from embedding simulation.

Appendix F

Internal Bremsstrahlung of J/ψ

The prediction from the Standard Model for radiative decays of Z bosons into lepton pairs was discussed by Fleischer and Jegerlehner [127]. The first observation of the radiative decay $J/\psi \rightarrow e^+e^-\gamma$ was reported by the E760 Collaboration at Fermilab [124]. The data was from an experiment in which J/ψ was formed in $\bar{p} + p$ annihilation. The observed branching ratio of the radiative decay $B(J/\psi \rightarrow e^+e^-\gamma, E_\gamma \geq 100 \text{ MeV})$ divided the branching ratio of J/ψ $B(J/\psi \rightarrow e^+e^-)$ was measured as 0.147 ± 0.022 .

Let's consider the decay $X \rightarrow l^+l^-$ of a heavy vector state with mass M into a pair of leptons with masses m_l . The lowest order decay width is

$$\Gamma_0 = \Gamma_0(X \rightarrow l^+l^-). \quad (\text{F.1})$$

The bremsstrahlung process

$$X(p_0) \rightarrow l^-(p_1) + l^+(p_2) + \gamma(k) \quad (\text{F.2})$$

is distributed in the phase space as:

$$\begin{aligned} \frac{1}{\Gamma_0} \frac{d^2\Gamma(X \rightarrow l^+l^-\gamma)}{d\zeta d\tau} &= P(\zeta, \tau) \\ &= \frac{\alpha}{2\pi} \left[\left(\frac{1+\zeta^2}{1-\zeta} \right) \left(\frac{1}{\tau} + \frac{1}{1-\zeta-\tau} \right) \right. \\ &\quad \left. - \frac{a}{2} \left(\frac{1}{\tau^2} + \frac{1}{(1-\zeta-\tau)^2} \right) - 2 \right], \end{aligned} \quad (\text{F.3})$$

where α is the fine structure constant, $\zeta = (p_1 + p_2)^2/M^2$, $\tau = (p_0 - p_1)^2/M^2$ and $a = 4m_l^2/M^2$, $a \leq \zeta \leq 1$. The distribution $P(\zeta)$ can be evaluated by integrating the distribution $P(\zeta, \tau)$ over the parameter τ :

$$\begin{aligned} \frac{1}{\Gamma_0} \frac{d\Gamma(X \rightarrow l^+l^-\gamma)}{d\zeta} &= P(\zeta) \\ &= \frac{\alpha}{\pi} \frac{1+\zeta^2}{1-\zeta} \left(\ln \frac{1+r}{1-r} - r \right). \end{aligned} \quad (\text{F.4})$$

Photons with sufficient energy can be detected. The fraction of decays corresponding to the emission of hard photon is

$$\begin{aligned} C_{hard}(E_{min}) &= \frac{1}{\Gamma_0} \Gamma(X \rightarrow l^+ l^- \gamma, E_\gamma > E_{min}) \\ &= \int_a^{1-2E_{min}/M} P(\zeta) d\zeta, \end{aligned} \quad (\text{F.5})$$

where E_{min} is the minimal photon energy. Given that $E_{min} \ll M/2$, The result of the integration is:

$$C_{hard}(E_{min}) = \frac{\alpha}{2\pi} \left[4 \ln \frac{m}{2E_{min}} \left(\ln \frac{M^2}{m_l^2} - 1 \right) - 3 \ln \frac{M^2}{m_l^2} - \frac{2}{3} \pi^2 + \frac{11}{2} \right]. \quad (\text{F.6})$$

The measurement of J/ψ *rightarrow* $e^+e^- \gamma$ from E760 experiment is in good agreement with the calculated C_{hard} in Fig. F.1.

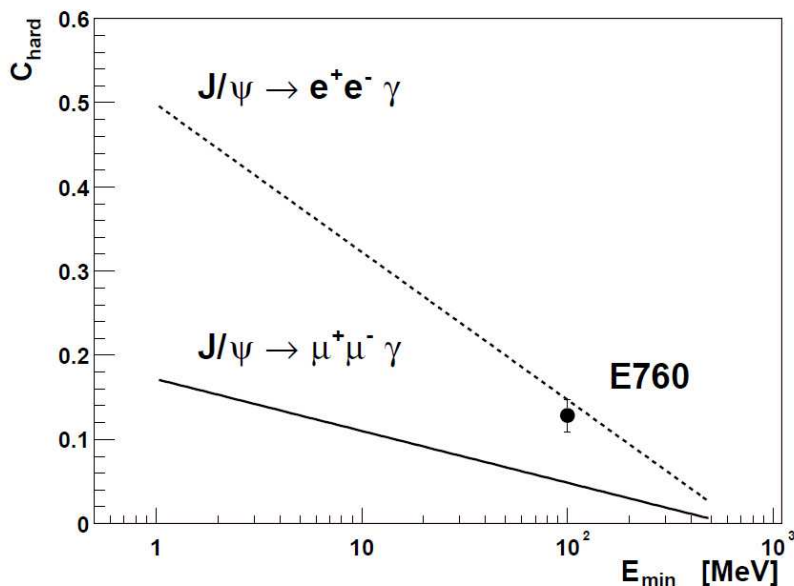


Figure F.1: Parameter C_{hard} as a function of minimal energy E_{min} of photon in the J/ψ rest frame for radiative decay $J/\psi \rightarrow \mu^+ \mu^- \gamma$ (solid line) and $e^+ e^- \gamma$ (dashed-line). The point with errors was evaluated from the E760 result.

Given that the invariant mass of $l^+ l^-$ pairs denotes as $m = (p^1 + p^2)^2$, the distribution $P(m)$ can be obtained by replacing the variable from ζ to m in Eq. (F.4)

$$\begin{aligned} \frac{1}{\Gamma_0} \frac{d\Gamma(X \rightarrow l^+ l^- \gamma)}{dm} &= P(m) \\ &= \frac{\alpha}{\pi} \frac{2m}{(M^2 - m^2)} \left(1 + \frac{m^4}{M^4} \right) \left(\ln \frac{1+r}{1-r} - r \right), \end{aligned} \quad (\text{F.7})$$

where $r = \sqrt{1 - 4m_l^2/m^2}$ is also a function of m .

Probability for J/ψ to decay with the emission of hard photons above the energy of E_{min} is given by C_{hard} and the mass distribution follows $P(m)$ in Eq. (F.7).

Appendix G

Data Table of the Experimental Results

In this chapter, experimental results of J/ψ yield and R_{AA} in Au+Au collisions are summarized.

G.1 Invariant p_T yield of J/ψ

Invariant p_T yield of J/ψ for MB and 0-20/20-40/40-93% are summarized in Table G.1 and Table G.2, respectively. Invariant p_T yield of J/ψ for finer centrality bins 0-10/10-20/20-30/30-40/40-60/60-93% are summarized in Table G.3.

centrality	p_T	$B/2\pi p_T d^2N/dp_T dy$ [(GeV/c) ⁻²] ± stat. ± uncorr. sys. ± corr. sys. error
MB	0.5	9.12e-06 ± 7.21e-07 ± 5.84e-07 ± 8.88e-07
MB	1.5	4.41e-06 ± 3.3e-07 ± 2.82e-07 ± 4.29e-07
MB	2.5	1.4e-06 ± 1.7e-07 ± 8.94e-08 ± 1.36e-07
MB	3.5	2.8e-07 ± 8.2e-08 ± 1.8e-08 ± 2.73e-08
MB	4.5	1.58e-07 ± 4.17e-08 ± 1.01e-08 ± 1.54e-08
MB	5.5	5.07e-08 ± 2.02e-08 ± 3.24e-09 ± 4.94e-09
MB	6.5	2.65e-08 ± 1.17e-08 ± 1.7e-09 ± 2.59e-09
MB	7.5	1.28e-08 ± 7.3e-09 ± 8.17e-10 ± 1.24e-09
MB	8.5	5.09e-09 ± 3.46e-09 ± 3.26e-10 ± 4.95e-10
MB	9.5	3.42e-09 ± 2.95e-09 ± 2.19e-10 ± 3.33e-10

Table G.1: Invariant Yield of J/ψ in MB Au+Au collisions

G.2 $\langle p_T^2 \rangle$ of J/ψ

Table G.4 is the summary of $\langle p_T^2 \rangle$ for each centrality class.

centrality	p_T	$B/2\pi p_T d^2N/dp_T dy$ $[(\text{GeV}/c)^{-2}] \pm \text{stat.} \pm \text{uncorr. sys.} \pm \text{corr. sys. error}$
0-20	0.5	$2.48\text{e-}05 \pm 3.18\text{e-}06 \pm 1.76\text{e-}06 \pm 2.55\text{e-}06$
0-20	1.5	$1.28\text{e-}05 \pm 1.46\text{e-}06 \pm 9.07\text{e-}07 \pm 1.32\text{e-}06$
0-20	2.5	$4.02\text{e-}06 \pm 7.39\text{e-}07 \pm 2.84\text{e-}07 \pm 4.12\text{e-}07$
0-20	3.5	$4.31\text{e-}07 \pm 3.37\text{e-}07 \pm 3.05\text{e-}08 \pm 4.42\text{e-}08$
0-20	4.5	$4.2\text{e-}07 \pm 1.79\text{e-}07 \pm 2.97\text{e-}08 \pm 4.3\text{e-}08$
0-20	5.5	$1.7\text{e-}07 \pm 9.04\text{e-}08 \pm 1.2\text{e-}08 \pm 1.74\text{e-}08$
0-20	6.5	$9.68\text{e-}08 \pm 5.63\text{e-}08 \pm 6.85\text{e-}09 \pm 9.92\text{e-}09$
0-20	7.5	$6.72\text{e-}08 \pm 3.78\text{e-}08 \pm 4.75\text{e-}09 \pm 6.89\text{e-}09$
0-20	8.5	$1.82\text{e-}08 \pm 1.55\text{e-}08 \pm 1.29\text{e-}09 \pm 1.87\text{e-}09$
20-40	0.5	$1.26\text{e-}05 \pm 1.57\text{e-}06 \pm 8.06\text{e-}07 \pm 1.17\text{e-}06$
20-40	1.5	$7.12\text{e-}06 \pm 7.6\text{e-}07 \pm 4.56\text{e-}07 \pm 6.6\text{e-}07$
20-40	2.5	$2.69\text{e-}06 \pm 4.09\text{e-}07 \pm 1.72\text{e-}07 \pm 2.49\text{e-}07$
20-40	3.5	$7.9\text{e-}07 \pm 2.12\text{e-}07 \pm 5.06\text{e-}08 \pm 7.33\text{e-}08$
20-40	4.5	$2.45\text{e-}07 \pm 9.34\text{e-}08 \pm 1.57\text{e-}08 \pm 2.27\text{e-}08$
20-40	5.5	$4.89\text{e-}08 \pm 4.06\text{e-}08 \pm 3.13\text{e-}09 \pm 4.54\text{e-}09$
20-40	6.5	$2.27\text{e-}08 \pm 1.8\text{e-}08 \pm 1.45\text{e-}09 \pm 2.1\text{e-}09$
40-93	0.5	$3.06\text{e-}06 \pm 3.21\text{e-}07 \pm 1.96\text{e-}07 \pm 2.7\text{e-}07$
40-93	1.5	$1.04\text{e-}06 \pm 1.27\text{e-}07 \pm 6.65\text{e-}08 \pm 9.16\text{e-}08$
40-93	2.5	$3.59\text{e-}07 \pm 6.73\text{e-}08 \pm 2.3\text{e-}08 \pm 3.17\text{e-}08$
40-93	3.5	$1.29\text{e-}07 \pm 3.69\text{e-}08 \pm 8.29\text{e-}09 \pm 1.14\text{e-}08$
40-93	4.5	$5.42\text{e-}08 \pm 2.03\text{e-}08 \pm 3.47\text{e-}09 \pm 4.78\text{e-}09$
40-93	5.5	$1.18\text{e-}08 \pm 1\text{e-}08 \pm 7.53\text{e-}10 \pm 1.04\text{e-}09$
40-93	6.5	$7.19\text{e-}09 \pm 4.41\text{e-}09 \pm 4.6\text{e-}10 \pm 6.34\text{e-}10$

Table G.2: Invariant Yield for 0-20/20-40/40-93% centrality classes

centrality	p_T	$B/2\pi p_T d^2 N/dp_T dy$ [(GeV/c) ⁻²] ± stat. ± uncorr. sys. ± corr. sys.
0-10	0.5	2.85e-05 ± 5.26e-06 ± 2.02e-06 ± 3.04e-06
0-10	1.5	1.4e-05 ± 2.39e-06 ± 9.89e-07 ± 1.49e-06
0-10	2.5	3.94e-06 ± 1.19e-06 ± 2.78e-07 ± 4.19e-07
0-10	3.5	7.85e-07 ± 5.73e-07 ± 5.55e-08 ± 8.36e-08
0-10	4.5	4.19e-07 ± 2.94e-07 ± 2.96e-08 ± 4.46e-08
0-10	5.5	2.28e-07 ± 1.66e-07 ± 1.61e-08 ± 2.43e-08
10-20	0.5	2.35e-05 ± 3.69e-06 ± 1.83e-06 ± 2.32e-06
10-20	1.5	1.18e-05 ± 1.72e-06 ± 9.22e-07 ± 1.17e-06
10-20	2.5	4.42e-06 ± 8.97e-07 ± 3.45e-07 ± 4.37e-07
10-20	3.5	4.01e-07 ± 3.7e-07 ± 3.13e-08 ± 3.96e-08
10-20	4.5	3.88e-07 ± 2.08e-07 ± 3.03e-08 ± 3.84e-08
10-20	5.5	1.19e-07 ± 8.13e-08 ± 9.26e-09 ± 1.17e-08
20-30	0.5	1.54e-05 ± 2.47e-06 ± 1.2e-06 ± 1.45e-06
20-30	1.5	9.78e-06 ± 1.28e-06 ± 7.64e-07 ± 9.22e-07
20-30	2.5	3.59e-06 ± 6.76e-07 ± 2.8e-07 ± 3.38e-07
20-30	3.5	7.17e-07 ± 3.16e-07 ± 5.6e-08 ± 6.76e-08
20-30	4.5	4.15e-07 ± 1.75e-07 ± 3.24e-08 ± 3.92e-08
20-30	5.5	8.28e-08 ± 5.43e-08 ± 6.47e-09 ± 7.81e-09
30-40	0.5	1.17e-05 ± 1.94e-06 ± 1e-06 ± 1.07e-06
30-40	1.5	4.5e-06 ± 8.27e-07 ± 3.87e-07 ± 4.12e-07
30-40	2.5	1.83e-06 ± 4.63e-07 ± 1.58e-07 ± 1.68e-07
30-40	3.5	8.98e-07 ± 2.82e-07 ± 7.72e-08 ± 8.23e-08
30-40	4.5	1.85e-07 ± 9.96e-08 ± 1.59e-08 ± 1.69e-08
30-40	5.5	7.95e-08 ± 6.15e-08 ± 6.84e-09 ± 7.29e-09
40-60	0.5	5.84e-06 ± 7.36e-07 ± 3.74e-07 ± 5.21e-07
40-60	1.5	2.23e-06 ± 3.07e-07 ± 1.43e-07 ± 1.98e-07
40-60	2.5	7.94e-07 ± 1.66e-07 ± 5.09e-08 ± 7.08e-08
40-60	3.5	2.59e-07 ± 8.69e-08 ± 1.66e-08 ± 2.31e-08
40-60	4.5	1.24e-07 ± 5.18e-08 ± 7.93e-09 ± 1.1e-08
40-60	5.5	3.46e-08 ± 2.31e-08 ± 2.22e-09 ± 3.08e-09
60-93	0.5	1.43e-06 ± 2.63e-07 ± 1.23e-07 ± 1.26e-07
60-93	1.5	3.69e-07 ± 8.77e-08 ± 3.18e-08 ± 3.24e-08
60-93	2.5	1.01e-07 ± 4.14e-08 ± 8.72e-09 ± 8.89e-09
60-93	3.5	4.88e-08 ± 2.78e-08 ± 4.2e-09 ± 4.28e-09
60-93	4.5	9.72e-09 ± 9.72e-09 ± 8.36e-10 ± 8.53e-10
60-93	5.5	1.15e-08 ± 8.76e-09 ± 9.91e-10 ± 1.01e-09

Table G.3: Invariant Yield for 0-10, 10-20, 20-30, 30-40, 40-60, 60-93%

centrality class	N_{col}	$\langle p_T^2 \rangle$ from data points ($p_T \leq 5 \text{ GeV}/c$)	$\langle p_T^2 \rangle$ from fit ($p_T \leq 5 \text{ GeV}/c$)
$p + p$	1	3.96 ± 0.17	4.07 ± 0.153
MB	257.8	$3.93 \pm 0.26^{+0.21}_{-0.22}$	$3.80 \pm 0.23^{+0.24}_{-0.24}$
0-20%	779	$3.68 \pm 0.23^{+0.21}_{-0.23}$	$3.65 \pm 0.33^{+0.22}_{-0.22}$
20-40%	297	$4.49 \pm 0.36^{+0.23}_{-0.24}$	$4.55 \pm 0.31^{+0.25}_{-0.26}$
40-93%	48.1	$4.27 \pm 0.42^{+0.25}_{-0.26}$	$3.64 \pm 0.43^{+0.42}_{-0.41}$
0-10%	955.4	$3.70 \pm 0.62^{+0.22}_{-0.23}$	$3.61 \pm 0.52^{+0.25}_{-0.25}$
10-20%	602.6	$3.77 \pm 0.48^{+0.24}_{-0.25}$	$3.75 \pm 0.40^{+0.24}_{-0.24}$
20-30%	373.8	$4.47 \pm 0.47^{+0.28}_{-0.29}$	$4.48 \pm 0.41^{+0.28}_{-0.30}$
30-40%	219.8	$4.76 \pm 0.55^{+0.35}_{-0.36}$	$4.55 \pm 0.60^{+0.50}_{-0.47}$
40-60%	90.6	$4.43 \pm 0.50^{+0.25}_{-0.26}$	$3.92 \pm 0.46^{+0.36}_{-0.38}$
60-93%	14.5	$3.44 \pm 0.72^{+0.28}_{-0.30}$	$2.51 \pm 0.63^{+0.45}_{-0.50}$

Table G.4: $\langle p_T^2 \rangle$ for each centrality class and $p + p$ obtained by data points and fitting results truncated up to 5 GeV/c .

G.3 R_{AA} as a function of centrality

Table G.5 is the summary of the R_{AA} as a function of p_T for MB/0-20/20-40/40-93% centrality class. The errors summarized in Table G.5 are the statistical error and the total systematic error (quadratic sum between uncorrelated and correlated systematic errors).

Table G.6 is the summary of the R_{AA} as a function of p_T for 0-10/10-20/20-30/30-40/40-60/60-93% centrality class.

centrality	p_T	$R_{AA} \pm \text{stat. error} \pm \text{total sys. error} \pm p + p \text{ ref. error}$
MB	0.5	$0.405 \pm 0.032 \pm 0.047 \pm 0.022$
MB	1.5	$0.394 \pm 0.0295 \pm 0.0457 \pm 0.020$
MB	2.5	$0.334 \pm 0.0407 \pm 0.0388 \pm 0.025$
MB	3.5	$0.264 \pm 0.0773 \pm 0.0307 \pm 0.039$
MB	4.5	$0.725 \pm 0.191 \pm 0.0842 \pm 0.227$
0-20%	0.5	$0.365 \pm 0.0467 \pm 0.0453 \pm 0.020$
0-20%	1.5	$0.379 \pm 0.043 \pm 0.0471 \pm 0.019$
0-20%	2.5	$0.318 \pm 0.0585 \pm 0.0395 \pm 0.024$
0-20%	3.5	$0.134 \pm 0.105 \pm 0.0167 \pm 0.020$
0-20%	4.5	$0.636 \pm 0.271 \pm 0.079 \pm 0.200$
20-40%	0.5	$0.487 \pm 0.0607 \pm 0.0546 \pm 0.026$
20-40%	1.5	$0.554 \pm 0.0591 \pm 0.0621 \pm 0.028$
20-40%	2.5	$0.56 \pm 0.0852 \pm 0.0628 \pm 0.041$
20-40%	3.5	$0.649 \pm 0.174 \pm 0.0728 \pm 0.095$
20-40%	4.5	$0.977 \pm 0.373 \pm 0.11 \pm 0.306$
40-93%	0.5	$0.778 \pm 0.0815 \pm 0.0844 \pm 0.042$
40-93%	1.5	$0.532 \pm 0.0651 \pm 0.0577 \pm 0.027$
40-93%	2.5	$0.492 \pm 0.0922 \pm 0.0534 \pm 0.036$
40-93%	3.5	$0.699 \pm 0.199 \pm 0.0759 \pm 0.102$
40-93%	4.5	$1.42 \pm 0.531 \pm 0.154 \pm 0.445$

Table G.5: R_{AA} for MB, 0-20, 20-40 and 40-93 centrality classes.

centrality	p_T	$R_{AA} \pm \text{stat.} \pm \text{total sys. error} \pm p + p \text{ ref. error}$
0-10%	0.5	$0.342 \pm 0.063 \pm 0.0436 \pm 0.018$
0-10%	1.5	$0.337 \pm 0.0576 \pm 0.043 \pm 0.017$
0-10%	2.5	$0.254 \pm 0.0769 \pm 0.0324 \pm 0.019$
0-10%	3.5	$0.2 \pm 0.146 \pm 0.0254 \pm 0.029$
0-10%	4.5	$0.518 \pm 0.364 \pm 0.066 \pm 0.162$
10-20%	0.5	$0.446 \pm 0.0701 \pm 0.056 \pm 0.024$
10-20%	1.5	$0.451 \pm 0.0657 \pm 0.0566 \pm 0.023$
10-20%	2.5	$0.452 \pm 0.0918 \pm 0.0568 \pm 0.033$
10-20%	3.5	$0.161 \pm 0.149 \pm 0.0203 \pm 0.024$
10-20%	4.5	$0.761 \pm 0.407 \pm 0.0955 \pm 0.238$
20-30%	0.5	$0.471 \pm 0.0755 \pm 0.0575 \pm 0.025$
20-30%	1.5	$0.602 \pm 0.0788 \pm 0.0735 \pm 0.030$
20-30%	2.5	$0.592 \pm 0.111 \pm 0.0722 \pm 0.044$
20-30%	3.5	$0.466 \pm 0.205 \pm 0.0569 \pm 0.068$
20-30%	4.5	$1.31 \pm 0.551 \pm 0.16 \pm 0.411$
30-40%	0.5	$0.607 \pm 0.101 \pm 0.076 \pm 0.033$
30-40%	1.5	$0.471 \pm 0.0867 \pm 0.059 \pm 0.024$
30-40%	2.5	$0.514 \pm 0.13 \pm 0.0644 \pm 0.038$
30-40%	3.5	$0.993 \pm 0.311 \pm 0.124 \pm 0.145$
30-40%	4.5	$0.993 \pm 0.535 \pm 0.124 \pm 0.311$
40-60%	0.5	$0.738 \pm 0.093 \pm 0.0806 \pm 0.040$
40-60%	1.5	$0.566 \pm 0.0781 \pm 0.0618 \pm 0.028$
40-60%	2.5	$0.54 \pm 0.113 \pm 0.0591 \pm 0.040$
40-60%	3.5	$0.694 \pm 0.233 \pm 0.0759 \pm 0.102$
40-60%	4.5	$1.61 \pm 0.675 \pm 0.176 \pm 0.505$
60-93%	0.5	$1.13 \pm 0.207 \pm 0.138 \pm 0.061$
60-93%	1.5	$0.586 \pm 0.139 \pm 0.0718 \pm 0.029$
60-93%	2.5	$0.431 \pm 0.176 \pm 0.0528 \pm 0.032$
60-93%	3.5	$0.818 \pm 0.465 \pm 0.1 \pm 0.120$
60-93%	4.5	$0.792 \pm 0.792 \pm 0.097 \pm 0.247$

Table G.6: R_{AA} for 0-10/10-20/20-30/30-40/40-60/60-93% centrality bins

Appendix H

J/ψ Production in $p + p$ Collisions at RHIC

Left in Fig. H.1 shows the invariant cross section of J/ψ $1/(2\pi p_T) \times Bd^2\sigma_{pp}^{J/\psi}/dydp_T$ as a function of p_T , where B is the branching ratio of e^+e^- decay channel. This gives the baseline for the measurement of J/ψ in A+B collisions. The dashed line is the fitting result of the invariant cross section using Kaplan function ($d\sigma_{J/\psi}^2/dp_T dy \propto p_T(1 + (p_T/c_0)^2)^{-6}$) as used in the measurement at lower energies [88]. $\langle p_T^2 \rangle$ was obtained from the fitting result and the result of $\langle p_T^2 \rangle$ at mid-rapidity is as follows: [86]:

$$\langle p_T^2 \rangle_{pp} = 4.14 \pm 0.18_{-0.20}^{+0.3} \text{ (GeV}/c)^2 \quad (\text{H.1})$$

Right in Fig. H.1 shows $\langle p_T^2 \rangle$ as a function of \sqrt{s} . $\langle p_T^2 \rangle$ as a function of \sqrt{s} can be described by $-2.4 + 1.2 \ln \sqrt{s}$.

J/ψ production cross section per unit rapidity was extracted by integrating invariant cross section over p_T range. The result at mid-rapidity is as follows:

$$\frac{Bd\sigma_{pp}^{J/\psi}}{dy} \Big|_{y=0} = 44.3 \pm 1.4 \text{ (stat.)} \pm 5.1 \text{ (sys.)} \pm 4.5 \text{ (normalization)} \text{ nb.} \quad (\text{H.2})$$

Production cross section of J/ψ , $B\sigma_{pp}^{J/\psi}$, was extracted by combining the results of $Bd\sigma_{pp}^{J/\psi}/dy$ at mid-rapidity and forward rapidity, by fitting the rapidity shape of $Bd\sigma_{pp}^{J/\psi}/dy$ with many theoretical and phenomenological shapes and by integrating them. The total cross section was obtained as

$$B\sigma_{pp}^{J/\psi} = 178 \pm 3 \text{ (stat.)} \pm 53 \text{ (sys.)} \pm 18 \text{ (normalization)} \text{ nb.} \quad (\text{H.3})$$

Figure H.2 shows the production cross section of J/ψ , $\sigma_{pp}^{J/\psi}$, as a function of \sqrt{s} . J/ψ production cross section at lower energies were taken from Ref. [89]. Solid and dashed lines are the prediction of color octet model with GRV98NLO and MRST2001NLO PDF function, respectively. PHENIX data point is consistent with the trend of world's data and with COM but unable to differentiate between PDF's.

Table H.1 and Table H.2 are the summary of the invariant cross section of J/ψ in $p + p$ collisions [86].

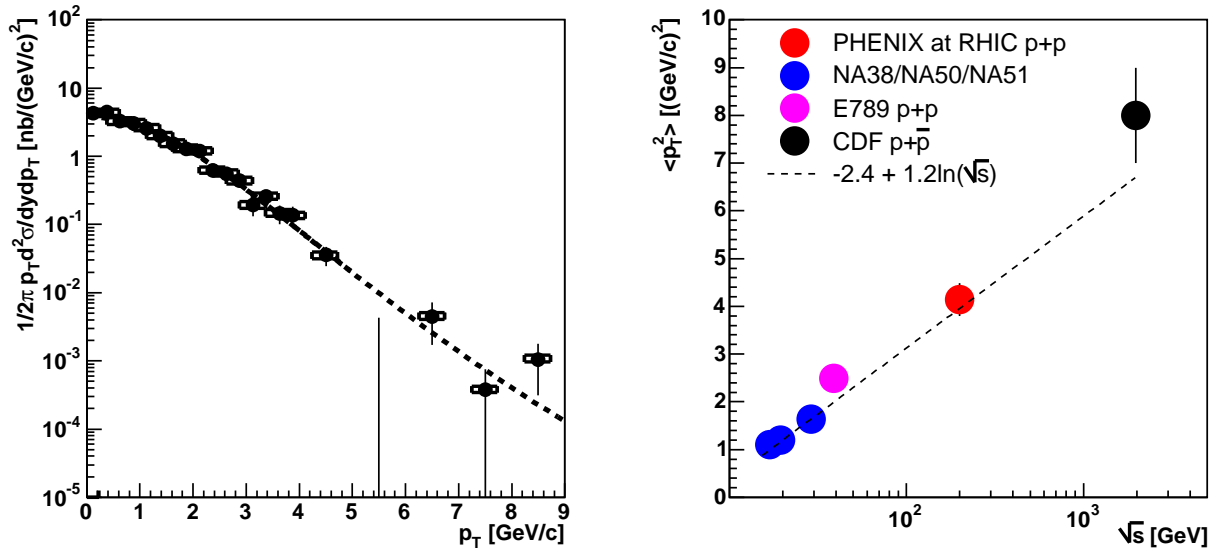


Figure H.1: Left : J/ψ invariant cross section as a function of p_T at mid-rapidity in 200 GeV $p+p$ collisions. Dashed line is the fitting result of Kaplan function. Right : PHENIX $\langle p_T^2 \rangle$ measurement compared to measurements at other energies as a function of \sqrt{s} [86]. Dashed line represents $-2.4 + 1.2 \ln \sqrt{s}$.

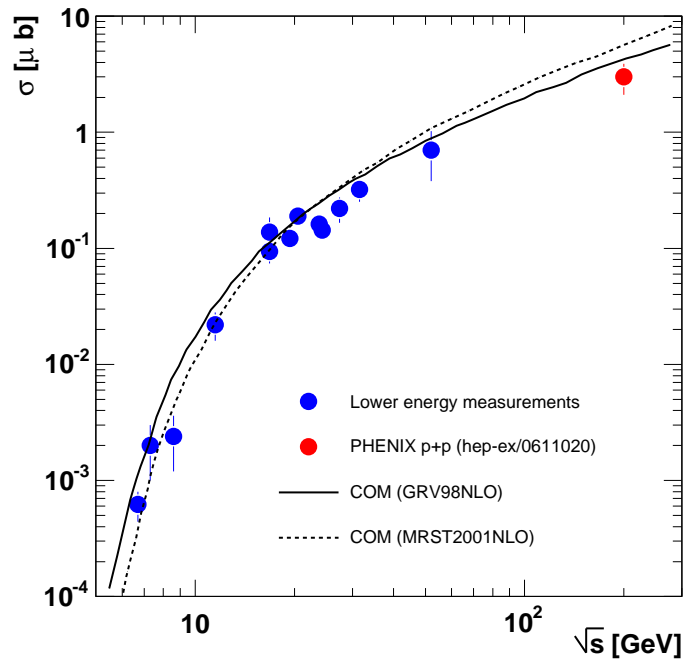


Figure H.2: Total cross section of J/ψ as a function of \sqrt{s} . Solid and dashed lines are the prediction of color octet model with GRV98NLO and MRST2001NLO PDF function, respectively.

p_T [GeV/ c]	$1/(2\pi p_T)Bd\sigma^2/dydp_T$ [nb]	uncorrelated error	correlated error	global sys. error
0.125	4.26	0.78	0.49	0.43
0.375	4.42	0.43	0.50	0.45
0.625	3.29	0.34	0.38	0.33
0.875	3.04	0.26	0.35	0.31
1.125	2.55	0.22	0.29	0.26
1.375	1.99	0.19	0.19	0.20
1.625	1.52	0.15	0.17	0.15
1.875	1.29	0.14	0.15	0.13
2.125	1.18	0.13	0.13	0.12
2.375	0.62	0.10	0.070	0.06
2.625	0.56	0.091	0.064	0.056
2.875	0.443	0.079	0.050	0.045
3.125	0.194	0.061	0.022	0.020
3.375	0.257	0.059	0.029	0.026
3.625	0.145	0.045	0.017	0.015
3.875	0.136	0.047	0.015	0.014
4.5	0.0356	0.0111	0.0041	0.0036
5.5	0.0000	0.0041884	0.0000	0.0000
6.5	0.00445	0.00273	0.00051	0.00045
7.5	0.000377	0.000998	0.000043	0.000038
8.5	0.00105	0.00074	0.00012	0.00011

Table H.1: Invariant cross section as a function of p_T (0.25 and 1 GeV/ c bin) in $p + p$ collisions at $\sqrt{s} = 200$ GeV at RHIC-PHENIX.

p_T [GeV/ c]	$1/(2\pi p_T)Bd\sigma^2/dydp_T$ [nb]	uncorrelated error	correlated error	global sys. error
0.5	3.671	0.197	0.418	0.371
1.5	1.824	0.091	0.208	0.184
2.5	0.681	0.050	0.078	0.069
3.5	0.173	0.025	0.019	0.017
4.5	0.0356	0.0111	0.0041	0.0036

Table H.2: Invariant cross section as a function of p_T (1 GeV/ c bin) in $p + p$ collisions at $\sqrt{s} = 200$ GeV at RHIC-PHENIX.

Bibliography

- [1] F. Karsh, Lect. Notes Phys. **583**, (2002) 209.
- [2] T. D. Lee, Nucl. Phys. **A538**, (1992) 3c.
L. McLerran, Rev. Mod. Phys. **58**, (1986) 1021.
- [3] T. Matusi and H. Satz, Phys. Lett. **B178**, (1986) 416.
- [4] M. C. Abreu *et al.*, (NA50 Collaboration), Phys. Lett. **B410**, (1997) 327.
- [5] D. J. Gross and F. Wilczek, Phys. Rev. Lett. **30**, (1973) 1343.
- [6] H. D. Politzer, Phys. Rev. Lett. **30**, (1973) 1346.
- [7] K. G. Wilson, Phys. Rev. **D10**, (1974) 2445.
- [8] J. B. Kogut, Rev. of Mod. Phys. **55**, (1983) 775.
- [9] H. Satz, Nucl. Phys. **A418**, (1984) 447.
- [10] F. Karsch E. Laermann and A. Peikert, Phys. Lett. **B478**, (2000) 447.
- [11] F. Karsch, Nucl. Phys. **A698**, (2002) 199.
- [12] O. Kaczmarek and F. Zantow, hep-lat/0503017
- [13] J. D. Bjorken, Phys. Rev. **D27**, (1983) 140.
- [14] T. Alber *et al.*, (NA49 Collaboration), Phys. Rev. Lett. **75**, (1995) 3814.
- [15] S. S. Adler *et al.*, (PHENIX Collaboration) Phys. Rev. **C71**, (2005) 034908.
- [16] A. Adare *et al.* (PHENIX Collaboration) nucl-th/0611020 (submitted to PRL)
- [17] J. J. Aubert *et al.*, Phys. Rev. Lett. **33**, (1974) 1404.
- [18] J. E. Augustin *et al.*, Phys. Rev. Lett. **33**, (1974) 1406.
- [19] K. Hagiwara *et al.*, Phys, Rev, **D66**, (2002) 010001.
- [20] E. Norrbin, T. Sjöstrand, Eur. Phys. J. **C17**, (2000) 137.

- [21] B. L. Combridge, Nucl. Phys. **B151**, (1979) 429.
- [22] W. Beenakker *et al.*, Nucl. Phys. **B351**, (1991) 507.
- [23] D. Kharzeev and H. Satz, Phys. Lett. **B366**, (1996) 316.
- [24] C. H. Chang *et al.*, Nucl. Phys. **B172**, (1980) 425.
- [25] E. L. Berger and D. Jones, Phys. Rev. **D23**, (1981) 1521.
- [26] G. A. Schuler hep-ph/9403387
- [27] J. P. Lansberg hep-ph/0507175
- [28] H. Fritzsche Phys. Lett. **B67**, (1977) 217.
- [29] M. Glück, J. F. Owens and E. Reya Phys. Rev. **D17**, (1978) 2324.
- [30] J. F. Amundson *et al.*, Phys. Lett. **B390**, (1997) 323.
- [31] . T. Affolder *et al.*, (CDF Collaboration), Phys. Rev. Lett. **85**, (2000) 2886.
- [32] G. T. Bodwin, E. Braaten and G. P. Lepage Phys. Rev. **D51**, (1995) 1125.
- [33] S. Gupta and K. Sridhar, Phys. Rev. **D54**, (1996) 5545.
- [34] M. Beneke and I. Z. Rothstein, Phys. Rev. **D54**, (1996) 2005.
- [35] I. Abt *et al.*, (HERA-B experiment) Phys. Lett. **B560**, (2003) 61.
- [36] L. Antoniazzi, *et al.*, (E705 Collaboration) Phys. Rev. **D46**, (1992) 4828.
L. Antoniazzi, *et al.*, (E705 Collaboration) Phys. Rev. Lett. **70**, (1993) 383.
- [37] T. Alexopoulos, *et al.*, (E771 Collaboration) Phys. Lett. **B374**, (1996) 271.
- [38] J. P. Lansberg hep-ph/0602091
- [39] H. Satz hep-ph/0512217
- [40] E. Eichten, *et al.*, Phys. Rev. **D21**, (1980) 203.
- [41] P. Arnold and L. G. Yaffe, Phys. Rev. **D52**, (1995) 7208.
- [42] M. Asakawa, T. Hatsuda, Phys. Rev. Lett. **92**, (2004) 012001.
- [43] S. Datta, *et al.*, Phys. Rev. **D69**, (2004) 094507.
- [44] T. Umeda, *et al.*, Eur. Phys. J. **C39**, (2005) 9.
- [45] A. Jakovac *et al.*, hep-lat/0611017
- [46] C. Y. Wong, Phys. Rev. **C72**, (2005) 034906.

- [47] W. Alberico, *et al.*, Phys. Rev. **D72**, (2005) 114011.
- [48] M. E. Peskin, Nucl. Phys. **B156**, (1979) 365.
G. Bhanot and M. E. Peskin, Nucl. Phys. **B156**, (1979) 391
- [49] D. Kharzeev and H. Satz, Phys. Lett. **B334**, (1996) 155.
- [50] M. Gazdzicki and M. I. Gorenstein, Phys. Rev. Lett. **83**, (1999) 4009.
- [51] L. Grandchamp, R. Rapp and G. E. Brown, Phys. Rev. Lett. **92**, (2004) 212301.
- [52] L. Yan, P. Zhuang, Nu. Xu, nucl-th/0608010 (accepted to PRL)
- [53] P. Braun-Munzinger, I. Heppe and J. Stachel, Phys. Lett. **B465**, (1999) 15.
- [54] P. Braun-Munzinger and J. Stachel Nucl. Phys. **A690**, (2001) 119.
- [55] E. L. Bratkovskaya, A. P. Kostyuk, *et al.*, Phys. Rev. **C 69**, (2004) 054903.
- [56] A. Adare *et al.*, (PHENIX Collaboration) hep-ex/0609010
- [57] S. S. Adler *et al.*, (PHENIX Collaboration) hep-ex/0609032
- [58] A. Adare *et al.*, (PHENIX Collaboration) nucl-ex/0611018
- [59] N. Armesto, A. Capella and E. G. Ferreira, Phys. Rev. **C59**, (1999) 359.
- [60] T. Barnes, nucl-th/0306031
- [61] F. O. Duraes *et al.*, Phys. Rev. **C68**, (2003) 035208.
- [62] C. Y. Wong, *et al*, Phys. Rev. **C65**, (2002) 014903.
- [63] A. Capella and D. Sousa, nucl-th/0110072
- [64] A. Capella, E. G. Ferreira and A. B. Kaidalov, Phys. Rev. Lett. **85**, (2000) 2080.
- [65] J. J. AUBERT *et al.*, Nucl. Phys. **B293**, (1987) 740.
- [66] P. Amaudruz *et al.*, Nucl. Phys. **B441**, (1995) 3.
- [67] S. R. Klein and R. Vogt, Phys. Rev. Lett. **91**, (2003) 142301.
- [68] K. J. Eskola, V. J. Kolhinen and R. Vogt, Nucl. Phys. **A696**, (2001) 729.
- [69] L. Frankfurt, V. Guzey and M. Strikman, Phys. Rev. **D71**, (2005) 054001.
- [70] C. Gerschel and J. Hüfner, Nucl. Phys. **A544**, (1992) 513.
- [71] J. Hüfner, Y. Kurihara and H. J. PIRNER, Phys. Lett. **B215**, (1988) 218.
- [72] A. Accardi, hep-ph/0212148

- [73] C. Baglin *et al.*, (NA38 Collaboration), Phys. Lett. **B220**, (1989) 471.
- [74] C. Baglin *et al.*, (NA38 Collaboration), Phys. Lett. **B262**, (1991) 362.
- [75] M. C. Abreu *et al.*, (NA38 Collaboration), Phys. Lett. **B449**, (1999) 128.
- [76] M. C. Abreu *et al.*, (NA38 Collaboration), Phys. Lett. **B466**, (1999) 408.
- [77] M. C. Abreu *et al.*, (NA50 Collaboration), Phys. Lett. **B410**, (1997) 337.
- [78] M. C. Abreu *et al.*, (NA50 Collaboration), Phys. Lett. **B438**, (1998) 35.
- [79] M. C. Abreu *et al.*, (NA50 Collaboration), Phys. Lett. **B499**, (2001) 195.
- [80] M. C. Abreu *et al.*, (NA50 Collaboration), Phys. Lett. **B553**, (2003) 167.
- [81] M. C. Abreu *et al.*, (NA51 Collaboration), Phys. Lett. **B438**, (1998) 35.
- [82] M. C. Abreu *et al.*, (NA50 collaboration) Eur. Phys. J. **C.39**, (2005) 335.
- [83] M. Nardi and H. Satz, Phys. Lett. **B442**, (1998) 14.
- [84] J. Badier *et al.*, (NA3 Collaboration) Z. Phys. **C20**, (1983) 101.
- [85] M. C. Abreu *et al.*, (NA38 Collaboration), Phys. Lett. **B423**, (1998) 207.
- [86] A. Adare *et al.*, hep-ex/0611020 (submitted to PRL)
- [87] S. S. Adler *et al.*, (PHENIX Collaboration) Phys. Rev. Lett **96**, (2006) 012304.
- [88] M. H. Schub *et al.*, Phys. Rev. **D52**, (1995) 3.
- [89] H. D. Sato, PhD Thesis, hep-ph/0305239
- [90] R. Vogt, Phys. Rev. **C71**, (2005) 054902.
- [91] K. Tuchin, Phys. Lett. **B593**, (2004) 66.
- [92] D. Kharzeev and K. Tuchin, Nucl. Phys. **A770**, (2006) 40.
- [93] A. B. Migdal Phys. Rev. **103**, (1956) 1811.
- [94] J. Hüfner and B. Z. Kopeliovich, Phys. Lett. **B445**, (1998) 223.
- [95] M. Harisson, T. Ludlam, S. Ozaki Nucl. Instr. Method **A499**, (2003) 235-244.
- [96] M. Hahn *et al.*, Nucl. Instr. Method **A499**, (2003) 245-263.
- [97] K. Adocox *et al.*, Nucl. Instr. Method **A499**, (2003) 469-479.
- [98] M. Allen *et al.*, Nucl. Instr. Method **A499**, (2003) 549-559.

- [99] K. Adocox *et al.*, Nucl. Instr. Method **A499**, (2003) 489-507.
- [100] H. Akikawa *et al*, Nucl. Instr. Method **A499**, (2003) 537-548.
- [101] C. Adler *et al*, Nucl. Instr. Method **A470**, (2001) 488-499.
- [102] S. N. White, Nucl. Instr. Method **A409**, (1998) 618.
- [103] A. J. Baltz *et al*, Nucl. Instr. Method **A417**, (1998) 1.
- [104] J. Jia, PhD Thesis, <https://www.phenix.bnl.gov/thesis.html>
- [105] A. Milov, PhD Thesis, <https://www.phenix.bnl.gov/thesis.html>
- [106] Y. Akiba *et al*, Nucl. Instr. Method **A433**, (1999) 143-148.
- [107] Hamamatsu Photonics K.K., Hamamatsu 430, Japan
- [108] T. C. Awes, *et al*, Nucl. Instr. Method **A499**, (2003) 537-548.
- [109] T. Isobe, *et al.*, PHENIX Internal Analysis Note 444.
- [110] T. Horaguchi, PhD Thesis, <https://www.phenix.bnl.gov/thesis.html>
- [111] S. H. Aronson *et al.*, Nucl. Instr. Method **A499**, (2003) 480-488.
- [112] D. Bn-Tzvi and M. B. Sandler, Patt. Rec. Lett 11.
- [113] J. T. Michell *et al.*, Nucl. Instr. Method **A482**, (2002) 491-512.
- [114] J. Burward-Hoy, PhD Thesis, <https://www.phenix.bnl.gov/thesis.html>
- [115] J. T. Michell, PHENIX Technical Notes, 384.
- [116] K. Reygers, PHENIX Internal Analysis Note 169
- [117] X. N. Wang and M. Gyulassy, Comp. Phys. Comm. **83**, (1994) 307.
- [118] M. Allen *et al.*, Nucl. Instr. Method **A499**, (2003) 549-559.
- [119] K. Homma *et al.*, PHENIX Analysis Note 107, 286
- [120] J. Nagle *et al.*, PHENIX Analysis Note 113
- [121] B. J. Glauber and G. Matthiae, Nucl. Phys. **B21**, (1970) 135.
- [122] C. W. De Jager, H. De Vries and C. De Vries Atomic Data and Nuclear Data Tables **14**, (1974) 479.
- [123] PYTHIA v5.602 <http://www.thep.lu.se/~torbjorn/Pythia.html>
- [124] T. A. Armstrong *et al*. Phys. Rev. **D54**, (1996) 7067.

- [125] A. Spiridonov hep-ex/0510076
- [126] D. M. Kaplan *et al.*, Phys. Rev. Lett. **40**, (1978) 435.
- [127] J. Fleischer and F. Jegerlehner, Z. Phys. **C26**, (1985) 629.
- [128] C. Baglin *et al.*, (NA38 collaboration) Phys. Lett **B220**, (1989) 471.
- [129] M. C .Abreu *et al.*, (NA38 collaboration) Phys. Lett **B466**, (1999) 408.
- [130] B. Alessandro *et al.*, (NA50 collaboration) Eur. Phys. J. **C.33**, (2004) 31.
- [131] D. M. Alde *et al.*, Phys. Rev. Lett. **66**, (1991) 133.
- [132] M. J. Leitch *et al.*, (E866 Collaboration) Phys. Rev. Lett. **84**, (200) 3256.
- [133] R. Vogt nucl-th/0507027
- [134] A. Capella and E. G. Ferreira, nucl-th/0505032
- [135] E. Scomparin *et al.*, (NA60 Collaboration) Nucl. Phys. **A774**, (2006) 67.
- [136] S. H. Lee and T. Song, Journal of Physics: Conference Series **50**, (2006) 168.
- [137] X. N. Wang and F. Yuan, Phys. Lett. **B540**, (2002) 62.
- [138] R. Rapp, D. Cabrera and H. Van HEES nucl-th/0608033
- [139] R. Rapp Eur. Phys. J. **C43** (2005) 91, hep-ph/0502208
- [140] X. Zhu, P. Zhuang, Nu. Xu, Phys. Lett. **B607**, (2005) 107.
- [141] A. Andronic, P. Braun-Munzinger, K. Redlich and J. Stachel Phys. Lett. **B571**, (2003) 36.
- [142] A. Andronic, P. Braun-Munzinger, K. Redlich and J. Stachel nucl-th/0611023
- [143] P. Braun-Munzinger and J. Stachel, Phys. Lett. **B490**, (2000) 196.
- [144] M. I. Gorenstein, A. P. Kostyuk, *et al.*, Phys. Lett. **B509**, (2001) 277.
- [145] E. L. Bratkovskaya, W. Cassing, *et al.*, Phys. Rev. **C67**, (2003) 054905.
- [146] R. Thews, Phys. Rev. **C73**, (2006) 014904.
- [147] R. Thews, hep-ph/0511292
- [148] R. Rapp and J. Wambach, Adv. Nucl. Phys. **25**, (2000) 1.
- [149] S. S. Adler *et al.*, (PHENIX Collaboration), Phys. Rev. Lett, **94**, (2005) 082301.
- [150] A. Andronic, P. Braun-Munzinger, J. Stachel Nucl. Phys. **A772**, (2006) 167.

- [151] M. Cacciari, P. Nason, R. Vogt Phys. Rev. Lett. **95**, (2005) 122001.
- [152] B. B. Back *et al.*, (PHOBOS Collaboration) Phys. Rev. Lett. **88**, (2002) 022302.
- [153] W. Cassing, E. L. Bratkovskaya, S. Juchem Nucl. Phys. **A674**, (2000) 249.
- [154] S. Digal, P. Petreczky, H. Satz, Phys. Rev. **D64**, (2001) 094015.
- [155] F. Karsch, D. Kharzeev, H. Satz, Phys. Lett. **B637**, (2006) 75.
- [156] M. Sitta, *et al.*, (NA50 Collaboration), hep-ex/0405060
- [157] . P. F. Kolb, R. Rapp, Phys. Rev. **C67**, (2003) 044903.
T. Hirano, K. Tsuda, Phys. Rev. **C66**, (2002) 054905.
- [158] K. Adcox *et al.*, Nucl. Phys. **A757**, (2005) 184.
- [159] J. P. Blaizot, P. M. Dinh and J. Y. Ollitrault, Phys. Rev. Lett. **85**, (2000) 4012.
- [160] J. P. Blaizot, and J. Y. Ollitrault, Phys. Rev. Lett. **77**, (1996) 1703.
- [161] A. K. Chaudhuri nucl-th/0610031
- [162] T. Hirano and Y. Nara, Phys. Rev. Lett. **91**, (2003) 082301.
- [163] T. Hirano and Y. Nara, Phys. Rev. **C69**, (2004) 034908.
- [164] T. Hirano and K. Tsuda, Phys. Rev. **C66**, (2002) 054905.